# Non-classical thermal transport and phase change at the nanoscale

Marc Calvo Schwarzwälder

Supervised by Prof. Timothy G. Myers
and Prof. F. Xavier Alvarez Calafell

Submitted in fullfillment of the requirements
for the degree of Doctor in Philosophy in Applied Mathematics
in the Facultat de Matemàtiques i Estadística
at the Universitat Politècnica de Catalunya.

June 2019, Barcelona, Spain.

CENTRE DE RECERCA MATEMÀTICA

UNIVERSITAT POLITÈCNICA
DE CATALUNYA
BARCELONATECH

*"Not everything that counts can be counted,*

*and not everything that can be counted counts."*

William Bruce Cameron, 1963.

# Acknowledgments

Firstly, I thank my supervisors Tim, Xavi and Matt for their help, guidance and patience during these three years. They have taught me a lot and all of this would have never been possible without them. In particular, I want to thank Tim for opening the doors to applied mathematics, first during the course “Models Matemàtics de la Tecnologia” during my bachelor and later for supervising my master thesis jointly with Xavi. I would like to express my gratitude to Matt for his supervision, especially during the last stages of my PhD.

I wish to thank the people of the University of Limerick and MACSI, especially to Sarah Mitchell, for helping me to develop my research (and social) skills during those three months that I spent in Ireland. Thanks to Gary, Niall, Giannis, Kevin, Alycia and all the other MACSI people for those great times.

Special gratitude goes to all the current and former members of the Mathematical Industry Group of the CRM. Thanks to Helena, Vinnie, Matt, Claudia and Francesc for the good times and the nice experiences we have had together. Thanks as well to Victor, Gemma, Nuria and all the other students I have met during these three years at the CRM, as well as thanks to the CRM staff for their support during this period. In the same manner, I thank Marina, Guillem, Dani, Pau and all the other PhD students of the UPC with whom I have been living nice experiences since we were undergraduate students.

I would also like to thank Xavi’s research group of the UAB, especially Pol and Albert, for their help and for the nice results that we have found together.

Voldria expressar el meu agraïment cap a la meva família, a la meva mare Susanne, al meu pare Mariano i als meus germans Alex i Miriam. Agraeixo també als meus amics el haver-me donat suport al llarg d’aquest període. Gràcies a la Rita, a l’Àlex, al Sergio, al

Pat, a l'Iñaki, al Cristian, al Siles, al Ramu, al Sergi, al Dario, al Davidi a tota la colla amb la que vaig fer aquell viatge inoblidable per Tailàndia, entre molts d'altres.

En especial, estic molt agraït a la Lorena per haver estat al meu costat aquests darrers anys, tant en els moments bons com en els no tan bons. Sense ella, arribar fins aquí mai no hagués estat possible.

Finally, I would also thank the Fundació La Caixa for the financial support received during these three years, and the Mathematics for Industry Network and the Fundació Ferran Sunyer i Balaguer for funding my stays in Limerick and Oxford respectively.

Gràcies, de tot cor, a tots el que heu estat al meu costat.

Marc

# Abstract

For 200 years, Fourier's law has been used to describe heat transfer with excellent results. However, as technology advances, more and more situations arise where heat conduction is not well described by the classical equations. Examples are applications with extremely short time scales such as ultra fast laser heating, or very small length scales such as the heat conduction through nanowires or nanostructures in general. In this thesis we investigate alternative models which aim to correctly describe the non-classical effects that appear in extreme situations and which Fourier's law fails to describe.

A popular approach is the Guyer-Krumhansl equation and the framework of phonon hydrodynamics. This formalism is particularly appealing from a mathematical point of view since it is analogous to the Navier-Stokes equations of fluid mechanics, and from a physical point of view, since it is able to describe the physics in a simple and elegant way.

In the first part of the thesis we use phonon hydrodynamics to predict the size-dependent thermal conductivity observed experimentally in nanostructures such as nanowires or thin films. In particular, we show that the Guyer-Krumhansl equation is suitable to capture the dependence of the thermal conductivity on the size of the physical system under consideration. During the modelling process we use the analogy with fluids to incorporate a slip boundary condition with a slip coefficient that depends on the ratio of the phonon mean free path to the characteristic size of the system. With only one fitting parameter we are able to accurately reproduce experimental observations corresponding to nanowires and nanorods of different sizes.

The second part of the thesis consists of studying the effect of the non-classical features on melting and solidification processes. We consider different extensions and incorporate them into the mathematical description of a solidification process in a simple, one-dimensional geometry. In chapter 5 we employ an effective Fourier law which replaces the original thermal conductivity by a size-dependent expression that accounts for non-local effects. In chapter 6 we use the Maxwell-Cattaneo and the Guyer-Krumhansl equations to formulate the Maxwell-Cattaneo-Stefan and the Guyer-Krumhansl-Stefan problems respectively. After performing a detailed asymptotic analysis we are able to reduce both models to a system of two ordinary differential equations and obtain excellent agreement with the corresponding numerical solutions. In situations near Fourier resonance, which is a particular case where non-classical effects in the Guyer-Krumhansl model cancel each other out, the solidification kinetics are very similar to those described by the classical model. However, in this case we see that non-classical effects are still observable in the evolution of the heat flux through the solid, which suggests that this is a quantity which is more convenient to determine the presence of these effects in phase change processes.

# Resum

La llei de Fourier ha estat una peça clau per a descriure la conducció de calor des de que fou proposada fa gairabé 200 anys. No obstant, a mesura que avança la tecnologia ens hi trobem més sovint amb situacions on les equacions clàssiques perden la seva validesa. En aquesta tesi investiguem alguns models alternatius que tenen com a objectiu descriure la conducció de calor en situacions on la llei de Fourier no és aplicable.

Un model que ha aconseguit establir-se com un extensió vàlida de la llei de Fourier és l'equació de Guyer-Krumhansl i el marc de la hidrodinàmica de fonons derivat d'aquesta. Es tracta d'un model particularment interessant, ja que les equacions són anàlogues a les equacions per a fluids dins de la hidrodinàmica clàssica. A la primera part de la tesi considerem aquesta equació per a descriure la conducció de calor estàtica per nanofibres de seccions transversals circulars i rectangulars. En particular, calculem una conductivitat tèrmica efectiva i trobem que és possible reproduïr els resultats experimentals amb un sol paràmetre d'adjust. En el cas de nanofibres cilíndriques, no és necessari cap paràmetre d'adjust si es consideren unes certes condicions de vora per al flux.

Una conseqüència d'haver de considerar extensions per a la llei de Fourier és que s'ha d'estudiar l'efecte que tenen aquests canvis en la descripció de processos de canvi de fase. En la segona part de la tesi investiguem els efectes que tenen diversos models sobre la solidificació d'un líquid unidimensional. Al capítol 5 estudiem el cas en el que considerem la conductivitat tèrmica com a una funció de la mida del sòlid i que incorpora característiques que són importants quan el tamany del sòlid és comparable a les longituds característiques dels fonons, mentres que al capítol 6 extenem la llei de Fourier incorporant termes d'ordres superiors. En ambdós casos, un anàlisi asimptòtic ens permet reduïr la complexitat del problema i proposar models reduïts formats per un parell de'equacions diferencials ordinàries.

Els resultats demostren que hi han casos on els efectes de nanoescala es cancel·len mutuament i on els nous models reprodüeixen el comportament clàssic, tot i que es poden observar diferències quantitatives més important en el cas del flux de calor que creua el sòlid.

# Outline

Chapters 1 and 2 introduce the reader to the topic. In chapter 1 we briefly introduce the basics of nanotechnology and review the classical equations for describing heat conduction and phase change phenomena. The motivations for investigating extensions to these classical equations and some popular models that can be found in the literature are explained in chapter 2.

The main body of this dissertation consists of chapters 3 to 6. These are presented in the form of research articles and hence they include a specific introductions and conclusions, which allows for an independent reading. Chapters 3 and 4 present a mathematical model to describe heat transfer mechanism in nanostructures as it is observed in experimental studies. These chapters have already been published [40, 41]. In chapters 5 and 6 we focus on the mathematical analysis of Stefan problems which incorporate non-Fourier constitutive laws to account for non-classical phenomena. These chapters have been submitted recently [38, 39].

Finally, chapter 7 contains a summary of the conclusions of each chapter, as well as some concluding remarks.

# List of publications

Publications 1 to 4 correspond to chapters 3 to 6 respectively. Publications 7 to 12 correspond to additional work where I did not lead the research.

1. M. Calvo-Schwarzwälder, M. G. Hennessy, P. Torres, T. G. Myers, F. X. Alvarez. *A slip-based model for the size-dependent effective thermal conductivity of nanowires.* International Communications in Heat and Mass Transfer 91: 57–63, 2018. Q1 in Condensed Matter Physics.

2. M. Calvo-Schwarzwälder, M. G. Hennessy, P. Torres, T. G. Myers, F. X. Alvarez. *Effective thermal conductivity of rectangular nanowires based on phonon hydrodynamics.* International Journal in Heat and Mass Transfer 126: 1120–1128, 2018. Q1 in Condensed Matter Physics.

3. M. Calvo-Schwarzwälder. *Non-local effects and size-dependent properties in Stefan problems with Newton cooling.* To appear in Applied Mathematical Modelling (submitted Feb. 2019, revised Apr. 2019). Q1 in Modelling and Simulation. arXiv:1902.00401

4. M. Calvo-Schwarzwälder, T. G. Myers, M. G. Hennessy. *The one-dimensional Stefan problem with non-Fourier heat conduction.* To appear in International Journal of Heat and Mass Transfer (submitted May 2019). Q1 in Condensed Matter Physics. arXiv:1905.06320

5. M. Calvo-Schwarzwälder. *A non-local formulation of the one-phase Stefan problem based on extended irreversible thermodynamics.* Research Perspectives CRM Barcelona, Summer 2018, Vol. 11. In: Trends in Mathematics Springer-Birkhäuser, Basel, 2019.

6. M. Calvo-Schwarzwälder, P. Torres, M. G. Hennessy, T. G. Myers, F. X. Alvarez. *Thermal transport equations and boundary conditions at the nanoscale.* To appear in Progress in Industrial Mathematics at ECMI 2018 (accepted Apr. 2019).
7. A. Beardo, M. Calvo-Schwarzwälder, J. Camacho, T. G. Myers, P. Torres, L. Sendra, F. X. Alvarez, J. Bafaluy. *Hydrodynamic heat transport in compact and holey silicon thin films.* Physical Review Applied 11: 034003, 2019. Q1 in Physics and Astronomy.
8. M. G. Hennessy, M. Calvo-Schwarzwälder, T. G. Myers. *Modelling ultra-fast nanoparticle melting with the Maxwell–Cattaneo law.* Applied Mathematical Modelling 69: 201–222, 2019. Q1 in Modelling and Simulation.
9. M. G. Hennessy, M. Calvo-Schwarzwälder, T. G. Myers. *Asymptotic analysis of the Guyer-Krumhansl-Stefan model for nanoscale solidification.* Applied Mathematical Modelling 61: 1–17, 2018. Q1 in Modelling and Simulation.
10. T. G. Myers, M. G. Hennessy, M. Calvo-Schwarzwälder. *The Stefan problem with variable thermophysical properties and phase change temperature.* To appear in SIAM Review (submitted Apr. 2019). Q1 in Applied Mathematics. arXiv:1904.05698
11. V. Cregan, T. G. Myers, S. L. Mitchell, H. Ribera, M. Calvo-Schwarzwälder. *Nanoparticle Growth via the Precipitation Method.* Progress in Industrial Mathematics at ECMI 2016: 357–364, 2018.
12. R. Bacsa, W. Bacsa, M. Calvo-Schwarzwälder, V. Cregan (report coordinator), M. Fernandez-Pendas, S. Fernandez-Mendez, B. Florio, N. Gómez Bastus, A. Marquina, I. Moyles, T. G. Myers, H. Ribera, S. Rusconi, S. Serna, C. Vázquez-Cendón, J. Piella. *Synthesis of monodisperse spherical nanocrystals.* Proceedings of the 115th ESGI, Centre de Recerca Matemàtica (Spain), 2016.

# Contents

# List of Figures

# List of Tables

# 1 | Introduction

## 1.1 Introduction to nanotechnology

The National Nanotechnology Initiative[1] defines nanotechnology as "the understanding and control of matter at the nanoscale, at dimensions between approximately 1 and 100 nanometres, where unique phenomena enable novel applications". Its focus lies on synthesizing, manipulating and understanding the properties of nanostructures as well as on developing applications and new technologies based on them. Famous examples of nanostructures are nanoparticles, carbon nanotubes (CNTs) or graphene layers. An example of nanoparticles during their synthesis is shown in Fig. 1.1.

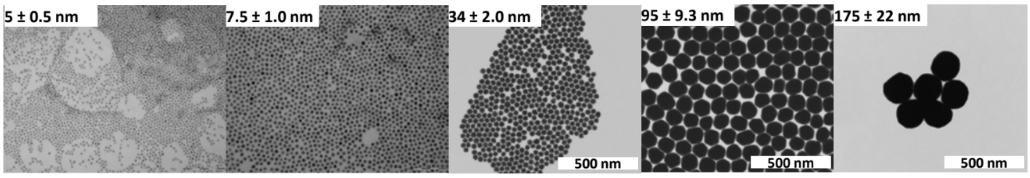

**Figure 1.1:** Gold nanoparticles with different size distributions observed by the Inorganic Nanoparticles Group at the Institut Català de Nanociència i Nanotecnologia (ICN2). The numerical values of the form $d^* \pm \sigma^*$ correspond to the mean diameter $d^*$ and the standard deviation $\sigma^*$.

In his talk entitled "There's Plenty of Room at the Bottom" given in 1959 at the California Institute of Technology, Richard Feynman opened the doors to the nanoscale by describing how to enable scientists to manipulate basic units of matter like single atoms or molecules [92]. However, the concept of nanotechnology did not appear until 1974, when it was introduced by the Japanese scientist Norio Taniguchi [227], who later, in 1999, received the 1st Lifetime Achievement Award by the European Society for Precision Engineering and

---

[1] https://www.nano.gov/

Nanotechnology in Bremen.

### 1.1.1 Applications of nanotechnology

In the last decade, nanoscience has become a very important research area of science. As will be explained later, nanostructures can exhibit large differences in their thermal, electrical, optical or chemical properties with respect to macroscale (bulk) materials. Moreover, nanostructures can be designed to have specific features, which allows them to be used in a wide range of areas. A large number of applications for nanodevices has been developed in the last decades, but making progress in theoretical and experimental research will provide tools for creating many more.

Due to the advances in engineering during the 20th century, companies have been able to produce transistors of sizes of the order of few nanometres [8, 194]. These structures are the building blocks for microprocessors and their size has been successfully reduced by more than 3 orders of magnitude in the last 45 years. The evolution in time of the size of the transistors is shown in Fig. 1.2 and is described by Moore's law [174], which originally predicted that the number of transistors in an integrated circuit would double every year.

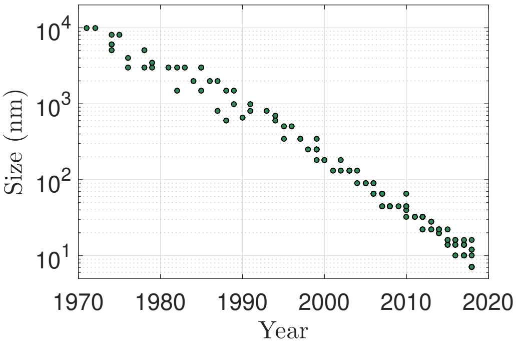

**Figure 1.2:** Evolution of the transistor size in the period 1974–2018. This trend was predicted by Moore and is known as Moore's law [174].

Nowadays, nanotechnology finds applications in many different areas. Some examples for

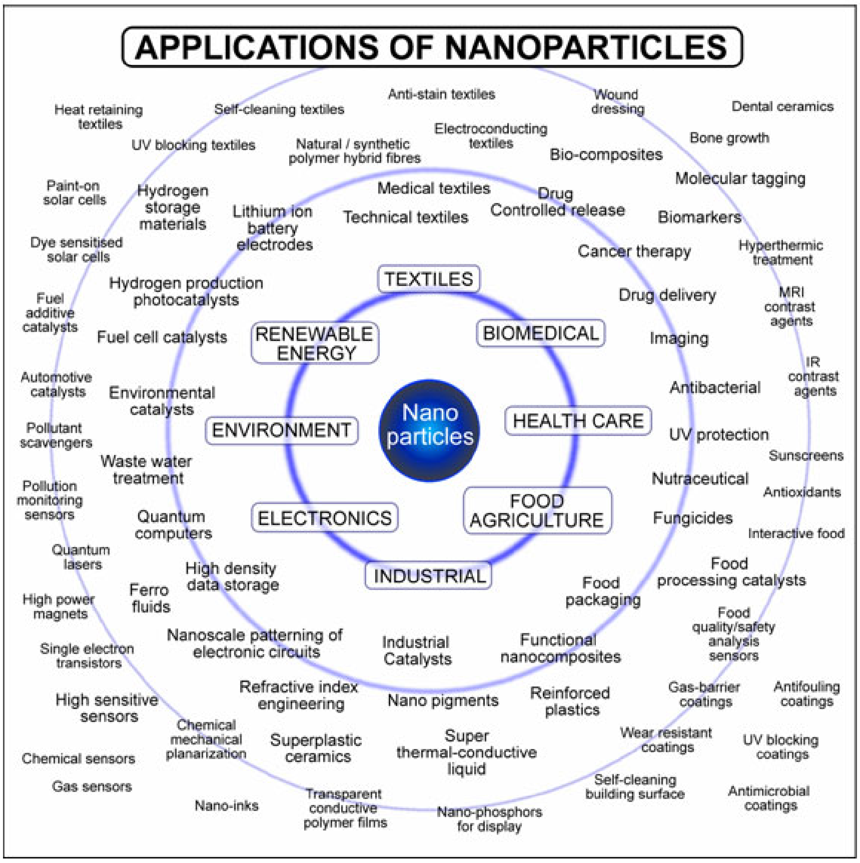

**Figure 1.3:** Chart taken from [236] which shows the large number of areas where applications of nanoparticles can be found.

the specific case of nanoparticles are listed in Fig. 1.3[2]. For instance, nanoparticles are used for the detection of cancer biomarkers [56] or in drug delivery systems during cancer therapies [57]. It has also been shown that the performance of batteries can be enhanced by using hollow nanoparticles [261]. We can even find applications in the textile industry, where nanotechnology has been used to develop water-resistant coatings or UV-protective clothing [208]. In electronics, quantum dots have been recently employed to create the quantum-dot enhanced film (QDEF)[141], a technology that can be found already in some TV displays in the market.

Apart from nanoparticles, many other nanostructures can be found in industrial applica-

---

[2] This chart has been provided by Inderscience Enterprises Ltd. Inderscience retains the copyright of the figure and original article from which the figure is taken.

tions. Nanowires, for instance, are used for the development of flexible screens [154] or long life lithium batteries [89]. Due to the remarkable electrical, thermal and mechanical properties of carbon nanotubes, these are used in energy storage or to reinforce composites with large strength-to-weight ratio, for example [3]. It has been shown that the steel of the Damascus blades contains carbon nanotubes [198], although this fact may be treated as anecdotal, since the required technology for deliberately manipulating these nanotubes did not exist at that time. On another note, graphene layers can be found in memory devices, electron absorbers or in light absorbers [48]. The thermal properties of semiconductor films and superlattices such as silicon or silicon-germanium can be exploited to develop highly efficient thermoelectric devices [29, 142, 204, 242], which are capable of converting thermal energy into electricity and vice versa.

### 1.1.2 Nanoscale vs. Macroscale

The increasing activity in nanoscale research is mostly attributed to the fact that, contrary to their macroscopic counterparts, nanostructures can exhibit a strong size- and shape-dependence of their chemical, electrical, thermal, optical, etc. properties and hence unexpected behaviour may occur. For instance, carbon nanotubes can act as conductors or insulators depending on how they are assembled [17]. In Fig. 1.4a it is shown how the size of gold nanoparticles can change the color of solutions containing them.

Since the focus of this work lies on heat transport, we will now briefly discuss some of the thermal properties which exhibit differences with respect to bulk materials. For instance, Buffat and Borel [28] observed that the melting temperature of a nanoparticle with a size around 2 nm can be up to 500 K less than for macroscopic objects. Molecular dynamics has provided data even below the nm regime [213]. This phenomenon is known as melting point depression and has also been studied for materials such as zinc oxide [98], tin [137] or aluminium [226], for example. The case of tin is shown in Fig. 1.4b. In the context of melting nanoparticles, a strong size-dependence of the latent heat release has been reported by several authors by means of experimental observations [123, 137] or molecular dynamics simulations [14, 67, 77, 148]. These simulations showed that the decrease in latent heat of tin nanoparticles was approximately of 45%, whereas the melting temperature shows a decrease of only 25% [14].

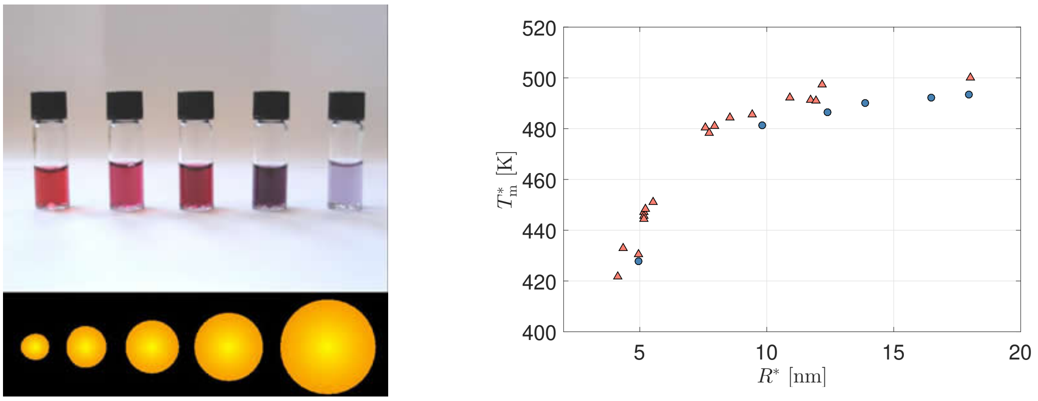

**(a)**

**(b)**

**Figure 1.4:** (a) Suspensions containing gold nanoparticles of different sizes. (b) Experimental observations of the melting temperature of tin nanoparticles with different radii. Triangles and circles correspond to data from Refs. [137, 254].

In addition to melting temperature and latent heat release, experimental observations show that thermal conductivity exhibits a strong dependence on the characteristic size of the device [55, 121, 142, 145, 200, 222], which is critical for applications involving heat removal [94] or for developing highly efficient thermoelectric devices [142], for instance. The object of interest for the latter are usually semiconducting materials such as silicon or gallium arsenide, due to their unique thermoelectrical properties [92, 266]. Some experimental results that can be found in the literature are listed in Table 1.1. It can be clearly observed how the thermal conductivity decreases drastically with the size of the nanowire, up to 83% in the case of silicon and 71% in the case of bismuth telluride. In these semiconducting materials, this reduction corresponds mainly to the contribution of phonons to heat transfer, which allows these materials to increase their thermoelectrical efficiency [92, 202, 266]. Being able to control and predict this phenomenon, known as phonon suppression [54, 120, 176], is crucial for making progress in thermoelectrics.

The size-dependence of the material properties is partially attributed to the increase of the ratio of surface-to-volume atoms. If we think of a cube formed by $n^3$ unit cubes (which here we take to represent atoms), it is easy to show that the number of units at the surface of the cube is given by $\mathcal{S}(n) = 6(n-1)^2 + 2$. For large values of $n$, we have $\mathcal{S}(n)/n^3 \ll 1$, i.e. the number of surface atoms is much less than the total number of atoms. However,

**Table 1.1:** Thermal conductivity of semiconductor nanowires of different sizes measured at 300 K.

| Material | Diameter [nm] | Thermal conductivity [W/mK] | Ref. |
|---|---|---|---|
| Si | 115 | 40.83 | [145] |
| Si | 56 | 25.68 | [145] |
| Si | 37 | 17.63 | [145] |
| Si | 22 | 6.86 | [145] |
| $Bi_2Te_3$ | 300 | 1.78 | [200] |
| $Bi_2Te_3$ | 52 | 0.72 | [200] |
| $Bi_2Te_3$ | 45 | 0.58 | [200] |
| $Bi_2Te_3$ | 25 | 0.52 | [200] |
| $Si_{0.9}Ge_{0.1}$ | 45 | 2 | [142] |
| $Si_{0.81}Ge_{0.19}$ | 62 | 1.6 | [142] |
| $Si_{0.59}Ge_{0.41}$ | 65 | 1.05 | [142] |

this ratio increases as we decrease the number of units forming the cube. In a cube formed by $3^3$ units, this ratio is $26/27 \approx 0.96$ whereas for $n = 2$ all the units are on the surface. On one hand, a larger surface-to-volume ratio implies that more atoms are in contact with the environment of the particle and thus reactions with the environment are more likely to happen. On the other hand, bonds between atoms are weaker at the surface since less atoms are bonded with each other, which, for instance, decreases the amount of energy required to break these bonds and thus decreases the melting temperature of the nanostructure, for example.

Many applications require knowledge about the thermal response of the specific device. In some cases, understanding the melting or solidification behaviour at small length- and time scales is also necessary. The goal of this dissertation, which will be described more in detail in Sec. 2.4, is extending the classical descriptions of heat transfer to more general models which are valid at the nanoscale and use these to adapt the description of phase change processes. However, before discussing possible extensions to the classical formulations, it will be insightful to briefly review the classical equations.

## 1.2 Introduction to heat transfer

In the first part of this dissertation we study different extensions of the classical equations and discuss their applicability to situations arising from nanotechnological applications. It is therefore insightful to briefly review the basic aspects of the classical theory. In the following sections we will introduce the reader to the classical heat transfer equations, boundary conditions and solution methods.

### 1.2.1 Fourier's law of heat conduction

Thermal conduction is the energy transport due to molecular activity. From a microscopic point of view we must distinguish two types of media. In fluids, which includes liquids and gases, heat conduction occurs due to the random collisions among molecules. In this way, energy is transferred from more energetic molecules to less energetic ones. In solids heat conduction occurs due to two phenomena: in conducting materials such as metals, heat conduction is dominated by the motion of free electrons, whereas for non- or semiconducting solids it is dominated by lattice vibrations, which can be understood as the motion of quasi-particles called phonons. In both cases, the collisions result in heat transport which occurs predominantly down a temperature gradient.

**Figure 1.5:** Lithograph of the French physicist and mathematician Jean-Baptiste Joseph Fourier (1768–1830) made by Jules Boilly in 1823 and displayed in the Academy of Sciences in Paris.

In the 19th century, these microscopic descriptions were not available to scientists and hence physical phenomena could only be described and studied by means of empirical laws (known as phenomenological laws). Additionally, the mathematical formulation of thermodynamics and the theory of differential equations were still in their initial stages and the mathematical tools that researchers had at their disposal were limited.

In 1822, the French physicist and mathematician Jean-Baptiste Joseph Fourier published his personal masterpiece “Théorie analytique de la chaleur” [86], making him the first scientist to mathematically describe heat conduction in solids. Previously another French man, Jean-Baptiste Biot, had published an article on heat diffusion in solids [23], but it was later proven that he had failed in the mathematical description [95, 184]. Nevertheless, Biot’s work was undoubtfully helpful for Fourier, who did acknowledge Biot’s contributions in an unpublished draft [95]. Surprisingly, Fourier’s contribution to science, which is nowadays recognized as one of the most valuable in history, did not receive a warm welcome. In fact, he had presented this theory already fiteen years previously, in 1807, in a paper called “Théorie de la Propagation de la Chaleur dans les Solides”, but this work had been rejected due to objections of researchers like Laplace, Lagrange and Biot himself.

Despite continuous criticism of Fourier’s first studies, his work was published by the time he was elected Secretary of the French Academy of Sciences. In his manuscript, Fourier postulated that heat flow was governed by a simple law, namely that the heat flux and temperature gradient were negatively proportional, i.e., that heat flows from hot regions to colder ones. The constant of proportionality was called “internal coefficient of conductibility”, but it is known nowadays as thermal conductivity. Originally, it was presented as an intrinsic property of every material, and hence independent of size or shape.

The work done by Fourier preceded similar phenomenological laws in other areas of physics. In a mixture, Fick’s law states that particles move from high to low concentrations [80] and is therefore completely analogous to Fourier’s law. Similarly, Darcy’s law is used to describe fluid flow through porous media relating the fluid velocity to a pressure gradient [63]. In electrodynamics, a current density and an electric field are proportionally related via Ohm’s law [187]. The Schrödinger equation in quantum mechanics [70, 97] can be understood as the heat equation arising from Fourier’s law with imaginary-valued thermal properties. Even in mathematical finance Fourier’s heat equation is used to describe the evolution in time of the prices of European Calls via the Black-Scholes equation [117, 206].

### 1.2.2 Governing equations

Fourier's law takes the form

$$\boldsymbol{Q}^* = -k^* \nabla T^*, \tag{1.1}$$

where $\boldsymbol{Q}^*$ is the heat flux, $\nabla T^*$ is the gradient of the temperature and $k^*$ is the thermal conductivity (originally termed the internal coefficient of conductibility). To provide a complete mathematical description of a heat conduction process, Eq. (1.1) has to be coupled to the equation of *conservation of internal energy*, which for a medium moving at a speed $\boldsymbol{v}^*$ reads

$$\rho^* \frac{\partial u^*}{\partial t^*} + \rho^* \nabla u^* \cdot \boldsymbol{v}^* + \nabla \cdot \boldsymbol{Q}^* = S^*, \tag{1.2}$$

where $\rho^*$ is the density, $u^*$ is the internal energy per unit mass and $S^*$ is a source (or sink) term. In Eq. (1.2), the second term corresponds to the energy being convected, whereas the third term refers to the energy being conducted through the boundary. Implicitly, in writing conservation of internal energy in this way we are neglecting gravity and effects related to pressure and viscosity [4]. Internal energy and temperature are usually related in terms of their differentials,

$$\mathrm{d}u^* = c^* \mathrm{d}T^*, \tag{1.3}$$

where $c^*$ is the specific heat of the medium. Combining Eqs. (1.1)–(1.3) yields, in absence of energy sources ($S^* \equiv 0$) and for a stationary medium ($\boldsymbol{v}^* \equiv 0$),

$$\rho^* c^* \frac{\partial T^*}{\partial t^*} = \nabla \cdot (k^* \nabla T^*), \tag{1.4}$$

which is known as the classical heat equation (CHE). Since $k^*$ is in reality a function of the temperature, Eq. (1.4) is actually non-linear. However, it is very common to neglect the dependence on the temperature of all parameters and to assume that they have a constant value, which yields

$$\frac{\partial T^*}{\partial t^*} = \alpha^* \nabla^2 T^*, \tag{1.5}$$

where $\alpha^* = k^*/(\rho^* c^*)$ is called the thermal diffusivity and $\nabla^2$ is the Laplacian operator. Mathematically, Eq. (1.5) describes heat conduction as a diffusive process governed by random collisions of the heat carriers.

A classical example, shown in Fig. 1.6, consists of a semi-infinite bar, initially at a constant temperature $T_0^*$, which is put in contact with an environment that has a higher

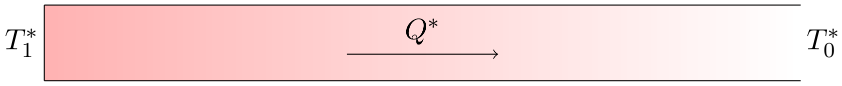

**Figure 1.6:** Conductive heat flux $Q^*$ through a semi-infinite bar, induced by a temperature difference $T_1^* - T_0^*$.

temperature $T_1^*$. The sudden temperature jump $T_1^* - T_0^* =: \Delta T^*$ creates a heat flux through the bar. According to Fourier's law, in this case the temperature is determined by the one-dimensional version of Eq. (1.5)

$$\frac{\partial T^*}{\partial t^*} = \alpha^* \frac{\partial^2 T^*}{\partial {x^*}^2}. \tag{1.6}$$

### 1.2.3 Boundary conditions

There is a wide spectrum of boundary conditions that can be used depending on the physical situation considered. The most common ones take the form [206]

$$a_1 T^* + a_2 \boldsymbol{Q}^* \cdot \boldsymbol{n} = a_3, \tag{1.7}$$

for some (not necessarily constant) coefficients. Boundary conditions of the form of Eq. (1.7) can be divided into *Dirichlet* ($a_1 \neq 0$, $a_2 = 0$), *Neumann* ($a_1 = 0$, $a_2 \neq 0$) and *Robin* ($a_1, a_2 \neq 0$) boundary conditions. Physically, the Dirichlet boundary condition represents that the temperature is fixed to a certain value at the boundary, whereas the Neumann conditions prescribes a given heat flux. The third choice, also termed a *radiation* condition, prescribes a heat flow at the boundary that is proportional to the difference $T^* - a_3/a_1$, which may be understood as the temperature difference at either side of the boundary.

Consider now the situation shown in Fig. 1.6. A first choice of boundary condition at $x^* = 0$ is

$$T^* = T_1^*, \qquad \text{at } x^* = 0. \tag{1.8}$$

We will refer to this condition as the fixed-temperature (FT) condition. Since the bar is assumed semi-infinite, we can assume that the change in temperature at $x^* = 0$ becomes negligible as $x^* \to \infty$, hence

$$T^* = T_0^*, \qquad \text{as } x^* \to \infty. \tag{1.9}$$

Finally, an initial condition for the temperature must be given. For the example considered in Fig. 1.6, this means assuming

$$T^* = T_0^*, \qquad \text{at } t^* = 0. \tag{1.10}$$

### 1.2.4 Non-dimensional formulation

Once the governing equations and the corresponding boundary conditions are given, the problem is brought into a non-dimensional form by scaling each of the variables with a typical value. In this way, one can determine the contribution of each term and the dominant effects in each of the different time regimes in which a specific problem might be divided.

For the example depicted in Fig. 1.6, the scale for the temperature is determined by the temperature difference across the wall $\Delta T^*$. Note, there is no natural length scale, hence we introduce an arbitrary scale $L^*$. Upon introducing a time scale $\tau^*$, we define the following non-dimensional quantities:

$$x = \frac{x^*}{L^*}, \quad t = \frac{t^*}{\tau^*}, \quad T = \frac{T^* - T_0^*}{\Delta T^*}. \tag{1.11}$$

In terms of these variables, Eq. (1.6) becomes

$$\frac{\partial T}{\partial t} = \frac{\tau^* \alpha^*}{L^{*2}} \frac{\partial^2 T}{\partial x^2}, \tag{1.12}$$

which suggests that the time scale should be chosen to be $\tau_D^* = L^{*2}/\alpha^*$ to balance the terms on either side of Eq. (1.12). For simplicity, we rewrite the differential operators as subindices, i.e., we write $\partial/\partial t = \Box_t$ and $\partial^2/\partial x^2 = \Box_{xx}$. The non-dimensional CHE then takes the form

$$T_t = T_{xx}. \tag{1.13a}$$

Since the chosen time scale balances the rate of change of the temperature with the diffusion process, it is often called the diffusive time scale. The non-dimensional boundary and initial conditions are

$$T = 1, \qquad \text{at } x = 0., \tag{1.13b}$$

$$T \to 0, \qquad \text{as } x \to \infty, \tag{1.13c}$$

$$T = 0, \qquad \text{at } t = 0. \tag{1.13d}$$

### 1.2.5 Solution methods

There exists a large number of strategies for solving a problem such as that defined by Eqs. (1.13). Typically, these can be divided into three categories: exact, approximate and numerical methods. Numerical methods do only provide solutions without giving any additional information to the specific problem and exact solutions may only exist in ideal situations, therefore approximate methods are crucial for providing physical understanding and making analytical progress in the problem under consideration.

#### Laplace transform

A common strategy to find analytical expressions is to transform the problem by means of integral transformations. The advantage is that the resulting equations are often much easier to solve. Unfortunately, inverting these transformations is usually difficult and numerical methods need to be employed to find the solution in the original variables.

For an arbitrary function $f(t)$, the Laplace transform is defined as

$$\mathcal{L}\left[f(t), t, \omega\right] = \int_0^\infty f(t)\exp(-\omega t)dt. \tag{1.14}$$

Due to this definition, when a function is said to be defined on a time-domain, its Laplace transform is said to be defined over the frequency-domain, since the dimensional form of $\omega$ must have dimensions of $t^{*-1}$. In the literature, the variable $s$ is often used instead of $\omega$. However, to avoid confusions with the solid-liquid interface that we will define in the next section, we will utilize the alternative variable $\omega$.

In terms of $U = \mathcal{L}\left[T(x,t), t, \omega\right]$, Eq. (1.13a) becomes

$$U_{xx} + \omega U = 0, \tag{1.15}$$

whose general solution is

$$U(x,\omega) = a_1\exp(\sqrt{\omega}x) + a_2\exp(-\sqrt{\omega}x). \tag{1.16}$$

The transformed boundary conditions are

$$U = \omega^{-1}, \qquad \text{at } x = 0, \tag{1.17a}$$

$$U \to 0 \qquad \text{as } x \to \infty. \tag{1.17b}$$

Applying Eq. (1.17) on Eq. (1.16) yields $a_1 = 0$ and $a_2 = \omega^{-1}$, hence

$$U(x, \omega) = s^{-1} \exp(-\sqrt{\omega} x). \tag{1.18}$$

The inverse transform of the latter is

$$T(x, t) = 1 - \operatorname{erf}\left(\frac{x}{2\sqrt{t}}\right), \tag{1.19}$$

where $\operatorname{erf}(\cdot)$ is the error function,

$$\operatorname{erf}(z) = \frac{2}{\sqrt{\pi}} \int_0^z \exp(-t^2) \mathrm{d}t. \tag{1.20}$$

In general, inverting a Laplace transform is extremely difficult and usually requires the use of numerical methods. Hence, when it is not possible to find an analytical expression, this method reduces to a numerical approach. However, it many cases it is possible to evaluate the inverse transformation at specific points of the domain such as the boundary, for instance. The solution obtained in the frequency-domain is also often used to study the properties of the solution in terms of the original variables.

Note, Eq. (1.19) implies that $T > 0$ for $x, t > 0$, i.e. the disturbance at the boundary is felt instantly in any point of the medium. This suggests that, according to Fourier's law, heat is transported with an infinite speed of propagation.

### Similarity solution

In some problems it is possible to find a solution in terms of similarity variables. For the heat equation, this method is suggested by the fact that the problem has no independent time- and length scales.

If we consider a variable $y$ of the form $y = axt^b$ ($a > 0$, $b \neq 0$) and assume $T(x, t) = f(y)$, then Eq. (1.13a) becomes

$$byf_y - a^2 t^{2b+1} f_{yy} = 0, \tag{1.21}$$

which suggests $b = -1/2$. Upon setting $a = \sqrt{2}/2$, we find that $f$ satisfies

$$yf_y + f_{yy} = 0, \tag{1.22}$$

subject to

$$f = 1, \qquad \text{at } y = 0, \tag{1.23a}$$

$$f \to 0, \qquad \text{as } y \to \infty. \tag{1.23b}$$

Integrating Eq. (1.22) twice and applying the boundary conditions gives the same solution as that obtained using the Laplace transform.

### Numerical solution

In a finite domain, Eq. (1.13a) can be easily integrated numerically using a finite differences scheme [217]. Assume that the bar has a finite length $L^*$, where $L^*$ is sufficiently large such that $T^*(L^*, t^*) = T_0^*$ until the time when integration stops. In the dimensionless variables this means that we replace Eq. (1.13c) by $T(1, t) = 0$.

A typical finite difference scheme consists of discretizing the space into a grid of $N + 1$ points of the form $x_i = i/N$ $(i = 0, ..., N)$ and time into points of the form $t_n = n\Delta t$ for a sufficiently small value $\Delta t$. The temperature can then be discretized in two ways, explicitly or implicitly. The first approach transforms the problem into $N + 1$ ordinary differential equations that have to be solved at each time step, the second approach leads to a system of $N + 1$ algebraic equations with $N + 1$ unknowns that has to be solved at every time step $n$. The second one is computationally more expensive, but it can be shown that it is always stable whereas the stability of the first methods depends on the choice of $\Delta t$ and $N$. A family of methods, called $\theta$-methods, combine both implicit and explicit methods. For $\theta = 1/2$, the methods is known as the Crank-Nicholson method [60].

Using the implicit discretization, the derivates in Eq. (1.13a) may be approximated using second-order differences for $x$:

$$T_t \approx \frac{T_i^{n+1} - T_i^n}{\Delta t}, \qquad T_x \approx \frac{T_{i+1}^{n+1} - T_{i-1}^{n+1}}{2\Delta x}, \qquad T_{xx} \approx \frac{T_{i+1}^{n+1} - 2T_i^{n+1} + T_{i-1}^{n+1}}{(\Delta x)^2} \tag{1.24}$$

where $\Delta x = N^{-1}$. The heat equation is then reduced to a set of $N - 1$ algebraic equations of the form

$$-\frac{\Delta t}{(\Delta x)^2} T_{i-1}^{n+1} + \left(1 + 2\frac{\Delta t}{(\Delta x)^2}\right) T_i^{n+1} - \frac{\Delta t}{(\Delta x)^2} T_{i+1}^{n+1} = T_i^n, \tag{1.25}$$

whereas the boundary conditions simply become

$$T_0^{n+1} = 1, \qquad T_{N+1}^{n+1} = 0, \tag{1.26}$$

The discretized initial conditions are

$$T_i^0 = 0, \qquad 0 \le i \le N + 1. \tag{1.27}$$

Upon defining $\boldsymbol{T}^n = (T_0^n, ..., T_N^n)$, the numerical scheme provides a temperature profile at each time step $n$ by solving the linear system $A\boldsymbol{T}^{n+1} = B\boldsymbol{T}^n + \boldsymbol{e}_1$, where the matrices $A, B \in \mathbb{R}^{(N+1)\times(N+1)}$ are defined by Eqs. (1.25) and (1.26) and $\boldsymbol{e}_1 = (1, 0, ...0)$. The initial condition is $\boldsymbol{T}^0 = (0, ..., 0)$.

### Approximate solution methods

Since the heat equation is linear, it is possible to find exact solutions as infinite sums of products of the form $a_n(t)\psi_n(x)$. This method is known as separation of variables or, more generally, as an eigenfunction expansion. It was developed by Fourier to solve his recently derived heat equation [86]. However, the fact that the solution consists of a sum of infinitely many terms which has to be truncated after a finite number of terms, this method is classified as approximate rather than an exact approach. However, in practise only a small number of terms is usually required in practise to obtain good agreement with numerical or exact solutions.

Another popular family of approximate solution methods are the ones derived from the heat balance integral method (HBIM) [93]. This method consists of approximating the solution by a polynomial of the form

$$T(x,t) \approx a\left(1 - \frac{x}{\delta}\right)^n, \tag{1.28}$$

where $\delta = \delta(t)$ is called the penetration depth. It represents an artificial length which refers to the smallest distance from where changes in temperature can be neglected, i.e., $T(x,t) \approx 0$ for $x \geq \delta$. The boundary condition at infinity can therefore be replaced by

$$T = 0, \qquad \text{at } x = \delta. \tag{1.29}$$

The simplest example is the quadratic approximation, i.e. setting $n = 2$. In other integral methods which extend the $n = 2$ form, the exponent is chosen to minimize a certain error measure (TIM) [177] or as a function of time which has to be determined as part of the solution (RIM) [172, 203].

For this example, let us fix $n = 2$. Substituting Eq. (1.28) into Eq. (1.13b) yields $a = 1$. To determine $\delta$, we integrate the heat equation over the domain $[0, \delta(t)]$ to obtain the heat balance integral

$$\frac{\mathrm{d}}{\mathrm{d}t}\int_0^\delta T dx - T(\delta, t)\delta' = [T_x]_0^\delta, \tag{1.30}$$

where we have applied Leibniz' formula on the left hand side. Applying the boundary conditions and substituting Eq. (1.28) we can reduce this to

$$\frac{1}{3}\frac{\mathrm{d}\delta}{\mathrm{d}t} = \frac{2}{\delta}, \tag{1.31}$$

which, using $\delta(0) = 0$, can be integrated to give

$$\delta(t) = \sqrt{12t}. \tag{1.32}$$

For an arbitrary $n > 1$, analogous calculations yield $\delta(t) = \sqrt{2n(n+1)t}$.

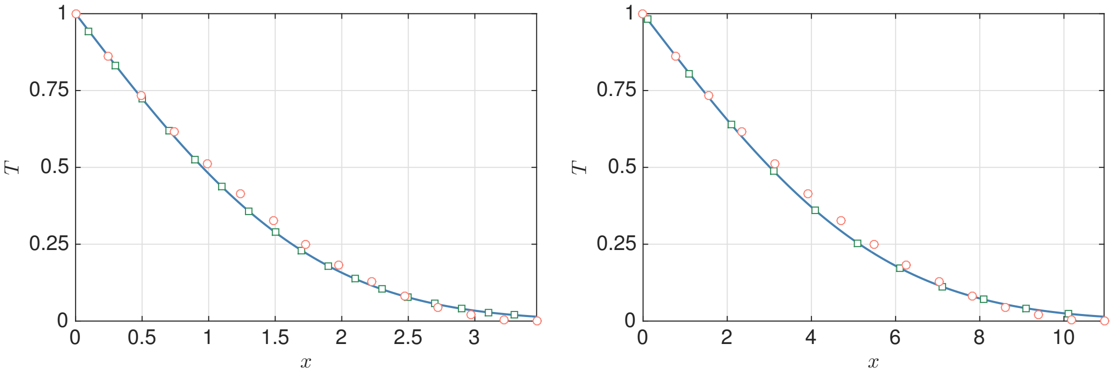

**(a)** $t = 1$. **(b)** $t = 10$.

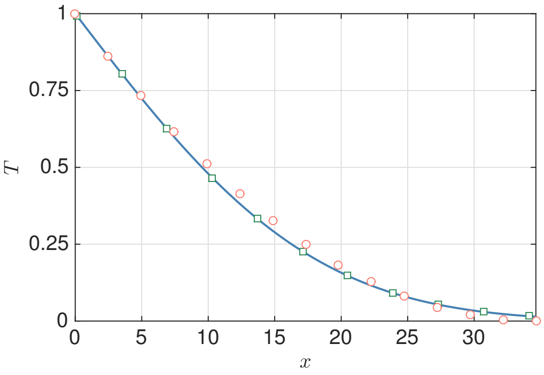

**(c)** $t = 100$.

**Figure 1.7:** Temperature profiles at different time instants. Solid lines, circles and squares corresponds respectively to the exact, HBIM and numerical solutions.

In Fig. 1.7 we show some temperature profiles corresponding to the problem defined by (1.13). As can be seen, despite its simplicity, the accuracy of the HBIM is remarkable.

### 1.2.6 Nanoscale effects in heat transfer

In this section we have introduced the main equations, boundary conditions and solution methods relative to the classical heat transfer theory. However, the different thermophysical properties of nanomaterials with respect to their macroscopic counterparts implies that the formulation of these equations must be reviewed. In chapter 2 we give a deeper description of the physical background and show that Fourier's law fails not only for small length scales, but also for short time scales or extremely low temperatures.

## 1.3 Introduction to Stefan problems

In many situations involving heat transfer, a medium undergoes a transition from one phase to another. The mathematical description of these phenomena is known as a Stefan problem and in the last century it has been widely studied. In this introductory chapter we will give a brief description of the classical formulation and solution techniques.

### 1.3.1 Mathematical modeling of a phase change process

The Stefan problem is a specific free boundary problem which describes the transition of a medium from one phase to another. Some examples are melting or solidification, for instance, which arise in nature and in many industrial processes. In the classical formulation, which we refer to as the classical Stefan problem, heat transfer inside the medium is described by Fourier's law. This type of problem is relatively well understood and a vast amount of literature can be found on it. For instance, we refer to the books by Alexiades and Solomon [4], Davis [64] or Gupta [103].

The Stefan problem was named after the Austrian physicist Josef Stefan (1835–1893) due to his work when deriving a mathematical formulation to describe ice formation in the Arctic and Antartic Oceans [224]. A more extensive review of his works can be found in Ref. [62]. In fact, Stefan was far from being the first to work on a mathematical description of phase change processes. A dedication from Hutton to Black in the former's manuscript "Dissertations on different subjects in natural philosophy" [119] shows that it was the latter who first introduced the concept of latent heat back in the 18th century. Lamé and Clapeyron later coupled this to the heat conduction theory developed by Fourier to study

**Figure 1.8:** Portrait of the Austrian physicist Josef Stefan (1835–1893) by K. Schoenbauer around 1880, provided by the Austrian Academy of Sciences.

the solidification of the Earth [138]. As shown later by Stefan, they discovered that the solification rate of the Earth from its initially liquid state was proportional to the square root of time. However, Stefan was the first to determine the constant of proportionality [224]. In a work published by Weber [252] it is shown that the German physicist Neumann had found an explicit solution to the problem studied by Lamé and Clapeyron. In recognition of his contribution, this is now known as the Neumann solution.

To illustrate the non-dimensionalisation procedure and the standard solution techniques, in the following sections we will now give the basic idea and equations describing a simple, one-dimensional melting process. Consider a solid, semi-infinite bar that is initially at a temperature $T_0^*$ below the melting temperature $T_{\mathrm{m}}^*$; see Fig. 1.9. Suddenly, the temperature of the environment that is in contact with the surface of the bar at $x^* = 0$ is raised to a temperature $T_1^* > T_{\mathrm{m}}^*$, which causes the bar to start melting. The moving interface which separates the liquid and solid phases is represented as $s^*(t^*)$, or simply $s^*$.

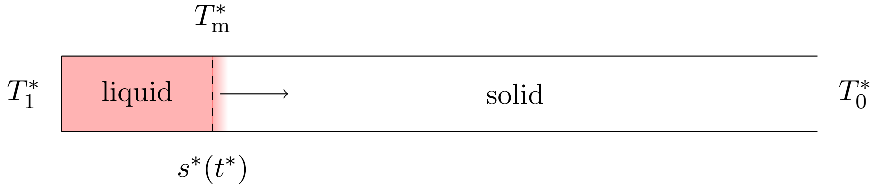

**Figure 1.9:** A semi-infinite bar, initially at a constant temperature $T_0^* \leq T_\mathrm{m}^*$, begins to melt from $x^* = 0$ due to a sudden temperature rise $T_1^* - T_0^*$, where $T_1^* > T_\mathrm{m}^*$.

### 1.3.2 Governing equations

Let $T_l^*$ and $T_s^*$ be respectively the temperature in the liquid and in the solid phases. If we assume that the thermophysical parameters are constant and that Fourier's law applies, then the heat flow in each phase is governed by the corresponding CHE,

$$\rho_l^* c_l^* \frac{\partial T_l^*}{\partial t^*} = k_l^* \frac{\partial^2 T_l^*}{\partial x^{*2}}, \qquad 0 < \ x^* < s^*, \tag{1.33a}$$

$$\rho_s^* c_s^* \frac{\partial T_s^*}{\partial t^*} = k_s^* \frac{\partial^2 T_s^*}{\partial x^{*2}}, \qquad x^* > s^*. \tag{1.33b}$$

For simplicity, we assume $\rho_s^* = \rho_l^* = \rho^*$, since otherwise the liquid phase would be expanding (or shrinking) and therefore an advective contribution $\boldsymbol{v}^* \cdot \nabla u^* \cdot$ should be not be neglected in Eq. (1.2)

The position of the interface is determined by the Stefan condition, which in its simplest form is

$$\rho^* L_\mathrm{m}^* \frac{\mathrm{d}s^*}{\mathrm{d}t^*} = Q_l^* - Q_s^*, \qquad \text{at } x^* = s^*, \tag{1.34}$$

where $L_\mathrm{m}^*$ is the latent heat of the material, i.e., the amount of energy required by a medium to change its phase. Applying Eq. (1.1), the Stefan condition can be given in terms of the temperature,

$$\rho^* L_\mathrm{m}^* \frac{\mathrm{d}s^*}{\mathrm{d}t^*} = -k_l^* \frac{\partial T_l^*}{\partial x^*} + k_s^* \frac{\partial T_s^*}{\partial x^*}, \qquad \text{at } x^* = s^*. \tag{1.35}$$

### 1.3.3 Boundary conditions

At the interface, the temperature in the liquid and solid phases has to be equal to the melt temperature, i.e.

$$T_l^*, T_s^* = T_\mathrm{m}^*, \qquad \text{at } x^* = s^*. \tag{1.36a}$$

Sufficiently far from the hot environment we do not expect any changes in temperature with respect to the initial value, hence

$$T_s^* \to T_0^*, \qquad \text{as } x^* \to \infty. \tag{1.36b}$$

There are different ways we could describe the heat transfer at the surface of the bar. On one hand, we can assume that the temperature at the boundary instantly reaches the larger value $T_1^*$, i.e.

$$T_l^* = T_1^* \qquad \text{at } x^* = 0. \tag{1.36c}$$

As will be discussed in afterwards, the problem admits an explicit solution when this form of boundary condition is employed. On the other hand, we can impose a form of radiation condition known as Newton cooling condition,

$$-k_l^* \frac{\partial T_l^*}{\partial x^*} = h^*(T_1^* - T_l^*), \qquad \text{at } x^* = 0. \tag{1.37}$$

The quantity $h^*$ is the heat transfer coefficient, which depends on the two media in contact at the boundary. Note, in the limit $h^* \to \infty$ we recover Eq. (1.36c).

Finally, recall that the liquid phase does not exist initially and hence no initial conditions for $T_l^*$ are required. The initial conditions are therefore reduced to

$$T_s^* = T_0^*, \qquad s^* = 0, \qquad \text{at } t^* = 0. \tag{1.38}$$

### 1.3.4 One-phase reduction

To determine the position of the solid-liquid interface, the temperature in both phases must be found. This is why the problem defined by Eqs. (1.33)–(1.38) is referred to as the two-phase Stefan problem. A common simplifying strategy is to assume that the temperature distribution of one of the phases is known, which reduces the problem to the so-called one-phase (or single-phase) Stefan problem. Assume that the initial temperature of the solid is the melt temperature, i.e., $T_0^* = T_{\mathrm{m}}^*$. Any raise in temperature will cause the solid to melt, and thus the solid temperature can be assumed to be constant in time, $T_s^* \equiv T_{\mathrm{m}}^*$. The solid temperature gradient in Eq. (1.35) vanishes and the Stefan condition becomes

$$\rho^* L_{\mathrm{m}}^* \frac{\mathrm{d}s^*}{\mathrm{d}t^*} = -k_l^* \frac{\partial T_l^*}{\partial x^*}, \qquad \text{at } x^* = s^*, \tag{1.39}$$

There are more strategies that allow the two-phase problem to be reduced to a single phase. For instance, many studies are based on different limits of the ratio of the thermal conductivity of the two phases $k_s^*/k_l^*$ [15, 79, 180, 183]. In this sense, the present one-phase formulation corresponds to the limit $k_s^*/k_l^* \to \infty$, i.e., to the assumption that heat is conducted through the solid infinitely faster than it is through the liquid.

The one-phase reduction is a very popular approach to reduce the complexity of the problem and it is usually in good agreement with the full model. More on one-phase Stefan problems may be found in the book by Hill [111]. To reduce the complexity of this example, from now on we consider the one-phase model.

### 1.3.5 Non-dimensional formulation

Note, there is no natural length scale for this problem. However, we know that the melting process is driven by the heat conduction through the liquid, and it therefore makes sense to choose time scale $\rho^* c_l^* L^{*2}/k_l^*$, where we have fixed an arbitrary length scale $L^*$. The temperature scale is determined by the boundary conditions on the extrema of the bar, $\Delta T^* = T_1^* - T_{\mathrm{m}}^*$. We define the following non-dimensional quantities:

$$x = \frac{x^*}{L^*}, \quad s = \frac{s^*}{L^*}, \quad t = \frac{k_l^* t^*}{\rho^* c_l^* L^{*2}}, \quad T = \frac{T_l^* - T_{\mathrm{m}}^*}{\Delta T^*}. \tag{1.40}$$

Upon writing derivatives in subscript form, the non-dimensional one-phase problem then becomes

$$T_t = T_{xx}, \qquad 0 < x < s, \tag{1.41a}$$

$$T = 1, \qquad \text{at } x = 0, \tag{1.41b}$$

$$T = 0, \qquad \text{at } x = s, \tag{1.41c}$$

$$\beta s_t = -T_x, \qquad \text{at } x = s, \tag{1.41d}$$

$$s = 0, \qquad \text{at } t = 0. \tag{1.41e}$$

The dimensionless quantity $\beta = L_{\mathrm{m}}^*/(c_l^* \Delta T^*)$ is called the Stefan number and represents the ratio of the latent heat to the sensible heat. For $\beta \gg 1$ the problem is dominated by conduction through the liquid, since $s_t = O(\beta^{-1})$ implies that the melting is slow. Conversely, a small Stefan number can be understood as fast melting and therefore the dynamics are dominated by the heat conduction through the growing phase.

In the dimensionless formulation the Newton condition takes the form

$$T_x = \mathrm{Nu}(T-1), \qquad \text{at } x=0, \tag{1.42}$$

where $\mathrm{Nu} = h^* L^*/k^*$ is the Nusselt number. When heat exchange between the environment and the medium occurs in the solid phase (for example, in solidification processes), this number is computed with the values corresponding to the solid phase and it is called Biot number, denoted by Bi. In both cases, these dimensionless numbers describe the amount of convective heat transfer relative to the conductive heat transfer.

From now on we will refer to the problem defined by Eqs. (1.41) as the FT-formulation, whereas NC-formulation will refer to the corresponding problem obtained after replacing Eq. (1.41b) by Eq. (1.42).

### 1.3.6 Solution methods

Exact solutions are extremely difficult to find and in most configurations they do not even exist. Some explicit solutions can be found for specific boundary conditions or assumptions on the parameters [46, 151, 207, 246, 263]. The use of numerical methods or approximate techniques is therefore mandatory. In this section we briefly review some classical solution methods that can be found in the literature.

**Exact solutions**

By means of the solution methods introduced in Secs. 1.2.5, we are able to compute an exact solution for the FT-formulation, termed the Neumann solution [4, 103, 111]. It is given by

$$T(x,t) = -1 + \frac{\mathrm{erf}\left(\frac{x}{2\sqrt{t}}\right)}{\mathrm{erf}(\lambda)}, \qquad s(t) = 2\lambda\sqrt{t}, \tag{1.43}$$

where $\lambda$ satisfies the transcendental equation

$$\sqrt{\pi}\lambda \mathrm{erf}(\lambda) e^{\lambda^2} = \beta^{-1}. \tag{1.44}$$

This reduces the problem to solving an algebraic equation, which is a much easier task than solving a PDE over a growing domain. Although solving Eq. (1.44) requires the use of numerical methods, approximate solutions can be found for large and small Stefan numbers by means of standard asymptotic expansions [79]. For large Stefan numbers, $\beta \gg 1$, we find

$$\lambda \approx (2\beta)^{-1/2}, \tag{1.45a}$$

whereas for $\beta \ll 1$ the solution to Eq. (1.44) can be approximated by

$$\lambda \approx [\log(1/\beta)]^{1/2}\left[1 - \frac{\log(\log(1/\beta))}{4\log(1/\beta)} - \frac{\log(\pi)}{4\log(1/\beta)}\right]. \tag{1.45b}$$

Figure 1.10a shows the Neumann solution in the alternative variable $\xi = x/s$, which transforms the moving domain $[0, s]$ into the unit interval $[0, 1]$, for different values of $\lambda$. Whereas in the limit $\lambda \to 0$ we can see a convergence to a profile which is linear in the variable $\xi$, in the opposite limit we observe the emergence of a boundary layer near $x = 0$, indicating that the bar melts faster than heat is conducted through the liquid. Figure 1.10b shows that large values for $\lambda$ are obtained only for extremely small values of $\beta$, which is due to the asymptotic behaviour given in Eq. (1.45b). In fact, for $\beta = 0.01$ we have $\lambda \approx 1.83$ and, for instance, the value $\lambda = 5$ is not achieved until $\beta = O(10^{-12})$. Since these orders of magnitude are never reached in practise [4], boundary layers such as the one observed in Fig. 1.10b are not expected to appear.

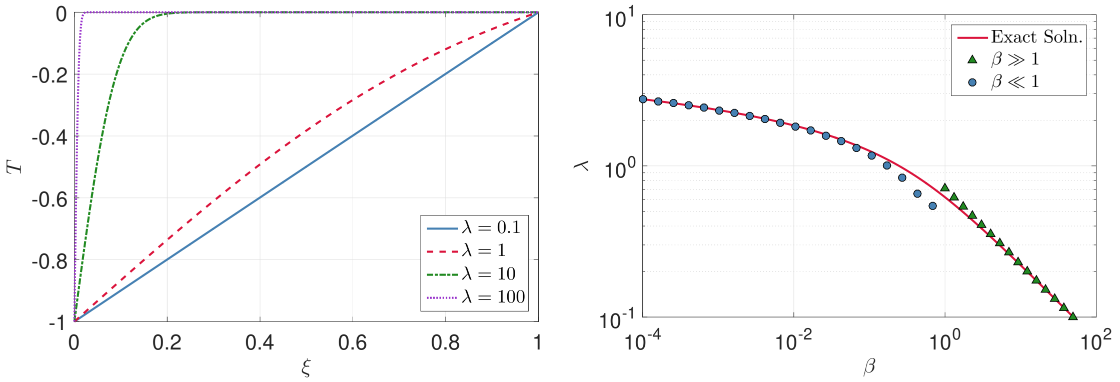

**(a)** **(b)**

**Figure 1.10:** (a) Neumann solution in terms of the transformed variable $\xi = x/s(t)$ for different values of $\lambda$. (b) Coefficient $\lambda$ as a function of the Stefan number $\beta$. The solid line corresponds to the solutions of Eq. (1.44), whereas triangles and circles refer to the asymptotic solutions for small and large Stefan numbers given in Eq. (1.45).

### Early-time dynamics

It often occurs in many free-boundary problems that one of the phases does not exist initially. Formally, this means that no initial conditions for the variables in that phase are required. In practice, numerical schemes require initial data and therefore a small-time analysis of the problem has to be carried out to find approximations of the variables that serve as initial conditions for the numerical scheme.

A priori, for the FT-formulation this is not required due to the existence of an explicit solution. However, for the sake of this introduction to solution methods for Stefan problems, we will perform the small-time analysis for the FT- and NC-formulations. To facilitate the analysis we will assume $\beta, \mathrm{Nu} = O(1)$.

The first step consists of introducing an artificial parameter $\epsilon \ll 1$ and assuming $t = O(\epsilon)$. To ensure that melting starts for $t > 0$ we need to balance terms in the Stefan condition, which first requires discussing the expected order of magnitude of the temperature.

**FT-formulation** According to the Eq. (1.41b), which implies that the temperature is instantly raised to the value $T = 1$, we assume $T = O(1)$. Assume now $x, s = O(\epsilon^a)$. Balancing terms in the Stefan condition then requires $\epsilon^{a-1} \sim \epsilon^{-a}$, hence $a = 1/2$. Upon introducing the new variables

$$\tilde{x} = \frac{x}{\sqrt{\epsilon}}, \quad \tilde{s} = \frac{s}{\sqrt{\epsilon}}, \quad \tilde{t} = \frac{t}{\epsilon}, \quad \tilde{T} = T, \tag{1.46}$$

all the terms in the heat equation and Stefan condition balance and the problem is equivalent to the problem in the original non-dimensional variables, hence $\tilde{s} = 2\lambda\sqrt{\tilde{t}}$, where $\lambda$ satisfies Eq. (1.44).

**NC-formulation** The underlying physics of Eq. (1.42) implies that the temperature will not differ much from the initial value $T = 0$, therefore we consider $T = O(\epsilon^a)$ for a certain $a > 0$. In addition, the liquid has not yet grown much, therefore $x, s = O(\epsilon^b)$ for $b > 0$. Balancing terms in the Stefan condition yields $\epsilon^{b-1} \sim \epsilon^{a-b}$. A second relation can be obtained from the Newton cooling condition. The only sensible balance is (recall, we assume Nu$= O(1)$) obtained for $\epsilon^{a-b} \sim 1$, hence we choose $a, b = 1$. Upon defining the scaled variables

$$\tilde{x} = \frac{x}{\epsilon}, \quad \tilde{s} = \frac{s}{\epsilon}, \quad \tilde{t} = \frac{t}{\epsilon}, \quad \tilde{T} = \frac{T}{\epsilon}, \tag{1.47}$$

the problem becomes

$$\tilde{T}_{\tilde{x}\tilde{x}} = O(\epsilon), \qquad 0 < \tilde{x} < \tilde{s}, \tag{1.48a}$$

$$\tilde{T}_{\tilde{x}} = -\mathrm{Nu} + O(\epsilon), \qquad \text{at } \tilde{x} = 0, \tag{1.48b}$$

$$\tilde{T} = 0, \qquad \text{at } \tilde{x} = \tilde{s}, \tag{1.48c}$$

$$\beta \tilde{s}_{\tilde{t}} = -\tilde{T}_{\tilde{x}}, \qquad \text{at } \tilde{x} = \tilde{s}, \tag{1.48d}$$

$$\tilde{s} = 0, \qquad \text{at } \tilde{t} = 0. \tag{1.48e}$$

At leading order, the temperature is $\tilde{T} = \mathrm{Nu}(\tilde{s} - \tilde{x})$, and therefore the interface is determined by the initial value problem (IVP)

$$\beta \tilde{s}_{\tilde{t}} = \mathrm{Nu}, \qquad \tilde{s}(0) = 0, \tag{1.49}$$

which gives $\tilde{s} = \mathrm{Nu}\beta^{-1}\tilde{t}$ or, in the original non-dimensional variables,

$$s(t) = \mathrm{Nu}\beta^{-1}t. \tag{1.50}$$

Contrary to the fixed-temperature solution, the latter predicts an initial melting rate $\mathrm{Nu}/\beta$. Physically, this behaviour is more realistic than the infinite melting rate predicted by the FT-formulation, since it predicts that for slow melting ($\beta \gg 1$) or for poor conduction through the liquid ($\mathrm{Nu} \ll 1$) we expect the initial melting rate to decrease.

### Asymptotic solutions for large Stefan numbers

A common assumption in Stefan problems is that $\beta \gg 1$. This is reasonable if we note that for common materials such as gold, tin or silicon we find $\mathcal{T} = O(100\ \mathrm{K})$ or larger [84, 107, 167, 199]. Therefore, provided that the temperature jump $\Delta T^*$ is sufficiently below 100 K then $\beta \gg 1$. Small Stefan numbers may be found in extreme situations, such as cryopreservation [4], where $\Delta T^*$ is large to ensure rapid freezing.

**FT-formulation** For $t = O(1)$ and $\beta \gg 1$ we have $s_t = O(\beta^{-1})$, which suggests that a larger time scale must be considered to capture the melting process. Assume $x, s = O(\delta)$

and $t = O(\tau)$, where $t \gg 1$. From Eq. (1.41b) we have $T = O(1)$ and therefore, to balance terms in Eq. (1.41d) we find $\tau\delta^{-2} = O(\beta)$. Introducing the new variables

$$\tilde{x} = \frac{x}{\delta}, \quad \tilde{s} = \frac{s}{\delta}, \quad \tilde{t} = \frac{t}{\tau}, \quad \tilde{T} = T, \tag{1.51}$$

and assuming $\tau\delta^{-2} = O(\beta)$, Eq. (1.41a) becomes,

$$T_{\tilde{x}\tilde{x}} = O(\beta^{-1}), \tag{1.52}$$

indicating that $T$ is harmonic at leading order. The Stefan is

$$\tilde{s}_{\tilde{t}} = -\tilde{T}_{\tilde{x}}, \qquad \text{at } \tilde{x} = \tilde{s}. \tag{1.53}$$

The leading-order solution to Eq. (1.52), subject to the boundary conditions

$$\tilde{T} = 1, \qquad \text{at } \tilde{x} = 0, \tag{1.54a}$$

$$\tilde{T} = 0, \qquad \text{at } \tilde{x} = \tilde{s}. \tag{1.54b}$$

is given by

$$\tilde{T}(\tilde{x}, \tilde{t}) = 1 - \frac{\tilde{x}}{\tilde{s}}. \tag{1.55}$$

Finally, using the Stefan condition we find an ordinary differential equation which determines the solid-liquid interface $\tilde{s}$,

$$\tilde{s}\tilde{s}_{\tilde{t}} = 1, \tag{1.56}$$

which can be solved analytically. Using $\tilde{s}(0) = 0$ we find

$$\tilde{s}(\tilde{t}) = \sqrt{2\tilde{t}}. \tag{1.57}$$

In the original non-dimensional variables, the position of the interface is given by

$$s(t) = \sqrt{\frac{2t}{\beta}}, \tag{1.58}$$

which coincides with the Neumann solution if $\lambda$ is substituted by its approximation for large Stefan numbers, Eq. (1.45).

**NC-formulation** For simplicity we will assume Nu$= O(1)$. In contrast to the fixed-temperature condition, the Newton cooling condition prevents the temperature from reaching the value $T = 1$ instantly (in fact, this value is never reached), which breaks the problem into different time regimes. By inspecting Eq. (1.42) we find three possible balances, which correspond to three different time regimes. The first time regime, where the term on the l.h.s. in the Newton condition balances the first term of the r.h.s., corresponds to the small-time analysis performed in the previous section. For $t \gg \epsilon$ we find $T, s \sim t/\beta$. Upon writing $t = \tau t'$, $x = \beta^{-1}\tau x'$, $s = \beta^{-1}\tau s'$ and $T = \beta^{-1}\tau T'$, the Newton condition becomes

$$T'_{x'} = \mathrm{Nu}(\beta^{-1}\tau T' - 1), \qquad \text{at } x' = 0, \tag{1.59}$$

and hence we need $\tau = O(\beta)$ to obtain a new balance with respect to the previous time regime. Using this scaling the terms in the Stefan condition balance and we find that, neglecting terms of order $\beta^{-1}$, $T'$ satisfies

$$T'_{x'x'} = O(\beta^{-1}), \qquad 0 < x' < s', \tag{1.60a}$$

$$T'_{x'} = \mathrm{Nu}(T' - 1), \qquad \text{at } x' = 0, \tag{1.60b}$$

$$T' = 0, \qquad \text{at } x' = s'. \tag{1.60c}$$

The leading-order solution to this is

$$T'(x', t') = \frac{\mathrm{Nu}(s' - x')}{1 + \mathrm{Nu}s'}. \tag{1.61}$$

Substituting the latter into the Stefan condition yields

$$s'_{t'} = \frac{\mathrm{Nu}}{1 + \mathrm{Nu}s'}, \tag{1.62}$$

and hence $s'$ satisfies

$$s' + \frac{1}{2}\mathrm{Nu}(s')^2 = \mathrm{Nu}t' + C \tag{1.63}$$

where $C$ is a constant of integration. The value of $C$ is determined by the matching condition $s' \sim \mathrm{Nu}t'$ as $t' \ll 1$, which yields $C = 0$. Using the fact that $s' > 0$ we finally find

$$s'(t') = \sqrt{\mathrm{Nu}^{-2} + 2t'} - \mathrm{Nu}^{-1}. \tag{1.64}$$

For $t' \gg 1$ we find $s' \sim \sqrt{2t'}$ and hence $T' \sim 1 - x'/s'$, which are the matching conditions for the third time regime, where the Newton condition has converged to the fixed-temperature condition.

In the original non-dimensional variables, the position of the solid-liquid interface in the NC-formulation is therefore given by

$$s(t) = \sqrt{\mathrm{Nu}^{-2} + 2\beta^{-1}t} - \mathrm{Nu}^{-1}, \tag{1.65}$$

which converges to Eq. (1.58) as Nu → ∞.

Note, for either FT- or NC conditions, the small-time behaviour is still retreived and hence these asymptotic solutions are able to capture the melting dynamics even for small times.

### Numerical solutions

A number of different approaches for finding numerical solutions to one-dimensional Stefan problems can be found in the literature [34, 122]. Two popular approaches in one-dimensional geometries are front-tracking [36, 136, 161], which has been applied to frameworks such as dendrite formation [130]; and front-fixing methods [35, 36, 173]. The first group consists of discretizing the problem using a fixed amount of grid points which are relocated after each iteration, whereas the latter use transformed variables to fix the domain. For more complex geometries, Chen et al. [53] introduced the level set method, which is based on defining a scalar function $\phi$ that describes the distance from a point to the moving boundary, whereas other researchers reformulated the Stefan problem in terms of the enthalpy of the system [33, 78, 201]. Methods have been proposed in which the interface was assumed to be a diffuse region between the two phases [30]. Liu and Mc Elwain [150] proposed a solution method for finite volumes based on finite elements. The HBIM and its variations are popular approaches [178, 182], too.

In this dissertation, numerical solutions will be based on the boundary-fixing approach, since it has been successfully implemented in other models on nanoscale phase change [82, 84, 85, 107, 108, 199]. This method consists of first applying a boundary fixing transformation and then afterwards implicitly discretizing the derivatives of the temperature and explicitly the derivatives of the solid-liquid interface. We define the new variable $\xi = x/s$, which transforms the differential operators into

$$\frac{\partial}{\partial t} \mapsto \frac{\partial}{\partial t} - \xi s s_t \frac{\partial}{\partial \xi}, \qquad \frac{\partial}{\partial x} \mapsto s^{-1}\frac{\partial}{\partial \xi}. \tag{1.66}$$

Thus, rewriting the temperature as $T(x,t) = u(\xi,t)$, Eq. (1.41a) becomes

$$u_t = \xi s^{-1} s_t u_\xi + s^{-2} u_{\xi\xi}, \tag{1.67}$$

which holds for $0 < \xi < 1$. At the moving interface we have

$$u = 0, \qquad \xi = 1, \tag{1.68}$$

whereas the FT- and NC-condition become respectively

$$u = 1, \qquad \text{at } \xi = 0, \tag{1.69}$$

and

$$s^{-1} u_\xi = \mathrm{Nu}(u-1), \qquad \text{at } \xi = 0. \tag{1.70}$$

Finally, the transformed Stefan condition takes the form

$$\beta s s_t = -u_\xi, \qquad \text{at } \xi = 1. \tag{1.71}$$

Note, to avoid singularities in the numerical method, due to the nonexistence of the liquid phase, the initial condition $s(0) = 0$ has to be substituted by an initial approximation to $u$ and $s$ for some small time $t_0$ [35, 173]. If $t_0$ is sufficiently small then we can substitute the initial conditions of the FT-formulation by the small-time solution of Sec. 1.3.6

$$u(\xi, t_0) \approx \frac{\mathrm{erf}(\lambda\xi)}{\mathrm{erf}(\lambda) - 1}, \qquad s(t_0) \approx \sqrt{2\beta^{-1} t_0}, \tag{1.72}$$

whereas in the NC-formulation we use

$$u(\xi, t_0) \approx \mathrm{Nu}^2 \beta^{-1} t_0 (1-\xi), \qquad s(t_0) \approx \mathrm{Nu}\beta^{-1} t_0. \tag{1.73}$$

The problem in the fixed domain is now discretised on a spatial grid of $N+1$ points of the form $\xi_i = \frac{i}{N}$ and a time grid with points of the form $t_n = t_0 + n\Delta t$. The derivatives of the temperature are discretized via

$$u_t \approx \frac{u_i^{n+1} - u_i^n}{\Delta t}, \quad u_\xi \approx \frac{u_{i+1}^{n+1} - u_{i-1}^{n+1}}{2\Delta\xi}, \quad u_{\xi\xi} \approx \frac{u_{i+1}^{n+1} - 2u_i^{n+1} + u_{i-1}^{n+1}}{(\Delta\xi)^2}, \tag{1.74}$$

where $u_i^{n+1} = u(\xi_i, t_n)$ and $\Delta\xi = N^{-1}$. Upon substituting these expressions into Eq. (1.67) and writing $s(t_n) = s^n$ and $s_t(t_n) = s_t^n$ we obtain $N-1$ algebraic equations of the form

$$A_i^n u_{i-1}^{n+1} + B_i^n u_i^{n+1} + C_i^n u_{i+1}^{n+1} = u_i^n, \qquad 1 \leq i \leq N-1, \tag{1.75}$$

with coefficients

$$A_i^n = \frac{\xi_i s_t^n \Delta t}{2s^n \Delta\xi} - \frac{\Delta t}{(s^n\Delta\xi)^2}, \quad B_i^n = 1 + \frac{2\Delta t}{(s^n\Delta\xi)^2}, \quad C_i^n = -\frac{\xi_i s_t^n \Delta t}{2s^n \Delta\xi} - \frac{\Delta t}{(s^n\Delta\xi)^2}. \tag{1.76}$$

Notice, we are discretizing $u$ implicitly whereas $s$ and $s_t$ are discretized explicitly. The boundary condition at the interface becomes

$$u_N^{n+1} = 0, \tag{1.77}$$

In the FT-formulation the remaining equation is

$$u_0^{n+1} = 1, \tag{1.78}$$

whereas in the NC-formulation it takes the form

$$\left(\mathrm{Nu} - \frac{3}{2s^n\Delta\xi}\right) u_0^{n+1} + \frac{2}{s^n\Delta\xi} u_1^{n+1} - \frac{1}{2s^n\Delta\xi} u_2^{n+1} = \mathrm{Nu}, \tag{1.79}$$

where we have used second order forward differences to discretise $u_\xi$ at $\xi = 0$. To update the position of the moving boundary we discretize Eq. (1.71) to first find $s_t^{n+1}$ and hence $s^{n+1}$,

$$s_t^{n+1} = -\frac{3u_N^{n+1} - 4u_{N-1}^{n+1} + u_{N-2}^{n+1}}{2\beta s^n \Delta\xi}, \qquad s^{n+1} = s^n + \Delta t s_t^{n+1}, \tag{1.80}$$

where we have used second order backward differences to discretise $u_\xi$ at $\xi = 1$.

In Figs. 1.11a–1.11c we show the evolution of the solid-liquid interface in both formulations for various values of the Stefan number. The asymptotic solutions for $\beta = 10, 100$ are clearly very accurate and demonstrate that this method represents a powerful tool for solving Stefan problems. The effect of the Nusselt number on the dynamics can be observed in Fig. 1.11d. Note, the NC-formulation converges very fast to the FT-formulation ($\mathrm{Nu} = \infty$) as we increase the Nusselt number.

### 1.3.7 Nanoscale effects in phase change processes

We have now presented the basic equations and solution methods for relative to the classical formulation of the Stefan problem. However, the fact that many key thermophysical properties become size-dependent at small length-scales and that the classical heat transfer theory has to be reviewed, suggests that the formulation of the Stefan problem should be reformulated to account for nanoscale effects.

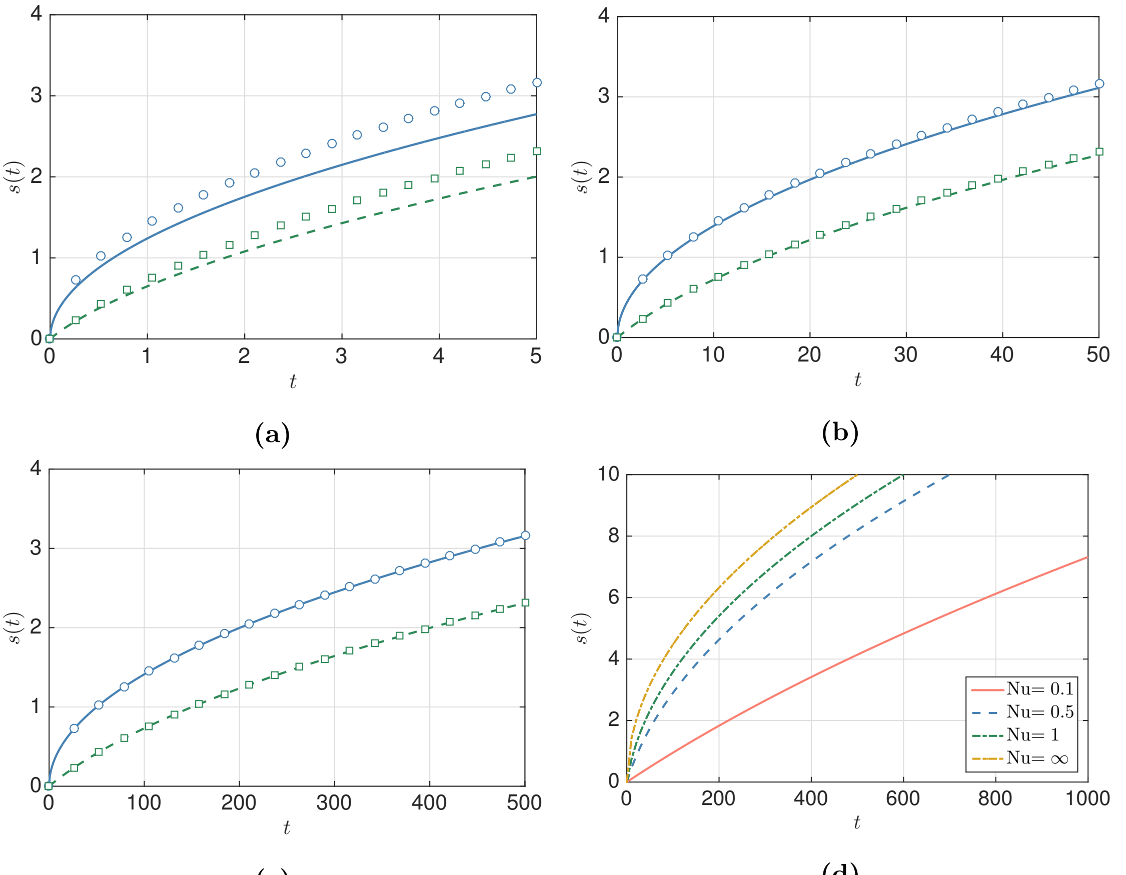

**(a)**

**(b)**

**(c)**

**(d)**

**Figure 1.11:** (a)–(c) Evolution of the solid-liquid interface for $\beta = 1, 10, 100$. Solid lines and circles correspond to the exact and asymptotic solutions in the FT-formulation, whereas dashed lines and squares refer to the numerical and asymptotic solutions of the NC-formulation. In the latter we have fixed Nu $= 1$. (d) Effect of the Nusselt number on the evolution of the interface. The Stefan number has been set to $\beta = 10$.

The second part of this dissertation deals with phase change processes and, in particular, with the study of extensions to the classical Stefan problem. Some of the non-classical features have already been studied in the framework of nanoscale phase change. For an extensive review of the state-of-the-art we refer to chapters 5 and 6.

# 2 | Beyond the classical heat conduction equations

## 2.1 Limitations of the classical theory

For the last 2 centuries, the classical theory has proven to be suitable for modelling many different situation. However, theoretical and experimental studies in the first decades of the 20th century have shown that Fourier's law fails under extreme conditions. A review of the heat transfer at the nanoscale can be found in several articles by Cahill et al. [31, 32] or Chen et al. [52], where the authors cover the main advances in the understanding of nanoscale heat transfer in the last two decades.

### 2.1.1 Experimental evidence for the breakdown of Fourier's law

Research into non-Fourier heat transfer began in the first half of the 20th century with the study of heat flow in liquid helium at temperatures near 0 K. Around 1940 the existence of thermal waves was discovered both experimentally and theoretically [131, 132, 139, 192, 228]. This phenomenon was termed second sound and soon other authors extended these studies to heat transfer in dielectric solids [104–106, 195, 251]. Although these non-Fourier regimes were initially thought to appear only at extremely low temperatures (∼2 K), recent studies show that these phenomena can occur also at ordinary temperatures [25, 45, 69, 100, 116, 143, 241].

Studies involving extremely short time scales, such as ultra-fast laser heating [25, 27, 125, 159, 196, 225, 230] or for transient heat conduction in microchips [102, 259], have reported discrepancies with respect to the classical theory. When it comes to phase change, theoretical and experimental studies predict extremely short melting times of typical nanostructures, such as nanoparticles [15, 84, 85, 134, 164, 179, 199, 255], which brings the applicability of Fourier's law in the formulation of the Stefan problem into question.

There exists a large number of experimental observations which show large differences between heat transfer in bulk materials and nanostructures. Multiple experiments show that understanding the underlying heat transport mechanisms in nanowires [121, 128, 142, 145, 200, 260], nanofilms [9, 10, 128, 129, 152, 153] or nanotubes [19, 47, 74, 87, 169, 170] often requires more complex models than Fourier's law. Most of these studies focus on the thermal conductivity and show that this poperty does not only depend on the size but also on the roughness of the boundaries, or the atomic structure in the case of nanotubes. Moreover, other studies show that Fourier's law is not capable of describing the heat dissipation from a nanostructure into a bulk material [113, 115, 216].

Time- and frequency-domain thermoreflectance (TDTR/FDTR) are popular strategies to measure thermal properties of materials; see Ref. [124]. However, many observations show that Fourier's law does not provide the necessary tools to give a correct description of the observed phenomena [110, 197, 235, 253, 265].

To understand the reasons behind the failure of Fourier's law we must first introduce some basic concepts of the microscopic description of thermal transport.

### 2.1.2 Fundamentals of phonon transport

In semiconductors, such as silicon or germanium, heat is mainly transported by lattice vibrations, which may be interpreted as quasiparticles called phonons. We briefly introduce some basic aspects concerning the properties of phonons, a deeper description may be found in the classical books by Ziman [266] or Kittel [133].

Since phonons can be understood as propagating waves, we can associate a frequency $\omega^*$ and a wave vector $\boldsymbol{q}^*$. In the literature, the wave vector is usually denoted by $\boldsymbol{k}^*$, we denote it by $\boldsymbol{q}^*$ to avoid later confusion with thermal conductivity. These quantities are not independent of each other, they are related by $\omega^* = \omega^*(q^*)$, where $q^* = |\boldsymbol{q}^*|$. This relation between frequency and wave vector is called the dispersion relation.

For a given frequency $\omega^*$ we can define physical quantities describing characteristic properties of the corresponding phonons. A macroscopic value, depending only on the temperature, can be obtained by considering averaged quantities

$$P^* = \int_0^{\omega_D^*} P_{\omega^*}^* D(\omega^*) d\omega^*, \tag{2.1}$$

where $P_{\omega^*}^*$ is an arbitrary property, $D$ is called the density of states [133] (denoted in the literature also by $DOS$) and $\omega_D^*$ is the maximal frequency at which a phonon is allowed to vibrate, called the Debye frequency. These averaged values are used in the Maxwell-Cattaneo and Guyer-Krumhansl models described below. Although they are computed from phonon properties, note that they do not give any microscopic information.

From the dispersion relation we define the phonon group velocity

$$\boldsymbol{v}_{\omega^*}^* = \frac{\partial \omega^*}{\partial q^*} \frac{\boldsymbol{q}^*}{q^*}. \tag{2.2}$$

For each frequency we can also define the phonon wavelength $\lambda_{\omega^*}^* = 2\pi/q_{\omega^*}^*$. While travelling through the medium, phonons experience different types of collisions which may be classified into normal (N) and resistive (R) scattering events. In N-processes, the phonon momentum is conserved, whereas R-processes do not conserve momentum. To each of these scattering processes we can associate a thermal relaxation time $\tau_{\omega^*,i}^*$, where $i = N, R$. These values represent the mean time between two consecutive collisions in a limiting transport regime where either N-processes dominate over R-processes or vice versa. The values of these relaxation times can be computed using the framework of the kinetic-collective model [18, 65, 66, 231–235] (KCM), which we will describe later. In Fig. 2.1 we show the values of the averaged quantities $\tau_R^*$ and $\tau_N^*$ for bulk silicon, computed for temperatures between 10 K and 1000 K via the KCM using an open acces code[1]. It can be seen that it spans multiple orders of magnitude and it can reach up to microseconds at around 10 K, which indicates that scattering events occur less frequently at low temperatures. On the other hand, it can be of the order of nano- to picoseconds for temperatures above 100 K, coinciding with the time scales of multiple ultra-fast laser applications [159, 225, 230].

When heat transport is dominated by phonons and assuming that the material is isotropic, the thermal conductivity is given by the (averaged) expression

$$k^* = \frac{1}{3} \rho^* c^* v^{*2} \tau_R^* \tag{2.3}$$

---

[1] https://physta.github.io/

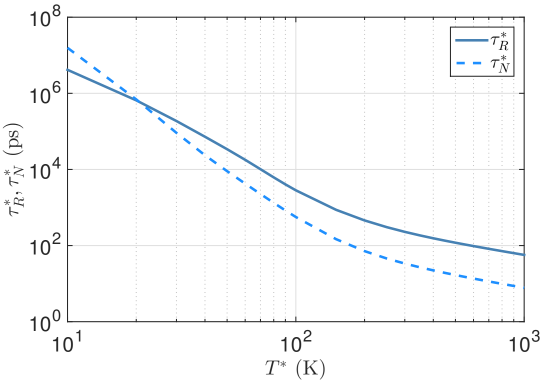

**Figure 2.1:** Normal and resistive relaxation times versus temperature in silicon, provided by the KCM [232].

where $v^* = |\boldsymbol{v}^*|$. This expression is also called lattice thermal conductivity. According to this definition, hypothetically increasing the frequency of R-processes (hence, decreasing $\tau_R^*$) would cause a decrease in thermal conductivity.

Associated to the relaxation times we can define the mean free path $\ell^*$, which represents the mean distance that a phonon travels in between two scattering events. In semiconductors, the mean free path is given by the relation

$$\ell^{*2} = \frac{1}{5} v^{*2} \tau_N^* \tau_R^*. \tag{2.4}$$

At room temperature, for silicon we have [52] $\lambda_{\mathrm{Si}}^* = O(1 \text{ nm})$ and $\ell_{\mathrm{Si}}^* = O(100 \text{ nm})$, which is comparable to the size of many nanoscale devices. Hence, observations of non-Fourier phenomena at low temperatures or small time- and length scales are closely related to the properties of phonons introduced in this section.

To illustrate this fact we may consider the mean free time for boundary scattering $\tau_B^*$, which is clearly a resistive process since momentum is not conserved. For a system of characteristic size $L^*$, the phonon-boundary scattering rate per unit frequency $\tau_{\omega^*,B}^{*-1}$ is given by [21, 22, 43, 65, 233]

$$\tau_{\omega^*,B}^{*-1} = \frac{v_{\omega^*}^*}{L^*}. \tag{2.5}$$

We can relate $\tau_B^*$ and $\tau_R^*$ via the Matthiessen rule [65, 233]

$$\tau_R^{*-1} = \tau_{R'}^{*-1} + \tau_B^{*-1}, \tag{2.6}$$

where $\tau_{R'}^*$ is the relaxation time related to other R-scattering processes. Hence, decreasing the size of the system increases the rate at which phonon-boundary scattering occurs, therefore reducing $\tau_R^*$ and furthermore reducing $k^*$. This is therefore one of the reasons causing a size-dependent behaviour of the thermal conductivity and, ultimately, the failure of Fourier's law (which describes $k^*$ as an intrinsic parameter only dependent of the material and not of its geometry).

Note, as we have remarked after introducing the averaged quantities in (2.1), quantites like $\tau_R^*$ or $\ell^*$ do not represent phonon properties in the strict way since they are averaged quantites. However, we keep the keyword phonon in their names to indicate that they are calculated from phonon properties.

### 2.1.3 Emergence of new heat transport regimes

From a microscopic point of view, Fourier's law describes heat conduction as a diffusive phenomenon driven by a temperature gradient, where collisions among heat carriers are described by Brownian motion. However, the observation of thermal waves in liquid helium [132, 192] highlighted new heat transport regimes which cannot be described by means of Fourier's law.

In the Fourier (or diffusive) regime, scattering occurs with a high frequency and hence $\tau_N^{*-1}, \tau_R^{*-1} \to \infty$. Conversely, in the so-called ballistic regime heat carriers do not suffer collisions while travelling through the medium. On one hand, this occurs if we increase the relaxation times associated to N-scattering and R-scattering, i.e. $\tau_N^{*-1}, \tau_R^{*-1} \to 0$. For instance, these large relaxation times can be observed at extremely low temperatures, as shown in Fig. 2.1. On the other hand, this phenomenon appears when the size of the medium is smaller than the phonon mean free path, i.e. $\ell^* \gg L^*$ or, equivalently, $\mathrm{Kn} \gg 1$, where $\mathrm{Kn} = \ell^*/L^*$ is called the Knudsen number. The limit $\mathrm{Kn} \to \infty$ is called the Casimir limit [43]. Figure 2.2 shows a sketch of these two limiting situations.

When the temperature of the medium or its size are increased and energy propagates through the medium in the form of heat waves, the ballistic regime is left behind and N-scattering is dominant, corresponding to the limit $\tau_N^{*-1} \to \infty$ and $\tau_R^{*-1} \to 0$ or, equivalently, $\tau_N^* \ll \tau_R^*$. As R-scattering begins to occur, the heat waves disappear and the diffusive regime is recovered. Interestingly, in this time regime the so-called memory effects appear,

**(a)** Diffusive transport (Kn≪ 1).　**(b)** Ballistic transport (Kn≫ 1).

**Figure 2.2:** Thermal transport through a sample from a hot interface (red) to a cold surface (blue) depending on the corresponding Knudsen number.

indicating that the state of the system depends on its previous state. This, for instance, does not happen in the diffusive regime, where each collision is treated as independent of the previous ones, in accordance with the idea of a random walk.

For systems with characteristic sizes comparable to the phonon wavelength, quantum effects become important [59, 190]. However, as discussed by Myers et al. [181], continuum theory does not hold at these extremely small length scales and hence we will not consider these cases since our interest lies in studying non-Fourier phenomena using different extensions to Fourier's law.

To model the transition between the ballistic and diffusive limits, various strategies have been proposed, as for example the super-diffusive or quasiballistic regime [243, 244] or the hydrodynamic regime, which was first studied by authors like Guyer and Krumhansl in the 20th century [104–106, 195] and has recently become a popular research area [40, 41, 99, 100, 143, 233–235]. It describes a situation where the frequencies of N- and R-scattering are comparable or even when R-scattering dominates heat transport, i.e. $\tau_R^{*-1} \geq \tau_N^{*-1}$. This regime is characterized by the emergence of so-called non-local effects and by a heat flow described by a Poiseuille-type phonon flow, which promoted the usage of the term phonon hydrodynamics. Although this transport regime was originally thought to be restricted to low temperatures, recent studies argue that this framework can be suitable to describe heat transfer at ordinary temperatures as well [25, 45, 69, 100, 116, 143, 241].

## 2.2 General heat transfer models

Theoretical models of heat transfer can be divided into three different categories. Micro- and mesoscopic approaches aim to give a description of heat transfer mechanisms at a microscopic level and therefore they determine the behaviour of the heat carriers (phonons, electrons, molecules, etc.), either individually or collectively by determining their distribution. Conversely, macroscopic models aim to describe the system by means of constitutive equations involving global variables such as temperature, energy or heat flux. Some examples of each category are shown in Fig. 2.3. We will briefly describe the first two approaches to afterwards focus on the macroscopic approaches.

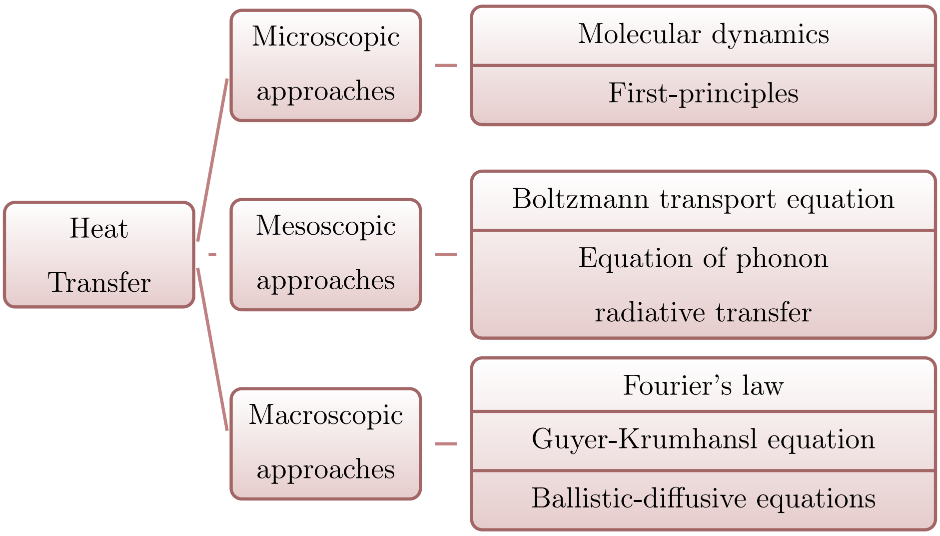

**Figure 2.3:** Heat transfer models can be classified into three groups depending on the modeling strategy.

### 2.2.1 Micro- and mesoscopic approaches

Microscopic approaches describe the behaviour of each heat carrier individually by solving the equations of motion for each heat carrier. Molecular dynamics (MD), for instance, emerged in classical mechanics and is based on Newton's second law, whereas the first-principle method is based on quantum mechanics and therefore the Schrödinger equation is employed. Contrary to the first method, the latter does not require a choice of a potential function and avoids the use of fitting parameters [26]. The large number of equations involved in these methods make them less suitable for evolution problems in complex geometries [58] and hence these approaches are used for computing thermal properties such as the phonon dispersion, the group velocity and, ultimately, thermal conductivity [31, 51, 109, 114, 147, 149, 162, 165, 193, 215, 260]. In fact, these methods are usually combined with mesoscopic methods explained below, where these phonon properties appear explicitly in the governing equations.

Although no fitting parameters are requiried in these methods, their implementation is usually very expensive in terms of computational time due to the extremely large number of equations involved.

Whereas microscopic models try to show the behaviour of each heat carrier, mesoscopic approaches group phonons according to their position, momentum and frequency. These methods are mainly based on the Boltzmann transport equation (BTE), which was first introduced by Joseph Boltzmann for rarefied gas transport [24] and later adapted by Peierls for phonon transport [191]. For each mode $\omega^*$ the BTE determines the distribution of phonons in the space $(t^*, \boldsymbol{x}^*, \boldsymbol{k}^*)$ via

$$\frac{\partial f^*_{\omega^*}}{\partial t^*} + \boldsymbol{v}^*_{\omega^*} \cdot \nabla_{\boldsymbol{x}^*} f^*_{\omega^*} + \boldsymbol{F}^* \cdot \nabla_{\boldsymbol{k}^*} f^*_{\omega^*} = J(f^*_{\omega^*}), \tag{2.7}$$

where $f^*_{\omega^*}(t^*, \boldsymbol{x}^*, \boldsymbol{k}^*)$ is the phonon distribution function and $\boldsymbol{F}^*$ are external forces. The term $J(\cdot)$ is called the collision operator and is the main reason for the complexity of the BTE, since it yields a non-linear integral term. This makes the BTE extremely difficult and computationally expensive to solve unless some simplifying assumptions are made. Near equilibrium, for instance, the BTE can be linearised to give the linearised Boltzmann transport equation (LBTE). However, analytical solutions to these equations cannot be found in practise unless some additional simplifications are made, such as the relaxation time approximation (RTA). The RTA approximates the collision term by $J(f^*_{\omega^*}) \approx (f^*_{\omega^*} - f^*_{\omega^*,0})/\tau^*_{\omega^*,R}$, where $f^*_{\omega^*,0}$ is the phonon equilibrium distribution, to which phonons relax as R-scattering occurs. By defining a phonon intensity $I^*_{\omega^*}$ from the distribution function $f^*_{\omega^*}$, Majumdar [157] transformed the LBTE into the equation of phonon radiative transfer (EPRT), which has been used in many studies [146, 155, 158].

Mesoscopic methods are often combined with microscopic approaches, since the latter can provide the necessary input for solving, for instance, the BTE. Analytical solutions to these models are rare and usually numerical methods are required. This has two drawbacks, which are high computational cost and, more importantly, the fact that they do not provide a clear physical picture which gives an understanding of the results.

### 2.2.2 Macroscopic approaches

Macroscopic approaches aim to describe a system by means of generalised constitutive laws and heat transport equations which are able to reproduce the classical diffusive behaviour, but also non-classical features that Fourier's law fails to describe. One of the main issues that has been attributed to Fourier's law in the past years is the fact that it leads to a parabolic heat equation which leads to the incorrect conclusion that heat is transported infinitely fast through a material. Cattaneo [44] and Vernotte [245] independently worked out that this issue could be overcome by incorporating an additional term into Fourier's law,

$$\tau_{MC}^{*} \frac{\partial \boldsymbol{Q}^{*}}{\partial t^{*}} + \boldsymbol{Q}^{*} = -k^{*} \nabla T^{*}. \tag{2.8}$$

The first term on the l.h.s of Eq. (2.8) is often called thermal inertia. This model is found in literature as the Maxwell-Cattaneo-Vernotte equation or simply Maxwell-Cattaneo equation (MCE), since many authors seem to neglect Vernotte's contributions. Conversely, the name Maxwell was included due to the similarities between this equation and the model proposed by the British physicist when he tried to provide a mathematical basis for the kinetic theory of gases [163]. In the original derivation of Eq. (2.8), the quantity $\tau_{MC}^{*}$ was introduced as a phenomenological parameter, but Guyer and Krumhansl later identified it as the resistive relaxation time, i.e. $\tau_{TM}^{*} = \tau_{R}^{*}$.

The time derivative of the heat flux is introduced to account for memory effects. To illustrate this fact we can simply integrate the MCE, subject to $\boldsymbol{Q}^{*}(\boldsymbol{x}^{*}, 0) = \boldsymbol{Q}_{0}^{*}(\boldsymbol{x}^{*})$, to obtain

$$\boldsymbol{Q}^{*}(\boldsymbol{x}^{*}, t^{*}) = \boldsymbol{Q}_{0}^{*}(\boldsymbol{x}^{*}) - \frac{k^{*}}{\tau_{R}^{*}} \int_{0}^{t^{*}} e^{-(t^{*}-\xi^{*})/\tau_{R}^{*}} \nabla T^{*}(\boldsymbol{x}^{*}, \xi^{*}) d\xi^{*}. \tag{2.9}$$

When combined with conservation of energy to eliminate the flux, we obtain a modified heat equation of the form

$$\tau_{R}^{*} \frac{\partial^{2} T^{*}}{\partial t^{*2}} + \frac{\partial T^{*}}{\partial t^{*}} = \alpha^{*} \nabla^{2} T^{*}, \tag{2.10}$$

which is equivalent to the wave equation with a damping term. This equation is called the hyperbolic heat equation (HHE) or relativistic heat equation and describes the propagation of a thermal wave with a finite speed $(\alpha/\tau_{R}^{*})^{1/2}$. This is termed the speed of second sound in the medium. By solving the LBTE, Guyer and Krumhansl derived an equation that accounts for both memory and non-local effects [105, 106],

$$\tau_R^* \frac{\partial \boldsymbol{Q}^*}{\partial t^*} + \boldsymbol{Q}^* = -k^* \nabla T^* + \ell^{*2} \left( \nabla^2 \boldsymbol{Q}^* + 2\nabla\nabla \cdot \boldsymbol{Q}^* \right). \tag{2.11}$$

This equation is known as the Guyer-Krumhansl equation (GKE) and it is probably one the most important equations in this dissertation, since chapters 3, 4 and 6 are based on this model. Memory and non-local effects are therefore introduced by considering higher-order derivatives of the flux in time and space respectively. When $\ell^*$ is much smaller than the characteristic size of the system, the second-order terms in Eq. (2.11) become negligible and the GKE reduces the MCE. Note, the form of the GKE is very similar to the equations of fluid dynamics where the flux represents the velocity of a viscous material due to the pressure gradient represented by the temperature. In this analogy, the quantity $\ell^{*2}/k^*$ might be understood as a thermal viscosity. Due to these similarities with the equations coming from fluid dynamics, the studies by Guyer, Krumhansl and their co-workers signified the starting point of the framework of phonon hydrodynamics [7, 18, 40, 41, 71, 73, 99, 100, 156, 233, 235, 264]. Using the vector identity $\nabla^2 \boldsymbol{A} = \nabla(\nabla \cdot \boldsymbol{A}) - \nabla \times \boldsymbol{A}$, we note that the GKE (2.11) introduces a very important novelty: the heat flux and the temperature gradient are not necessarily parallel. Microscopically, this might be understood by the presence of R-scattering, which does not conserve the phonons' momentum. Based on the original derivation of the GKE, De Tomas et al. [65, 66, 231, 232, 234, 235] proposed the kinetic-collective model (KCM), which splits the phonon population into kinetic or collective subpopulations depending on their scattering behaviour. In the framework of the KCM, thermal properties appearing in the equations are computed microscopically using ab initio methods, reducing the number of fitting parameters and providing excellent results compared to experimental data.

In the line of phonon hydrodynamics, Guo and co-workers proposed the thermomass model [42, 71–73, 101, 238, 248–250]. Based on Einstein's mass-energy relation, the authors developed the concept of thermomass and claimed that phonon flow is governed by the same equations as fluid flow. By defining gas properties for the phonon flow such as drift velocity, density or pressure, the authors end up with the thermomass equation (TME)

$$\tau_{TM}^* \left( \frac{\partial \boldsymbol{Q}^*}{\partial t^*} + 2(\boldsymbol{v}_{TM}^* \cdot \nabla)\boldsymbol{Q}^* \right) + \boldsymbol{Q}^* = -(1-b)k^* \nabla T^*, \tag{2.12}$$

where $\tau_{TM}^*$ is a relaxation time related to the speed of sound in gas, $\boldsymbol{v}_{TM}^*$ is the phonon drift velocity and $b$ is the square of the thermal Mach number, a dimensionless parameter introduced by the authors. Specific details of the derivation of Eq. (2.12) can be found in the thesis of one of Guo's former students [247]. Non-Fourier effects in the TME are caused by the inertial force of the thermomass [101] and, in particular, non-local effects are described by the quantity $\boldsymbol{\ell}_{TM}^* = \tau_{TM}^* \boldsymbol{v}_{TM}^*$ and hence appear as first-order derivatives of the flux, in contrast to the GKE. Moreover, the form of the TME shown in Eq. (2.12) is a simplified form of the original model, since the phonon drift velocity in the original derivation is given in terms of the heat flux and hence the second term in Eq. (2.12) is actually a non-linear. However, to simplify the example shown below we will consider $\boldsymbol{v}_{TM}^*$ a constant value.

Another popular model is the dual-phase-lagging equation (DPLE) [159, 160, 168, 237, 239, 240]. It was introduced by Tzou, who extended the Maxwell-Cattaneo equation by introducing a delay time in both the heat flux and the temperature gradient,

$$\boldsymbol{Q}^*(\boldsymbol{x}^*, t^* + \tau_Q^*) = -k^* \nabla T^*(\boldsymbol{x}^*, t^* + \tau_T^*), \tag{2.13}$$

where $\tau_Q^*$ and $\tau_T^*$ are phenomenological parameters accounting for the time lag prior the coexistence of a temperature gradient and a heat flux. The first order approximation of Eq. (2.13) gives

$$\tau_Q^* \frac{\partial \boldsymbol{Q}^*}{\partial t^*} + \boldsymbol{Q}^* = -k^* \nabla T^* - k^* \tau_T^* \frac{\partial}{\partial t^*} \nabla T^*. \tag{2.14}$$

Setting $\tau_T^* = 0$ gives the single-phase-lagging model, which is analogous to the MCE with the correspondence $\tau_Q^* = \tau_R^*$. The DPLE is analogous to another phenomenological model that can be found in the literature, known as the Jeffreys-type equation [126]. The l.h.s. of Eq. (2.13) was later replaced by $\boldsymbol{Q}^*(\boldsymbol{x}^* + \boldsymbol{\ell}_Q^*, t^* + \tau_Q^*)$ to account for non-local effects [238, 258]. To first order, the non-local DPLE (N-DPLE) becomes

$$\tau_Q^* \frac{\partial \boldsymbol{Q}^*}{\partial t^*} + (\boldsymbol{\ell}_Q^* \cdot \nabla)\boldsymbol{Q}^* + \boldsymbol{Q}^* = -k^* \nabla T^* - k^* \tau_T^* \frac{\partial}{\partial t^*} \nabla T^*. \tag{2.15}$$

Similar to the TME, this equation incorporates non-local effects (by construction) already in form of first-order terms, although higher-order approximations could be considered.

In the early 2000's, Chen introduced the ballistic-diffusive equations, which divide the phonon population into ballistic and diffusive phonons [49, 50]. Upon decomposing phonon intensity, internal energy and heat flux into their ballistic and diffusive contributions, Chen derives an equation for the diffusive part very similar to the HHE but including a term relative to the ballistic contribution. Nevertheless, this model cannot be considered entirely macroscopic because it requires solving the EPRT to determine the ballistic heat flux. Vermeersch et al. proposed a partial differential equation with fractional derivatives to describe super-diffusive heat transport [243, 244].

Parallel to the development of extensions to the classical heat conduction laws, new frameworks extending the classical thermodynamic formalism were required [144, 189]. To prevent heat waves from causing a negative entropy production, Jou et al. [127, 140] proposed the framework of extended irreversible thermodynamics (EIT), where the heat flux and higher-order fluxes (flux of the flux, etc.) were considered as independent variables. Most of the macroscopic models introduced here can also be derived from this framework. Based on EIT, Alvarez and Jou [5] proposed an effective Fourier law where the bulk thermal conductivity is replaced by a size-dependent effective thermal conductivity, showing good agreement with experimental data. Several authors have used this effective thermal conductivity to incorporate non-local effects into the MCE and refer to this model as the improved MCE [5, 159].

## 2.3 Heat conduction through a semi-infinite solid

To illustrate the differences between the macroscopic models introduced above, we consider a simple example where a heat flux is created in a semi-infinite medium by raising the temperature at the origin. We consider a semi-infinite bar, initially at a constant temperature $T_0^*$. Suddenly, the temperature at $x^* = 0$ is raised to a value $T_1^*$, creating a heat flux through the solid. A similar example was considered in chapter 1, see Fig. 1.6.

We will mainly focus on the GKE and the MCE. The latter can be understood as a limit of the first. Comments on the thermomass and the dual-phase-lagging models follow in further sections.

In one spatial dimension, the GKE takes the form

$$\tau_R^* \frac{\partial Q^*}{\partial t^*} + Q^* = -k^* \frac{\partial T^*}{\partial x^*} + 3\ell^{*2} \frac{\partial^2 Q^*}{\partial x^{*2}}. \tag{2.16}$$

The boundary and initial conditions are

$$T^* = T_1^*, \qquad \text{at } x^* = 0, \tag{2.17a}$$

$$T^* \to T_0^*, \qquad \text{as } x^* \to \infty, \tag{2.17b}$$

$$T^* = Q^* = 0, \qquad \text{at } t^* = 0, \tag{2.17c}$$

i.e. we assume that the disturbance at $x^* = 0$ is not noticed sufficiently far away from the origin, and no heat flux is present initially.

### 2.3.1 Non-dimensional formulation

Let us introduce the dimensionless quantities

$$x = \frac{x^*}{L^*}, \quad t = \frac{t^*}{\tau_D^*}, \quad T = \frac{T^* - T_0^*}{\Delta T^*}, \quad Q = \frac{k^* \Delta T^* Q^*}{L^*}, \tag{2.18}$$

where $\Delta T^* = T_1^* - T_0^*$, $L^*$ is an arbitrary length and $\tau_D^* = L^{*2}/\alpha^*$ is the diffusive time scale introduced in the previous chapter. Note, this scaling corresponds to the classical non-dimensionalisation employed in Sec. 1.2 and hence the non-classical behaviour of the system will be described by means of new dimensionless parameters. In the non-dimensional formulation, conservation of energy takes the form

$$T_t + Q_x = 0, \tag{2.19}$$

where we have introduced the subscript notation for the derivatives. The dimensionless GKE is

$$\gamma Q_t + Q = -T_x + \eta^2 Q_{xx}, \tag{2.20}$$

where the parameters $\gamma = \tau_R^*/\tau_D^*$ and $\eta^2 = 3\ell^{*2}/L^{*2}$ are the dimensionless relaxation time and squared mean free path respectively. In the literature, $\gamma$ is known as the Cattaneo number and corresponds to the ratio of the non-classical time scale $\tau_R^*$, which describes a wave-like heat propagation, to classical time scale $L^{2*}/\alpha^*$, which is the characteristic time for diffusive heat transfer. The non-classical parameter $\eta$ is proportional to Kn and hence describes the presence of non-local effects.

The non-dimensional boundary and initial conditions are

$$T = 1, \qquad \text{at } x = 0, \tag{2.21a}$$

$$T \to 0, \qquad \text{as } x \to \infty, \tag{2.21b}$$

$$T = Q = 0, \qquad \text{at } t = 0. \tag{2.21c}$$

Note, we can combine Eqs. (2.19) and (2.20) to obtain

$$\gamma Q_t + Q = -T_x - \eta^2 T_{xt}, \tag{2.22}$$

In particular, for $\gamma = \eta^2$ we can express Eq. (2.22) as

$$\gamma F_t + F = 0, \tag{2.23}$$

where $F = Q + T_x$. Using Eq. (2.21c) we obtain $F(x, 0) = 0$ and hence $F(x, t) = 0$ for $t > 0$, from where we recover Fourier's law. This phenomenon is known as Fourier resonance [25, 241].

We can combine conservation of energy and the GKE to eliminate $Q$, which gives the Guyer-Krumhansl heat equation (GKHE)

$$\gamma T_{tt} + T_t = T_{xx} + \eta^2 T_{txx}, \tag{2.24}$$

For $\eta^2 = 0$ we obtain the one-dimenensional, dimensionless form of Eq. (2.10). Note, Eq. (2.24) is second-order in time and requires an initial profile of the thermal speed $T_t$. Evaluating Eq. (2.19) at $t = 0$ and using the initial conditions for $Q$ yields

$$T_t(x, 0) = 0. \tag{2.25}$$

### 2.3.2 Numerical solution

The finite difference method is a simple technique to find numerical solutions of multiple problems [217]. Let us assume that the bar has a finite (dimensionless) length $\delta$ which represents a distance beyond which the disturbance at the origin is not noticed. Therefore, the boundary condition at $x \to \infty$ is replaced by $T(\delta, t) = 0$. Upon defining the scaled quantities $\bar{t} = t/\delta^2$, $\bar{x} = x/\delta$, $\bar{T} = T$, $\bar{\gamma} = \gamma/\delta^2$ and $\bar{\eta} = \eta/\delta$, the problem becomes

$$\bar{\gamma}\bar{T}_{\bar{t}\bar{t}} + \bar{T}_{\bar{t}} = \bar{T}_{\bar{x}\bar{x}} + \bar{\eta}^2 \bar{T}_{\bar{t}\bar{x}\bar{x}}, \qquad 0 < \bar{x} < 1, \tag{2.26a}$$

$$\bar{T} = 1, \qquad \text{at } \bar{x} = 0, \tag{2.26b}$$

$$\bar{T} = 0, \qquad \text{at } \bar{x} = 1, \tag{2.26c}$$

$$\bar{T} = \bar{T}_{\bar{t}} = 0, \qquad\qquad \text{at } \bar{t} = 0. \tag{2.26d}$$

We now replace the unit interval by a grid of $N + 1$ points of the form

$$\bar{x}_0 = 0 < ... < \bar{x}_i = \frac{i}{N} < 1 = \bar{x}_N, \tag{2.27}$$

whereas time is discretised in a sequence of points of the form $t_n = n\Delta t$. The time derivatives are discretised as

$$\bar{T}_{\bar{t}} \approx \frac{\bar{T}_i^{n+1} - \bar{T}_i^n}{\Delta t}, \qquad \bar{T}_{\bar{t}\bar{t}} \approx \frac{\bar{T}_i^{n+1} - 2\bar{T}_i^n + \bar{T}_i^{n-1}}{(\Delta t)^2}, \tag{2.28a}$$

whereas derivatives with respect to $x$ become

$$\bar{T}_{\bar{x}} \approx \frac{\bar{T}_{i+1}^{n+1} - \bar{T}_{i-1}^{n+1}}{2\Delta x}, \qquad \bar{T}_{\bar{x}\bar{x}} \approx \frac{\bar{T}_{i+1}^{n+1}, -2\bar{T}_i^{n+1} + \bar{T}_{i-1}^{n+1}}{(\Delta x)^2} \tag{2.28b}$$

where $\Delta x = 1/N$. The mixed derivatives are approximated by

$$\begin{aligned} \bar{T}_{\bar{t}\bar{x}} &\approx \frac{\bar{T}_{i+1}^{n+1} - \bar{T}_{i-1}^{n+1}}{2\Delta t\Delta x} - \frac{\bar{T}_{i+1}^{n} - \bar{T}_{i-1}^{n}}{2\Delta t\Delta x}, \\ \bar{T}_{\bar{t}\bar{x}\bar{x}} &\approx \frac{\bar{T}_{i+1}^{n+1} - 2\bar{T}_i^{n+1} + \bar{T}_{i-1}^{n+1}}{\Delta t(\Delta x)^2} - \frac{\bar{T}_{i+1}^{n} - 2\bar{T}_i^{n} + \bar{T}_{i-1}^{n}}{\Delta t(\Delta x)^2}. \end{aligned} \tag{2.28c}$$

Replacing the derivatives in Eq. (2.26a) by the approximation introduced in (2.28), we obtain a set of $N - 1$ algebraic equations of the form

$$A_{i,i-1}\bar{T}_{i-1}^{n+1} + A_{i,i}\bar{T}_i^{n+1} + A_{i,i+1}\bar{T}_{i+1}^{n+1} = b_i^n, \tag{2.29a}$$

where $b_i^n = f(\bar{T}_{i-1}^n, \bar{T}_i^n, \bar{T}_{i+1}^n, \bar{T}_i^{n-1})$. The boundary conditions become

$$\bar{T}_0^{n+1} = 1, \tag{2.29b}$$

$$\bar{T}_N^{n+1} = 0, \tag{2.29c}$$

whereas initially we have

$$\bar{T}_i^0 = \bar{T}_i^1 = 0, \qquad i = 0, ..., N. \tag{2.30}$$

Figure 2.4 shows the evolution of the temperature according to Fourier's law. As it can be observed, the temperature at the heated boundary instantly reaches the value $T = 1$ and the heat diffuses into the medium. A very different behaviour is observed in Fig. 2.5, which shows the temperature on the plane $(x, t)$ according to the MCE. We can clearly see that

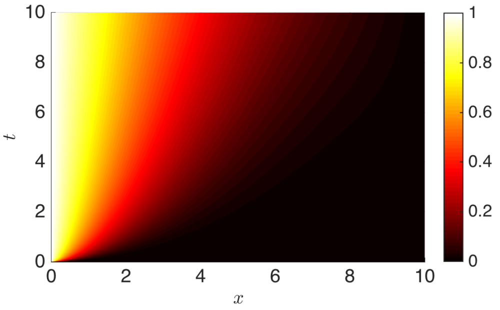

**Figure 2.4:** Contour plot showing the evolution of the temperature profile using Fourier's law.

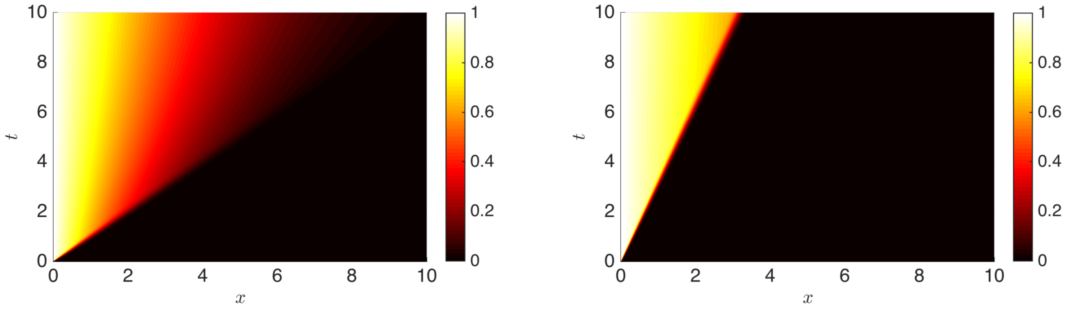

**(a)** $\gamma = 1$

**(b)** $\gamma = 10$

**Figure 2.5:** Contour plots showing the evolution of the temperature profile using the MCE with different values of $\gamma$.

the heat propagates in form of a sharp wave that starts to diffuse after a certain period of time. Additionally, we observe that the speed of propagation decreases as $\gamma$ increases. This can be understood by looking at the HHE, which is a wave equation with an additional damping term that describes the propagation of a temperature wave with a (dimensionless) speed $\gamma^{-1/2}$. Finally, we also observe that the transition from a wave-like propagation to a diffusive transport is delayed as we increase $\gamma$. This could be understood by performing an asymptotic analysis for large values of $\gamma$.

In Fig. 2.6 we show the evolution of the temperature for different values of $\gamma$ and $\eta^2$. We do not show the plots for the cases $\gamma = \eta^2$ because, as discussed earlier, this would reproduce

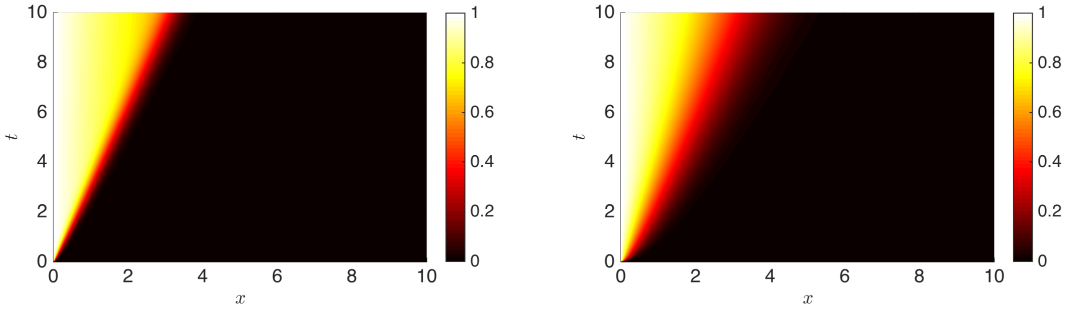

**(a)** $\gamma = 10$, $\eta^2 = 0.1$ **(b)** $\gamma = 10$, $\eta^2 = 1$

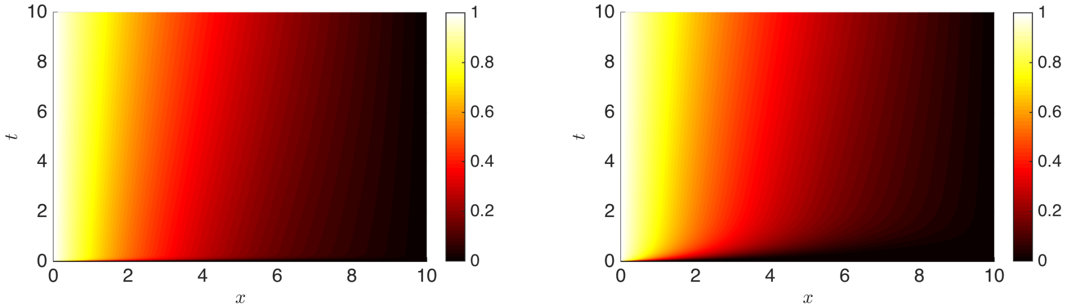

**(c)** $\gamma = 0.1$, $\eta^2 = 10$ **(d)** $\gamma = 1$, $\eta^2 = 10$

**Figure 2.6:** Contour plots showing the evolution of the temperature profile using the GKE with different values of $\gamma$ and $\eta^2$.

the classical temperature profile shown already in Fig. 2.4. The four different panels show two of the possible scenarios. When $\gamma > \eta^2$, Figs. 2.6a and 2.6b show that the memory term dominates initially and a wave-like propagation of the temperature is observed. By comparing Figs. 2.5b and 2.6b we observe that non-local effects are responsible for gradually smoothing the propagating disturbance and accelerating the transition from a pure wave-like transport to a diffusive one. Conversely, Figs. 2.6c and 2.6d show that, when heat transport is dominated by non-local term effects, the wave-like character disappears and the temperature propagates much faster than as predicted by Fourier's law. However, in Fig. 2.6d we see that the presence of the memory term does lead to an initial propagation in form of a temperature wave, although this is overcome very fast and is barely noticeable if we decrease $\gamma$ even more, as shown in Fig. 2.6c.

By comparing Figs. 2.4–2.6, we can draw two main conclusions. On one hand, when heat transport is dominated by memory effects and the disturbance propagates in the form of a travelling wave. Due to this behaviour, heat transport occurs slower than in the classical case. On the other hand, non-local effects accelerate the propagation of heat into the medium. In particular, the Fourier resonance phenomenon arises from these opposite effects cancelling each other out.

### 2.3.3 Heat conduction using the thermomass model

The one-dimensional TME is given by

$$\tau_{TM}^{*}\frac{\partial Q^{*}}{\partial t^{*}}+\ell_{TM}^{*}\frac{\partial Q^{*}}{\partial x^{*}}+Q^{*}=-(1-b)k^{*}\frac{\partial T^{*}}{\partial x^{*}}. \tag{2.31}$$

In dimensionless form, the latter becomes

$$\gamma_{TM}Q_t+\eta_{TM}Q_x+Q=-(1-b)T_x, \tag{2.32}$$

where $\gamma_{TM}=\alpha^{*}\tau_{TM}^{*}/L^{*2}$ and $\eta_{TM}=2\ell_{TM}^{*}/L^{*}$. In silicon, at room temperature we have $b\ll 1$ [101], hence we will set $b=0$ on the r.h.s to reduce the number of parameters. Upon combining Eqs. (2.19) and (2.32) we obtain the one-dimensional heat equation for the thermomass model

$$\gamma_{TM}T_{tt}+\eta_{TM}T_{tx}+T_t=T_{xx}, \tag{2.33}$$

which can be solved using a numerical scheme similar to the one proposed earlier for the GKHE.

The results of the numerical simulations are shown in Fig. 2.7. As in the case of the Guyer-Krumhansl formalism, the initial disturbance at $x=0$ propagates in the form of a sharp temperature wave that relaxes after a certain period of time. However, this occurs for any combination of the dimensionless parameters $\gamma_{TM}$ and $\eta_{TM}$. Mathematically, this is due to the fact that Eq. (2.33) is hyperbolic, in contrast to the parabolic character of the GKHE. Although in this case non-local effects do not eliminate the hyperbolicity of the heat equation, similarly to the GKHE they are responsible for enhancing heat transfer in the medium, as we see by comparing Figs. 2.7a and 2.7c with Figs. 2.7b and 2.7d. Conversely, increasing $\gamma_{TM}$ decreases the speed of propagation into the medium.

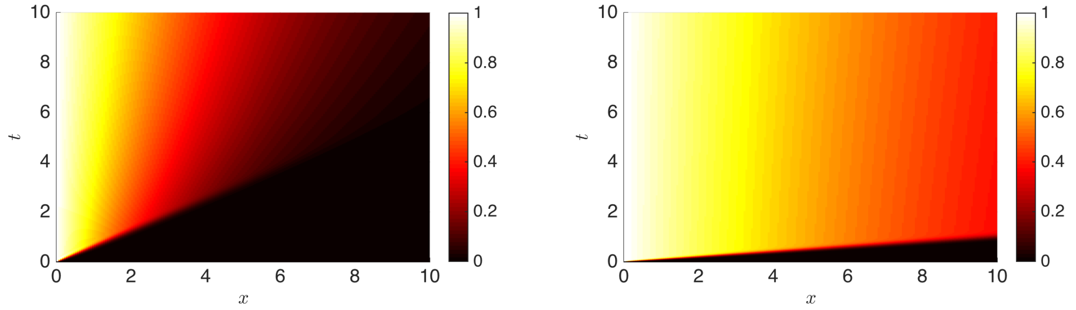

**(a)** $\gamma_{TM}, \eta_{TM} = 1$ **(b)** $\gamma_{TM} = 1$, $\eta_{TM} = 10$

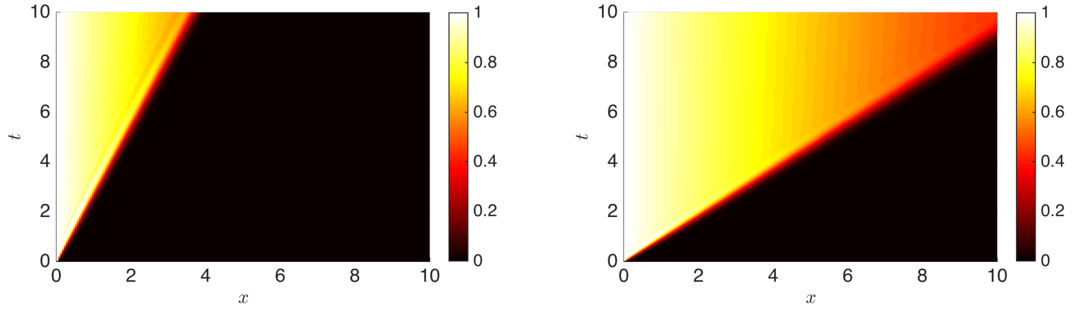

**(c)** $\gamma_{TM} = 10$, $\eta_{TM} = 1$ **(d)** $\gamma_{TM} = 10$, $\eta_{TM} = 10$

**Figure 2.7:** Contour plots showing the evolution of the temperature profile using the TME with different values of $\gamma_{TM}$ and $\eta_{TM}$.

### 2.3.4 Heat conduction using the non-local dual-phase-lagging model

In one dimension, the N-DPLE is

$$\tau_Q^* \frac{\partial Q^*}{\partial t^*} + \ell_Q^* \frac{\partial Q^*}{\partial x^*} + Q^* = -k^* \frac{\partial T^*}{\partial x^*} - k^* \tau_T^* \frac{\partial^2 T^*}{\partial t^* \partial x^*}, \tag{2.34}$$

which can be combined with conservation of energy to give

$$\tau_Q^* \frac{\partial Q^*}{\partial t^*} + \ell_Q^* \frac{\partial Q^*}{\partial x^*} + Q^* = -k^* \frac{\partial T^*}{\partial x^*} + \alpha^* \tau_T^* \frac{\partial^2 Q^*}{\partial x^{*2}}. \tag{2.35}$$

In dimensionless form, Eq. (2.35) becomes

$$\gamma_Q Q_t + \eta_Q Q_x + Q = -T_x + \gamma_T Q_{xx}, \tag{2.36}$$

where $\gamma_Q = \alpha^* \tau_Q^*/L^{*2}$, $\gamma_T = \alpha^* \tau_T^*/L^{*2}$ and $\eta_Q = \ell_Q^*/L^*$. Combining Eq. (2.36) with conservation of energy yields

$$\gamma_Q T_{tt} + \eta_Q T_{tx} + T_t = T_{xx} + \gamma_T T_{txx}, \tag{2.37}$$

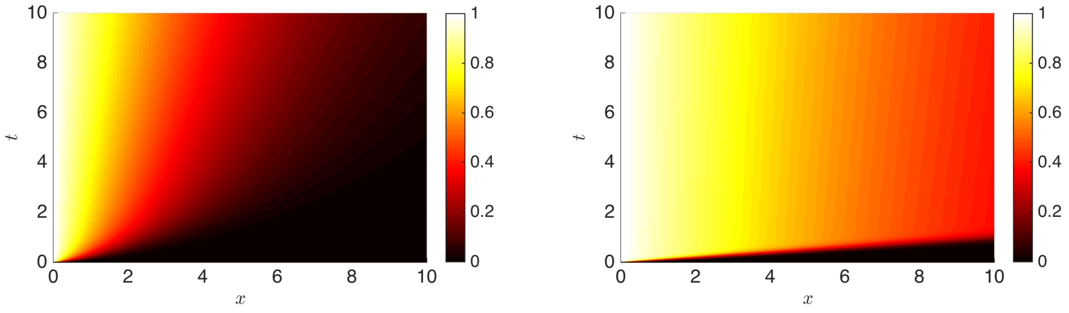

**(a)** $\gamma_Q = \eta_Q = \gamma_T = 1$

**(b)** $\gamma_Q = \gamma_T = 1$, $\eta_Q = 10$

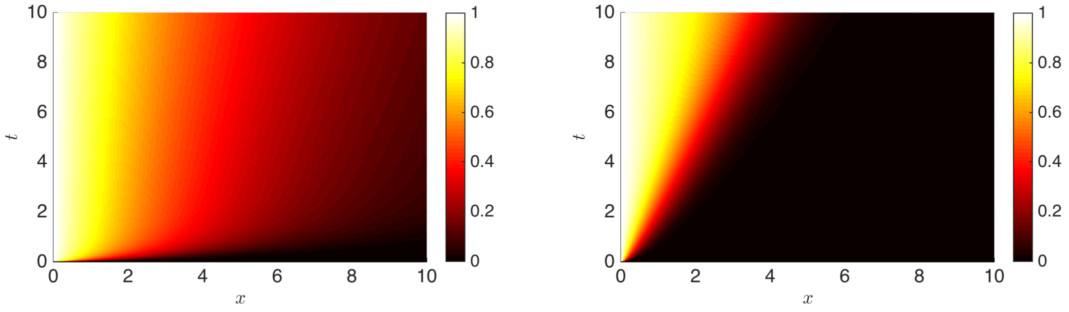

**(c)** $\gamma_Q = \eta_Q = 1$, $\gamma_T = 10$

**(d)** $\eta_Q = \gamma_T = 1$, $\gamma_Q = 10$

**Figure 2.8:** Contour plots showing the evolution of the temperature profile using the N-DPLE with different values of $\gamma_Q$, $\eta_Q$ and $\gamma_T$.

Contrary to the previous models, non-local effects are described by two terms instead of only one. In the numerical simulations shown in Fig. 2.8 we can observe that the features from the GKE and the TME can be recovered by increasing the corresponding non-local parameter: increasing $\eta_Q$ causes the temperature to evolve as in Fig. 2.7b, whereas for large values of $\gamma_T$ we recover a behaviour similar to the GKHE. When the term $T_{tt}$ is dominant ($\gamma_Q \gg 1$), we can observe a wave-like propagation with a strong damping, which comes from having two non-local terms, in contrast to the GKE or the TME.

## 2.4 Objectives of this dissertation

In this chapter we have reviewed some popular macroscopic models which aim to extend the classical Fourier law to account for non-classical heat transport mechanisms. In each of the models considered in Sec. 2.3, the differences with respect to the classical heat transport are described by new parameters with dimensions of time and space. In the case of the NDPLE these parameters are introduced in a phenomenological way and their physical meaning remains unclear. For the quantities introduced in the TME, some discussion about their physical interpretation is provided, yet the presence of a non-linear term suggests that little analytical progress can be made with this model unless the linearised version (2.12) is considered. Conversely, the GKE is a linear equation which involves parameters that have a clear physical interpretation and that may be computed from phonon properties by means of first principles, for instance. Hence, in the following chapters we focus will mainly be on the GKE and the MCE.

In particular, we attempt to address the following questions:

1. Is the Guyer-Krumhansl formalism suitable for capturing the size-dependence of the thermal conductivity that has been observed experimentally in nanowires with different cross-sections?
2. Which are the correct boundary conditions that have to be applied?
3. How do non-classical contributions in the governing equations alter the phase change kinetics?

From these questions we note that the objectives of this work are therefore twofold. On one hand, we wish to study the applicability of the Guyer-Krumhansl formalism and the framework of phonon hydrodynamics for predicting the experimentally measured thermal conductivity. If possible, we want to provide analytical expressions to facilitate the understanding of the non-classical effects. On the other hand, we intend to incorporate non-classical heat conduction equations into the mathematical formulation of phase change processes to assess the effects caused by these non-classical contributions.

# 3 | Hydrodynamic thermal transport in nanowires

M. Calvo-Schwarzwälder, M. G. Hennessy, P. Torres, T. G. Myers and F. X. Alvarez.
A slip-based model for the size-dependent effective thermal conductivity of nanowires.
International Communications in Heat and Mass Transfer 91: 57–63, 2018.
Impact factor: 3.781. Q1 in Condensed Matter Physics.

## 3.1 Introduction

Nanotechnology is currently the focus of extensive research due to its wide range of applications in fields such as industry and medicine [1, 56, 61, 88, 89, 154, 205]. Nanowires, in particular, are being used in technologies relating to solar cells [88], flexible screens [154], detection of cancerous cells [56], and energy storage [89]. A key issue facing the practical use of nanodevices is thermal management [31]. Inefficient regulation of heat can lead to large temperatures and melting, possibly resulting in device failure. Understanding and predicting heat flow on the nanoscale is therefore crucial for the manufacturing and operation of nanotechnologies.

It is widely known that many thermophysical material properties become size-dependent at the nanoscale [28, 137, 145, 214, 226, 229, 254, 256]. Buffat and Borel [28] showed a dramatic decrease of the melting temperature of gold nanoparticles of almost 50% from the bulk value. For aluminium nanoparticles, a decrease in latent heat by a factor of four has been reported [226]. Experimental observations also demonstrate that the thermal conductivity in silicon nanowires is much lower than the theoretical value predicted by kinetic theory [145]. For instance, it is reported that, at room temperature, the thermal conductivity of Si nanowires with a diameter of 37 nm decreases by approximately 87% with respect to the bulk value. Furthermore, when the characteristic size of the system is much smaller than the phonon mean free path, the thermal conductivity shows an approximately linear dependence on size [6, 7, 156, 238].

The size dependence of the thermal conductivity of nanosystems is attributed to the fact that, on the nanoscale, the transport of thermal energy is a ballistic process driven by infrequent collisions between thermal energy carriers known as phonons. This is in contrast to macroscopic heat transfer, which is a diffusive processes driven by frequent phonon collisions. As the size of a device becomes commensurate with the phonon mean free path, bulk phonons are more likely to collide with a boundary than with each other. The ability of a nanodevice to conduct thermal energy, therefore, becomes strongly influenced by the scattering dynamics at the boundary as well as the geometrical structure (e.g., size and shape) of this boundary.

Due to the fundamentally different manner in which heat is transported across nanometer length scales in comparison to heat flow at the macroscale, Fourier's law is unable to provide an accurate description of heat conduction in this regime [47]. Different approaches to modelling nanoscale heat flow have been developed in order to capture the ballistic nature of energy transport and size dependence of the effective thermal conductivity (ETC). These approaches can be classified into three main categories: microscopic, mesoscopic and macroscopic models. Microscopic approaches, such as molecular dynamics or Monte-Carlo methods [55], focus on the evolution of every single phonon while mesoscopic models group them together depending on their wavelength and wavevector. Micro and mesoscopic models are mainly based on the Boltzmann transport equation (BTE) and its solution under different approximations. A popular example is the equation of phonon radiative transfer (EPRT) [158], where an expression for the ETC similar to the classical expression from kinetic theory is derived, although here an effective mean free path is now considered. However this model is based on the gray approximation and thus considers a single phonon group velocity and lifetime. A more general model where these quantities are mode-dependent was presented by McGaughey et al. [166]. Starting again from the BTE, Alvarez et al. [5, 6] extract a continued-fraction expression to describe the ETC in thin films. Other models, such as those of Callaway [37] and Holland [112], also consider phonon distributions rather than single phonons, but Mingo et al. [171] showed that they fail when predicting the ETC for Si or Ge nanowires.

Macroscopic models aim to describe global variables of the system, such as the temperature and the heat flux. A recent approach at the macroscopic scale is the thermomass model, where heat carriers are assumed to have a finite mass determined by Einstein's mass-energy relation [238, 247, 248]. Other approaches are based on the Guyer-Krumhansl equation (GKE) [105, 106], which is derived from a linearized BTE in dielectric crystals. This equation has become popular since it is analogous to the extensively studied Navier-Stokes equations (NSEs) and it is one of the simplest extensions to Fourier's law that includes memory and non-local effects. Models based on the GKE are included in the framework of phonon hydrodynamics [127]. For instance, Alvarez et al. [7] use the analogy between the GKE and the NSEs to derive an expression for the ETC in circular nanowires, splitting the heat flux into two separate contributions. This work has been extended to elliptical and rectangular nanowires [211]. However, since the size of the phonon mean free path depends on temperature, the assumptions on which they base their reductions are only valid for low temperatures or very small sizes. Dong et al. [73] find an expression for the ETC by solving the full GKE at steady state, although their no-slip boundary condition leads to a quadratic dependence of the ETC on the characteristic size of the device for large Knudsen numbers instead of the known linear behaviour. This does not happen in the case of the expression derived by Ma [156], where a fixed flux is imposed on the outer boundary. However, Ma's solution for the nanowire shows a very poor match to data (their paper contains an error in that they plot the thin film solution in their figure for the nanowire; this actually shows reasonable agreement with the data). Further, most of the existing models are only validated at room temperature and therefore a deeper assessment of their accuracy is required.

In this chapter, we introduce a new phenomenological slip boundary condition that, when used with the GKE, results in ETC predictions that are in excellent agreement with experimental data for Si nanowires over a range of radii and temperatures. The proposed

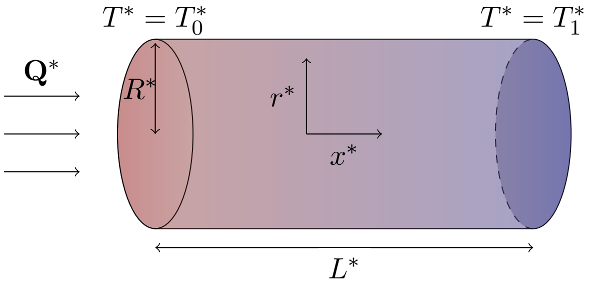

**Figure 3.1:** A circular nanowire with radius $R^*$ and length $L^*$ is held at different temperatures $T_0^*$, $T_1^*$ at the left and right ends respectively, which induces a heat flux $\mathbf{Q}^*$.

model is remarkably simple and only requires knowledge of the temperature dependence of the bulk thermal conductivity and phonon mean free path, both of which may be obtained experimentally or computationally, making it well suited for use in practical applications. A detailed comparison of the proposed and existing models is performed, the results of which show that the proposed model consistently yields the most accurate predictions of the ETC compared to existing models. Furthermore, this comparison establishes the validity of each model in terms of temperature and nanowire radius.

## 3.2 Mathematical model

We consider a circular nanowire (NW) of radius $R^*$ and length $L^*$ that is suspended in a vacuum; see Fig. 3.1. The radius of the NW is assumed to be much smaller than its length, i.e., $R^*/L^* = \epsilon \ll 1$. A temperature gradient $\Delta T^* = T_0^* - T_1^* > 0$ is imposed along the axial direction of the NW by fixing the temperature at its left and right ends to be $T_0^*$ and $T_1^*$, respectively. The thermal flux that is driven by this temperature gradient is assumed to be axisymmetric. Therefore, it is sufficient to consider a two-dimensional model with radial and axial coordinates $r^*$ and $x^*$, respectively. The mathematical model will consist of an equation representing conservation of thermal energy and the GKE describing the evolution of the thermal flux.

### 3.2.1 Governing equations

Conservation of energy requires

$$\frac{\partial \mathfrak{u}^*}{\partial t} = -\nabla \cdot \mathbf{Q}^*, \tag{3.1}$$

where $\mathfrak{u}^*(T^*)$ is the internal energy per unit mass and $T^*$ is the temperature. The thermal flux $\mathbf{Q}^* = v^*\hat{\mathbf{r}} + w^*\hat{\mathbf{x}}$ is assumed to satisfy the GKE

$$\tau^* \frac{\partial \mathbf{Q}^*}{\partial t} + \mathbf{Q}^* = -k^*\nabla T^* + \ell^{*2}\left(\nabla^2\mathbf{Q}^* + 2\nabla\nabla \cdot \mathbf{Q}^*\right), \tag{3.2}$$

where $v^*$ and $w^*$ are the radial and axial components of the heat flux, $\tau^*(T^*)$ is the total mean free time, $k^*(T^*)$ is the bulk thermal conductivity in the kinetic collective model (KCM) framework [65, 66, 234], and $\ell^*(T^*)$ is a non-local length related to the bulk phonon mean free path (MFP), i.e., the mean distance between phonon-phonon collisons. Zhu et al. [264] propose that $\ell^*$ is the geometric mean of the bulk MFP and a local MFP, the latter of which decreases near a boundary. Here, we opt for simplicity and model the decrease in MFP near the boundary through the slip boundary condition. For convenience, we will not write the temperature dependence of the parameters explicitly unless it is required due to the context. However, we note that, for the temperature ranges considered here, both the bulk thermal conductivity and non-local length mononotically decrease with temperature. As will be shown in Sec. 3.4, the non-local length of silicon decreases from about 5 $\mu$m at 50 K to 55 nm at 300 K.

The first term on the l.h.s. of (3.2) captures memory effects and, in particular, the dependence of heat flux on the history of the temperature gradient. The second term on the r.h.s. of (3.2) captures non-local effects, such as the interaction of phonons with the boundary of the NW. When the characteristic time and length scales are much larger than the resistive mean free time and non-local length, the GKE (3.2) reduces to Fourier's law.

For the remainder of the paper, we restrict our attention to the case of steady-state heat flow. This focus is motivated by the available experimental data. Under the steady-state assumption, $\partial \mathfrak{u}^*/\partial t = \partial \mathbf{Q}^*/\partial t = 0$. Conservation of energy (3.1) and the GKE (3.2) then reduce to

$$\nabla \cdot \mathbf{Q}^* = 0, \tag{3.3a}$$

$$\mathbf{Q}^* = -k^*\nabla T^* + \ell^{*2}\nabla^2\mathbf{Q}^*. \tag{3.3b}$$

This system is clearly analogous to an incompressible, viscous flow with a source term proportional to the velocity. Under this analogy, the parameter $\mu^* = \ell^{*2}/k^*$ may be interpreted as a thermal viscosity. These observations allow us to use well-known techniques from viscous flow to analyse the problem.

### 3.2.2 Boundary conditions

The boundary conditions for the temperature at the endpoints of the NW are

$$T^* = T_0^*, \qquad x^* = 0 \tag{3.4a}$$

$$T^* = T_1^*, \qquad x^* = L^*, \tag{3.4b}$$

where $T_0^* > T_1^*$. Due to the symmetry of the problem the boundary conditions at $r^* = 0$ are straightforward,

$$v^* = \frac{\partial w^*}{\partial r^*} = 0, \qquad r^* = 0. \tag{3.5}$$

We assume that no heat flows across the outer boundary, i.e.,

$$v^* = 0, \qquad r^* = R^*. \tag{3.6}$$

Finally, on the edge of the NW we continue the analogy with fluid dynamics and employ a slip condition,

$$w^* = -\ell_s^* \frac{\partial w^*}{\partial r^*}, \qquad r^* = R^*, \tag{3.7}$$

where $\ell_s^*$ is the slip length. In accordance with previous authors (see, e.g., Refs. [7, 264]), we will assume that the slip length is proportional to the non-local length, i.e., $\ell_s^* = C\ell^*$, where $C$ is a dimensionless parameter that encodes detailed information about phonon-boundary scattering and surface roughness. This form of boundary condition is discussed in more detail in Refs. [7, 210]. The basic idea is that a slip condition can capture crucial contributions to the thermal flux from reflected phonons. A no-slip condition neglects such contributions, resulting in predictions of the thermal flux and hence ETC that decrease too rapidly with the radius of the NW.

Various forms for the parameter $C$ appear in the literature. Alvarez *et al.* [7] write $C$ in terms of the specular parameter $p$, which describes the precise nature of phonon scattering (i.e., specular or diffuse). A similar approach is presented in Zhu et al. [264], although the authors essentially treat $p$, and hence $C$, as a fitting parameter. Sellitto et al. [210] write $C$ in terms of the surface geometry and then expand it as a power series in the temperature, resulting in a model with an excessive number of fitting parameters. Here, we take a more practical approach and write $C$ as a simple exponential, $C = \exp(-R^*/\ell^*)$, which is similar in form to the expression derived for and used in the specific case of a two-dimensional rectangular nanolayer by Zhu *et al.* [264]. The proposed exponential form does not involve any fitting parameters and it inherits a temperature dependence through the bulk non-local length $\ell^*(T^*)$. The motivation for this expression is as follows. If the non-local length is much less than the NW radius, $\ell^* \ll R^*$, then phonons are more likely to collide with each other than with the boundary and the influence of reflected phonons will be small, corresponding to a no-slip condition. Conversely, if the non-local length is much larger than the NW radius, $\ell^* \gg R^*$, then phonon-boundary scattering is more likely than phonon-phonon collisions. In this case, phonons reflections will strongly influence the flow, which is captured in a slip condition.

### 3.2.3 Reduction of the equations

We may reduce the governing equations by exploiting the separation between the axial and radial length scales. First, we introduce non-dimensional variables

$$r = \frac{r^*}{R^*}, \qquad x = \frac{x^*}{L^*}, \qquad v = \frac{v^*}{v_0^*}, \qquad w = \frac{w^*}{w_0^*}, \qquad T = \frac{T^* - T_1^*}{\Delta T^*}, \qquad k = \frac{k^*}{k_0^*}, \tag{3.8}$$

where $v_0^*$ and $w_0^*$ are (unknown) typical values of the axial and radial components of the heat flux and $k_0^*$ is a reference value for the bulk thermal conductivity. A relationship between $v_0^*$ and $w_0^*$ is obtained by requiring both terms in (3.3a) to have the same magnitude, which ensures that energy is conserved in the leading-order problem. This yields $v_0^* = \epsilon w_0^*$. Finally, the classical scale for the axial flux is chosen, $w_0^* = k_0^* \Delta T^*/L^*$, which ensures that Fourier's law is recovered in the classical limit, i.e., when the Knudsen number $\mathrm{Kn} = \ell^*/R^*$ tends to zero.

After non-dimensionalising the model given by (3.3) we obtain

$$T_r = O\left(\epsilon^2\right), \tag{3.9a}$$

$$w = -kT_x + \mathrm{Kn}^2\left[r^{-1}\left(rw_r\right)_r + O\left(\epsilon^2\right)\right], \tag{3.9b}$$

$$r^{-1}(rv)_r + w_x = 0. \tag{3.9c}$$

where we have introduced the subscript notation for derivatives. Since $\epsilon \ll 1$ we may neglect the small terms and arrive at the governing equation for heat flow in a NW

$$T_r = 0, \tag{3.10a}$$

$$w = -kT_x + \mathrm{Kn}^2 r^{-1}\left(rw_r\right)_r, \tag{3.10b}$$

$$r^{-1}(rv)_r + w_x = 0. \tag{3.10c}$$

Equation (3.10a) indicates $T \approx T(x)$ (to the order of the neglected terms), which simplifies the integration of Eqn. (3.10b). Notice also that if $\mathrm{Kn} \ll 1$ then the classical (non-dimensional) Fourier's law is retrieved,

$$w_{\mathrm{F}} = -kT_x. \tag{3.11}$$

The boundary conditions for $v$ become

$$v = 0, \qquad \text{at } r = 0, \tag{3.12a}$$

$$v = 0, \qquad \text{at } r = 1, \tag{3.12b}$$

whereas for $w$ we have

$$w_r = 0, \qquad \text{at } r = 0, \tag{3.13a}$$

$$w = -\mathrm{Kn}Cw_r, \qquad \text{at } r = 1, \tag{3.13b}$$

and, finally,

$$T = 1, \qquad \text{at } x = 0, \tag{3.14a}$$

$$T = 0, \qquad \text{at } x = 1. \tag{3.14b}$$

## 3.3 Calculation of the effective thermal conductivity

The ETC is defined as the ratio of the heat flux per unit area to the temperature gradient driving this flux. In non-dimensional form, the ETC may be expressed as

$$k_{\mathrm{eff}} = \frac{\bar{Q}}{-T_x}, \tag{3.15}$$

where the heat flux per unit area is

$$\bar{Q} = 2\int_0^1 rw(r,x)\,dr\,. \tag{3.16}$$

Calculating the integral in (3.16) requires solving Eqn. (3.10b) for the axial component of the flux $w$, which is trivial because the temperature does not depend on the radial coordinate. Upon solving (3.10b) and applying the boundary conditions (3.13), we find that

$$w(r,x) = -k\left(1 - \frac{I_0(r/\mathrm{Kn})}{I_0(1/\mathrm{Kn}) + CI_1(1/\mathrm{Kn})}\right)T_x, \tag{3.17}$$

where $I_\nu$ is the modified Bessel function of the first kind of order $\nu$. The heat flux per unit area may then be calculated as in (3.16), which yields

$$\bar{Q} = -k\left(1 - \frac{2\mathrm{Kn}I_1(1/\mathrm{Kn})}{I_0(1/\mathrm{Kn}) + CI_1(1/\mathrm{Kn})}\right)T_x. \tag{3.18}$$

According to its definition in (3.15), the ETC is finally given by

$$\frac{k^*_{\text{eff}}}{k^*} = 1 - \frac{2\mathrm{Kn}I_1(1/\mathrm{Kn})}{I_0(1/\mathrm{Kn}) + CI_1(1/\mathrm{Kn})} \tag{3.19}$$

In principle, the temperature can be calculated from (3.18) by first noting that, at steady state, the flux $\bar{Q}$ must be uniform in the axial direction: if a different amount of energy enters the wire to that leaving, then the temperature must vary with time. Due to the temperature dependence of the parameters appearing in (3.18), we have that $T$ satisfies a nonlinear ODE of the form

$$T_x = f(T, \bar{Q}), \tag{3.20}$$

which is analogous to the Reynolds equation in fluid mechanics [186]. Solving the first-order ODE (3.20) and imposing the boundary condition $T = 1$ at $x = 0$ determines the temperature in terms of the flux $\bar{Q}$. Subsequently applying the boundary condition $T = 0$ at $x = 1$ to the solution for the temperature enables the flux to be obtained.

Due to the dependence of $\mathrm{Kn} = \ell^*(T^*)/R^*$ on temperature and the radius of the NW, Eqn. (3.19) can be reduced to simpler expressions in some limiting cases. For instance, at very low temperatures or for very small radii we have $\mathrm{Kn} \gg 1$. Using $I_0(\xi) = 1 + O(\xi^2)$ and $I_1(\xi) = \xi/2 + O(\xi^3)$ for $\xi \ll 1$, as well as $C(\mathrm{Kn}) = 1 - \mathrm{Kn}^{-1} + O(\mathrm{Kn}^{-2})$ for $\mathrm{Kn} \gg 1$, we find that (3.19) can then be reduced to

$$\frac{k^*_{\text{eff}}}{k^*} = \frac{1}{2\mathrm{Kn}} + O\left(\frac{1}{\mathrm{Kn}^2}\right), \quad \mathrm{Kn} \gg 1, \tag{3.21}$$

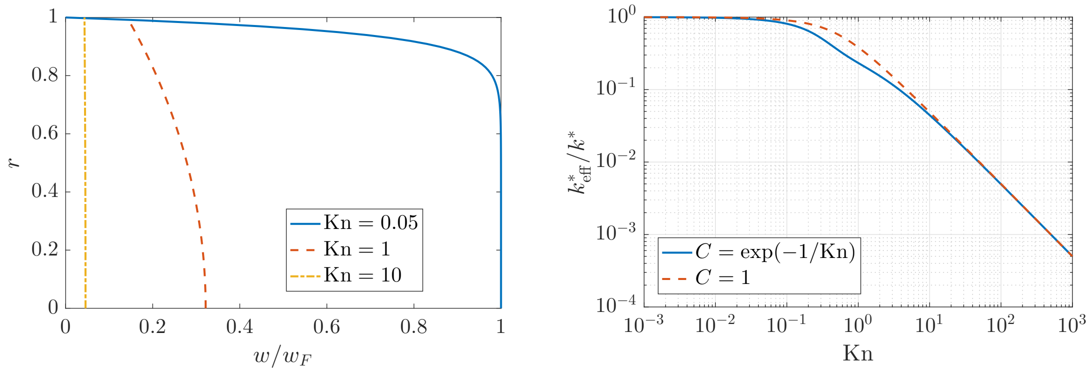

**(a)** **(b)**

**Figure 3.2:** (a) Axial component of the heat flux according to Eqn. (3.17) with $C = \exp(-1/\text{Kn})$ for different values of Kn and scaled with the classical heat flux $w_{\text{F}}$. Solid, dashed and dashed-dotted lines correspond to $\text{Kn} = 0.05$, $\text{Kn} = 1$ and $\text{Kn} = 10$ respectively. (b) The dependence of the ETC given by (3.19) on the Knudsen number for two choices of the function $C$.

from which we deduce $k^*_{\text{eff}} \propto R^*$, in agreement with previous theoretical results [6, 7, 156, 238]. In deriving the leading-order term in (3.21), only the leading contribution to $C$, given by $C \sim 1$, is required. Thus, any alternative expression of $C$ that has a large-Kn expansion of the form $C = 1 + O(\text{Kn}^{-\alpha})$, with $\alpha > 0$, will result in the asymptotic behaviour $k^*_{\text{eff}}/k^* \sim (2\text{Kn})^{-1}$ as $\text{Kn} \to \infty$. For larger devices or at high temperatures, where $\text{Kn} \ll 1$, the ETC should reduce to its classical value as non-local effects become negligible. To show this, we use the relation [209] $I_1(\xi)/I_0(\xi) = 1 - (2\xi)^{-1} + O(\xi^{-2})$ for $\xi \gg 1$ in (3.19) to obtain

$$\frac{k^*_{\text{eff}}}{k^*} = 1 - 2\text{Kn} + O\left(\text{Kn}^2\right), \quad \text{Kn} \ll 1; \tag{3.22}$$

hence the conductivity tends to the bulk value as $\text{Kn} \to 0$. The asymptotic behaviour $k^*_{\text{eff}}/k^* \sim 1 - 2\text{Kn}$ as $\text{Kn} \to 0$ will be true for all functional forms of $C$ with the limit $C \to 0$ as $\text{Kn} \to 0$.

To aid with the physical interpretation of the model solutions and their asymptotic limits, the radial dependence of the axial flux $w$ is plotted for three Knudsen numbers ($\text{Kn} = 0.05$, 1, and 10) in Fig. 3.2 (a). The ETC, given by (3.19), is plotted as a function of the Knudsen number in Fig. 3.2 (b) for two choices of the function $C$. The figures make it clear that there are three distinct regimes to consider, corresponding to diffusive ($\text{Kn} \ll 1$), ballistic ($\mathrm{Kn} \gg 1$), and mixed ($\mathrm{Kn} = O(1)$) modes of thermal energy transport. The three values of the Knudsen number in Fig. 3.2 (a) are chosen to clearly illustrate how the axial flux varies across these three regimes.

For small Knudsen numbers, $\mathrm{Kn} \ll 1$, the phonon MFP is small compared to the radius of the NW. Phonons in the bulk are therefore more likely to collide with each other before reaching the boundary of the NW and scattering. This corresponds to the boundary condition $w \to 0$ as $\mathrm{Kn} \to 0$. Due to the relatively small influence of non-local effects, thermal energy in the bulk is transported with little resistance across the NW, with an axial flux that approximates the classical flux $w_F$ predicted by Fourier's law. However, there is a thin boundary layer near the edge of the NW where the flux rapidly decreases to zero in order to satisfy the no-slip condition. The (dimensional) width of this boundary layer is $O(\ell^*)$, reflecting the fact that boundary effects become relevant on length scales that are commensurate with the phonon MFP. As the Knudsen number tends to zero, the width of this boundary layer does so as well. The restricted transport of thermal energy in the boundary layer leads to a slight reduction in the ETC compared to its bulk value, which is captured in the small-Kn limit of $k_{\mathrm{eff}}$ given by (3.22) and shown in Fig. 3.2 (b) by the slow reduction in $k^*_{\mathrm{eff}}/k^*$ as Kn increases from $10^{-3}$ to $10^{-1}$.

In the limit of large Knudsen number, $\mathrm{Kn} \gg 1$, the phonon MFP greatly exceeds the radius of the NW. Phonons therefore collide more frequently with the boundary than with each other, resulting in a substantial decrease in the flow of thermal energy. The strong influence of non-local effects and large slip length lead to an axial flux that is uniform along the radial direction and, in particular, close to its value on the boundary, $w \sim \mathrm{Kn}^{-1} w_F/2$. Therefore, as $\mathrm{Kn} \to \infty$, corresponding to an arbitrarily large MFP relative to the NW radius, the axial flux tends to zero. The restricted transport of energy in this regime results in a marked decrease in the ETC, the magnitude of which also scales linearly with $\mathrm{Kn}^{-1}$, as demonstrated in Eq. (3.21).

The proportionality between the flux $w$ and the inverse Knudsen number $\mathrm{Kn}^{-1}$ can be understood by drawing on the analogy between nanoscale heat transfer and fluid dynamics. In the limit of large Kn (analogous to large viscosity), the net force exerted by the temperature gradient (analogous to pressure) on an arbitrary cross section of the NW must balance the net traction (i.e., shear stress) along its circumference,

$$\pi k T_x \sim 2\pi \mathrm{Kn}^2 w_r, \qquad \text{at } r = 1. \tag{3.23}$$

From Eq. (3.23) it is seen that the rate of shear strain, $w_r$, induced by the temperature gradient is small and of size $O(\mathrm{Kn}^{-2})$. The scaling for the flux (analogous to velocity) is determined by the slip condition (3.13), yielding $w \sim \mathrm{Kn}\,\partial w/\partial r \sim \mathrm{Kn}^{-1} w_F/2$, where the rate of strain has been eliminated using (3.23) and $C$ has been approximated by its leading-order contribution $C \sim 1$ as $\mathrm{Kn} \gg 1$. Thus, the scaling with $\mathrm{Kn}^{-1}$ arises from the combination of large $O(\mathrm{Kn})$ slip length and small $O(\mathrm{Kn}^{-2})$ rate of strain.

The case of $\mathrm{Kn} = O(1)$ corresponds to an intermediate regime where the length scales of the NW radius and MFP are the same order of magnitude. Boundary scattering plays an important role and the order-one slip length leads to a parabolic-like flux. Unlike the large- and small-Kn regimes, the ETC is strongly dependent on the functional form of $C$ when $\mathrm{Kn} = O(1)$. Figure 3.2 (b) shows the ETC when $C = \exp(-1/\mathrm{Kn})$ (solid line) and $C = 1$ (dashed line). The former corresponds to the situation where the slip length $\ell_s^*$ is smaller than the non-local length $\ell^*$ (recall that $\ell_s^* = \ell^* C$). Taking $C = 1$ implies that the slip length and MFP are equal. The exponential form of $C$ results in a slight kink near $\mathrm{Kn} = 1$. In physical terms, this kink is associated with a reduced ETC compared to the $C = 1$ case and is the consequence of a smaller slip length and hence axial flux. Using $C = 1$ smooths out this kink and yields higher values of the ETC due to greater slip.

## 3.4 Results and discussion

The prediction of the ETC is now compared against experimental data measured from Si nanowires with diameters $D^* = 2R^* = 37$ nm, 56 nm, and 115 nm at temperatures ranging from $T^* = 50$ K up to 300 K [145]. Evaluating the ETC prediction requires knowledge of the temperature dependence of the non-local length $\ell^*$ and thermal conductivity $k^*$. These two quantities are obtained from first principles in the KCM framework [65, 66, 234] using an open-source code [232]. A more detailed explanation is given in Appendix A. The bulk MFP ranges from 55 nm to 5 $\mu$m, corresponding to Knudsen numbers between 2.98 and 262 ($D^* = 37$ nm), 1.97 and 173 ($D^* = 56$ nm), and 0.958 and 84.2 ($D^* = 115$ nm).

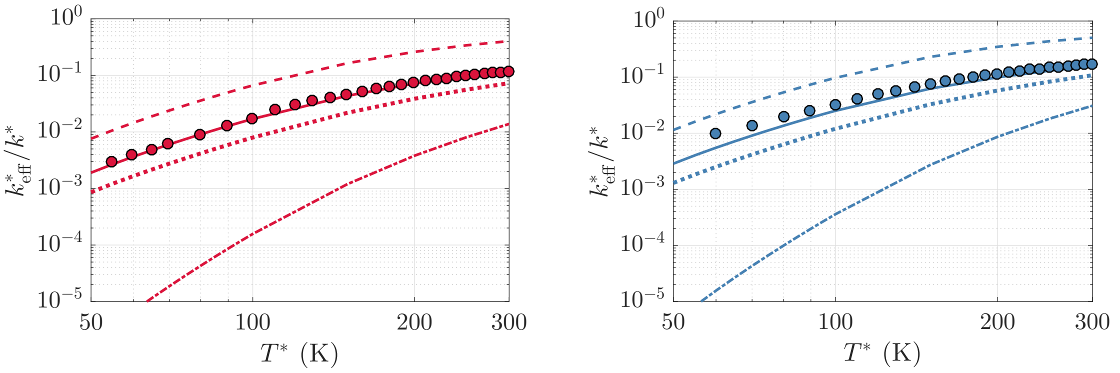

**(a)** $D^* = 37$ nm.

**(b)** $D^* = 56$ nm.

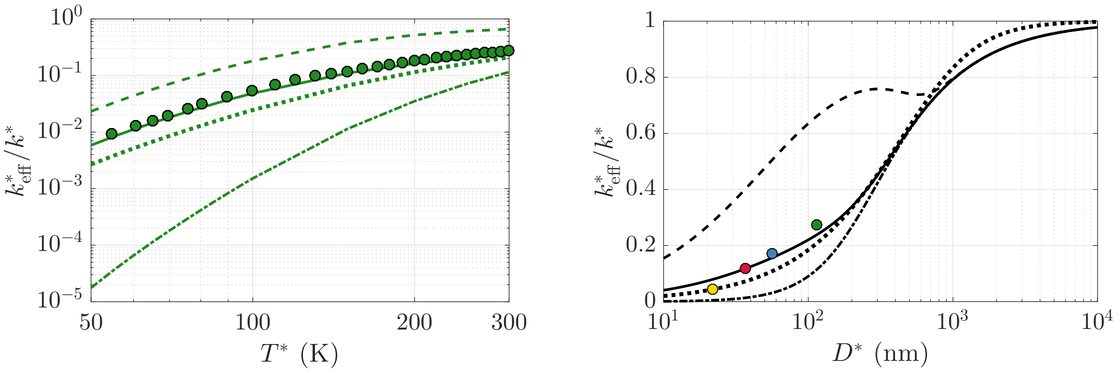

**(c)** $D^* = 115$ nm.

**(d)** $T^* = 300$ K.

**Figure 3.3:** Comparison of theoretical predictions and experimental data for $k^*_{\mathrm{eff}}$ in Si NWs of varying radii and temperature. Solid lines correspond to Eqn. (3.19); dashed, dotted and dashed-dotted lines represent the model predictions given by Refs. [6, 73, 156], respectively; and circles denote experimental data [145].

Thus, the exponential form of $C$ will be relevant when comparing the ETC prediction to the experimental data. Indeed, we find poor agreement when the the dependence of $C$ on Kn is neglected and $C$ is held at unity.

Figure 3.3 shows the ETC predicted by (3.19) (solid lines) and experimentally measured values of the ETC (symbols) as functions of temperature for three NW diameters (Figs. 3.3 (a)–(c)) and as functions of the diameter for a fixed temperature (Fig. 3.3 (d)). The ETC $k^*_{\mathrm{eff}}$ is normalised against the bulk value $k^*$ to highlight the relative change that occurs as the diameter of the NW and non-local length decrease. In all cases, the theoretical predictions are in excellent agreement with the experimental data.

The dashed, dotted, and dashed-dotted lines in Fig. 3.3 represent theoretical predictions of the ETC computed from existing models found in Refs. [6, 73, 156], respectively. It is clear that that the model proposed here consistently yields predictions that are more representative of the experimental data. The models of Ma [156] and Dong et al. [73], both of which are based on the GKE, are unable to quantitatively capture the experimental data associated with all three NW diameters. These inaccuracies can be attributed to the different boundary conditions that are used in their models. Dong et al. [73] employ a no-slip boundary condition, equivalent to $C = 0$ in our model. Imposing this boundary condition leads to particularly large errors at low temperatures (or large Knudsen numbers). Moreover, the calculated ETC becomes quadratically dependent on the NW radius, i.e., $k^*_{\text{eff}}/k^* \propto R^{*2}$, which contradicts the experimentally measured linear dependence between these two quantities. Ma [156] instead considers a prescribed flux on the boundary, which leads to substantial inaccuracies across the whole temperature range. The expression for the ETC presented by Alvarez and Jou [6] gives the most accurate prediction of the three existing models, although it generally underestimates the experimentally measured values. A distinguishing feature of Alvarez and Jou's expression is that it is derived from the linearised Boltzmann equation rather than the GKE. This derivation does not explicitly account for the cylindrical geometry of the nanowire and thus no boundary conditions can be imposed along the outer edge, which may contribute to the errors seen in Fig. 3.3. In comparison to the models derived from the GKE, the model of Alvarez and Jou predicts that the ETC converges more rapidly to the macroscopic value with increasing NW diameter; see Fig. 3.3 (d). However, the lack of experimental data for microscale NW diameters prevents the models from being validated in this regime.

## 3.5 Conclusion

We have proposed a new phenomenological slip model that can be coupled with the Guyer–Krumhansl equation in order to obtain an analytical expression for the size-dependent ETC in thin nanowires. A key advantage of the proposed model is that it only requires knowledge of the bulk thermal conductivity and MFP and does not involve any fitting parameters. The prediction of the ETC of Si nanowires is found to be in excellent agreement with experimental measurements, which is particularly remarkable given the simple nature of the underlying model. When compared against existing models for the ETC, we observed that the proposed model yielded the most accurate predictions in all cases.

Crucial to the success of our model is the condition imposed on axial flux $w^*$ at the outer boundary of the nanowire. Similar models, but with different boundary conditions, were shown to be in poor agreement with much of the experimental data. It is surprising that the present choice, based purely on an analogy with viscous fluid flow, works so well without resorting to any parameter fitting. Consequently, in our future work, we intend to further investigate the precise form of the boundary condition and, ideally, produce an expression based on a detailed physical model.

Finally, although we focused on circular nanowires, the model could, in principle, be applied to arbitrary geometries. Analytical solutions could be sought in the case of simple geometries such as rectangular nanofilms. In the case of complex geometry, the model could be straightforwardly implemented in finite element software, enabling a broad range of scenarios to be explored.

# 4 | Hydrodynamic thermal transport in rectangular nanorods

M. Calvo-Schwarzwälder, M. G. Hennessy, P. Torres, T. G. Myers and F. X. Alvarez.
Effective thermal conductivity of rectangular nanowires based on phonon hydrodynamics.
International Journal in Heat and Mass Transfer 126: 1120–1128, 2018.
Impact factor: 3.458. Q1 in Condensed Matter Physics.

## 4.1 Introduction

Advances in manufacturing processes have brought us to the stage where reliable nanoscale devices are now commonplace. However, in most current and predicted applications of nanostructures, there is a strong concern over the management of heat [32]. One specific issue with heat removal is the dramatic decrease of the thermal conductivity at the nanoscale in comparison to the bulk value [11, 121, 145, 152]. This decrease can be rationalised in terms of the manner by which thermal energy is transported across the macroscale and nanoscale. At the macroscale, heat transfer is a diffusive process driven by frequent collisions between thermal energy carriers known as phonons. In contrast, the transport of thermal energy across the nanoscale is a ballistic process driven by infrequent collisions between phonons. As the size of a device approaches that of the phonon mean free path, the phonons become more likely to collide with a boundary than with each other. This results in a conductivity which is more strongly influenced by the scattering dynamics at the boundary than collisions in the bulk. Consequently, thermal energy is transported less efficiently across the nanosystem, yielding a decrease in the thermal conductivity from the bulk value of the material.

Developing mathematical models to aid in the understanding of heat flow has proved problematic due to the breakdown of Fourier's law at small time and length scales [47, 113, 125]. With the aim of accurately predicting the effective thermal conductivity (ETC) of nanosystems, a variety of theoretical models of nanoscale heat transport have been proposed, either based on micro- and mesoscopic approaches [37, 112] or from a macroscopic point of view [5, 7, 41, 73, 156, 211, 238, 264]. A popular approach is the phonon hydrodynamics model [5, 7, 41, 73, 156, 211, 264], which is based on the Guyer–Krumhansl equation (GKE) [105, 106]. This model was first presented to describe heat transfer in the so-called hydrodynamic regime, where phonon flow behaves as a rarefied gas due to the dominance of normal scattering, i.e., scattering which conserves quasi-momentum, over resistive scattering, which does not conserve phonon quasi-momentum [99, 105, 106]. It was originally believed that the hydrodynamic transport regime only occurs at extremely low temperatures. However, recent ab initio calculations have demonstrated that phonon hydrodynamics can be valid even at room temperature [100, 143, 265]. As with many other macroscopic models such as the thermomass model [71, 238] or the equation of phonon radiative transfer [158], the GKE can derived from the Boltzmann transport equation (BTE) [24] or from the extended irreversible thermodynamics (EIT) framework [127]. Thus, the GKE provides a link between microscopic (kinetic) and macroscopic (continuum) models. Another attractive feature of the phonon hydrodynamics model is that the governing equations are analogous to those seen in viscous fluid mechanics, which provides an intuitive conceptual framework for model development and interpretation. The analogy between the phonon hydrodynamics and fluid dynamics models has prompted researchers to apply the well-known slip boundary condition to thermal transport [7, 41, 211, 264]. In fact, it has been shown that this form of boundary condition naturally arises from the discrete BTE [257] and from the EIT framework [99]. With the correct choice of slip length, this approach was shown to provide excellent agreement with experimental measurements of the ETC of silicon nanowires [41].

Aside from circular nanowires, studies employing the slip boundary condition are mainly confined to two-dimensional thin-film geometries [7, 211, 264]. Although the reduced dimensionality of this geometry enables a simple, closed-form expression for the ETC to be obtained, it can only be applied to nanowires with extremely small cross-sectional aspect ratios. However, rectangular nanowires with aspect ratios as high as 0.64 have been reported in the literature [121]. Unlike the thin-film geometry, the cross section of a rectangular nanowire will have two additional boundaries, as well as four corners, that will be detrimental to thermal transport. Therefore, the geometry of the rectangular cross section will play a key role in determining the ETC of the nanowire and have practical consequences in terms of thermal regulation in nanodevices.

The purpose of the present study is to use the phonon hydrodynamic model with a slip boundary condition to calculate the ETC in a rectangular nanowire, with the aim of gaining an improved understanding of how finite cross-sectional geometries influence nanoscale heat transport. Of particular interest is determining the nanowire geometry that leads to the most efficient transport of heat. Theoretical predictions of the ETC are compared against experimentally measured values. We show that the model is able to accurately capture the experimental data across a wide range of temperatures.

The chapter is organised as follows. The model and boundary conditions are presented in Sec. 4.2 and expressions for the ETC are given in Sec. 4.3. In Sec. 4.4, the modelling results are discussed and the theoretical predictions are compared against experimental data.

## 4.2 Mathematical model

We model the transport of thermal energy across a long nanowire with rectangular cross section that is suspended in a vacuum; see Fig. 4.1. The length of the nanowire $L_3^*$ is assumed to be much greater than both the half-width $L_1^*$ and half-height $L_2^*$ of the cross section. The $^*$ notation is used to denote dimensional quantities. Without loss of generality, the cross section can be taken to be wider than it is tall, $L_2^*/L_1^* < 1$. Under these conditions, the cross-sectional aspect ratio $\phi = L_2^*/L_1^*$ and the longitudinal aspect ratio $\epsilon = L_2^*/L_3^*$ satisfy $\epsilon \ll \phi < 1$. The transverse coordinates $x^*$ and $y^*$ denote points within a given cross section whereas the longitudinal coordinate $z^*$ describes distances along the length of the nanowire. The origin of the cross section $(x^*, y^*) = (0, 0)$ is chosen to coincide with the center of the rectangular face. The transport of heat is driven by a longitudinal temperature gradient $\Delta T^* > 0$ that is imposed by fixing the temperature $T^*$ at the ends of the nanowire to be $T^* = T_0^* + \Delta T^*$ at $z^* = 0$ and $T^* = T_0^*$ at $z^* = L_3^*$. The thermal flux is assumed to be symmetric about the $x^* = 0$ and $y^* = 0$ planes.

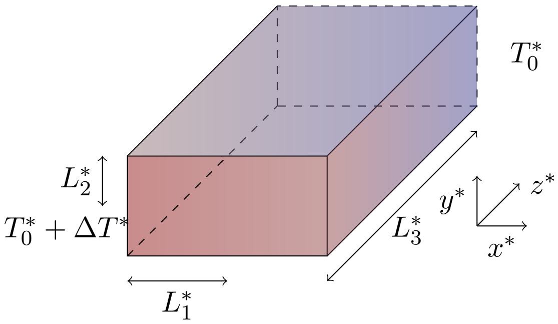

**Figure 4.1:** The experimental setup consists of a rectangular nanowire of length $L_3^*$ and with a cross-section of dimensions $2L_1^* \times 2L_2^*$. The heat flux $\mathbf{Q}^*$ is induced by a constant temperature difference $\Delta T^* > 0$.

### 4.2.1 Governing equations

The mathematical model consists of an equation representing conservation of thermal energy and the GKE (or hydrodynamic equation) describing the evolution of the thermal flux. Under the steady-state assumption, the governing equations are

$$\nabla \cdot \mathbf{Q}^* = 0, \tag{4.1a}$$

$$\mathbf{Q}^* = -k^* \nabla T^* + \ell^{*2} \nabla^2 \mathbf{Q}^*, \tag{4.1b}$$

where $\mathbf{Q}^* = u^* \hat{\mathbf{x}}^* + v^* \hat{\mathbf{y}}^* + w^* \hat{\mathbf{z}}^*$ is the thermal flux written in terms of Cartesian components, $k^*(T^*)$ is the bulk thermal conductivity, and $\ell^*(T^*)$ is a non-local length related to the bulk phonon mean free path (MFP), *i.e.*, the mean distance between phonon-phonon collisions. In the original equation derived by Guyer and Krumhansl, the parameter $\ell^*$ represents the bulk MFP defined as $\ell^{*2} = (v^{*2} \tau_N^* \tau_R^*)/5$, where $v^*$ is the phonon group velocity and $\tau_N^*$ and $\tau_R^*$ are the normal and resistive mean free times, i.e., the mean times for normal and resistive scattering. Other researchers have proposed alternative definitions for $\ell^*$, such as the geometric mean of the bulk MFP and a local MFP, the latter of which decreases near a boundary [264]. We take $\ell^*$ to be the non-local length computed from the kinetic collective model (KCM), which is an accurate approach for predicting the thermal conductivity in a number of materials [234]. We refer to Appendix A for a more detailed description of how $\ell^*$ is obtained from the KCM.

For simplicity, the dependence of the parameters on the temperature will not be explicitly written unless required by the context. The second term on the r.h.s. of (4.1b) accounts for non-local effects, i.e. phonon collisions. The strong increase in the length scale $\ell^*$ as the temperature decreases can make non-local effects relevant in relatively large systems, including those with dimensions exceeding the nanoscale [127, 231].

The size-dependent effective thermal conductivity (ETC) of the nanowire $k^*_{\text{eff}}$ is defined as in terms of the mean thermal flux through a cross section $\bar{Q}^*$ and the longitudinal temperature gradient $\partial T^*/\partial z^*$ as

$$k^*_{\text{eff}} = -\frac{\bar{Q}^*}{\partial T^*/\partial z^*}, \quad \bar{Q}^* = \frac{1}{4L_1^*L_2^*}\int_{-L_2^*}^{L_2^*}\int_{-L_1^*}^{L_1^*} w^* \, \mathrm{d}x^* \mathrm{d}y^*. \tag{4.2}$$

By construction, this is the only component that is not tangential to the cross-section. Therefore, to compute the effective thermal conductivity of a rectangular slab, we need to find only the normal component of the heat flux $w^*$.

### 4.2.2 Boundary conditions

The boundary conditions for the temperature at the endpoints of the nanowire are

$$T^* = T_0^* + \Delta T^*, \quad \text{at } z^* = 0, \tag{4.3a}$$

$$T^* = T_0^*, \quad \text{at } z^* = L_3^*. \tag{4.3b}$$

Furthermore, it is sufficient to solve the equations in the region $x^*, y^* \geq 0$ due to the symmetry of the system. The symmetry conditions at the interior boundaries ($x = 0$ or $y = 0$) are straightforward,

$$u^* = 0, \quad \frac{\partial v^*}{\partial x^*} = 0, \quad \frac{\partial w^*}{\partial x^*} = 0, \quad \text{at } x^* = 0, \tag{4.4a}$$

$$\frac{\partial u^*}{\partial y^*} = 0, \quad v^* = 0, \quad \frac{\partial w^*}{\partial y^*} = 0, \quad \text{at } y^* = 0. \tag{4.4b}$$

At the exterior boundaries of the nanowire ($x^* = L_1^*$ or $y^* = L_2^*$) we impose two types of boundary condition. The normal component of the flux is assumed to vanish to ensure that no energy is lost during the heating process. For components of the flux that are tangential to the surface, we impose slip conditions with a slip length $\ell_s^*$. The boundary conditions are therefore given by

$$u^* = 0, \qquad v^* = -\ell_s^* \frac{\partial v^*}{\partial x^*}, \qquad w^* = -\ell_s^* \frac{\partial w^*}{\partial x^*}, \qquad \text{at } x^* = L_1^*, \tag{4.4c}$$

$$u^* = -\ell_s^* \frac{\partial u^*}{\partial y^*}, \qquad v^* = 0, \qquad w^* = -\ell_s^* \frac{\partial w^*}{\partial y^*}, \qquad \text{at } y^* = L_2^*. \tag{4.4d}$$

Microscopically, slip refers to the mean direction that phonons travel after they collide with a boundary and are reflected. Non-zero slip implies that more phonons are reflected forwards than backwards, corresponding to a positive value of the tangential flux at the boundary. A no-slip condition implies that the same number of phonons are reflected forwards and backwards, leading to the net tangential flux being zero at the boundary. Slip and no-slip correspond to specular and diffuse modes of scattering, respectively. Thus, the use of slip conditions enables different scattering modes to be captured in the model.

As previously done by other authors [7, 41, 211, 212, 264], we assume the slip length $\ell_s^*$ is directly proportional to the non-local length $\ell^*$ and write $\ell_s^* = C\ell^*$, where $C$ is a dimensionless parameter that contains information about the interactions between phonons and the boundary of the nanowire. Various forms of $C$ appear in the literature that account for diffusive and specular modes of phonon scattering [7, 264], surface roughness [210], and temperature effects [41, 210]. Previous slip-based models of heat flow focus on the case of two-dimensional thin films [7, 210, 264] or axisymmetric cylindrical nanowires [41]. In both cases, the outer boundary where the slip condition is applied is infinitely long and one dimensional, so the parameter $C$ is independent of space. For the rectangular nanowires considered here, the parameter $C$ is expected to depend on the in-plane transverse coordinates $x^*$ and $y^*$ to account for the behaviour (e.g. increased scattering) of phonons near corners [266]. Therefore, we will assume that $C$ is function of the transverse coordinates as well as the temperature so that $C = C(x^*, y^*, T^*)$, where $x^*$ and $y^*$ in this context correspond to points on the boundary. Specific forms of $C$ will be described below.

### 4.2.3 Reduction of the equations

The governing equations can be simplified by exploiting the long geometry of the nanowire and the similarity between the steady GKE and Stokes equations for incompressible viscous flow. The reduction of the model is analogous to the lubrication approximation in fluid mechanics, which is a common technique for simplifying the governing equations of a viscous fluid confined to a thin-film geometry; see Ockendon and Ockendon [186] for details. We first introduce dimensionless variables defined as $x = x^*/L_1^*$, $y = y^*/L_2^*$, $z = z^*/L_3^*$, $T = (T^* - T_0^*)/\Delta T^*$, $u = \phi\epsilon^{-1}u^*/w_0^*$, $v = \epsilon^{-1}v^*/w_0^*$, $w = w^*/w_0^*$ and $k(T) = k^*(T^*)/k_0^*$, where $k_0^* = k^*(T_0^*)$ is a reference value of the bulk thermal conductivity and $w_0 = k_0^*\Delta T^*/L_3^*$ corresponds to the classical value of the longitudinal thermal flux. To simplify notation, derivates will be now denoted by subscripts. Using these dimensionless variables in the governing equations shows that the transverse temperature gradients are small, $T_x = O(\phi^{-2}\epsilon^2)$ and $T_y = O(\epsilon^2)$, and may be neglected provided $(\epsilon/\phi)^2 \ll 1$. The classical Fourier flux, in dimensionless form, can then be defined as $w_F = -kT_z$. By writing the dimensionless longitudinal component of the thermal flux in terms of the Fourier flux as $w(x, y, z) = w_F(z)W(x, y)$, it can be shown that $W$ satisfies

$$W - \mathrm{Kn}^2\left(\phi^2\frac{\partial^2 W}{\partial x^2} + \frac{\partial^2 W}{\partial y^2}\right) = 1, \tag{4.5}$$

where small terms of $O(\epsilon^2)$ and $O(\phi^{-2}\epsilon^2)$ have been neglected. The parameter $\mathrm{Kn} = \ell^*(T^*)/L_2^*$ is the Knudsen number and determines the dominance of the non-local effects on the heat transport. The corresponding boundary conditions are given by

$$W_x = 0, \qquad \text{at } x = 0, \tag{4.6a}$$

$$W_y = 0, \qquad \text{at } y = 0, \tag{4.6b}$$

$$W + \phi C\mathrm{Kn}\, W_x = 0, \qquad \text{at } x = 1, \tag{4.6c}$$

$$W + C\mathrm{Kn}\, W_y = 0, \qquad \text{at } y = 1. \tag{4.6d}$$

The dimensionless ETC can be defined in terms of the flux $W$ as

$$\frac{k_{\text{eff}}}{k} = \int_0^1\int_0^1 W(x, y)\, \mathrm{d}x\, \mathrm{d}y. \tag{4.7}$$

The corresponding dimensional expression $k_{\text{eff}}^*$ is obtained after multiplying $k_{\text{eff}}$ with the previously chosen scale $k_0^*$.

## 4.3 Calculation of the effective thermal conductivity

When $C$ depends on the transverse coordinates $x$ and $y$, solutions to Eqs. (4.5) and (4.6) in general must be obtained using numerical methods. However, in this section, we present analytical expressions for the ETC that are valid under specific limits and assumptions. We first consider the case of a thin nanofilm, characterised by a nanowire with a small cross-sectional aspect ratio $\phi$. We then compute a series expansion of the ETC in the case of spatially uniform slip coefficient $C$. Finally, we examine the small- and large-Kn limits of the ETC for general slip coefficients.

### 4.3.1 The thin-film limit

For small cross-sectional aspect ratios, $\phi \ll 1$, the nanowire becomes a thin film. Taking $\phi \to 0$ with $\epsilon \ll \phi$ in Eq. (4.5) leads to an ordinary differential equation that can be solved using standard methods. The ETC can then be written as

$$\frac{k_{\text{eff}}}{k} = 1 - \int_0^1 \frac{\text{Kn}\tanh(1/\text{Kn})}{1 + C(x,1)\tanh(1/\text{Kn})}\,\mathrm{d}x + O(\phi). \tag{4.8}$$

In the case of uniform slip coefficient, the leading-order contributions to Eq. (4.8) reduce to the expression for the ETC of a thin film obtained by previous authors [212, 264]. The terms of order $O(\phi)$ account for small changes in the thermal flux due to interactions between phonons and the $x = 1$ boundary.

For the remainder of this section, we will focus on solutions to the problem in the case when $\phi$ is not small.

### 4.3.2 Spatially uniform slip length

Under the assumption that the constant $C$ is independent of space, the boundary value problem defined by Eqs. (4.5) and (4.6) can be solved analytically by means of an eigenfunction expansion [75]. The eigenfunctions are of the form $\Psi_{n,m}(x, y) = \cos(\eta_n x)\cos(\mu_m y)$, where the eigenvalues $\eta_n$ and $\mu_m$ are respectively the $n^{th}$ and $m^{th}$ solutions of

$$\cot(\eta_n) = \phi C \text{Kn}\eta_n, \qquad \cot(\mu_m) = C\text{Kn}\mu_m. \tag{4.9}$$

The longitudinal flux can be written as

$$w(x, y, z) = -kf(x, y; \mathrm{Kn})T_z, \tag{4.10a}$$

where

$$f(x, y; \mathrm{Kn}) = \sum_{n,m\geq 0} \frac{c(\eta_n)c(\mu_m)}{1 + \mathrm{Kn}^2(\phi^2\eta_n^2 + \mu_m^2)} \cos(\eta_n x)\cos(\mu_m y), \quad c(t) = \frac{2\sin(t)}{t + \sin(t)\cos(t)}. \tag{4.10b}$$

By inserting Eq. (4.10) into Eq. (4.7) and integrating term by term, we find that

$$k_{\mathrm{eff}} = k \sum_{n,m\geq 0} \frac{c(\eta_n)\sin(\eta_n)c(\mu_m)\sin(\mu_m)}{\eta_n\mu_m(1 + \mathrm{Kn}^2(\phi^2\eta_n^2 + \mu_m^2))}, \tag{4.11}$$

which is valid for all values of the Knudsen number Kn. Furthermore, it can be shown that the terms of the series decay as $(nm)^{-2}$ and therefore only a small number of terms is required in practice.

### 4.3.3 Asymptotic approximation for small Knudsen numbers

Naively taking $\mathrm{Kn} \to 0$ in Eq. (4.5) shows that $W(x, y) = 1$. However, this solution does not satisfy the slip conditions at $x = 1$ or $y = 1$, which implies there are thin boundary layers near these outer boundaries. In fact, the problem for $\mathrm{Kn} \ll 1$ can be broken down into four spatial regions: (i) the bulk region away from the outer boundaries where $W \simeq 1$; (ii) a boundary layer of width $O(\mathrm{Kn})$ near $x = 1$; (iii) a second boundary layer of width $O(\mathrm{Kn})$ near $y = 1$; and (iv) a corner layer near $x = y = 1$ where the two boundary layers overlap. In terms of the integral for the ETC given in Eq. (4.7), region (i) gives the classical value of the ETC, since the flux in this region coincides with the classical Fourier flux. Regions (ii) and (iii) give small $O(\mathrm{Kn})$ corrections that account for phonon collisions with the outer boundaries away from the corners. Region (iv) accounts for even smaller $O(\mathrm{Kn}^2)$ corrections due to corner effects. In the calculations below, we will neglect the corner layer to obtain the first two terms in the small-Kn expansion of the ETC.

The solution in the boundary layer near $x = 1$ can be obtained by writing $x = 1-(\phi\mathrm{Kn})\tilde{x}$ and $W(x, y) = \tilde{W}(\tilde{x}, y)$. Using this scaling in Eqs. (4.5)–(4.6) and taking $\mathrm{Kn} \to 0$ gives the problem

$$\tilde{W} - \tilde{W}_{\tilde{x}\tilde{x}} = 1, \tag{4.12a}$$

with boundary conditions

$$\tilde{W} - C(1,y)\tilde{W}_{\tilde{x}} = 0, \quad \text{at } \tilde{x} = 0, \tag{4.12b}$$

$$\tilde{W} \to 1, \quad \text{as } \tilde{x} \to \infty. \tag{4.12c}$$

The solution to Eq. (4.12) is given by

$$\tilde{W}(\tilde{x}, y) = 1 - \frac{\exp(-\tilde{x})}{1 + C(1,y)}. \tag{4.13}$$

A similar approach can be used to determine the solution in the boundary layer at $y = 1$. By writing $y = 1 - \mathrm{Kn}\,\hat{y}$ and $W(x,y) = \hat{W}(x,\hat{y})$ in Eqs. (4.5)–(4.6) and taking $\mathrm{Kn} \to 0$, it can be shown that $\hat{W}$ is given by

$$\hat{W}(x, \hat{y}) = 1 - \frac{\exp(-\hat{y})}{1 + C(x,1)}. \tag{4.14}$$

The composite asymptotic solution, which is a single expression that includes contributions from each of the spatial regions (minus those from the corner layer), can be written as

$$W(x,y) = 1 - \frac{\exp[-(1-x)/(\phi\mathrm{Kn})]}{1 + C(1,y)} - \frac{\exp[-(1-y)/\mathrm{Kn}]}{1 + C(x,1)}. \tag{4.15}$$

Using Eq. (4.15) in Eq. (4.7) shows that the ETC is given by

$$\frac{k_{\mathrm{eff}}}{k} = 1 - \mathrm{Kn}\left[\phi \int_0^1 \frac{\mathrm{d}y}{1 + C(1,y)} + \int_0^1 \frac{\mathrm{d}x}{1 + C(x,1)}\right] + O(\mathrm{Kn}^2). \tag{4.16}$$

If the slip length is spatially uniform, Eq. (4.16) reduces to $k_{\mathrm{eff}}/k = 1 - \mathrm{Kn}(1 + \phi)/(1 + C) + O(\mathrm{Kn}^2)$.

### 4.3.4 Asymptotic approximation for large Knudsen numbers

The strong influence of boundary effects when the Knudsen number is large leads to a substantial reduction in the thermal flux. As discussed in Calvo et al. [41], the flux scales like $W = O(\mathrm{Kn}^{-1})$ in the limit as $\mathrm{Kn} \to \infty$. Thus, after writing $W(x,y) = \mathrm{Kn}^{-1}\bar{W}(x,y)$ in Eqs. (4.5)–(4.6), the problem for the rescaled flux $\bar{W}$ is given by

$$\mathrm{Kn}^{-1}\bar{W} - \mathrm{Kn}\left(\phi^2\bar{W}_{xx} + \bar{W}_{yy}\right) = 1, \tag{4.17}$$

subject to

$$\bar{W}_x = 0, \quad \text{at } x = 0, \tag{4.18a}$$

$$\bar{W}_y = 0, \quad \text{at } y = 0, \tag{4.18b}$$

$$\bar{W} + \phi C \mathrm{Kn}\, \bar{W}_x = 0, \quad \text{at } x = 1, \tag{4.18c}$$

$$\bar{W} + C \mathrm{Kn}\, \bar{W}_y = 0, \quad \text{at } y = 1. \tag{4.18d}$$

By integrating the Eq. (4.17) over the cross-sectional area and using the boundary conditions (4.18), we find that

$$\mathrm{Kn}^{-1} \int_0^1 \int_0^1 \bar{W}(x,y)\ \mathrm{d}x\,\mathrm{d}y + \left[\phi \int_0^1 C^{-1}(1,y)\bar{W}(1,y)\ \mathrm{d}y + \int_0^1 C^{-1}(x,1)\bar{W}(x,1)\ \mathrm{d}x\right] = 1. \tag{4.19}$$

Provided that $C(x,y) \gg \mathrm{Kn}^{-1}$, taking $\mathrm{Kn} \to \infty$ in Eqs. (4.17)–(4.18) shows that $\bar{W}$ is constant in space. The integral relation in Eq. (4.19) then enables $\bar{W}$ and hence $W$ to be easily determined. Therefore, we have that

$$\frac{k_{\mathrm{eff}}}{k} = \mathrm{Kn}^{-1}\left[\phi \int_0^1 C^{-1}(1,y)\ \mathrm{d}y + \int_0^1 C^{-1}(x,1)\ \mathrm{d}x\right]^{-1} + O(\mathrm{Kn}^{-2}) \tag{4.20}$$

as $\mathrm{Kn} \to \infty$. In the case of spatially uniform slip lengths, Eq. (4.20) reduces to $k_{\mathrm{eff}}/k = C\mathrm{Kn}^{-1}/(1+\phi) + O(\mathrm{Kn}^{-2})$.

## 4.4 Results and discussion

We first examine how changes to the Knudsen number affect both the longitudinal thermal flux and the ETC for fixed values of $\phi = 1$, corresponding to square nanowires, and $C = 1$. Panels (a) and (b) of Figure 4.2 show contour maps of the normalised flux $w/w_F$ for two values of the Knudsen number: $\mathrm{Kn} = 0.1$ (Fig. 4.2 (a)) and $\mathrm{Kn} = 10$ (Fig. 4.2 (b)). The corresponding normalised ETC, $k_{\mathrm{eff}}/k$, is shown as a function of the Knudsen number in Fig. 4.2 (c).

For small Knudsen numbers, the non-local length is much less than the cross-sectional dimensions of the nanowire. Phonons in the bulk will frequently collide with each other, resulting in diffusive transport of heat that is not strongly influenced by the finite geometry of the cross section. Indeed, as shown in Fig. 4.2 (a), the normalised flux in the bulk is close to unity and thus coincides with the diffusive Fourier flux. However, there is a region of ballistic transport near the exterior boundaries of the nanowire, where phonon-boundary

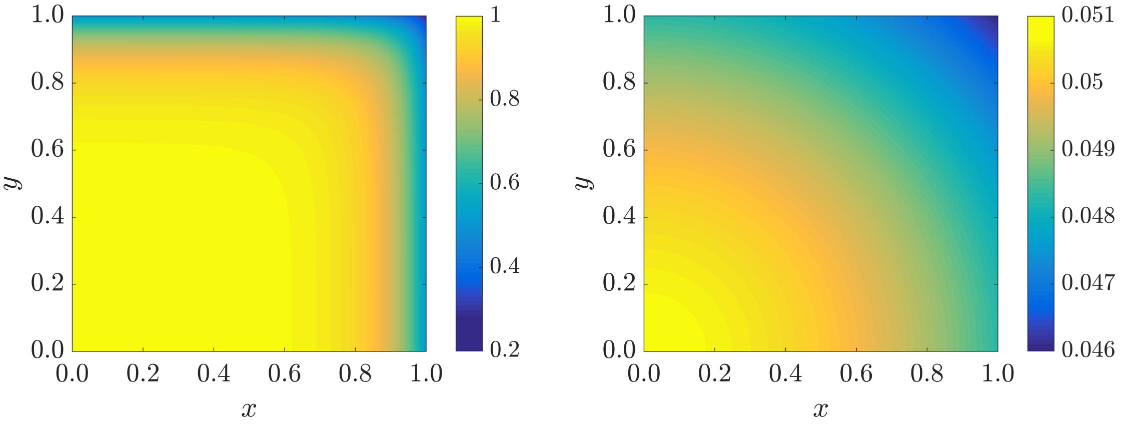

**(a)** $w/w_F$ for $\mathrm{Kn} = 0.1$

**(b)** $w/w_F$ for $\mathrm{Kn} = 10$

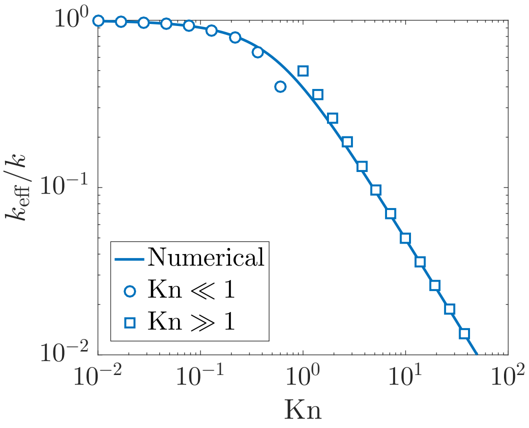

**(c)** $k_{\mathrm{eff}}/k$

**Figure 4.2:** (a)–(b): Contour maps of the normalised longitudinal thermal flux $w/w_F$, where $w_F = -kT_x$ is the classical Fourier flux, for two values of the Knudsen number: $\mathrm{Kn} = 0.1$ and $\mathrm{Kn} = 10$. (c): The dependence of the normalised ETC $k_{\mathrm{eff}}/k$ on the Knudsen number. The asymptotic solution for $\mathrm{Kn} \ll 1$ and $\mathrm{Kn} \gg 1$ is given by Eqs. (4.16) and (4.20), respectively. In all panels, $\phi = 1$ and $C = 1$.

scattering becomes relevant. In this ballistic region, there is a rapid decrease in the flux from its bulk value of approximately $w_F$ across dimensional length scales of order $\ell^*$ (or non-dimensional length scales of order Kn). Surprisingly, the thermal flux does not tend to zero at the exterior boundaries, despite the fact that naively taking $\mathrm{Kn} \to 0$ in the boundary conditions (4.6) appears to yield the no-slip condition. However, the gradient of the flux scales like $\mathrm{Kn}^{-1}$ near the exterior boundaries, cancelling the Kn in the slip coefficient and preventing the no-slip condition from being recovered in the small-Kn limit. This is shown explicitly in Sec. 4.3.3.

Given that the non-classical, ballistic region of transport is confined to a thin boundary layer when the Knudsen number is small, the ETC is well approximated by its classical value, $k_{\mathrm{eff}}/k \simeq 1$, for $\mathrm{Kn} \ll 1$. In fact, as shown in Sec. 4.3.3, the small $O(\mathrm{Kn})$ correction in the asymptotic approximation (4.16) accounts for the reduced heat transport that occurs in the boundary layers. The asymptotic approximation (4.16) is plotted as circles in Fig. 4.2 (c) and is in excellent agreement with the numerically computed curve (solid line) obtain from the full model.

For large Knudsen numbers, the non-local length greatly exceeds the dimensions of the cross section. In this case, phonons frequently collide with the exterior boundary, leading to a substantial reduction in the transport of thermal energy across the nanowire; see Fig. 4.2 (b). As discussed by Calvo et al. [41] in the case of circular nanowires, the flux for large Knudsen numbers is of order $\mathrm{Kn}^{-1}$. Furthermore, due to the large effective slip coefficient, the transverse gradients in the flux are small, resulting in a roughly uniform thermal flux over the cross-sectional area. The greatly reduced thermal transport in the large-Kn regime is reflected by the relatively low values of the ETC, which is also proportional to $\mathrm{Kn}^{-1}$, as seen from the asymptotic result (4.20). As noted by previous authors [7, 41], the slip boundary condition is crucial for obtaining an ETC that scales with $\mathrm{Kn}^{-1}$ for $\mathrm{Kn} \gg 1$ from the hydrodynamic model, which is required for agreement with experimental data (see, for example, Ref. [21] or the data below). The asymptotic expression for the ETC (4.20) is shown as the squares in Fig. 4.2 (c) and is in excellent agreement with the numerical calculations.

Figures 4.2 (a) and (b) show that, regardless of the value of the Knudsen number, the thermal flux attains its minimum value at the corner of the nanowire. This minimum is a consequence of the imperfect slip that occurs at the boundaries, which leads to greater resistance to heat flow (i.e. more phonon reflections) in the corners.

We now examine how changes to the cross-sectional geometry affect the ETC for a fixed value of $C = 1$. Figure 4.3 (a) shows the ETC of a two-dimensional thin film ($\phi \to 0$), a rectangular nanowire ($\phi = 1/2$), and a square nanowire ($\phi = 1$). For comparison purposes, we also plot the ETC for a circular nanowire obtained by Calvo et al. [41]. As the cross-sectional aspect ratio $\phi$ decreases from one to zero, the ETC increases for all values of the Knudsen number. To understand the reason for this increase, it is helpful to recall that $\phi$ is defined in terms of the dimensions of the cross section as $\phi = L_2^*/L_1^*$ and the Knudsen number is defined as $\mathrm{Kn} = \ell^*/L_2^*$. Thus, decreasing $\phi$ for fixed Kn is equivalent to increasing $L_1^*$ for fixed $L_2^*$. The consequential increase in cross-sectional area essentially leads to the corners of the nanowire becoming further separated, thereby reducing their negative impact on the thermal flux. In the case of a thin film ($\phi \to 0$), there are no corners to reduce the flux; hence, the ETC of a thin film is greater than the ETC of square and rectangular nanowires. Interestingly, however, the ETC of a circular nanowire, which has no corners at all, is virtually identical to the ETC of a square nanowire. This similarity can be rationalised in terms of the hydraulic diameter of the nanowires, defined as $D^* = 4A^*/P^*$, where $A^*$ and $P^*$ are the (dimensional) cross-sectional area and perimeter, respectively. For the rectangular nanowires considered here, we can write $D^*_{\mathrm{rect}} = 4L_2^*/(1 + \phi)$; for circular nanowires of radius $R^*$, we find that $D^*_{\mathrm{circ}} = 2R^*$. The hydraulic diameters of square and circular nanowires will be equal if the half-height $L_2^*$ is the same as the radius $R^*$. It is also possible to introduce an equivalent Knudsen number based on the hydraulic diameter, $\mathrm{Kn}' = 2\ell^*/D^*$. Unlike the Knudsen number $\mathrm{Kn} = \ell^*/L_2^*$, the equivalent Knudsen number $\mathrm{Kn}'$ simultaneously captures the $x$ and $y$ dimensions of the nanowire. For square and circular nanowires, the equivalent Knudsen numbers $\mathrm{Kn}'$ are the same, and both are equal to the original Knudsen number Kn. Furthermore, by extending the asymptotic analysis of Sec. 4.3.4 to nanowires of arbitrary cross section, we find that the ETC, in the limit of large equivalent Knudsen number and constant slip coefficient $C$, can be written as

$$k_{\mathrm{eff}}/k \sim (C/4)(D^*/\ell^*), \tag{4.21}$$

revealing that the limiting behaviour of the ETC is indeed the same for square and circular

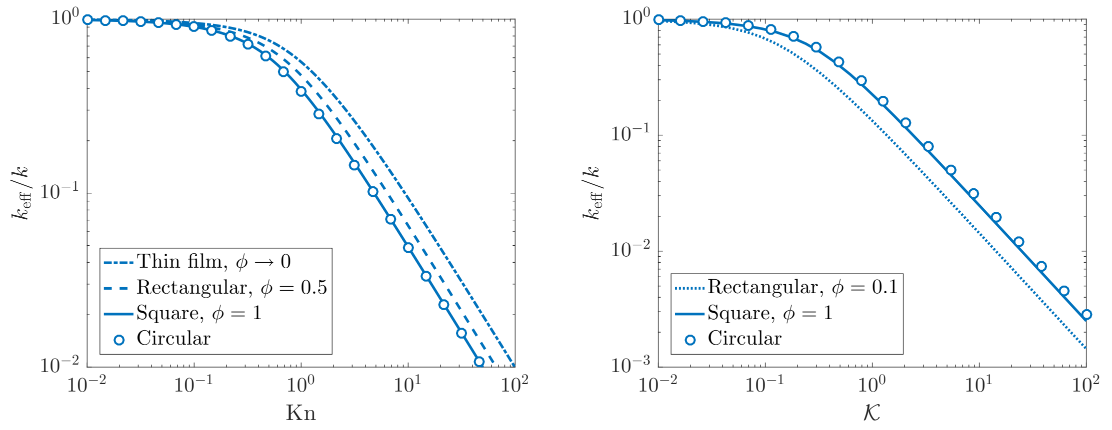

**(a)** **(b)**

**Figure 4.3:** The dependence of the normalised ETC $k_{\mathrm{eff}}/k$ on (a) the Knudsen number Kn and (b) the effective Knudsen number $\mathcal{K} = \ell^*/\sqrt{A^*}$ for various cross-sectional aspect ratios $\phi$. Also shown in the normalised ETC of a circular nanowire [41]. Fixed values of $\mathcal{K}$ correspond to fixed values of the cross-sectional area $A^*$. In both panels a value of $C = 1$ was used.

nanowires. Equation (4.21) shows that, regardless of the nanowire geometry, the ETC for large Knudsen numbers is set by the non-local length and the hydraulic diameter.

To better understand the role of the nanowire geometry, we now investigate how the ETC varies with $\phi$ for fixed cross-sectional areas $A^* = 4L_1^* L_2^*$, keeping $C = 1$. In order to maintain a constant area $A^*$ in the dimensionless model, we need to account for how the Knudsen number $\mathrm{Kn} = \ell^*/L_2^*$ varies with $\phi$ through $L_2^*$. To do so, we first note that $L_2^*$ can be written as $L_2^* = \sqrt{\phi A^*/4}$. The Knudsen number can then be written in terms of the aspect ratio $\phi$ as $\mathrm{Kn} = (2/\sqrt{\phi})\mathcal{K}$, where $\mathcal{K} = \ell^*/\sqrt{A^*}$ is an effective Knudsen number that is independent of the shape of the cross section and which remains constant as $\phi$ varies. Similar to the equivalent Knudsen number $\mathrm{Kn}'$, the effective Knudsen number $\mathcal{K}$ also accounts for the full two-dimensional geometry of the nanowire rather than the length along one particular dimension. Figure 4.3 (b) compares the ETC of a rectangular and a square nanowire with $\phi = 0.1$ and $\phi = 1$, respectively, over a range of $\mathcal{K}$. Contrary to the results of Fig. 4.3 (a), here we see that for a fixed value of $\mathcal{K}$, corresponding to a fixed area $A^*$, increases in the cross-sectional aspect ratio $\phi$ lead to increases in the ETC. This relationship stems from the fact that as the aspect ratio $\phi$ decreases, the exterior boundaries

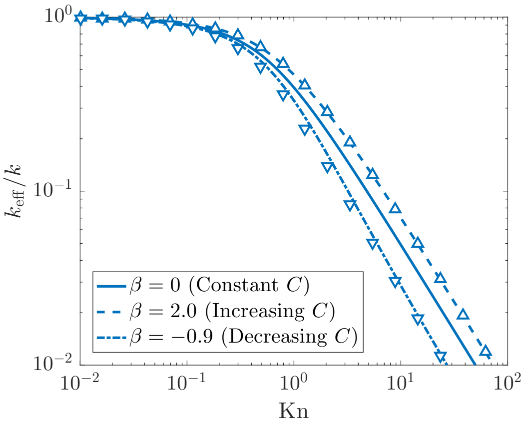

**Figure 4.4:** The influence of non-uniform slip coefficients $C$ on the normalised ETC $k_{\text{eff}}/k$ of a square nanowire ($\phi = 1$). Lines correspond to the ETC computed using the slip coefficient in (4.22). The cases $\beta = 0$, $\beta = 2$, and $\beta = -0.9$ correspond slip coefficients that are constant, increasing towards a corner, and decreasing towards a corner. The upwards- and downwards-pointing triangles denote the ETC computed using the equivalent slip coefficients (4.23a) and (4.23b), respectively.

at $y^* = \pm L_2^*$ become closer together and the bulk heat flow becomes dominated by phonon scattering at these surfaces. The ETC of the circular nanowire is also shown in Fig. 4.3 (b) and is found to be slightly greater than the square for all values of $\mathcal{K}$ due to the lack of corners. In plotting the ETC for the circular nanowire, the Knudsen number has been written as $\text{Kn} = \sqrt{\pi}\,\mathcal{K}$. Thus, for a fixed cross-sectional area, the circular nanowire is the most efficient transporter of thermal energy, with the thin film being the worst.

The influence of the slip coefficient $C$ on thermal transport has been discussed by Zhu et al. [264] in the context of a thin film ($\phi \to 0$) under the assumption that $C$ is a constant. In summary, larger values of $C$ lead to less resistance to heat flow and thus to greater values of the thermal flux and ETC. A distinguishing feature of rectangular nanowires is that the slip coefficient $C$ may depend on the boundary coordinates to account for the change in phonon behaviour near corners. To explore this behaviour with our model, we consider a square nanowire ($\phi = 1$) and a simple form of the slip coefficient given by

$$C(x, y) = \alpha + \beta(x^2 + y^2 - 1), \tag{4.22}$$

where $\alpha$ and $\beta$ are constants that satisfy $\alpha > 0$ and, to ensure $C$ remains positive, $\beta > -\alpha$. The parameter $\beta$ controls the curvature of the slip coefficient. If $\beta < 0$ ($\beta > 0$) then $C$

decreases (increases) towards a corner. The lines in Fig. 4.4 represent numerical calculations of the ETC using finite differences in the case of $\alpha = 1.0$ and $\beta = -0.9$, 0, and 2.0. Slip coefficients that decrease (increase) towards a corner lead to a corresponding decrease (increase) in the ETC, as these amplify (counteract) the resistance to thermal transport occurring at the corners. Qualitatively, the dependence of the ETC on the Knudsen number is similar to the case when the slip coefficient is constant. This naturally leads to the question of whether it is possible to define an equivalent, *constant* slip coefficient, $C_{\text{equiv}}$, that yields quantitatively similar results to the non-uniform slip coefficient (4.22). One possibility for obtaining an equivalent slip coefficient is to match the limiting behaviour of the ETC for large Knudsen numbers. From Sec. 4.3.4, the large-Kn behaviour of the ETC for a constant slip coefficient in the case of a square nanowire is given by $k_{\text{eff}}/k \sim (C_{\text{equiv}}/2)\text{Kn}^{-1}$. By inserting the slip coefficient (4.22) into (4.20), performing the integration, and equating the result to $(C_{\text{equiv}}/2)\text{Kn}^{-1}$, we find an equivalent slip constant given by

$$C_{\text{equiv}} = \frac{\sqrt{\alpha\beta}}{\arctan\left(\sqrt{\beta/\alpha}\right)}, \qquad \beta > 0, \tag{4.23a}$$

$$C_{\text{equiv}} = \frac{\sqrt{\alpha|\beta|}}{\operatorname{arctanh}\left(\sqrt{|\beta|/\alpha}\right)}, \quad \beta < 0. \tag{4.23b}$$

The upwards- and downwards-pointing triangles in Fig. 4.4 show the ETC computed with the equivalent slip coefficients given by (4.23a) and (4.23b), respectively. The quantitative agreement between the ETCs computed using the equivalent and non-uniform slip conditions is remarkable. For $\alpha = 1$, we find that $C_{\text{equiv}} \simeq 1.48$ when $\beta = 2$ and $C_{\text{equiv}} \simeq 0.52$ when $\beta = -0.9$. Thus, local increases (decreases) in the slip coefficient due to corner effects are equivalent to increases (decreases) in the bulk slip coefficient, highlighting the non-local nature of nanoscale heat transport.

To validate the model, we compare theoretical predictions of the ETC against experimental measurements carried out using silicon wires by Inyushkin et al. [121]. The rectangular wires are of dimension $2L_1^* = 3.12$ mm, $2L_2^* = 2.00$ mm, and $L_3^* = 20.5$ mm. Although the wires are macroscopic in size, they are held at temperatures for which their dimensions are much smaller than the MFP of phonons. The longitudinal and cross-sectional aspect ratios of the wire are $\epsilon \simeq 0.098$ and $\phi \simeq 0.64$, respectively. Temperature gradients ranging from 0.01 K to 0.2 K were imposed across the length of the wire. The temperature at

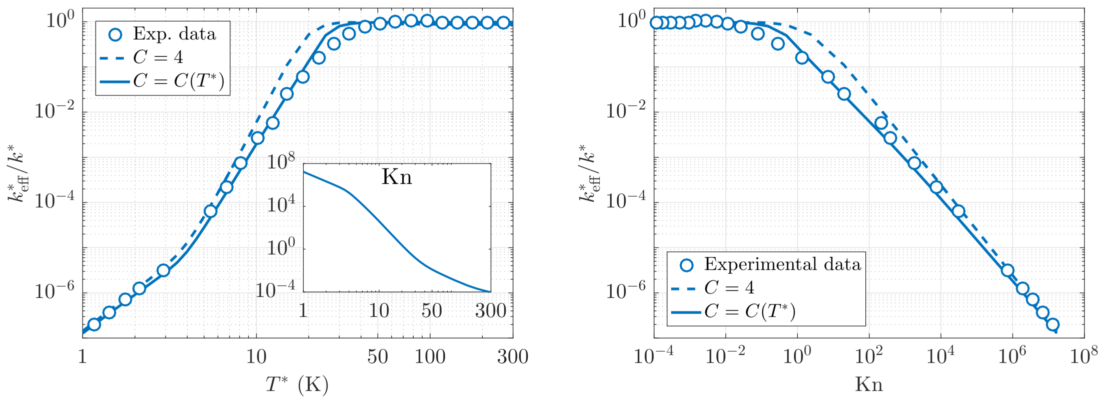

**(a)** **(b)**

**Figure 4.5:** Comparison experimental measurements (circles) of the ETC for rectangular wires [121] with theoretical predictions computed using a constant $C = 4$ (dashed lines) and a temperature-dependent $C(T^*) = 4\exp(-T^*/T^*_c)$ (solid lines) slip coefficients. The inset of panel (a) shows the temperature dependence of the Knudsen number.

the end point of the wire was held between 0.5 K and 293 K, allowing both the hydrodynamic (low temperature) and diffusive (high temperature) regimes of thermal transport to be explored. Numerically evaluating the theoretical ETC requires knowledge of the temperature-dependent non-local length and the bulk thermal conductivity. These quantities have been extracted from first-principle calculations based on the KCM framework [234] using open-source code [232], as described in Appendix A.

The experimental measurements of the ETC, normalised by the bulk thermal conductivity, are shown as circles in Fig. 4.5. Panels (a) and (b) of this figure plot the ETC as a function of the temperature and Knudsen number, respectively. The inset shows the temperature dependence of the Knudsen number, allowing Figs. 4.5 (a) and (b) to be connected. The Knudsen number is small for temperatures exceeding 50 K (Kn $\simeq 0.013$). Consequently, the experimental measurements of the ETC coincide with the bulk thermal conductivity. However, as the temperature is decreased below 50 K, the Knudsen number becomes order one in magnitude and the ETC begins to rapidly decrease from its bulk value. The large-Kn regime is entered as the temperature falls below 10 K (Kn $\simeq 400$) and the measurements of the ETC follow the $\text{Kn}^{-1}$ scaling that was derived from the $\text{Kn} \gg 1$ limit of the model.

We first attempt to capture the experimental data using the model with a constant slip coefficient. Although this is the simplest choice available, it is also motivated by the discussion surrounding Fig. 4.4, which argues that spatially non-uniform slip coefficients can yield quantitatively similar results. An estimate of the slip coefficient can be obtained by fitting the experimental data points for $\mathrm{Kn} > 10^6$ to the large-Kn limit of the ETC given by (4.20). This procedure produces the value of $C \simeq 4$. This value of $C$ agrees with the results obtained using the Mathiessen rule in previous works [234, 262]: in the limit $\mathrm{Kn} \to \infty$ the effective thermal conductivity for a thin film ($\phi \to 0$) is $k^*_{\text{eff}} \approx (2H^*/\ell^*)k^*$, where $H^* = 2L^*_2$ is the thickness of the film. The dashed lines in the main panels of Fig. 4.5 denote the theoretical prediction of the ETC using $C = 4$. The model prediction is remarkably accurate for Knudsen numbers above $10^2$ ($T^* < 10$ K). The model also gives accurate predictions for Knudsen numbers below $10^{-2}$ ($T^* > 50$ K), where the bulk thermal conductivity is recovered and the value of the slip coefficient becomes irrelevant. The over-estimation of the ETC by the model across intermediate values of the Knudsen number ranging from $10^{-2}$ to $10^2$ (temperatures between 10 K and 50 K) is attributed to the assumption of a constant slip coefficient, which is too large in this region. Evidently, the slip coefficient must begin to decrease as the temperature increases. The temperature dependence of the slip coefficient can be rationalised in terms of the dynamics of phonon-boundary scattering. As the temperature increases, diffuse scattering becomes increasingly dominant over specular scattering [210], with specular scattering becoming negligible at a critical temperature $T^*_c$ depending on the roughness of the nanowire and phonon wavelength [10]. Diffuse scattering emits phonons in and against the direction of the temperature gradient and therefore leads to a vanishing thermal flux at the exterior boundary of the wire, which is captured by a slip coefficient that tends towards zero for temperatures $T^*$ exceeding the critical value $T^*_c$. Therefore, we propose a simple exponential form for the slip coefficient given by $C(T^*) = 4\exp(-T^*/T^*_c)$. We treat $T^*_c$ as a fitting parameter whose value will depend on the physical and geometrical (roughness) characteristics of the nanowire. From a visual inspection of Fig. 4.5 (a), noticeable differences between the experimental and theoretical predictions with $C = 4$ begin to occur when $T^* \simeq 9$ K, marking the temperature at which the slip coefficient begins to decrease. Taking $T^*_c = 9$ in the exponential form of $C$ yields the ETC predictions given by the solid lines in Fig. 4.5, which show a considerable improvement over the estimates with $C = 4$. The model gives accurate predictions over nearly the entire temperature range; however, some errors do persist for temperatures around 30 K. Refined estimates of the ETC can likely be obtained using a physical model for the slip coefficient that more accurately describes the nature of phonon-boundary interactions. For now, we leave formulating such a model as a key area of future research.

The existing discrepancies of our model with respect to experimental data can also be understood from the Truncated Lévy Flights (TLF) framework [243, 244]. According to the TLF theory, when the dominant characteristic length of the thermal transport is reduced (i.e. the phonon MFP), phonon transport moves from the diffusive to ballistic (or hydrodynamic) regime through a superdiffusive transport regime, which has an ETC that is smaller than the expected from the simple diffusive-ballistic transition. Notice that here the analogy ballistic-hydrodynamic refers to a transport regime dominated by a single characteristic length scale.

In silicon, when the temperature decreases below 50 K, phonons with a MFP larger than ∼3 mm (of the order of width and height of the slab) begin to appear. While at high temperature (diffusive regime) those phonons do not have a significant contribution, at very low temperatures (ballistic or hydrodynamic regime) they are removed from the model by the boundary conditions. In the diffusive-ballistic transition around 7–50 K, where these phonons can be important, the present model over-estimates the experimental data, as a single characteristic non-local length in the transport equation is not able to capture the superdiffusive transition.

## 4.5 Conclusion

We use a hydrodynamic model of thermal transport, based on the Guyer–Krumhansl equation, with a slip boundary condition to calculate the ETC of rectangular nanowires. An analytical solution for the ETC is obtained in the case of a constant slip coefficient by writing the thermal flux as an eigenfunction expansion. For spatially non-uniform slip coefficients, asymptotic methods are employed to calculate the leading approximations valid for small and large Knudsen numbers. An attractive feature of the asymptotic approach is that it can be straightforwardly applied to nanowires with arbitrary cross section, enabling the ETC to be calculated with ease for a range of geometries that might be non-trivial to implement using standard computational techniques.

A key advantage of the proposed model is that it is based on a minimal number of free parameters. Both the non-local length and the bulk thermal conductivity can be calculated as a function of temperature using open-source software [232] and considered as known quantities. For sufficiently small temperatures, the correct slip coefficient is approximately four, in accordance with previous work [234, 262]. This enables the ETC predictions to be obtained without any fitting parameters in this regime. To account for changes in the slip coefficient with increasing temperature, a simple exponential form with a single fitting parameter is used. A comparison between experiment and theory reveals that the model is able to accurately predict the ETC across a wide range of temperatures, which is particularly remarkable given the simple nature of the underlying model. Future studies will focus on deriving an expression for the slip coefficient using a detailed physical model. By writing the slip coefficient in terms of known physical quantities rather than fitting parameters, the predictability of the proposed hydrodynamic model can be greatly improved, yielding accurate estimates for the ETC across arbitrary temperature ranges and providing key insights into how thermal energy will be distributed across nanosystems.

# 5 The Stefan problem with a size-dependent thermal conductivity

M. Calvo-Schwarzwälder.
Non-local effects and size-dependent properties in Stefan problems with Newton cooling.
To appear in Applied Mathematical Modelling (submitted Feb. 2019, revised Apr. 2019).
arXiv:1902.00401v2
Impact factor: 2.617. Q1 in Modelling and Simulation.

## 5.1 Introduction

It is widely accepted that heat conduction at small length scales differs from the classical description [32, 47, 83]. There exist a wide range of theoretical models which extend Fourier's law to account for non-local effects which become dominant on length scales comparable to the phonon mean free path (MFP). The models may be classified into micro-, meso- or macroscopic models depending on whether the aim is focused on describing the behaviour of the individual heat carriers, the evolution of their distribution or related macroscopic quantities, such as the temperature or the heat flux. Examples for micro- and mesoscopic models are molecular dynamics, Monte Carlo simulations [55], the Boltzmann transport equation (BTE) [24] or the equation of phonon radiative transfer [158]. The equations involved in these approaches often require excessive computational effort and it is therefore more sensible to aim for a macroscopic equation which captures the physics of the problem. Popular macroscopic models are the Maxwell–Cattaneo law [44], the thermomass model [71, 248] or the Guyer–Krumhansl equation (GKE) [105, 106] and the framework of phonon hydrodynamics developed from it [71, 99, 127, 235].

Based on the BTE and on the framework of extended irreversible thermodynamics [127], Alvarez and Jou [5] derived a model for heat flow with a size-dependent effective thermal conductivity (ETC). This was able to capture non-local effects and showed good agreement with experimental data. Hennessy et al. [107] show that such an ETC can also be derived when the GKE is included into the formulation of the Stefan problem. Recently, Font [82] proposed a simpler non-classical formulation of the Stefan problem which includes an effective Fourier law where a size-dependent ETC replaces the bulk thermal conductivity. He showed that, even when the temperature at the boundary is instantly set to the temperature of the cold environment, the problem of an initially infinite solidification rate is avoided by incorporating a size-dependent ETC.

The popular fixed-temperature condition is a specific limit of a more general boundary condition known as the Newton cooling condition. In this chapter we aim to generalise the model proposed by Font by considering cooling conditions at the interface between the material and its environment. For large Biot (or Nusselt) numbers, this condition converges to the fixed-temperature condition. Formulations of the Stefan problem where Newton cooling conditions are applied, can be found in the framework of nanoparticle melting [108, 179, 199] or nanowire melting [81]. Hennessy et al. [108] recently proposed an extended form of cooling condition accounting for memory effects. However, the case of small Biot number is not considered in these studies. In Sec. 5.2.4 we explain the importance of this limit.

## 5.2 Mathematical model

We consider a liquid bath, initially at the phase change temperature $T_\mathrm{f}^*$, that occupies the space $x^* \geq 0$. The $^*$ notation refers to dimensional quantities. Due to a low temperature $T_\mathrm{e}^*$ applied at $x^* = 0$, the liquid starts to undergo a solidification process and a solid starts growing into the liquid occupying the space $0 \leq x^* \leq s^*(t^*)$; see Fig. 5.1. For simplicity, the specific heat $c^*$, the density $\rho^*$ and the bulk thermal conductivity $k^*$ are assumed to be constant, and no supercooling will be considered.

**Figure 5.1:** A liquid bath, initially at the freezing temperature $T_\mathrm{f}^*$, starts to solidify due to a low external temperature $T_\mathrm{e}^*$.

### 5.2.1 Governing equations

The process is driven by the heat flow in the solid phase. The liquid remains at the freezing temperature $T_\mathrm{f}^*$ for all time. The temperature $T^*$ and heat flux $Q^*$ in the solid are related via conservation of energy, which in one spatial dimension takes the form

$$c^*\rho^*\frac{\partial T^*}{\partial t^*}+\frac{\partial Q^*}{\partial x^*}=0. \tag{5.1}$$

In the classical formulation, the heat flux is determined by the gradient of the temperature,

$$Q^*=-k^*\frac{\partial T^*}{\partial x^*}. \tag{5.2}$$

For a system of characteristic size $L^*$, Alvarez and Jou [5] propose substituting the bulk thermal conductivity $k^*$ by

$$k_\mathrm{eff}^*(L^*)=2k^*\left(\frac{L^*}{\ell^*}\right)^2\left(\sqrt{1+\left(\frac{\ell^*}{L^*}\right)^2}-1\right). \tag{5.3}$$

where $\ell^*$ is the phonon mean free path. The ratio $\ell^*/L^*$ is the Knudsen number and it determines the dominance of non-local effects in heat transport. In the limit $L^* \ll \ell^*$ (Kn$\gg$ 1), Eq. (5.3) reduces to $k^* \approx 2k_0^*L^*/\ell^*$, which is in accordance with experimental data [145]. Conversely, in the limit $\ell^* \gg L^*$ (Kn$\ll$ 1) the classical limit $k_\mathrm{eff}^* = k^*$ is retrieved. In the current problem the system length-scale is determined by the size of the solid region, hence $k_\mathrm{eff}^*(L^*) = k_\mathrm{eff}^*(s^*)$ and we obtain

$$q^*=-k_\mathrm{eff}^*(s^*)\frac{\partial T^*}{\partial x^*}, \tag{5.4}$$

which we assume to govern heat conduction through the solid. Upon combining Eqs. (5.1) and (5.4) we obtain

$$c^* \rho^* \frac{\partial T^*}{\partial t^*} = k^*_{\text{eff}}(s^*) \frac{\partial^2 T^*}{\partial x^{*2}}, \tag{5.5}$$

which we assume to govern heat conduction through the solid. For $s^* \gg \ell^*$ we have $k^*_{\text{eff}} \approx k^*$ and hence the classical heat equation obtained from Eq. (5.2) is recovered.

### 5.2.2 Boundary and initial conditions

The heat exchange at the interface between the material and the environment is governed by a Newton cooling condition

$$Q^* = h^*(T^*_{\text{e}} - T^*), \qquad \text{at } x^* = 0, \tag{5.6}$$

where $h^*$ is the heat transfer coefficient. Contrary to the fixed temperature condition $T^* = T^*_{\text{e}}$, which corresponds to the limit $h^* \to \infty$, the cooling condition does not lead to an infinite initial solidification rate [4, 81, 103, 199]. Assuming that Eq. (5.4) holds at the boundaries, Eq. (5.6) becomes

$$-k^*_{\text{eff}}(s^*) \frac{\partial T^*}{\partial x^*} = h^*(T^*_{\text{e}} - T^*), \qquad \text{at } x^* = 0. \tag{5.7}$$

At the solid-liquid interface, the temperature of the solid is equal to the freezing temperature,

$$T^* = T^*_{\text{f}}, \qquad \text{at } x^* = s^*. \tag{5.8}$$

The evolution of the interface is determined by an energy balance which is known as the Stefan condition In its simplest form, this is

$$\rho^* L^*_m \frac{\mathrm{d}s^*}{\mathrm{d}t^*} = -Q^*, \qquad \text{at } x^* = s^*, \tag{5.9}$$

where $L^*_m$ is the latent heat of fusion. Using Eq. (5.4) we write

$$\rho^* L^*_m \frac{\mathrm{d}s^*}{\mathrm{d}t^*} = k^*_{\text{eff}}(s^*) \frac{\partial T^*}{\partial x^*}, \qquad \text{at } x^* = s^*. \tag{5.10}$$

Finally, at $t^* = 0$ we assume that no solid has been produced and that the liquid bath is at the phase change temperature,

$$T^* = Q^* = s^* = 0, \qquad \text{at } t = 0. \tag{5.11}$$

### 5.2.3 Non-dimensional formulation

The temperature scale is given by the temperature jump at $x^* = 0$, that is, $\Delta T^* = T^*_\mathrm{f} - T^*_\mathrm{e}$. The natural length scale of the problem is the mean free path $\ell^*$ and hence we choose the corresponding diffusive time scale $c^*\rho^*\ell^{*2}/k^*$, which balances the terms in Eq. (5.1). Consequently, we introduce the dimensionless quantities $x = x^*/\ell^*$, $s = s^*/\ell^*$, $t = k^*t^*/(c^*\rho^*\ell^{*2})$ and $T = (T^* - T^*_\mathrm{f})/\Delta T^*$. Upon writing derivatives as indices, the dimensionless equations are

$$T_t = f(s)T_{xx}, \qquad 0 < x < s, \tag{5.12a}$$

$$f(s)T_x = \mathrm{Bi}(1 + T), \qquad \text{at } x = 0, \tag{5.12b}$$

$$T = 0, \qquad \text{at } x = s, \tag{5.12c}$$

$$\beta s_t = f(s)T_x, \qquad \text{at } x = s, \tag{5.12d}$$

$$s = 0, \qquad \text{at } t = 0, \tag{5.12e}$$

where $\beta = L^*_m/(c^*\Delta T)$ and $\mathrm{Bi} = h^*\ell^*/k^*$ are the Stefan number and the Biot number respectively. In melting problems, the latter is also called Nusselt number because the material in contact with the environment is in liquid state. Finally, $f(s) = 2s\left(\sqrt{s^2+1} - s\right)$ is the non-dimensional form of $k^*_\mathrm{eff}$.

Note, due to the way in which the problem has been scaled, the mean free path has been eliminated from the ETC and is only present in the Biot number. In fact, the dimensionless position of the interface $s(t)$ can now be understood as an effective Knudsen number depending on time, since it corresponds to the ratio of the size of the growing solid to the mean free path.

The effect of the Stefan number on the evolution of the interface in formulations with a fixed temperature has been studied by many authors; see the books by Gupta [103] or Alexiades and Solomon [4], for example. However, when Newton cooling conditions are applied, the behaviour of the system when varying Bi has to be studied as well.

### 5.2.4 Parameter estimation

In this chapter we will use the thermophysical parameters of silicon, since it is material that is widely used in theoretical studies [5, 82, 82, 145, 234]. The values of the relevant physical quantities are given in Table B.1.

The Stefan number can be parametrized in terms of the temperature change as $\beta = \mathcal{T}^*/\Delta T$ and where $\mathcal{T}^* = L_m^*/c^*$. Using the values given in Table B.1 we find $\mathcal{T}^* \approx 1731.6$ K. Therefore, even for a temperature drop of 100 K we still obtain $\beta \approx 17.3$. For other materials such has tin, lead or gold, we find that $\mathcal{T}^*$ is of the order of hundreds of Kelvin [84, 108, 199], and hence we can still expect large Stefan numbers for temperature changes of tens of Kelvin. However, since the liquid is assumed to be initially at the freezing temperature, only a small temperature change is needed to drive the solidification process and thus we expect $\beta \gg 1$.

The Biot number can be expressed as $\mathrm{Bi} = h^*/\mathcal{H}^*$, where for silicon $\mathcal{H}^* = k^*/\ell^* \approx 2.5 \times 10^9$ W/m$^2$·K. Determining the heat transfer coefficient $h^*$ is complicated, since its value depends on the environment and the material. Nonetheless, there is a maximal value $h^*_{\mathrm{max}}$ beyond which the material would simply vaporise. Ribera and Myers [199] provide the expression $h^*_{\mathrm{max}} = c^*\sqrt{\rho^* B^*/3}$, where $B^*$ is the bulk modulus. For silicon we have $B^* \approx 10^{11}$ kg/m·s$^2$ [13], therefore $h^*_{\mathrm{max}} \approx 7.6 \times 10^9$ W/m$^2$·K and hence $\mathrm{Bi}_{\mathrm{max}} \approx 2.2$. However, the order of magnitude of $h^*_{\mathrm{max}}$ is extremely large and is never reached in practical situations [16], thus $h^* \ll h^*_{\mathrm{max}}$ generally.

Hence, throughout this study we will assume $\beta \gg 1$ and $\mathrm{Bi} \ll 1$. If necessary, the relative size of $\beta$ to Bi will be discussed during the analysis.

## 5.3 Numerical solution

There exist few analytical solutions to practical Stefan problems. However, in the case of a constant thermal conductivity, i.e. $f(s) = 1$, and a fixed temperature condition at $x = 0$, it is possible to obtain an exact solution, termed the Neumann solution [4, 103, 111]. Such a solution does not exist with a Newton cooling condition, not even in the case of constant thermal conductivity, and thus we need to explore numerical and approximate methods to solve the problem with $f \neq 1$. Furthermore, the expected sizes of the Biot and Stefan numbers allow us to perform an asymptotic analysis to distinguish different time regimes of interest and obtain analytical expressions in most of them.

A usual approach to obtain numerical solutions of Stefan problems is to first introduce an alternative variable which transforms the moving domain into the unit interval. The numerical scheme to solve the resulting problem consists of discretizing explicitly for the temperature and implicitly for the interface position and the interface speed [82, 84, 85, 199]. In addition, since the solid does not exist initially, a small time analysis must be performed to obtain a valid initial condition for the numerical scheme.

### 5.3.1 Formulation in a fixed domain

We define the new variable $\xi = x/s$ and rewrite the temperature as $T(x,t) = u(\xi,t)$, which transforms Eqs. (5.12a)–(5.12d) into

$$s u_t = \xi s_t u_\xi + F(s) u_{\xi\xi}, \qquad 0 \le \xi \le 1, \tag{5.13a}$$

$$F(s) u_\xi = \mathrm{Bi}(1+u), \qquad \text{at } \xi = 0, \tag{5.13b}$$

$$u = 0, \qquad \text{at } \xi = 1, \tag{5.13c}$$

$$\beta s_t = F(s) u_\xi, \qquad \text{at } \xi = 1, \tag{5.13d}$$

where we have defined $F(s) = 2(\sqrt{1+s^2} - s)$ for simplicity. This formulation breaks down as $t \to 0$ and hence the initial condition for $s$ must be substituted by an approximate value at a small time $t_0$.

### 5.3.2 Small-time approximation

Since the solid phase does not exist initially, a small-time analysis has to be carried out to study the initial dynamics of the system. To facilitate the analysis, we assume the remaining dimensionless numbers are order one in magnitude. In this way, the small-time behaviour applies to more limits that may arise in other situations where, for instance, the Stefan number is expected to be small [4]. An analysis of the results for asymptotic limits of these parameters can be performed afterwards. Let now $t \ll 1$ and assume that the solid-liquid interface is approximated by an expression of the form $s \approx \lambda t^p$ (hence $s_t \approx p\lambda t^{p-1}$), where $\lambda$ and $p$ are constants to be determined. Neglecting terms of order $t^{2p}$ gives $F \approx 2(1-\lambda t^p)$ and thus Eq. (5.13d) can be written as

$$\frac{1}{2}\beta\lambda p \left(t^{p-1} + \lambda t^{2p-1}\right) = u_\xi, \tag{5.14}$$

where we have used $(1-z)^{-1} \approx 1+z$ for $z \ll 1$ and $u_\xi$ is evaluated at $\xi = 1$. The only possible way to balance with the r.h.s. of Eq. (5.14) is obtained by setting $p = 1$, hence

$$s \approx \lambda t, \qquad s_t \approx \lambda, \qquad F \approx 2(1-\lambda t), \tag{5.15}$$

provided $t \ll 1$. In particular, Eq. (5.15) predicts that the solid initially grows at a finite rate $\lambda$ independent of the choice of boundary condition at $x = 0$. The fixed boundary condition is known to predict an infinite freezing (or melting) rate [4, 81, 84, 85, 103, 199], so the size-dependent ETC produces a more realistic growth rate.

Substituting Eq. (5.15) into Eqs. (5.13a)–(5.13c) and taking the limit $t \to 0$ yields a second order boundary value problem for $u$

$$\lambda \xi u_\xi + 2u_{\xi\xi} = 0, \tag{5.16a}$$

$$2u_\xi = \mathrm{Bi}(1+u), \qquad \text{at } \xi = 0 \tag{5.16b}$$

$$u = 0, \qquad \text{at } \xi = 1. \tag{5.16c}$$

The solution to (5.16) is

$$u(\xi) = \mathrm{Bi}\frac{\mathrm{erf}\left(\sqrt{\lambda}\xi/2\right) - \mathrm{erf}\left(\sqrt{\lambda}/2\right)}{2\sqrt{\lambda/\pi} + \mathrm{Bi}\,\mathrm{erf}\left(\sqrt{\lambda}/2\right)}, \tag{5.17}$$

where $\mathrm{erf}(z) = 2\pi^{-1/2}\int_0^z \exp(-t^2)dt$ is the error function. Finally, $\lambda$ is determined by substituting Eqs. (5.15) and (5.17) into Eq. (5.14) and taking the limit $t \to 0$, which yields an equation for $\lambda$

$$\lambda + \frac{\sqrt{\pi}}{2}\mathrm{Bi}\sqrt{\lambda}\mathrm{erf}\left(\frac{\sqrt{\lambda}}{2}\right) = \frac{\mathrm{Bi}}{\beta}e^{-\lambda/4}. \tag{5.18}$$

For a fixed value of Bi it is trivial to find $\beta(\lambda)$, which can be used to plot the exact solution on the $(\beta, \lambda)$-plane. The same argument is valid for $\mathrm{Bi}(\lambda)$ for a fixed $\beta$. However, finding $\lambda$ for fixed values of Bi and $\beta$ requires the use of numerical methods.

Recall, Eq. (5.18) has been obtained under the assumption $\mathrm{Bi}, \beta = O(1)$. Since we are interested in the limits $\mathrm{Bi}, \beta^{-1} \ll 1$, we can perform an asymptotic analysis on Eq. (5.18) to find an approximate solution in this specific limit.

In the limit $\mathrm{Bi}, \mathrm{Bi}/\beta \to 0$, Eq. (5.18) yields $\lambda \to 0$, which indicates $\lambda = O(\delta)$ for some $\delta = \delta(\mathrm{Bi}, \beta) \ll 1$. We can make the approximations

$$\mathrm{erf}\left(\frac{\sqrt{\lambda}}{2}\right) \approx \frac{\sqrt{\lambda}}{\sqrt{\pi}} - \frac{\lambda\sqrt{\lambda}}{12\sqrt{\pi}}, \qquad \exp\left(\frac{\lambda}{4}\right) \approx 1 + \frac{\lambda}{4}, \tag{5.19}$$

which reduces Eq. (5.18) to

$$\left(1+\frac{\mathrm{Bi}}{2}\right)\lambda+\frac{1}{4}\left(1+\frac{\mathrm{Bi}}{3}\right)\lambda^2+O(\lambda^3)=\frac{\mathrm{Bi}}{\beta}. \tag{5.20}$$

Note, the r.h.s of Eq. (5.20) represents the driving force of the solidification process, therefore a balance with the l.h.s is required. Since $\lambda \ll 1$, this balance is only achieved if we choose $\lambda = O(\mathrm{Bi}/\beta)$. Then we seek a solution for $\lambda$ as a power series

$$\lambda = \delta\lambda_0 + \delta^2\lambda_1 + O(\delta^3). \tag{5.21}$$

where $\delta = \mathrm{Bi}/\beta$. Introducing this expansion into Eq. (5.18) yields a subproblem for each power of $\delta$. The first- and second-order subproblems are

$$\left(1+\frac{\mathrm{Bi}}{2}\right)\lambda_0=1, \qquad \left(1+\frac{\mathrm{Bi}}{2}\right)\lambda_1+\frac{1}{4}\left(1+\frac{\mathrm{Bi}}{3}\right)\lambda_0^2=0, \tag{5.22}$$

which gives $\lambda_0 = 2/(2+\mathrm{Bi})$ and $\lambda_1 = -(3+\mathrm{Bi})\lambda_0^3/12$ and hence

$$\lambda = \frac{2}{2+\mathrm{Bi}}\frac{\mathrm{Bi}}{\beta} - \frac{2(\mathrm{Bi}+3)}{3(2+\mathrm{Bi})^3}\frac{\mathrm{Bi}^2}{\beta^2} + O\left(\frac{\mathrm{Bi}^3}{\beta^3}\right). \tag{5.23}$$

In Fig. 5.2 we compare this approximation to the exact solution of Eq. (5.18) and observe an excellent agreement across the entire range $\mathrm{Bi}, \beta^{-1} \in (10^{-3}, 1)$.

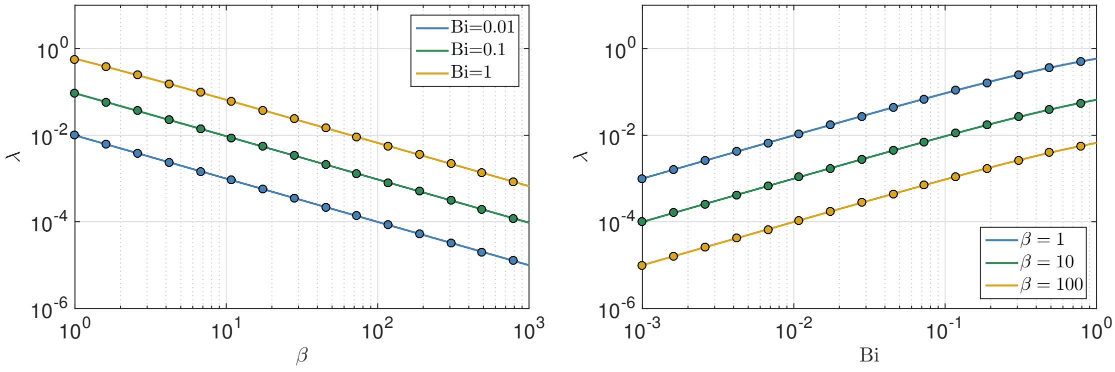

**(a)** **(b)**

**Figure 5.2:** (a) Solution to Eq. (5.18) as a function of $\beta$, for various values of the Biot number Bi. (b) Solution to Eq. (5.18) as a function of Bi, for various values of the Stefan number $\beta$. Solid lines correspond to the exact solutions and circles refer to the asymptotic approximation given in Eq. (5.23).

Consider now the first-order approximation. Substituting into Eq. (5.17) and using Eq. (5.19) we can reduce $u$ to

$$u(\xi) \approx \frac{\mathrm{Bi}(\xi-1)}{2+\mathrm{Bi}}, \tag{5.24}$$

which may be used to approximate the temperature profile at a small time $t_0$ for Bi, $\beta^{-1} \ll 1$.

### 5.3.3 Numerical scheme

The problem in the fixed domain is now discretized on a spatial grid of $N+1$ points of the form $\xi_i = \frac{i}{N}$ and a time grid with points of the form $t_n = t_0 + n\Delta t$. In interior points of the domain, derivatives are approximated using second order central differences:

$$\frac{\partial u}{\partial t} \approx \frac{u_i^{n+1} - u_i^n}{\Delta t}, \quad \frac{\partial u}{\partial \xi} \approx \frac{u_{i+1}^{n+1} - u_{i-1}^{n+1}}{2\Delta \xi}, \quad \frac{\partial^2 u}{\partial \xi^2} \approx \frac{u_{i+1}^{n+1} - 2u_i^{n+1} + u_{i-1}^{n+1}}{(\Delta \xi)^2}, \tag{5.25}$$

where $u_i^n = u(\xi_i, t_n)$ and $\Delta\xi = N^{-1}$. Upon substituting these expression into Eq. (5.13a) and writing $s = s^n$ and $\mathrm{d}s/\,\mathrm{d}t = s_t^n$ we obtain $N-1$ algebraic equations of the form

$$A_i^n u_{i-1}^{n+1} + B_i^n u_i^{n+1} + C_i^n u_{i+1}^{n+1} = s^n u_i^n, \qquad 1 \le i \le N-1, \tag{5.26}$$

with coefficients

$$A_i^n = \frac{\xi_i s_t^n \Delta t}{2\Delta\xi} - \frac{F(s^n)\Delta t}{(\Delta\xi)^2}, \quad B_i^n = s^n + 2\frac{F(s^n)\Delta t}{(\Delta\xi)^2}, \quad C_i^n = -\frac{\xi_i s_t^n \Delta t}{2\Delta\xi} - \frac{F(s^n)\Delta t}{(\Delta\xi)^2}. \tag{5.27}$$

Using Eq. (5.13c) we obtain

$$u_N^{n+1} = 0, \tag{5.28}$$

whereas the Newton condition at $\xi = 0$ becomes, after using second order forward differences,

$$\left(1 + \frac{3}{2}\alpha^n\right) u_0^{n+1} - 2\alpha^n u_1^{n+1} + \frac{1}{2}\alpha^n u_2^{n+1} = -1, \tag{5.29}$$

where $\alpha^n = F(s^n)/(\mathrm{Bi}\Delta\xi)$. To update the position of the moving boundary we discretize Eq. (5.13d) explicitly for $s$ to find $s^{n+1}$,

$$s^{n+1} = s^n + \Delta t F(s^n) \frac{3u_N^{n+1} - 4u_{N-1}^{n+1} + u_{N-2}^{n+1}}{2\beta\Delta\xi}, \tag{5.30}$$

where we have used second order backward differences to discretize $u_\xi$ at $\xi = 1$.

## 5.4 Asymptotic analysis

In [82], an asymptotic analysis for the formulation with a fixed-temperature condition is performed under the assumption of a large Stefan number. In the case of the Newton cooling condition, the asymptotic analysis depends also on Bi and potentially on the relative size of Bi to $\beta$. In order to simplify the analysis we will focus only on three time regimes, which correspond to $s \ll 1$, $s = O(1)$ and $s \gg 1$.

**First time regime** This is given by $t = O(\varepsilon)$, where $\varepsilon \ll 1$ is an artificial parameter, and it has already been partially studied during the small-time analysis. It describes the initial stage of the solidification, where the solid has not grown much yet, therefore $x, s = O(\epsilon_1)$ for some small $\epsilon_1 \ll 1$. In addition, the small Biot number indicates that the influx of heat is very small and therefore the temperature is not expected to differ much from its initial value, $T = O(\epsilon_2)$ for $\epsilon_2 \ll 1$. Upon defining the scaled variables $t = \varepsilon\hat{t}$, $x = \epsilon_1\hat{x}$, $s = \epsilon_1\hat{s}$ (thus $f \approx 2\epsilon_1\hat{s}$) and $T = \epsilon_2\hat{T}$, by balancing terms in the Newton condition we find $\epsilon_2 = \mathrm{Bi}$. To ensure that freezing occurs at $\hat{t} > 0$ we need to balance both sides of Eq. (5.12d), which yields $\epsilon_1 = \mathrm{Bi}\beta^{-1}\varepsilon \ll \varepsilon$. At the leading order, the system in the new variables reads

$$\hat{T}_{\hat{x}\hat{x}} = 0, \qquad 0 \le \hat{x} \le \hat{s}, \tag{5.31a}$$

$$2\hat{s}\hat{T}_{\hat{x}} = 1, \qquad \text{at } \hat{x} = 0, \tag{5.31b}$$

$$\hat{T} = 0, \qquad \text{at } \hat{x} = \hat{s}, \tag{5.31c}$$

$$\hat{s}_{\hat{t}} = 2\hat{s}\hat{T}_{\hat{x}}, \qquad \text{at } \hat{x} = \hat{s}, \tag{5.31d}$$

$$\hat{s} = 0, \qquad \text{at } \hat{t} = 0, \tag{5.31e}$$

After applying the boundary conditions (5.31b) and (5.31c), the solution to Eq. (5.31a) is

$$\hat{T} = \frac{\hat{x} - \hat{s}}{2\hat{s}}, \tag{5.32}$$

and therefore the position of the interface is determined by

$$\hat{s} = \hat{t}. \tag{5.33}$$

In the original non-dimensional variables we find

$$T(x,t) = \mathrm{Bi}\frac{x - s}{2s}, \qquad s(t) = \mathrm{Bi}\beta^{-1}t \tag{5.34}$$

for $t \ll 1$. Notice that this temperature profile coincides with the small-time profile given in Eq. (5.24) when terms of order $\mathrm{Bi}^2$ are neglected.

**Second time regime** The approximation $f \approx 2s$ fails for $s = O(1)$. From Eq. (5.34) we find $t = O(\mathrm{Bi}^{-1}\beta)$ and $T = O(\mathrm{Bi})$. Upon defining the new variables $x = x'$, $s = s'$, $t = \mathrm{Bi}^{-1}\beta t'$ and $T = \mathrm{Bi}T'$, the leading order problem for $T'$ becomes

$$T'_{x'x'} = 0, \qquad 0 \le x' \le s', \tag{5.35a}$$

$$f(s')T'_{x'} = 1, \qquad x' = 0, \tag{5.35b}$$

$$T' = 0, \qquad x' = s', \tag{5.35c}$$

whose solution is

$$T'(x', t') = \frac{x' - s'}{f(s')}, \tag{5.36}$$

The solid-liquid interface is therefore determined by

$$s'_{t'} = 1, \tag{5.37}$$

subject to the matching condition

$$s' \sim t', \quad t' \to 0. \tag{5.38}$$

In the original dimensional variables the solution in this time regime is therefore

$$T(x, t) = \mathrm{Bi}\frac{x - s}{f(s)}, \qquad s(t) = \mathrm{Bi}\beta^{-1}t, \tag{5.39}$$

for $t = O(\mathrm{Bi}^{-1}\beta)$, which captures the previous time regime as well due to the behaviour of $f$ for small values of $s$.

**Third time regime** We now assume $s \gg 1$ and therefore $f \approx 1$. The correct balance is obtained by choosing $t = O(\mathrm{Bi}^{-2}\beta)$, $x, s = O(\mathrm{Bi}^{-1})$ and $T = O(1)$, which yields, upon writing $t = \mathrm{Bi}^{-2}\beta\tilde{t}$, $x = \mathrm{Bi}^{-1}\tilde{x}$, $s = \mathrm{Bi}^{-1}\tilde{s}$ and $T = \tilde{T}$,

$$\tilde{T}_{\tilde{x}\tilde{x}} = 0, \qquad 0 \le \tilde{x} \le \tilde{s}, \tag{5.40a}$$

$$f(\tilde{s})\tilde{T}_{\tilde{x}} = 1 + \tilde{T}, \qquad \text{at } \tilde{x} = 0, \tag{5.40b}$$

$$\tilde{T} = 0, \qquad \text{at } \tilde{x} = \tilde{s}, \tag{5.40c}$$

$$\tilde{s}_{\tilde{t}} = f(\tilde{s})\tilde{T}_{\tilde{x}}, \qquad \text{at } \tilde{x} = \tilde{s}. \tag{5.40d}$$

The solution to (5.40) is given by

$$\tilde{T}(\tilde{x}, \tilde{t}) = \frac{\tilde{x} - \tilde{s}}{\tilde{s} + f(\tilde{s})}, \tag{5.41}$$

and thus the interface is determined by

$$\tilde{s}_{\tilde{t}} = \frac{f(\tilde{s})}{\tilde{s} + f(\tilde{s})}, \tag{5.42}$$

which can be integrated to give

$$C + 4\tilde{t} = \tilde{s}^2 + \tilde{s}\sqrt{1+\tilde{s}^2} + 4\tilde{s} + \text{arcsinh}(\tilde{s}), \tag{5.43}$$

where $C$ is a constant of integration to be determined to match the previous time regime. Using Eq. (5.39) we find $\tilde{s} \sim \tilde{t}$ for $\tilde{t} = O(\text{Bi})$, which gives $C = 0$ at leading order. In the original dimensionless variables the temperature profile is

$$T(x,t) = \frac{x-s}{s + \text{Bi}^{-1} f(s)}, \tag{5.44a}$$

whereas the solid-liquid interface is determined by

$$\frac{4\text{Bi}}{\beta} t = \text{Bi}s^2 + s\sqrt{1+(\text{Bi}s)^2} + 4s + \text{Bi}^{-1}\text{arcsinh}(\text{Bi}s). \tag{5.44b}$$

To obtain $s$ we must invert Eq. (5.44b) numerically. Equivalently, it can be calculated integrating

$$s_t = \frac{f(s)}{\beta(s + \text{Bi}^{-1} f(s))}, \tag{5.45}$$

which captures all the previous time regimes and can thus be solved using the initial condition $s(0) = 0$.

We can consider a fourth time regime, where the Newton condition converges to the fixed temperature condition, as it can be observed by assuming $\tilde{x} \gg 1$ in Eq. (5.40b). However, observe that Eq. (5.45) already captures this regime, since $s \to \infty$ yields $f \to 1$ and $s_t \propto s^{-1}$, from where the classical behaviour $s \sim \sqrt{t}$ is recovered.

## 5.5 Results and discussion

In Fig. 5.3 we show the numerical and asymptotic solutions of the non-classical formulation and compare them against the classical solution for constant thermal conductivity. This is done for different choices of Bi and $\beta$.

Firstly, we observe that the asymptotic solution is in good agreement with the numerical solution. Only in Fig. 5.3 (a) do some discrepancies appear for larger times. This is due to the ratio Bi/$\beta$, whose value in the case of Fig. 5.3 (a) is at least one order of magnitude larger than in the other cases. Recall that the asymptotic solution is based on the assumption Bi/$\beta \ll 1$ and hence, as Bi/$\beta$ approaches unity, higher order terms should be included to increase the accuracy of the asymptotic solution.

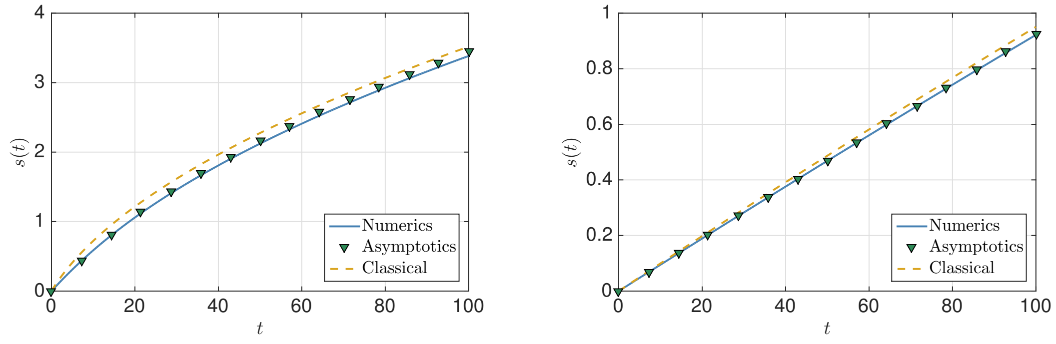

**(a)** $\beta = 10$, $\mathrm{Bi} = 1$.

**(b)** $\beta = 10$, $\mathrm{Bi} = 0.1$.

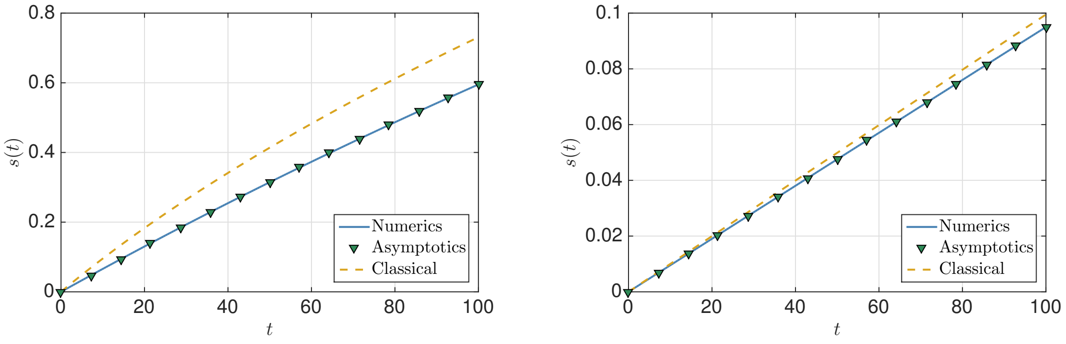

**(c)** $\beta = 100$, $\mathrm{Bi} = 1$.

**(d)** $\beta = 100$, $\mathrm{Bi} = 0.1$.

**Figure 5.3:** Evolution of the solid-liquid interface for $\mathrm{Bi} = 1$ and $\beta = 1, 10$. Solid lines correspond to the numerical solutions, symbols refer to the solutions of Eq. (5.45). The dashed line shows the corresponding classical solution.

Secondly, we observe that the speed of the solid-liquid interface decreases as we decrease the Biot number and the usual square-root profile transforms into a linear one. Furthermore, as we decrease Bi both classical and non-classical formulations tend to the same solution and non-local effects described by the size-dependent ETC seem to become less important. For $\mathrm{Bi} = 0.01$, which we do not show here, both the classical and non-classical profiles are indistinguishable for $\beta \in (10, 100)$. In fact, our asymptotic analysis indicates that we expect a linear profile until $t = O(\beta/\mathrm{Bi})$ with a slope $\mathrm{Bi}/\beta$. The same slope is obtained in the small-time analysis of the classical formulation (see Chapter 1). Physically, the convergence of both solutions to the same profile can be understood by recalling that small

Biot numbers correspond to a situation where heat flow is limited by the heat exchange with the environment rather than heat conduction through the bulk [20], which implies that the form of thermal conductivity employed should not matter in this case.

In Fig. 5.3 (c) it can also be observed that large deviations between the non-classical and classical formulations appear for large values of $\beta$. This may be understood by recalling that the Stefan number corresponds to a slow solidification, since $s_t \propto \beta^{-1}$. Thus, non-local effects remain for a longer time period due to the small growth rate, which causes these larger deviations between both formulations.

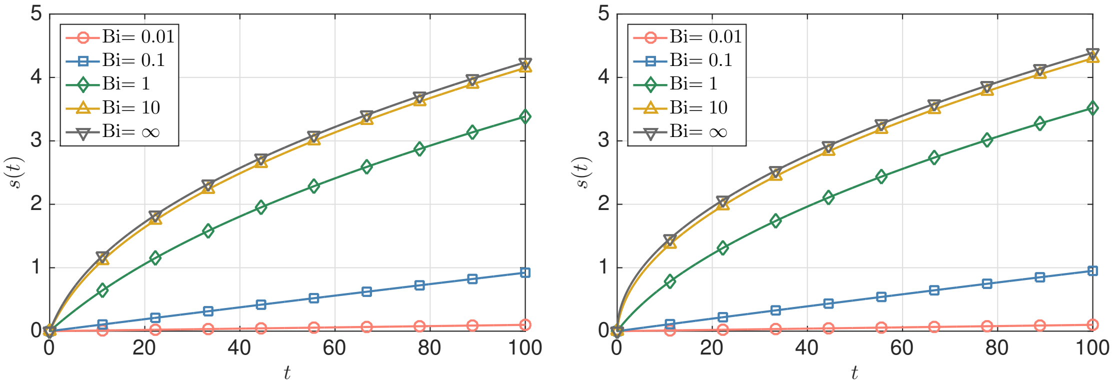

**(a)** Effective Fourier law, $\beta = 10$.

**(b)** Classical Fourier law, $\beta = 10$.

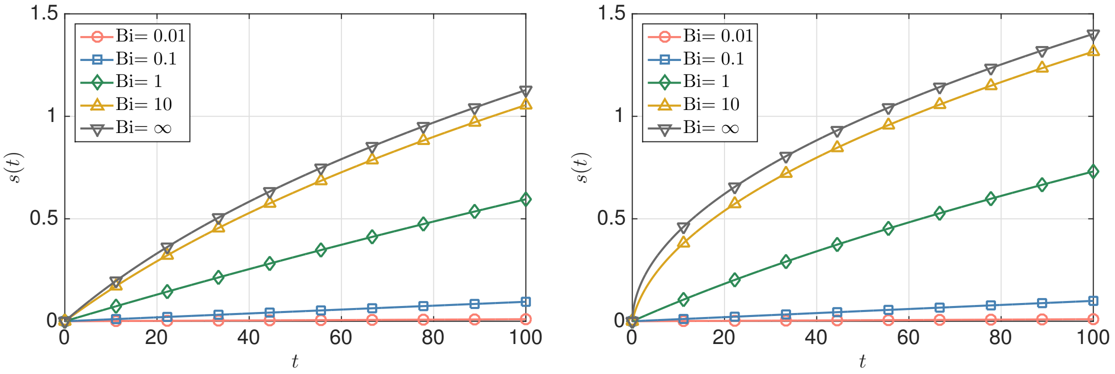

**(c)** Effective Fourier law, $\beta = 100$.

**(d)** Classical Fourier law, $\beta = 100$.

**Figure 5.4:** Evolution of the solid-liquid interface for different values of Bi, according to the non-classical (panels (a) and (c)) and classical (panels (b) and (d)) formulations. The case Bi $= \infty$ corresponds to the fixed-temperature condition $T(0,t) = -1$.

To illustrate the general case of an arbitrary Biot number, in Fig. 5.4 we show the evolution of the solid-liquid interface for different values of the Stefan and Biot numbers according to the classical and non-classical formulations. For $\beta = 10$, differences between both formulations are considerably less than for the larger value $\beta = 100$. In Fig. 5.5 we have plotted the evolution in time of the absolute difference of both formulations for different values of $\beta$ and Bi. We observe the existence of two regimes: in the first regime, due to the presence of non-local effects, differences between the classical and modified formulations increase, whereas in the second time regime they decrease as non-local effects disappear. By observing Figs. 5.4 (a) we see that this change in behaviour occurs when $s \approx 1$. In the case of $\beta = 100$ the second time regime enters later due to the fact that solidification is slower and hence the presence of non-local effects is significant for a longer period of time.

Hence, these results suggest that non-local effects become less important if we decrease the Biot number, which corresponds to a poor heat conduction through the solid, or by decreasing the Stefan number, which corresponds to fast solidification. In the first case, the choice of thermal conductivity does not alter the evolution of $s(t)$ significantly. In the latter, non-local effects disappear due to the fast growth of the solid phase.

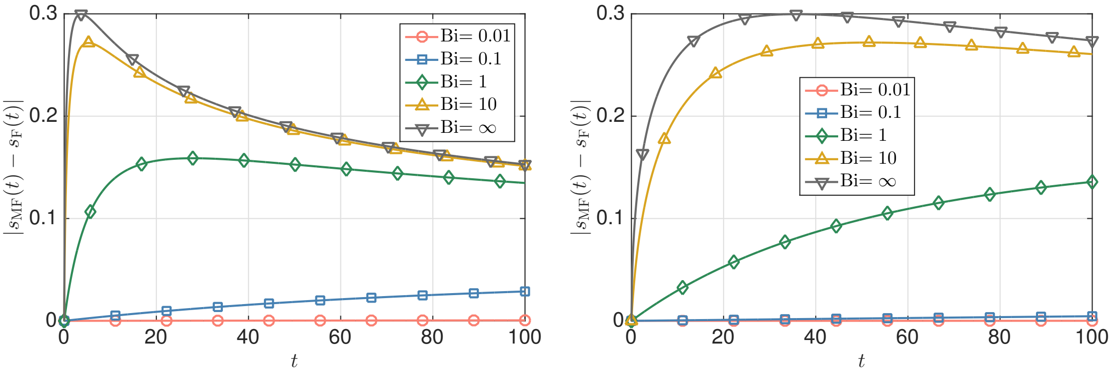

**(a)** $\beta = 10$.  **(b)** $\beta = 100$.

**Figure 5.5:** Evolution of the absolute difference $|s_{\mathrm{NF}}(t) - s_{\mathrm{F}}(t)|$, where $s_{\mathrm{MF}}$ and $s_{\mathrm{F}}$ represent the position of the interface according to the modified and classical formulations.

The effect of the Biot number on the temperature can be observed in Fig. 5.7, which shows the evolution of the temperature profiles according the non-classical and classical formulations for different values of Bi and for $\beta = 10$. For early times the size of the solid is small, which leads to a small ETC and hence changes in temperature in the non-classical formulation occur mainly near $x = 0$. This happens independent of the value of Bi, as it can be seen by comparing panels (a), (c) and (e). In addition, it can seem that diffusion

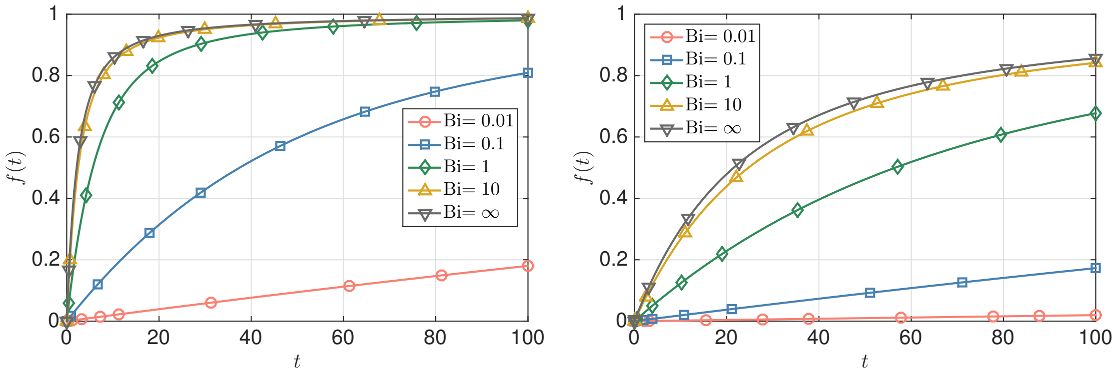

**(a)** $\beta = 10$.  **(b)** $\beta = 100$.

**Figure 5.6:** Evolution of the effective thermal conductivity as a function of time (computed as $f(t) = f(s(t))$) for different values of the Biot number Bi. The case Bi $= \infty$ corresponds to the fixed temperature condition $T(0,t) = -1$.

is enhanced as Bi decreases, in contradiction to the fact that conduction becomes worse in this limit. We must recall that the spatial coordinate used in Fig. 5.7 is the alternative variable $\xi = x/s$, and hence the growth rate of the solid is not shown here. Hence, the temperature profiles must be observed together with the growth of the solid for these values of Bi, shown in Figs. 5.4 (a). Another indicator for a worse conduction for small values of Bi is the range of temperatures shown in the color bars of the corresponding plots.

In the classical formulation, diffusion through the solid occurs normally and changes in temperature appear gradually through the crystal. Similarly as in the case of the non-classical formulation, panels (b), (d) and (f) of Fig. 5.7 must be observed by having in mind the corresponding growth rates of the solid-liquid in, shown in Fig. 5.4 (b).

We can also see that the initial differences between the temperature profiles for a fixed Bi disappear as time increases, which is caused by the fact that the growth of the solid leads to an increase of the ETC, which finally converges to the classical conductivity.

## 5.6 Conclusion

In this chapter we have formulated a mathematical model for a one-dimensional solidification process with a size-dependent thermal conductivity and a Newton cooling condition at the fixed boundary. Numerical and asymptotic solution methods have been proposed and

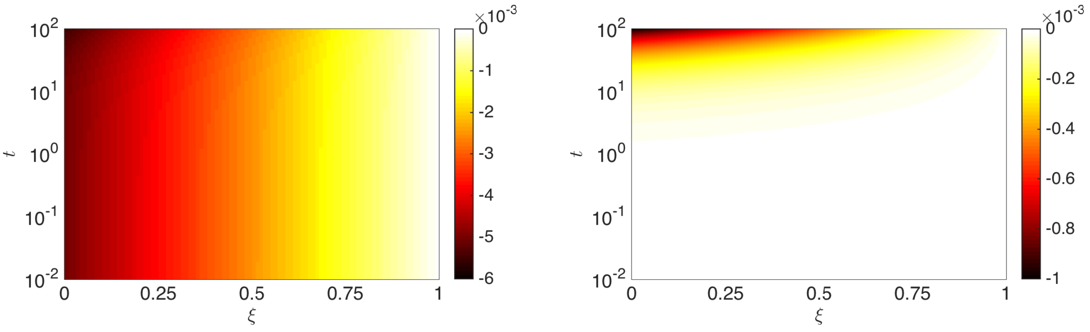

**(a)** Effective Fourier law, $\mathrm{Bi} = 0.01$.

**(b)** Classical Fourier law, $\mathrm{Bi} = 0.01$.

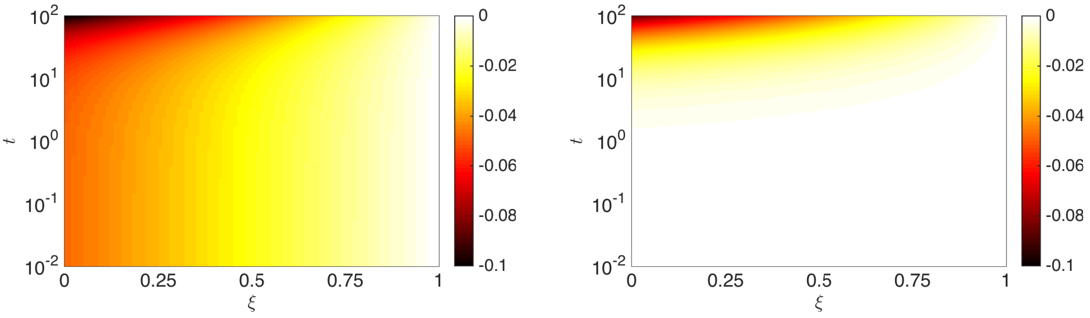

**(c)** Effective Fourier law, $\mathrm{Bi} = 0.1$.

**(d)** Classical Fourier law, $\mathrm{Bi} = 0.1$.

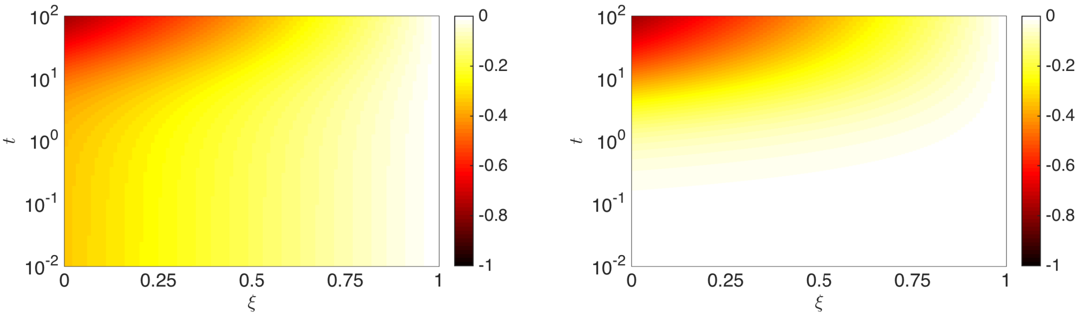

**(e)** Effective Fourier law, $\mathrm{Bi} = 1$.

**(f)** Classical Fourier law, $\mathrm{Bi} = 1$.

**Figure 5.7:** Heat maps showing the evolution of the temperature according to the effective and classical Fourier laws in the transformed coordinate $\xi$. In all the panels the value $\beta = 10$ has been used.

compared, showing good agreement for the range of parameters considered. In contrast to previous studies, we have studied the limit of a small Biot number, which seems more physically realistic than the high value of previous studies. We have observed that non-local effects tend to disappear as the Biot number decreases, which seems surprising since the initial solidification rate is proportional to Bi and thus non-local effects would have been expected to be present for longer periods of time. This result has been attributed to poor conduction in both the classical and the modified formulations due to the Biot number being small, since this implies that the heat exchange with the environment at the fixed boundary dominates over the heat conduction through the growing solid. Similarly, as we decrease the Stefan number the presence of non-local effects is reduced to an initial stage of the process that is overcome rapidly due to the higher speed of the solid-liquid interface.

# 6 The Stefan problem with non-Fourier heat conduction

M. Calvo-Schwarzwälder, M. G. Hennessy and T. G. Myers.
The one-dimensional Stefan problem with non-Fourier heat conduction.
To appear in International Journal of Heat and Mass Transfer (submitted May 2019).
arXiv:1905.06320
Impact factor: 3.891. Q1 in Condensed Matter Physics.

## 6.1 Introduction

Heat conduction at small length or time scales is dominated by effects which are not well described by the classical equations [32]. For instance, it has been observed that the thermal conductivity, which was introduced as a material-intrinsic property and therefore independent of size or shape, exhibits size-dependent behaviour at small length scales [145]. The understanding and correct description of the underlying thermal physics is of vital importance for future applications of nanostructures. For instance, an incorrect description of the thermal response of nanoscale devices can lead to melting and eventually device failure [185]. Novel applications such as laser melting involve phase change at very short time scales [12, 91, 153].

When the characteristic length or time scales of a physical system are comparable to the characteristic length or time scales of the heat carriers, non-classical effects are expected to dominate the heat-transfer mechanisms [32, 40, 41, 216, 235]. In semiconductors such as silicon or germanium, these energy carriers are predominantly phonons, which may be understood as lattice vibrations. These quasi-particles have two associated important physical quantities: the mean free path and the thermal relaxation time. From a microscopic point of view, these represent the mean distance and time that phonons travel between collisions. We can then distinguish two thermal relaxation times, normal and resistive, depending on whether or not phonon momentum is conserved after the collision.

A number of different models extending the classical Fourier law can be found in the literature. In this paper we focus our attention to the Maxwell-Cattaneo equation [44, 245] and the Guyer-Krumhansl equation [105, 106]. Other popular continuum models are the dual phase lag model [237, 239] or the thermomass model [42, 101, 249]. The first incorporates a time lag into all the terms appearing in Fourier's law, although the physical interpretation of the new parameters remains unclear. The latter uses the Einstein energy-mass relation to describe heat conduction as the motion of a gas formed by particles with non-zero mass called thermons. In this case, a non-linear term emerges in the governing equations, which complicates the mathematical analysis. In contrast to these models, the Guyer-Krumhansl and Maxwell-Cattaneo models involve linear equations where the parameters have a clear physical meaning.

The Maxwell-Cattaneo equation was proposed in the 1950s to remove the infinite speed of heat propagation implicit to Fourier's law. Mathematically, this model extends Fourier's law by incorporating a new term which accounts for the time lag between the imposition of a temperature gradient and the creation of a heat flux. This new term leads to the flux depending on the history of the temperature gradient and is thus referred to as a memory term. In the 1960s Guyer and Krumhansl [105, 106] proposed an extension to Fourier's law derived from the Boltzmann transport equation (BTE) [24] which accounts for memory and non-local effects. Whereas memory effects are important for short times or high frequencies, non-local effects become relevant at small length scales. Although this formalism was initially thought to be applicable only in low-temperature situations ($\sim 2$ K), recent experimental observations show that it is also suitable for describing heat transfer at room temperature or above [100, 143, 235]. Jou et al. [127] later showed that both the

Maxwell-Cattaneo and the Guyer-Krumhansl equations can be derived using the framework of extended irreversible thermodynamics (EIT).

The classical mathematical description of a phase-change process, known as the Stefan problem, is based on Fourier's law [103]. Some authors have incorporated the Maxwell-Cattaneo equation into the formulation of the Stefan problem to model rapid solidification processes [221], cryopreservation [2, 68], cryosurgery for lung cancer treatments [135], and nanoparticle melting [108]. Other authors have studied the Stefan problem with Maxwell-Cattaneo conduction from a point of view of mathematical analysis [90, 96, 223]. Recently, Hennessy et al. [107] performed a detailed asymptotic analysis of the one-dimensional Stefan problem with Guyer-Krumhansl conduction, where it is shown that non-classical effects can lead to important differences in the solidification kinetics with respect to Fourier's law. Sobolev [218, 220] solved different non-Fourier formulations under the assumption of constant interface velocity. To account for non-local effects, some authors [38, 39, 82] recently proposed a formulation of the Stefan problem based on Fourier's law with an effective thermal conductivity dependent on the size of the solid. From a microscopic point of view, Font and Bresme [83] published a work where non-classical effects in a melting process were observed using molecular dynamics.

In this chapter we aim to provide tools for detecting non-classical heat transport mechanisms in phase-change processes. For this we study the solidification kinetics in a one-dimensional geometry using the Maxwell-Cattaneo and Guyer-Krumhansl models of heat conduction. The solid is assumed to grow from a small seed crystal, which splits the process into two major regimes, with the first capturing the heat conduction through the seed crystal and the second describing the solidification kinetics. Our asymptotic analysis shows that these two time regimes can be split into multiple sub-regimes, with each of them describing different physical phenomena. We show that, although both conduction models describe the initial transport of heat through the seed crystal in different ways, the solidification process can be captured by reducing the full problem to the same system of ordinary differential equations, which provides excellent agreement with numerical simulations. The results are then applied to the solidification of silicon, where we conclude that the motion of the interface does not necessarily give information about non-Fourier heat transport. Conversely, the evolution of the heat flux is able to provide valuable insights about non-classical modes of heat transfer.

## 6.2 Mathematical model

To elucidate the roles of non-Fourier conduction mechanisms during solidification, we consider a simple one-dimensional geometry consisting of a liquid bath, which is initially at the phase change temperature $T_{\mathrm{f}}^*$, where the $^*$ notation denotes dimensional quantities. Due to a cold temperature $T_{\mathrm{e}}^*$ in the environment in contact with the bath at $x^* = 0$, the liquid starts solidifying and a solid phase grows into the bath, occupying the space $[0, s^*(t^*)]$. A schematic of the physical scenario is depicted in Fig. 5.1. By assuming that the liquid phase is at the phase-change temperature, any decrease in temperature will cause solidification to occur. In this way we can focus on the heat transfer in the solid, which drives the solidification process and is where the non-classical phenomena are expected to occur.

### 6.2.1 Governing equations

Conservation of energy in the solid is described by

$$c^* \rho^* \frac{\partial T^*}{\partial t^*} + \frac{\partial Q^*}{\partial x^*} = 0, \tag{6.1}$$

where $Q^*$, $T^*$, $c^*$ and $\rho^*$ are respectively the heat flux, the temperature, the specific heat capacity and the density of the solid. In the classical formulation, the mathematical description is completed by assuming that the heat flux is determined by Fourier's law, which in one dimension is

$$Q^* = -k^* \frac{\partial T^*}{\partial x^*}, \tag{6.2}$$

where $k^*$ is the bulk thermal conductivity of the solid. In the present study this will be replaced by the Maxwell-Cattaneo equation (MCE) or the Guyer-Krumhansl (GKE). In one spatial dimension, the GKE takes the form

$$\tau_R^* \frac{\partial Q^*}{\partial t^*} + Q^* = -k^* \frac{\partial T^*}{\partial x^*} + 3\ell^{*2} \frac{\partial^2 Q^*}{\partial x^{*2}}, \tag{6.3}$$

where $\tau_R^*$ is the resistive thermal relaxation time, which is the mean time between consecutive phonon collisions which do not conserve momentum, and $\ell^*$ represents the phonon mean free path, i.e. the mean distance between two collisions. The factor 3 in the last term appears due to different second-order terms collapsing to a single contribution in one dimension. The first term of the left-hand side and the second term of the right-hand side of (6.3) represent respectively memory and non-local effects. The prior are important at small time scales and therefore critical for the initial stages of the solidification process. Non-local effects appear due to two reasons. Firstly, they are caused by the non-negligible rate of normal scattering, i.e. phonon collisions are more likely to conserve their momentum and relaxation effects are delayed. Secondly, non-local effects are important when the characteristic size of the system is comparable to the mean free path.

The GKE can be reduced to the MCE by neglecting the term corresponding to non-local effects, i.e. by setting $\ell^* = 0$ in Eq. (6.3). The two approaches, although similar, are based on different frameworks: the GKE is derived from the BTE whereas the MCE is a phenomenological approach to account for finite heat carrier speed. However, it was later shown that both can be derived within the EIT framework [127, 140].

### 6.2.2 Boundary and initial conditions

At the boundary $x^* = 0$ we impose a fixed-temperature condition given by

$$T^* = T^*_{\mathrm{e}}, \qquad \text{at } x^* = 0^*. \tag{6.4}$$

A boundary condition of the form of Eq. (6.4) predicts an initially infinite rate of phase change [4, 84, 85, 103] when the growing phase initially has zero size. In practice, other forms of boundary conditions should be applied, such as the Newton cooling condition. This has been used in the modelling of melting of nanoparticles [199] and nanowires [81], and leads to a significant increase of the melting times. The cooling condition has also been used in a recent study by Hennessy et al. [107], where a thorough asymptotic analysis of the Guyer-Krumhansl-Stefan problem is performed. The same authors also considered a cooling condition accounting for memory effects when studying the melting behaviour of nanoparticles using the MCE [108]. In this problem, we will assume that solidification begins from a seed crystal of finite size and thus the condition (6.4) can be used without inducing an unphysical infinite rate of phase change.

At the moving interface we impose that the temperature is equal to the phase-change temperature,

$$T^* = T^*_{\mathrm{f}}, \qquad \text{at } x^* = s^*, \tag{6.5}$$

which implies continuity in temperature across the interface. Other authors claim that a jump condition for the temperaure should be utilized at the interface [90, 96, 219]. Based on a diffuse interface model, Hennessy et al. [108] show that, when the MCE is used to model the melting of nanoparticles, the jump condition avoids the phenomenon of supersonic melting [175, 218, 221], which may appear when (6.5) is used. In the case of nanoparticle melting, the onset of supersonic phase change is due to the spherical geometry of system and the fact that less energy is required to melt the surface of smaller solid cores. Thus, the rate of melting increases and eventually becomes unbounded as the radius of the nanoparticle decreases to zero. As there is no mechanism for supersonic solidification in this one-dimensional Cartesian problem, it is sufficient to consider the case of temperature continuity, which is derived from the jump condition in the limit of slow phase change.

In its simplest form, the Stefan condition is given by

$$\rho^* L^*_m \frac{\mathrm{d}s^*}{\mathrm{d}t^*} = -Q^*, \qquad \text{at } x^* = s^*, \tag{6.6}$$

where $L^*_m$ is the latent heat. We assume that solidification starts from an initial seed crystal of size $s^*_c$, formed, for instance, by heterogeneous nucleation, where the temperature is equal to the temperature of the liquid. Since we are using continuum models to describe the growth of the solid, additional assumptions on the size of the seed crystal need to be made. We will assume that its thickness is of the order of nanometres, large enough for continuum theory to hold [181]. The initial conditions are therefore

$$s = s^*_c, \qquad T^* = T^*_{\mathrm{f}}, \qquad Q^* = 0, \qquad \text{at } t^* = 0. \tag{6.7}$$

Conservation of energy (6.1) and the GKE (6.3) can be combined to give

$$\tau^*_R \frac{\partial Q^*}{\partial t^*} + Q^* = -k^* \left( \frac{\partial T^*}{\partial x^*} + \frac{3\ell^{*2}}{\alpha^*} \frac{\partial^2 T^*}{\partial x^* \partial t^*} \right), \tag{6.8}$$

with $\alpha^* = k^*/(\rho^* c^*)$ being the bulk thermal diffusivity. This form shows that non-local effects are related to instantaneous changes of the temperature gradient, whereas memory effects are described temporal changes of the flux (which can be related to the time integral of the temperature gradient). In the special case where $\tau^*_R = 3\ell^{*2}/\alpha^*$, it is easy to see that

Fourier's law is recovered from (6.8). This phenomenon has been termed Fourier resonance [25, 241]. Alternatively, it is possible to eliminate the flux from the equation to obtain the Guyer-Krumhansl heat equation (GKHE)

$$\tau_R^* \frac{\partial^2 T^*}{\partial t^{*2}} + \frac{\partial T^*}{\partial t^*} = \alpha^* \frac{\partial^2 T^*}{\partial x^{*2}} + 3\ell^{*2} \frac{\partial^3 T^*}{\partial x^{*2} \partial t^*}. \tag{6.9}$$

In the limit $\ell^* \to 0$ we obtain the heat equation for the MCE, which in the literature is termed the hyperbolic heat equation (HHE).

### 6.2.3 Non-dimensional formulation

Since the classical solidification kinetics are expected to be recovered for sufficiently large times, we will employ the typical scales used to non-dimensionalise the classical equations. In this way, the importance of non-classical contributions will be described by new dimensionless parameters.

The natural length scale of the problem is the initial size of the solid, $x^*, s^* = O(s_c^*)$. Time is then scaled as $t^* = O(\tau_D^*)$ with $\tau_D^* = s_c^{*2}/\alpha^*$, which corresponds to the time scale for diffusion through the initial seed crystal. The temperature scale is defined by the difference between the freezing and environment temperatures, $\Delta T = T_\mathrm{f}^* - T_\mathrm{e}^*$. Balancing terms in (6.1) then requires $Q^* = O(Q_0^*)$, where $Q_0^* = k^* \Delta T / s_c^*$. Based on these typical scales we introduce the following non-dimensional variables:

$$x = \frac{x^*}{s_c^*}, \qquad t = \frac{t^*}{\tau_D^*}, \qquad T = \frac{T^* - T_\mathrm{f}^*}{\Delta T}, \qquad Q = \frac{Q^*}{Q_0^*}, \qquad s = \frac{s^*}{s_c^*}. \tag{6.10}$$

In these variables, conservation of energy (6.1) and the GKE (6.3) become

$$T_t + Q_x = 0, \tag{6.11a}$$

$$\gamma Q_t + Q = -T_x + \eta^2 Q_{xx}, \tag{6.11b}$$

where we have introduced the subscript notation to denote derivatives. The new parameters in (6.11b) are $\gamma = \tau_R^*/\tau_D^*$ and $\eta = 3^{1/2}\ell^*/s_c^*$, which represent the dimensionless forms of the relaxation time and mean free path. In the literature, $\gamma$ is often called the Cattaneo number, whereas $\eta$ is proportional to the ratio of the mean free path to the initial size of the system and termed the Knudsen number.

The non-dimensional boundary, Stefan, and initial conditions become

$$T = -1, \qquad \text{at } x = 0, \tag{6.12a}$$

$$T = 0, \qquad \text{at } x = s(t), \tag{6.12b}$$

$$\beta s_t = -Q, \qquad \text{at } x = s(t), \tag{6.12c}$$

$$T = Q = 0, \quad s = 1, \qquad \text{at } t = 0, \tag{6.12d}$$

where $\beta = L_m^*/(c^*\Delta T)$ is the Stefan number and represents the ratio of latent heat to sensible heat.

In the dimensionless formulation, (6.8) becomes

$$\gamma Q_t + Q = -T_x - \eta^2 T_{xt}, \tag{6.13}$$

and Fourier resonance appears if the non-classical dimensionless parameters coincide, $\gamma = \eta^2$. Finally, the dimensionless GKHE (6.9) then takes the form

$$\gamma T_{tt} + T_t = T_{xx} + \eta^2 T_{xxt}. \tag{6.14}$$

### 6.2.4 Parameter estimation

For this study we use the values of the thermophysical properties of silicon near the phase change temperature, summarized in Table B.1. More details can be found in Appendix B.

Independent of the underlying model, the dynamics of the solidification process are affected by the Stefan number $\beta$, which can be parametrized in terms of the temperature scale as $\beta = \mathcal{T}^*/\Delta T$. For silicon we find $\mathcal{T}^* \approx 1731.6$ K, hence even by setting the environmental temperature to 0 K (thus $\Delta T = 1687$ K) we find $\beta > 1$. Since our study involves an external temperature that is far above absolute zero, we therefore assume $\beta \gg 1$, in accordance with previous studies.

The Cattaneo number $\gamma$ represents the ratio of the time scales of the ballistic and diffusive heat transport regimes. For $\gamma \ll 1$, heat transfer is dominated by diffusion, whereas it becomes ballistic for $\gamma \gg 1$. The Cattaneo number may be parametrized as $\gamma = (L^*/s_c^*)^2$, where $L^* = \sqrt{\alpha^* \tau_R^*}$ is an effective length where memory effects become non-negligible. Upon using the values given in Table B.1, we find $L^* \approx 17.32$ nm. The Knudsen number $\eta$ corresponds to the ratio of the size of the initial crystal seed to the mean free path and therefore characterises the impact of non-local effects on the initial transport of heat. Using the values in Table B.1 we obtain $\eta \approx \ell^*_{\text{eff}}/s^*_c$, where $\ell^*_{\text{eff}} = 3^{1/2}\ell^* \approx 15.23$ nm is the effective mean free path. Since we assume the size of the seed crystal to be of the order of nanometres, we expect $\gamma, \eta \gg 1$ and thus heat conduction through the solid will initially be dominated by non-classical effects.

Finally, the typical scale of the flux may be parametrized in terms of the Stefan number and the initial size of the seed crystal, $Q^*_0 = (k^* L^*_m/c^*) \times (\beta s^*_c)^{-1}$. For silicon, $k^* L^*_m/c^* \approx 3.8 \times 10^{-4}$ W/m.

## 6.3 Numerical solution

To solve the problem numerically, we transform the growing domain $[0, s(t)]$ to the unit interval $[0, 1]$ and then use finite differences to reformulate the problem as a set of algebraic equations.

### 6.3.1 Formulation in a fixed domain

Upon introducing the alternative space coordinate $\xi = x/s(t)$, which transforms the growing domain into the unit interval, the derivatives become

$$\frac{\partial}{\partial t} \mapsto \frac{\partial}{\partial t} - \xi \frac{s_t}{s}\frac{\partial}{\partial \xi}, \qquad \frac{\partial}{\partial x} \mapsto \frac{1}{s}\frac{\partial}{\partial \xi}, \qquad \frac{\partial^2}{\partial x^2} \mapsto \frac{1}{s^2}\frac{\partial^2}{\partial \xi^2}. \tag{6.15}$$

To avoid performing this transformation on the second-order time derivative in (6.14), which becomes a particularly complicated expression, we introduce an auxiliary variable $v = T_t$ to write the problem solely in terms of first-order time derivatives. Hence, we let $T(x,t) = u(\xi,t)$, $T_t(x,t) = v(\xi,t)$ and $Q(x,t) = w(\xi,t)$. In these variables, $u$ and $v$ are determined by

$$\gamma v_t - \gamma \frac{s_t}{s}\xi v_\xi + v - \eta^2 \frac{1}{s^2} v_{\xi\xi} - \frac{1}{s^2} u_{\xi\xi} = 0, \tag{6.16a}$$

$$v - u_t + \frac{s_t}{s}\xi u_\xi = 0, \tag{6.16b}$$

which are obtained from the GKHE (6.14) and the definition of $v$. Evaluating (6.11a) at $t = 0$ and applying the initial condition $Q = 0$ (hence $Q_x = 0$ at $t = 0$) yields $T_t = 0$ at $t = 0$. From the boundary conditions (6.12a)-(6.12b) we find

$$u = -1, \qquad \text{at } \xi = 0, \tag{6.16c}$$

$$u = 0, \qquad \text{at } \xi = 1, \tag{6.16d}$$

$$v = 0, \qquad \text{at } \xi = 0, \tag{6.16e}$$

$$v + \frac{s_t}{s} u_\xi = 0, \qquad \text{at } \xi = 1. \tag{6.16f}$$

The transformed flux $w$ can be determined by the transformed GKE

$$\gamma w_t - \gamma \frac{s_t}{s} \xi w_\xi + w - \eta^2 \frac{1}{s^2} w_{\xi\xi} = -\frac{1}{s} u_\xi. \tag{6.17a}$$

Assuming that conservation of energy holds at $\xi = 0, 1$, we find the boundary and initial conditions

$$w_\xi = 0, \qquad \text{at } \xi = 0, \tag{6.17b}$$

$$w_\xi = s_t u_\xi, \qquad \text{at } \xi = 1, \tag{6.17c}$$

$$w = 0, \qquad \text{at } t = 0. \tag{6.17d}$$

Note, in principle no boundary conditions for $w$ are needed since we could use (6.13) to write (6.17a) in terms of $w$, $w_t$, and derivatives of $u$ and $v$, the latter of which are already known from (6.16).

Finally, the transformed Stefan condition is

$$\beta s_t = -w, \qquad \text{at } \xi = 1. \tag{6.18}$$

From this formulation we obtain the numerical solution by solving (6.16), (6.17) and (6.18) at each time step using finite differences.

### 6.3.2 Small-time approximation

Numerical experimentation has shown that replacing the initial conditions for $u$, $v$, and $w$ with approximate solutions that are valid for arbitrarily small times $t \ll 1$ greatly improves the stability of the computational scheme when solving the GKE (for $\eta \neq 0$). By carrying out a small-time analysis of the model, which is described in Sec. 6.4, we find that the solution at time $t_0 \ll 1$ can be approximated by

$$u \approx -1 + \operatorname{erf}\left(\frac{\xi}{2\sqrt{\zeta t_0}}\right), \tag{6.19a}$$

$$v \approx -\frac{\xi}{2\sqrt{\pi \zeta t_0^3}} \exp\left(-\frac{\xi^2}{4\zeta t_0}\right), \tag{6.19b}$$

$$w \approx -\sqrt{\frac{\zeta}{\pi t_0}} \exp\left(-\frac{\xi^2}{4\zeta t_0}\right). \tag{6.19c}$$

where $\zeta = \eta^2/\gamma$ represents an effective thermal conductivity. When solving the MCE, the original initial conditions $u(\xi, 0) = v(\xi, 0) = w(\xi, 0) = 0$ can be used.

### 6.3.3 Numerical scheme

We discretize the unit interval into $N + 1$ equidistant points of the form $\xi_i = i\Delta\xi$, where $i = 0, ..., N$ and $\Delta\xi = 1/N$. Similarly, we consider time instants of the form $t_n = t_0 + n\Delta t$, where $t_0$ is the starting time and $n \geq 0$.

At each time step we first solve (6.16), then use this information to update the heat flux by solving (6.17), and finally we update the position of the solid-liquid interface using (6.18). For this we discretize the derivatives of $u, v, w$ implicitly, i.e.

$$u_t \approx \frac{u_i^{n+1} - u_i^n}{\Delta t}, \qquad u_\xi \approx \frac{u_{i+1}^{n+1} - u_{i-1}^{n+1}}{2\Delta\xi}, \qquad u_{\xi\xi} \approx \frac{u_{i+1}^{n+1} - 2u_i^{n+1} + u_{i-1}^{n+1}}{(\Delta\xi)^2} \tag{6.20}$$

whereas at $\xi = 1$ we use

$$u_\xi|_{\xi=1} \approx \frac{3u_N^{n+1} - 2u_{N-1}^{n+1} + u_{N-2}^{n+1}}{2\Delta\xi}, \tag{6.21}$$

to retain second-order accuracy in space. The boundary conditions for $w$ are discretized analogously. Upon writing $s \approx s^n$ and $s_t \approx s_t^n$, the discretized form of (6.16) is a set of $2N + 2$ linear equations that can be expressed as

$$A_1^n \begin{pmatrix} \boldsymbol{u}^{n+1} \\ \boldsymbol{v}^{n+1} \end{pmatrix} = A_2^n \begin{pmatrix} \boldsymbol{u}^n \\ \boldsymbol{v}^n \end{pmatrix} - \boldsymbol{e}_1, \tag{6.22}$$

for certain matrices $A_1^n, A_2^n \in \mathbb{R}^{2(N+1)\times 2(N+1)}$ and where $\boldsymbol{e}_1 = (1, 0, ...., 0)^T \in \mathbb{R}^{2(N+1)}$ and $\boldsymbol{u}^{n+1} = (u_0^{n+1}, ..., u_N^{n+1})^T$, $\boldsymbol{v}^{n+1} = (v_0^{n+1}, ..., v_N^{n+1})^T$. To find $\boldsymbol{w}^{n+1}$ we discretize (6.17) at each grid point, using central differences in interior points and forwards/backwards differences at the boundaries. This gives a linear system for $\boldsymbol{w}^{n+1}$ of the form

$$B_1^n \boldsymbol{w}^{n+1} = B_2^n \boldsymbol{w}^n - B_3^n \boldsymbol{u}^{n+1}, \tag{6.23}$$

for certain matrices $B_1^n, B_2^n, B_3^n \in \mathbb{R}^{(N+1)\times(N+1)}$. Finally, we obtain the updated value of the position and speed of the interface by

$$s_t^{n+1} = -\beta^{-1} w_N^{n+1}, \qquad s^{n+1} = s^n + \Delta t s_t^{n+1}. \tag{6.24}$$

## 6.4 Asymptotic analysis

### 6.4.1 Asymptotic analysis of the Maxwell-Cattaneo-Stefan problem

In this section we consider (6.11) with $\eta = 0$ and perform an asymptotic analysis of the problem assuming $\gamma, \beta \gg 1$, which corresponds to a limit where memory effects are strong. In the case when $\gamma = O(1)$ and $\beta \gg 1$, we find that the leading-order solidification kinetics are identical to those predicted by Fourier's law.

We can combine Eqs. (6.11b) and (6.11a) to eliminate $Q$, which yields the hyperbolic heat equation (HHE)

$$\gamma T_{tt} + T_t = T_{xx}. \tag{6.25}$$

Mathematically, this equation describes the propagation of a temperature wave with a finite speed $\gamma^{-1/2}$. Damping is initially negligible, but appears gradually as the wave travels through the seed crystal. From a microscopic point of view, damping appears as the number of resistive collisions increases.

Heat conduction through the crystal can be split into three time regimes. The first time regime captures the propagation of the disturbance at $x = 0$ and the second time regime captures the collision of the wave against the solid-liquid interface. In the third time regime we enter a pseudo-steady state where the flux becomes a function of time and the solidification process eventually begins.

**First time regime** Due to the fact that $T = -1$ at $x = 0$ and $s(0) = 1$ we have $T, s = O(1)$. Additionally, the initial wave-like behaviour of the temperature implies $x = O(\gamma^{-1/2}t)$ and damping effects are negligible for $t \ll \gamma$. Finally, balancing terms in Eq. (6.11a) requires $Q = O(\gamma^{-1/2})$. By introducing the scaled variables defined by $t = \hat{t}$, $x = \gamma^{-1/2}\hat{x}$, $Q = \gamma^{-1/2}\hat{Q}$, $T = \hat{T}$ and $s = \hat{s}$, the Stefan condition becomes $\hat{s}_{\hat{t}} = O(\gamma^{-1/2}\beta^{-1})$, hence $\hat{s} = 1$ at leading order, which reduces the problem to

$$\hat{Q}_{\hat{t}} + \gamma^{-1}\hat{Q} = -\hat{T}_{\hat{x}}, \qquad \hat{x}, \hat{t} > 0, \tag{6.26a}$$

$$\hat{T}_{\hat{t}} + \hat{Q}_{\hat{x}} = 0, \qquad \hat{x}, \hat{t} > 0, \tag{6.26b}$$

$$\hat{T} = -1, \qquad \text{at } \hat{x} = 0, \tag{6.26c}$$

$$\hat{T} \to 0, \qquad \text{as } \hat{x} \to \infty, \tag{6.26d}$$

$$\hat{T} = \hat{Q} = 0, \qquad \text{at } \hat{t} = 0. \tag{6.26e}$$

The leading-order problem can be solved using the method of characteristics, giving $\hat{T} = -\mathcal{H}(\hat{t} - \hat{x})$ and $\hat{Q} = -\mathcal{H}(\hat{t} - \hat{x})$, where $\mathcal{H}$ is the Heaviside function. The solution therefore corresponds to a travelling wave that propagates with constant velocity. The position of the wavefront is given by $\hat{x}_f(\hat{t}) = \hat{t}$. An examination of the large-time behaviour shows that $\hat{x}_f = O(\hat{t})$ and $\hat{Q}, \hat{T} = O(1)$ as $\hat{t} \to \infty$, which determine the scales for the second time regime.

**Second time regime** By looking at the scaled system (6.26), a new balance arises for $\hat{t} = O(\gamma)$, which implies $x = O(\gamma^{1/2})$ and hence $x \gg 1$. This suggests that one should first consider the time regime where the heat wave hits the boundary, i.e., we force $x_f = O(1)$ and hence $t = O(\gamma^{1/2})$. Additionally, we have $T, s = O(1)$ and $Q = O(\gamma^{-1/2})$ in order to match to the solution in the previous time regime. In the corresponding scaled variables $\tilde{x}, \tilde{s}, \tilde{t}, \tilde{Q}$ and $\tilde{T}$, the Stefan condition becomes $\tilde{s}_{\tilde{t}} = O(\beta^{-1})$, hence we still do not have any interface motion at leading order. In these variables, the problem is similar to (6.26), with the only difference in the spatial domain,

$$\tilde{Q}_{\tilde{t}} + \gamma^{-1/2}\tilde{Q} = -\tilde{T}_{\tilde{x}}, \qquad 0 < \hat{x} < 1, \tag{6.27a}$$

$$\tilde{T}_{\tilde{t}} + \tilde{Q}_{\tilde{x}} = 0, \qquad 0 < \tilde{x} < 1, \tag{6.27b}$$

$$\tilde{T} = -1, \qquad \text{at } \tilde{x} = 0, \tag{6.27c}$$

$$\tilde{T} = 0, \qquad \text{at } \tilde{x} = 1, \tag{6.27d}$$

with $\tilde{T} \sim -\mathcal{H}(\tilde{t} - \tilde{x})$ and $\tilde{Q} \sim -\mathcal{H}(\tilde{t} - \tilde{x})$ as $\tilde{t} \sim 0$ as matching conditions.

We first solve the leading-order problem for the temperature, which satisfies the wave equation $\tilde{T}_{\tilde{t}\tilde{t}} = \tilde{T}_{\tilde{x}\tilde{x}}$ in the bulk. The matching condition corresponds to a right-moving travelling wave and satisfies the bulk equation. Thus, the solution for $0 < \tilde{t} < 1$ is given by $\tilde{T} = -\mathcal{H}(\tilde{t} - \tilde{x})$. When $\tilde{t} = 1$, this wave collides with the boundary at $\tilde{x} = 1$ and reflects. To determine the dynamics of this reflection, we shift the origin using the transformation $\tilde{x} = \tilde{x}' + 1$ and write the solution for the temperature in terms of an incoming wave $\tilde{T}_I$ and a reflected wave $\tilde{T}_R$ as $\tilde{T} = \tilde{T}_I(\tilde{t} - \tilde{x}') + T_R(\tilde{t} + \tilde{x}')$. Imposing the condition $\tilde{T} = 0$ when $\tilde{x}' = 0$ gives that $T_R = -T_I$, implying that the reflected wave destructively interferes with the incoming wave. The resulting solution for the temperature is a left-moving travelling wave given by $\tilde{T} = -\mathcal{H}(\tilde{t} + \tilde{x} - 2)$ valid for $1 < \tilde{t} < 2$. When $\tilde{t} = 2$, the wave collides with the left boundary at $\tilde{x} = 0$, again creating a reflected wave. By writing the temperature as $\tilde{T} = -1 + \tilde{T}'$, the same analysis can be used to show that the reflected wave destructively interferes with the incoming wave, resulting in a right-moving travelling wave given by $\tilde{T} = -\mathcal{H}(\tilde{t} - \tilde{x} - 2)$ for $2 < \tilde{t} < 3$. As this solution is identical (up to a translation in time) to that for $0 < \tilde{t} < 1$, the sequence of destructive reflections repeats itself. Importantly, we find that $\tilde{T} = O(1)$ for all times in this regime.

The dynamics for the flux are much more interesting and can be determined by solving (6.27a) using the known solutions for the temperature. For $0 < \tilde{t} < 1$, the flux is also a right-moving travelling wave given by $\tilde{Q} = -\mathcal{H}(\tilde{t} - \tilde{x})$. However, the collision with the boundary at $\tilde{x} = 1$ results in constructive interference. This can be seen by writing the solution for the temperature for $1 < \tilde{t} < 2$ as $\tilde{T} = \tilde{T}_I(\tilde{t} - \tilde{x}') - \tilde{T}_I(\tilde{t} + \tilde{x}')$. The corresponding solution for the flux is $\tilde{Q} = \tilde{T}_I(\tilde{t} - \tilde{x}') + \tilde{T}_I(\tilde{t} + \tilde{x}')$; thus, the right-moving incoming wave and left-moving reflected wave add in a constructive manner. We find that $\tilde{Q} = -1 - \mathcal{H}(\tilde{t} + \tilde{x} - 2)$ for $1 < \tilde{t} < 2$, corresponding to a left-moving travelling wave which takes on values between $-2$ and $-1$. Repeating the analysis shows that the collision with the boundary at $\tilde{x} = 0$ is also constructive, resulting in a solution for the flux given by $\tilde{Q} = -2 - \mathcal{H}(\tilde{t} - \tilde{x} - 2)$ for $2 < \tilde{t} < 3$, which, again, is a right-moving travelling wave. In this case, the flux ranges from $-3$ to $-2$ across $\tilde{x}$. The sequence of constructive reflections continues, each time reducing the flux by one unit. Thus, the asymptotic behaviour of the flux is given by $\tilde{Q} = O(\tilde{t})$ for $\tilde{t} \gg 1$.

Having determined the behaviour of the temperature and flux for large times, we are now in a position to determine the relevant scales for the next time regime. It turns out there are two main choices depending on the relative sizes of $\beta$ and $\gamma$. One one hand, if $\gamma \ll \beta$, a new balance in the governing equations is obtained by setting $\tilde{t} = O(\gamma^{1/2})$ and $\tilde{Q} = O(\gamma^{1/2})$,

$$\tilde{Q}_{\tilde{t}} + \tilde{Q} = -\tilde{T}_{\tilde{x}}, \tag{6.28}$$

$$\tilde{Q}_{\tilde{x}} = O(\gamma^{-1}), \tag{6.29}$$

whereas the Stefan condition becomes

$$\tilde{s}_{\tilde{t}} = O(\gamma\beta^{-1}). \tag{6.30}$$

This scaling implies that the travelling waves start to become damped, which is associated with a relaxation to the classical Fourier profiles; however, solidification has yet to begin. On the other hand, if $\gamma \gg \beta$, then we can balance both sides of the Stefan condition by setting $\tilde{t} = O(\beta^{1/2})$ and $\tilde{Q} = O(\beta^{1/2})$. In this case, the rescaled equations are

$$\tilde{Q}_{\tilde{t}} = -\tilde{T}_{\tilde{x}} + O(\gamma^{1/2}\beta^{-1/2}), \tag{6.31}$$

$$\tilde{Q}_{\tilde{x}} = O(\beta^{-1}), \tag{6.32}$$

$$\tilde{s}_{\tilde{t}} = -\tilde{Q}, \tag{6.33}$$

implying that solidification begins before the thermal waves become damped. Both of these scalings result in a quasi-steady scenario whereby the flux is uniform ($\tilde{Q}_x = 0$) and the temperature profile is linear (which is seen by differentiating the MCE with respect to $\tilde{x}$).

**Third time regime** As previously discussed, the choice of the time scale depends on the relative size of $\gamma$ to $\beta$. For simplicity, we can consider the distinguished limit where $\gamma^{-1/2}\beta^{1/2} = \alpha = O(1)$. Based on the large-time analysis of the previous time regime we take $t = O(\gamma^{1/2}\beta^{1/2})$, $Q = O(\gamma^{-1/2}\beta^{1/2})$ and $x, s, T = O(1)$. In the corresponding scaled variables $\bar{t}, \bar{x}, \bar{s}, \bar{Q}$ and $\bar{T}$, the problem becomes

$$\bar{Q}_{\bar{t}} + \alpha\bar{Q} = -\bar{T}_{\bar{x}}, \qquad 0 < \bar{x} < \bar{s}, \tag{6.34a}$$

$$\bar{Q}_{\bar{x}} = 0, \qquad 0 < \bar{x} < \bar{s}, \tag{6.34b}$$

$$\bar{T} = -1, \qquad \text{at } \bar{x} = 0, \tag{6.34c}$$

$$\bar{T} = 0, \qquad \text{at } \bar{x} = \bar{s}, \tag{6.34d}$$

$$\bar{s}_{\bar{t}} = -\bar{Q}, \qquad \text{at } \bar{x} = \bar{s}, \tag{6.34e}$$

with matching conditions given by the previous time regime. Differentiating Eq. (6.34a) with respect to $x$ gives that $T$ is linear in space and hence, applying Eqs. (6.34c) and (6.34d), we find

$$\bar{T}(\bar{t}, \bar{x}) = \frac{\bar{x}}{\bar{s}} - 1. \tag{6.35}$$

Using this expression in (6.34a) yields

$$\bar{Q}_{\bar{t}} + \alpha\bar{Q} = -\frac{1}{\bar{s}}, \tag{6.36}$$

subject to the initial condition $\bar{Q}(0) = 0$ due to the large time behaviour $\tilde{Q} \sim -\tilde{t}$ in the previous time regime. Note, for $\bar{t} \gg 1$ we find $\bar{Q} \sim -1/(\alpha\bar{s})$ and hence, using (6.34e), the classical behaviour $\bar{s} \sim \bar{t}^{1/2}$ is obtained. The reduced model given by (6.34e) and (6.36) can also be used when $\alpha \ll 1$, corresponding to the case when $\gamma \gg \beta$. From an asymptotic point of view, this case can be studied using matched asymptotic expansions in terms of $\alpha$ through the introduction of additional time and length scales.

### 6.4.2 Asymptotic analysis of the Guyer-Krumhansl-Stefan problem

As we show now, the presence of non-local effects leads to a completely different small-time behaviour of the problem. This is due to the fact that governing equations are mathematically very different in the cases $\eta = 0$ and $\eta > 0$. In the first case we obtain the HHE, which is a hyperbolic equation and describes the propagation of a heat wave, contrary to the GKHE, which is a parabolic equation. In this section we will perform an asymptotic analysis of (6.11) assuming that either memory or non-local effects are strong.

#### Enhanced memory effects

Let us assume that $\gamma \gg \eta = O(1)$, i.e. that heat transport in the seed crystal is initially dominated by memory effects. Additionally we assume $\beta \gg 1$.

The initial heat conduction through the solid can be divided into four time regimes. In the first time regime, heat conduction is described by an effective Fourier law. In the second time regime, both memory and non-local effects enter the leading-order problem, giving rise to a wave-like propagation of heat that is analogous to one-dimensional viscoelastic wave propagation. The third time regime captures the refections of the thermal waves with the boundaries. In the fourth regime, the system tends towards a quasi-steady state and solidification begins. Non-local effects are negligible but memory effects persist.

**First time regime** At the beginning of the process we have $T, s = O(1)$ due to the boundary condition at $x = 0$ and the initial condition for $s$. Assume now $t = O(\epsilon)$, where $\epsilon$

is an arbitrarily small parameter. Balancing terms in (6.11a) requires $xQ^{-1} = O(\epsilon)$. Since $\epsilon \ll 1$ and $\gamma \gg 1$, the terms $Q_t$ and $Q$ in (6.11b) cannot balance. The same happens for the terms $T_x$ and $Q_{xx}$ on the r.h.s. of (6.11b). Hence, $Q_t$ must balance either $T_x$ or $Q_{xx}$. The first case yields $x = O(\gamma^{-1}\epsilon^2)$ and $Q = O(\gamma^{-1}\epsilon)$, which would eliminate $Q_t$ from the leading order equation. Hence, the only sensible balance is given by the two non-classical contributions, which gives $x = O(\gamma^{-1/2}\epsilon^{1/2})$ and $Q = O(\gamma^{-1/2}\epsilon^{-1/2})$. In terms of the new variables defined by $T = \hat{T}$, $x = \gamma^{-1/2}\epsilon^{1/2}\hat{x}$, $s = \hat{s}$, $t = \epsilon\hat{t}$ and $Q = \gamma^{-1/2}\epsilon^{-1/2}\hat{Q}$, the Stefan condition becomes $\hat{s}_{\hat{t}} = O(\gamma^{-1/2}\beta^{-1}\epsilon^{1/2})$, thus $\hat{s} \approx 1$, and the G-K equation becomes

$$\hat{Q}_{\hat{t}} + \gamma^{-1}\epsilon\hat{Q} = -\epsilon\hat{T}_{\hat{x}} + \eta^2\hat{Q}_{\hat{x}\hat{x}}. \tag{6.37}$$

Since $\epsilon$ is arbitrarily small, the leading order problem becomes

$$\hat{Q}_{\hat{t}} = \eta^2\hat{Q}_{\hat{x}\hat{x}}, \qquad \hat{x}, \hat{t} > 0, \tag{6.38a}$$

$$\hat{T}_{\hat{t}} + \hat{Q}_{\hat{x}} = 0, \qquad \hat{x}, \hat{t} > 0, \tag{6.38b}$$

$$\hat{T} = -1, \qquad \text{at } \hat{x} = 0, \tag{6.38c}$$

$$\hat{T} = 0, \qquad \text{as } \hat{x} \to \infty, \tag{6.38d}$$

$$\hat{q} = \hat{T} = 0, \qquad \text{at } \hat{t} = 0, \tag{6.38e}$$

Equations (6.38a) and (6.38b) can be combined to give

$$\hat{Q}_{\hat{t}} = -\eta^2\hat{T}_{\hat{x}\hat{t}}, \tag{6.39}$$

from where we recover Fourier's law after integrating with respect to time and applying Eq. (6.38e). The problem is therefore equivalent to a classical heat conduction problem in a semi-infinite domain with an effective thermal conductivity $\eta^2$. As suggested by the fact that the length scale has remained undetermined, this problem admits a solution in terms of a similarity variable $\hat{y} = \hat{x}/\sqrt{\hat{t}}$. In terms of the original non-dimensional variables, the solution takes the form

$$T(x,t) = \operatorname{erf}\left(\frac{x}{2\sqrt{\zeta t}}\right) - 1, \qquad Q(x,t) = -\sqrt{\frac{\zeta}{\pi t}}\exp\left(-\frac{x^2}{4\zeta t}\right), \tag{6.40}$$

where $\zeta = \eta^2/\gamma$.

**Second time regime** Equation (6.37) indicates that the previous time regime breaks down for $t = O(1)$, since the term $T_x$ enters the leading order problem. From the previous time regime we find $x, Q = O(\gamma^{-1/2})$, whereas $s, T = O(1)$. Upon defining the new variables $T = \tilde{T}$, $x = \gamma^{-1/2}\tilde{x}$, $s = \tilde{s}$, $t = \tilde{t}$ $q = \gamma^{-1/2}\tilde{q}$, we obtain again $\tilde{s}_{\tilde{t}} = O(\gamma^{-1/2}\beta^{-1})$, hence $\tilde{s} \approx 1$, and

$$\tilde{T}_{\tilde{t}} + \tilde{Q}_{\tilde{x}} = 0, \qquad \tilde{x}, \tilde{t} > 0, \tag{6.41a}$$

$$\tilde{Q}_{\tilde{t}} = -\tilde{T}_{\tilde{x}} + \eta^2 \tilde{Q}_{\tilde{x}\tilde{x}}, \qquad \hat{x}, \hat{t} > 0, \tag{6.41b}$$

$$\tilde{T} = -1, \qquad \text{at } \tilde{x} = 0, \tag{6.41c}$$

$$\tilde{T} = 0, \qquad \text{as } \tilde{x} \to \infty. \tag{6.41d}$$

By eliminating the flux $\tilde{Q}$, we find that the temperature satisfies a linear viscoelastic equation given by

$$\tilde{T}_{\tilde{t}\tilde{t}} = \tilde{T}_{\tilde{x}\tilde{x}} + \eta^2 \tilde{T}_{\tilde{x}\tilde{x}\tilde{t}}, \tag{6.42}$$

with the additional condition that $\tilde{T}_{\tilde{t}}(\tilde{x}, 0) = 0$. The large-time limit of (6.42) implies that the solution for the temperature is given by a right-moving travelling wave that has an interior, moving boundary layer located at $\tilde{x} = \tilde{t}$ that captures weak non-local ("viscous") effects. The solution for the temperature for $\tilde{x} = O(\tilde{t})$ with $\tilde{t} \gg 1$ can be written as

$$\tilde{T}(\tilde{x}, \tilde{t}) = \begin{cases} \tilde{T}_{\text{up}}(\tilde{x} - \tilde{t}), & \tilde{x} < \tilde{t}, \\ \tilde{T}_{\text{inner}}(\tilde{x}, \tilde{t}), & \tilde{x} - \tilde{t} = O(1), \\ \tilde{T}_{\text{down}}(\tilde{x} - \tilde{t}), & \tilde{t} < \tilde{x}, \end{cases} \tag{6.43}$$

where the upstream and downstream solutions $\tilde{T}_{\text{up}}$ and $\tilde{T}_{\text{down}}$ are, in principle, obtained by matching to the solution for $O(1)$ times and the inner solution in the boundary layer is

$$\tilde{T}_{\text{inner}} = \frac{1}{2}(\tilde{T}_{\text{up}}(0) + \tilde{T}_{\text{down}}(0)) + \frac{1}{2}(\tilde{T}_{\text{down}}(0) - \tilde{T}_{\text{up}}(0))\text{erf}\left(\frac{\tilde{x} - \tilde{t}}{2^{1/2}\eta\tilde{t}^{1/2}}\right). \tag{6.44}$$

This solution reveals that the temperature will remain $O(1)$ in size for large times. The large-time approximation to the flux can be obtained via (6.41a) and shown to remain $O(1)$ in size for large times as well. The boundary layer at $\tilde{x} = \tilde{t}$ acts as the diffuse wavefront of the propagating thermal wave.

**Third time regime** This time regime is analogous to the second time regime of the MC case, in which thermal waves propagate and collide with the boundaries of the crystal. The first collision occurs at the right boundary when $t = \gamma^{1/2}$. Therefore, in this time regime we choose a length scale of $x = O(1)$ and a time scale of $t = O(\gamma^{1/2})$. The heat flux has not changed in magnitude, therefore we choose a flux scale of $Q = O(\gamma^{-1/2})$ as in the previous time regime. Additionally, we have $s, T = O(1)$. In terms of the corresponding scaled variables $\bar{x}, \bar{s}, \bar{t}, \bar{Q}$ and $\bar{T}$, the Stefan condition takes the form $\bar{s}_{\bar{t}} = O(\beta^{-1})$ and hence $\bar{s} \approx 1$, which leads to the problem

$$\bar{T}_{\bar{t}\bar{t}} + \gamma^{-1/2}\bar{T}_{\bar{t}} = \bar{T}_{\bar{x}\bar{x}} + \eta^2\gamma^{-1/2}\bar{T}_{\bar{x}\bar{x}\bar{t}}, \qquad 0 < \bar{x} < 1, \tag{6.45a}$$

$$\bar{T}_{\bar{t}} + \bar{Q}_{\bar{x}} = 0, \qquad 0 < \bar{x} < 1, \tag{6.45b}$$

$$\bar{T} = -1, \qquad \text{at } \bar{x} = 0, \tag{6.45c}$$

$$\bar{T} = 0, \qquad \text{at } \bar{x} = \bar{1}, \tag{6.45d}$$

where the flux has been eliminated from the GKE to produce (6.45a). Naively taking $\gamma \to \infty$ in the GKHE (6.45a) shows that the temperature satisfies the same leading-order problem as in the second time regime of the MC case and thus we can expect similar wave propagation and destructive interference to occur. The main difference is that non-local effects will influence the temperature and flux profiles near the wavefront. Remarkably, they do not influence the reflection dynamics to leading order.

We first consider the dynamics that occur before the thermal wave collides with the right boundary ($0 < \bar{t} < 1$). The leading-order solutions for the temperature and flux can be constructed using matched asymptotic expansions and are found to be given by $\bar{T}(\bar{x}, \bar{t}) = \mathcal{F}(\bar{x}, \bar{t})$ and $\bar{Q}(\bar{x}, \bar{t}) = \mathcal{F}(\bar{x}, \bar{t})$ where

$$\mathcal{F}(\bar{x}, \bar{t}) \equiv \frac{1}{2}\,\mathrm{erf}\left(\frac{\gamma^{1/4}(\bar{x} - \bar{t})}{2^{1/2}\eta\bar{t}^{1/2}}\right) - \frac{1}{2}. \tag{6.46}$$

Equation (6.46) is analogous to the Heaviside function that was found in the second time regime of the MC case, but it now accounts for the diffuse nature of the wave front which has a finite width of $O(\gamma^{-1/4}\eta t^{1/2})$.

To understand the dynamics of the reflection that occurs at $\bar{x} = 1$ when $\bar{t} = 1$, we write $\bar{x} = 1 + \eta^2\gamma^{-1/2}\bar{x}'$ and $\bar{t} = 1 + \eta^2\gamma^{-1/2}\bar{t}'$ so that the temperature now satisfies $\bar{T}_{\bar{t}'\bar{t}'} = \bar{T}_{\bar{x}'\bar{x}'} + \bar{T}_{\bar{x}'\bar{x}'\bar{t}'}$. The bulk equation admits wave solutions of the form $\bar{T} \sim \mathrm{e}^{i(k\bar{x}' - \omega\bar{t}')}$, where $\omega = \pm(ik/2)[k + (k^2-4)^{1/2}]$. Since $\omega$ is complex for wavenumbers that satisfy $k < 2$, these short-wave modes are attenuated during wave propagation. By considering a single wave mode, writing the temperature as an incoming and reflected wave, $\bar{T} = \bar{T}_I \mathrm{e}^{i(k\bar{x}'-\omega\bar{t}')} + \bar{T}_R \mathrm{e}^{i(-kx-\omega\bar{t}')}$, and applying the boundary condition $\bar{T} = 0$ when $\bar{x}' = 0$, we find that $\bar{T}_R = -\bar{T}_I$. That is, the reflected wave has the same amplitude as the incoming wave but opposite sign, leading to destructive interference again. Moreover, non-local effects to not alter the amplitude of the reflected wave. By considering a single-mode wave solution for the flux, we find from conservation of energy that $\bar{Q} = (\omega/k)[\bar{T}_I \mathrm{e}^{i(k\bar{x}'-\omega\bar{t}')} + \bar{T}_I \mathrm{e}^{i(-k\bar{x}'-\omega\bar{t}')}]$. Therefore, the reflection of the flux wave leads to the same constructive interference as before.

Using the superposition principle, the solutions for the temperature and flux after the first reflection, but before the second reflection with the left boundary, can be written as

$$\bar{T} = \mathcal{F}(\bar{x}, \bar{t}) - \mathcal{F}(2 - \bar{x}, \bar{t}), \tag{6.47a}$$

$$\bar{Q} = \mathcal{F}(\bar{x}, \bar{t}) + \mathcal{F}(2 - \bar{x}, \bar{t}), \tag{6.47b}$$

for $1 < \bar{t} < 2$. In fact, since the second terms of (6.47) are exponentially small for $\bar{t} < 1$, these expressions are valid for $0 < \bar{t} < 2$. By further exploiting the asympototic limits of the function $\mathcal{F}$, the solution for times given by $0 < \bar{t} < 2N$, where $N$ is an integer, is given by

$$\bar{T}(\bar{x}, \bar{t}) = \sum_{n=0}^{N-1} \left[\mathcal{F}(\bar{x} + 2n, \bar{t}) - \mathcal{F}(2(n+1) - \bar{x}, \bar{t})\right], \tag{6.48a}$$

$$\bar{Q}(\bar{x}, \bar{t}) = \sum_{n=0}^{N-1} \left[\mathcal{F}(\bar{x} + 2n, \bar{t}) + \mathcal{F}(2(n+1) - \bar{x}, \bar{t})\right]. \tag{6.48b}$$

Physically, the expression in (6.48) can be interpreted as a collection of right- and left- moving travelling waves, each of which has a diffuse wavefront that broaden in time according to a $O(t^{1/2})$ scaling law. From these solutions we can deduce that $\bar{T} = O(1)$ and $\bar{Q} = O(\bar{t})$ as $\bar{t} \to \infty$.

We are now in a position to determine the next time regime using the asymptotic behaviour of the temperature and flux for large $\bar{t}$. Using the current scaling, the GKE can be written as $\bar{Q}_{\bar{t}} + \gamma^{-1/2}\bar{Q} = -\bar{T}_{\bar{x}} + \eta^2\gamma^{-1/2}\bar{Q}_{\bar{x}\bar{x}}$, indicating that the second term on the left-hand side becomes relevant when $\bar{t} = O(\gamma^{1/2})$. Alternatively, balancing both terms in the Stefan condition implies that solidification will occur when $\bar{t} = O(\beta^{1/2})$. The choice of the time scale will therefore depend on the relative size $\gamma$ to $\beta$.

**Fourth time regime** We consider the distinguished limit where $\gamma^{-1/2}\beta^{1/2} = \alpha = O(1)$. We choose $t, Q = O(\gamma^{1/2}\beta^{1/2})$, whereas $x, s, T = O(1)$. In the new variables $\check{x}, \check{s}, \check{t}, \check{Q}$ and $\check{T}$, the leading order problem takes the form

$$\check{Q}_{\check{t}} + \alpha\check{Q} = -\check{T}_{\check{x}}, \qquad 0 < \check{x} < \check{s}, \tag{6.49a}$$

$$\check{Q}_{\check{x}} = 0, \qquad 0 < \check{x} < \check{s}, \tag{6.49b}$$

$$\bar{T} = -1, \qquad \text{at } \bar{x} = 0, \tag{6.49c}$$

$$\bar{T} = 0, \qquad \text{at } \bar{x} = \bar{s}, \tag{6.49d}$$

$$\check{s}_{\check{t}} = -\check{Q}, \qquad \text{at } \bar{x} = \bar{s}, \tag{6.49e}$$

with matching conditions provided by the previous time regime. This system is analogous to (6.34) and hence the GKE has effectively reduced to the MCE, since non-local effects have become negligible. Interestingly, this has happened before the solidification process has begun.

### Enhanced non-local effects

Here we assume $\beta, \eta^2 \gg \gamma = O(1)$, therefore non-local effects are the dominant non-classical feature of heat transport. There are three time regimes to consider. The first time regime captures the initial heat flux through the seed crystal described by an effective form of Fourier's law. In the second time regime, both memory and non-local terms enter the leading-order problem; however, unlike the case of enhanced memory effects where the temperature satisfied a viscoelastic wave equation, now the problem is quasi-steady and the temperature profile is linear. Solidification begins in the second time regime but eventually terminates due to the diminishing influence of the non-classical conduction mechanisms that drive phase change. In the third time regime, the classical contribution to the flux from temperature gradients becomes dominant, allowing solidification to restart.

**First time regime** We consider heat flow across the entire seed crystal and take $x = O(1)$. Since $T = O(1)$, conservation of energy implies that $Q = O(t)$. The only sensible balance in

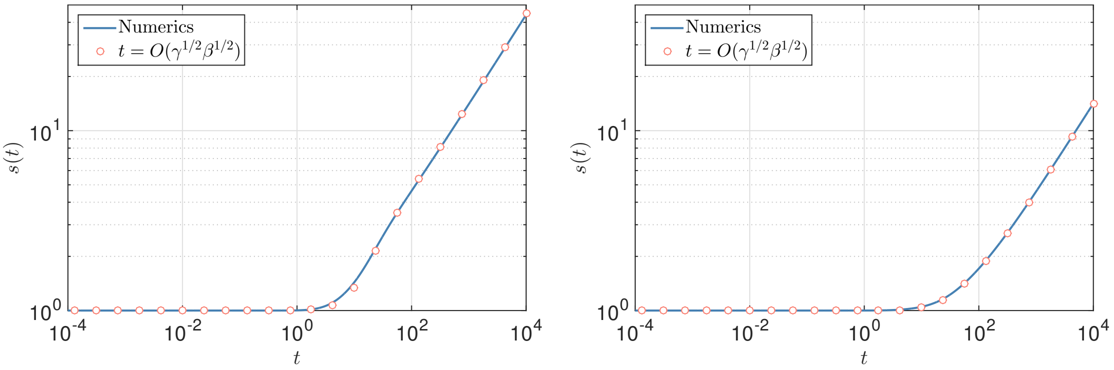

**(a)** $\gamma = 10, \beta = 10.$ **(b)** $\gamma = 10,\ \beta = 100.$

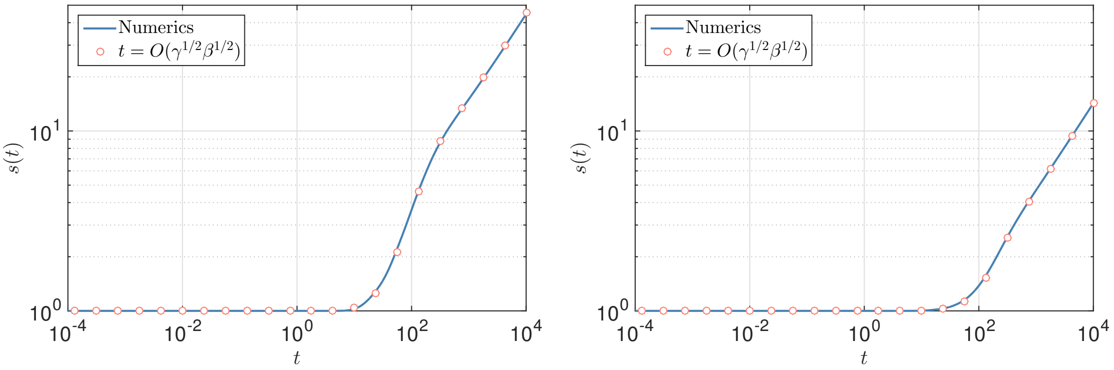

**(c)** $\gamma = 100, \beta = 10.$ **(d)** $\gamma = 100,\ \beta = 100.$

**Figure 6.1:** Evolution of the interface for different values of $\beta$ and $\gamma$, according to numerical simulation and the solution of the ODE in the fourth time regime. The dimensionless mean free path has been set to unity.

Eq. (6.11b) is obtained by balancing the non-classical contributions, which gives $t = O(\eta^{-2})$. Defining $T = \hat{T}$, $x = \hat{x}$, $s = \hat{s}$, $t = \eta^{-2}\hat{t}$ $Q = \eta^2\hat{Q}$ we find $\hat{s}_{\hat{t}} = O(\beta^{-1})$ and thus solidification is negligible at leading order. Upon neglecting terms of order $\eta^{-4}$, the remaining equations become

$$\gamma\hat{Q}_{\hat{t}} + \eta^{-2}\hat{Q} = \hat{Q}_{\hat{x}\hat{x}}, \qquad 0 < \hat{x} < 1,\ \hat{t} > 0, \tag{6.50a}$$

$$\hat{T}_{\hat{t}} + \hat{Q}_{\hat{x}} = 0, \qquad 0 < \hat{x} < 1,\ \hat{t} > 0, \tag{6.50b}$$

$$\hat{T} = -1, \qquad \text{at } \hat{x} = 0, \tag{6.50c}$$

$$\hat{T} = 0, \qquad \text{at } \hat{x} = 1, \tag{6.50d}$$

$$\hat{Q} = \hat{T} = 0, \qquad \text{at } \hat{t} = 0, \tag{6.50e}$$

We can combine (6.50b) and (6.50a) to obtain (after neglecting the $O(\eta^{-2})$ term)

$$\gamma \hat{Q}_{\hat{t}} = -\hat{T}_{\hat{x}\hat{t}}, \tag{6.51}$$

from where we recover Fourier's law. The problem is therefore equivalent to a classical heat conduction problem in the unit interval and with an effective thermal conductivity $\gamma^{-1}$. The large-time solution for the temperature is $\hat{T} \sim \hat{x} - 1$, whereas $\hat{Q} \sim -\gamma^{-1}$.

There are two possible choices for the next time regime. On one hand, for $\hat{t} = O(\beta)$ the terms in the Stefan condition balance and the solidification enters the leading order problem. On the other hand, a new balance in (6.50a) is obtained for $\hat{t} = O(\eta^2)$. The choice of the next time scale therefore depends on the relative size of $\eta^2$ to $\beta$. However, notice that (6.50b) reduces to $\hat{Q}_{\hat{x}} \sim 0$ for either choice and hence the pseudo-steady state is reached before solidification begins.

**Second time regime** As discussed previously, the choice of the time scale depends on the relative size of $\eta^2$ to $\beta$. Let us consider the distinguished limit $\beta\eta^{-2} =: \alpha = O(1)$ and choose $t = O(\alpha)$. From the previous time regime we have $Q = O(\eta^2)$ and $x, s, T = O(1)$. In the corresponding scaled variables $T = \tilde{T}$, $x = \tilde{x}$, $s = \tilde{s}$, $t = \alpha\tilde{t}$ and $Q = \eta^2\tilde{Q}$, the Stefan condition becomes

$$\tilde{s}_{\tilde{t}} = -\tilde{Q}, \qquad \text{at } \tilde{x} = \tilde{s}, \tag{6.52}$$

and, upon neglecting terms of order $\eta^{-2}$, the remaining equations take the form

$$\gamma\tilde{Q}_{\tilde{t}} + \alpha\tilde{Q} = -\tilde{T}_{\tilde{x}\tilde{t}}, \qquad 0 < \tilde{x} < \tilde{s}, \tag{6.53a}$$

$$\tilde{Q}_{\tilde{x}} = 0, \qquad 0 < \tilde{x} < \tilde{s}, \tag{6.53b}$$

$$\tilde{T} = -1, \qquad \text{at } \tilde{x} = 0, \tag{6.53c}$$

$$\tilde{T} = 0, \qquad \text{at } \tilde{x} = \tilde{s}. \tag{6.53d}$$

Taking derivatives with respect to $\tilde{x}$ in (6.53a) yields $\tilde{T}_{\tilde{x}\tilde{x}\tilde{t}} = 0$. Additionally, from the previous time regime we have the matching condition $\tilde{T}_{\tilde{x}\tilde{x}} \sim 0$ for $\tilde{t} = O(\beta^{-1})$, therefore $\tilde{T}_{\tilde{x}\tilde{x}} = 0$ and hence, applying the boundary conditions,

$$\tilde{T}(\tilde{x}, \tilde{t}) = \frac{\tilde{x}}{\tilde{s}} - 1, \tag{6.54}$$

which reduces (6.53a) to

$$\gamma \tilde{Q}_{\tilde{t}} + \alpha \tilde{Q} = \frac{\tilde{s}_{\tilde{t}}}{\tilde{s}^2}. \tag{6.55}$$

Using (6.52) and the fact that $\tilde{Q}_{\tilde{t}} = (\partial \tilde{Q}/\partial \tilde{s})\tilde{s}_{\tilde{t}}$ we find that $\tilde{Q}$ is given by

$$\tilde{Q}(\tilde{s}) = -\gamma^{-1}\left[\frac{1}{\tilde{s}} + \alpha(1-\tilde{s})\right], \tag{6.56}$$

where we have applied the matching condition $\tilde{Q} \sim -\gamma^{-1}$ and $\tilde{s} \sim 1$ for $\tilde{t} = O(\beta^{-1})$. Replacing $\tilde{Q}$ in (6.52) by this expression yields

$$\tilde{s}_{\tilde{t}} = \gamma^{-1}\left[\frac{1}{\tilde{s}} + \alpha(1-\tilde{s})\right]. \tag{6.57}$$

In particular, we observe that the initial solidification kinetics are similar to those predicted by the classical formulation, since $\tilde{s} \sim 1$ for $\tilde{t} \ll 1$ and hence $\tilde{s}_{\tilde{t}} \sim 1/(\gamma\tilde{s})$. In the original dimensionless variables we have $s_t = O(\eta^2)$, which indicates that non-local effects accelerate the solidification process. Interestingly, as the solid grows into the liquid, we find $\tilde{s}_{\tilde{t}} \to 0$ as $\tilde{s} \to (1+\sqrt{1+4\alpha^{-1}})/2 = \tilde{s}_0$ and therefore $\tilde{Q} \to 0$ as the interface approaches this value. Hence, the problem becomes stationary at the end of this regime and the interface tends to the value $\tilde{s}_0 = O(1)$. However, as the flux decreases and the time increases, the term $T_x$ enters the leading order problem and solidification starts again. The only possible balance for $\tilde{Q} \ll 1$ and $\tilde{t} \gg 1$ is when $\tilde{Q} = O(\eta^{-2})$ and $\tilde{t} = O(\eta^2)$, which also keeps the terms in the Stefan condition balanced, allowing solidification to start again as we enter the next regime.

**Third time regime** From the previous time regime we have $t = O(\beta)$ and $s, x, T, Q = O(1)$. Introducing the scaled variables $\bar{t}, \bar{x}, \bar{s}, \bar{T}, \bar{Q}$, the equations become

$$\bar{Q} = -\bar{T}_{\bar{x}} - \alpha^{-1}\bar{T}_{\bar{x}\bar{t}}, \qquad 0 < \bar{x} < \bar{s}, \tag{6.58a}$$

$$\bar{Q}_{\bar{x}} = 0, \qquad 0 < \bar{x} < \bar{s}, \tag{6.58b}$$

$$\bar{T} = -1, \qquad \text{at } \bar{x} = 0, \tag{6.58c}$$

$$\bar{T} = 0, \qquad \text{at } \bar{x} = \bar{s}, \tag{6.58d}$$

$$\bar{s}_{\bar{t}} = -\bar{Q}, \qquad \text{at } \bar{x} = \bar{s}. \tag{6.58e}$$

Upon differentiating (6.58a) with respect to $\bar{x}$ gives $\alpha\bar{T}_{\bar{x}\bar{x}} + \bar{T}_{\bar{x}\bar{x}\bar{t}} = 0$. Since the temperature profile $\bar{T}$ is linear in the previous time regime we find $\bar{T}_{\bar{x}\bar{x}} = 0$ and hence

$$\bar{T}(\bar{x}, \bar{t}) = \frac{\bar{x}}{\bar{s}} - 1. \tag{6.59}$$

Thus, the flux is given by

$$\bar{Q}(\bar{t}) = -\frac{1}{\bar{s}} + \frac{\bar{s}_{\bar{t}}}{\alpha \bar{s}^2}, \tag{6.60}$$

and hence $\bar{s}$ is determined by

$$\bar{s}_{\bar{t}} = \frac{\alpha \bar{s}}{1 + \alpha \bar{s}^2}. \tag{6.61}$$

In particular, we find $\bar{s}_{\bar{t}} \sim \bar{s}^{-1}$ for $\bar{t} \gg 1$, recovering so the classical solidification kinetics by the end of this time regime. The solution to (6.61) can be given implicitly,

$$\frac{1}{\alpha}\log(\bar{s}) + \frac{1}{2}\bar{s}^2 = \bar{t} + \bar{C} \tag{6.62}$$

or in terms of the LambertW function,

$$\bar{s}(\bar{t}) = \sqrt{\frac{1}{\alpha} W\left(\alpha e^{2\alpha(\bar{t}+\bar{C})}\right)}. \tag{6.63}$$

The value of $C$ is found by imposing $\bar{s} \sim \tilde{s}_0$ for $\bar{t} = O(\eta^{-2})$ we find that $\bar{C} = \tilde{s}_0^2/2 + \alpha^{-1}\log \tilde{s}_0$.

As suggested by the large-time behaviour of (6.61), the classical dynamics are recovered in the fourth time regime, given by $\bar{x}, \bar{s} \sim \bar{t}^{1/2}$, $\bar{Q} \sim \bar{t}^{-1/2}$ and $\bar{t} = O(\eta^2)$.

## 6.5 Reduced formulation

As shown in the asymptotic analysis in the Sec. 6.4, by the time that solidification occurs, the heat flux becomes approximately uniform in space: $Q_x \simeq 0$. This leads to the so-called quasi-steady regime, since differentiating the GKE (6.11b) with respect to $x$ then leads to $T_{xx} \simeq 0$ and hence time is present only due to the boundary condition (6.12b). This quasi-steady regime also appears in the classical formulation under the assumption $\beta \gg 1$, allowing the system to be reduced to a simple ordinary differential equation (ODE) for the position of the interface [64]. Our asymptotic analysis reveals that a similar procedure can be considered here even in the case of strongly non-classical effects. Applying the boundary conditions (6.12a) and (6.12b) implies that the temperature is given by

$$T(x,t) = \frac{x}{s} - 1. \tag{6.64}$$

Upon using (6.64) in (6.13), and then (6.12c) to eliminate the arising term with $s_t$, yields

$$Q_t = -\gamma^{-1}\left[\frac{1}{s} + \left(\frac{\eta^2}{\beta s^2} + 1\right) Q\right]. \tag{6.65}$$

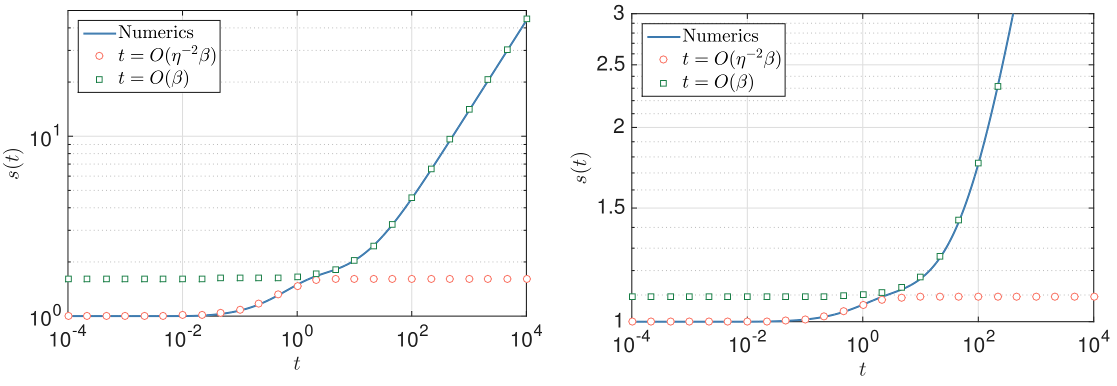

**(a)** $\eta^2 = 10, \beta = 10$. **(b)** $\eta^2 = 10$, $\beta = 100$.

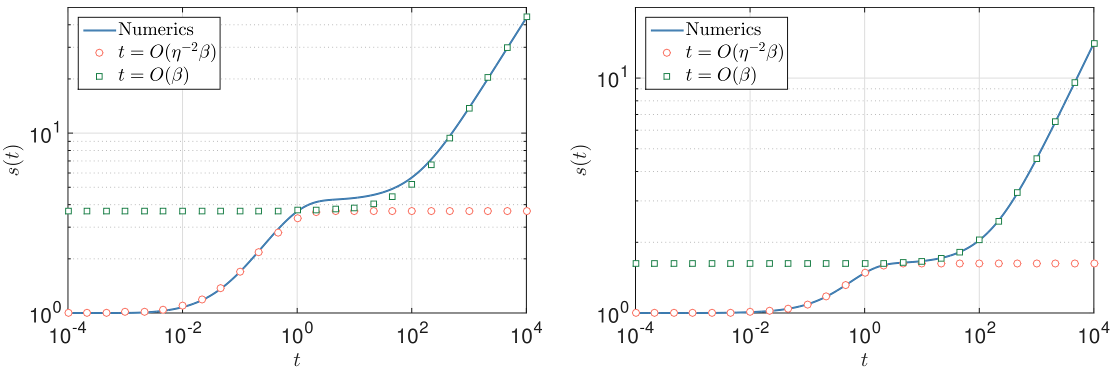

**(c)** $\eta^2 = 100, \beta = 10$. **(d)** $\eta^2 = 100$, $\beta = 100$.

**Figure 6.2:** Evolution of the interface for different values of $\beta$ and $\eta^2$, according to numerical simulation and the solutions of the second and third time regimes. The dimensionless mean free time has been set to unity.

The asymptotic analysis shows that the appropriate matching condition is given by

$$Q(0) = -\eta^2/\gamma. \tag{6.66}$$

Note, this initial condition is valid for both the Guyer-Krumhansl and Maxwell-Cattaneo models, since the limit $\eta \to 0$ gives the initial condition $Q(0) = 0$ which corresponds to the small time behaviour of the MC-Stefan problem. Hence, based on the asymptotic analysis we are able to reduce a problem involving two partial differential equations in a growing domain into a pair of coupled ordinary differential equations (6.12c) and (6.65).

## 6.6 Results and discussion

We are now in position to compare the different solidification kinetics in the limits of dominant non-classical effects and to assess the validity of the reduced formulation. Afterwards we apply the results to the solidification of silicon using the parameter values discussed in Sec. 6.2.4.

To compare the classical and non-classical heat conduction models, it will be insightful to consider the mean flux $\langle Q\rangle$, defined by

$$\langle Q\rangle = \frac{1}{s}\int_0^s Q\,dx\,. \tag{6.67}$$

Note, this quantity is uniform in space and, moreover, it coincides with the heat flux $Q$ when the temperature enters in the quasi-steady regime.

### 6.6.1 MC conduction with enhanced memory

For $\gamma, \beta \gg 1$ with $\gamma = O(\beta)$ or larger, the asymptotic analysis shows that we can split the solidification process into three time regimes. The first time regime occurs when $t = O(1)$ and captures the initial propagation of a heat wave from the cooled boundary into the seed crystal. The second time regime, $t = O(\gamma^{1/2})$, describes the transport of heat across the entirety of the seed crystal. This regime also captures the reflections of thermal waves that occur when they collide with the boundaries of the crystal. We find that the temperature waves destructively interfere, thus keeping the temperature $O(1)$ in size. However, the flux waves undergo constructive interference and thus the magnitude of the flux scales like $O(t)$. Due to the large Stefan number, no appreciable solidification occurs during the first and second time regimes. In the third time regime, $t = O(\gamma^{1/2}\beta^{1/2})$, the temperature settles into its quasi-steady (linear) profile and solidification begins. Memory effects are relevant during the initial stages of solidification but diminish with time until Fourier's law is recovered. If $\gamma \gg 1$ but $\gamma \ll \beta$, then memory effects diminish before solidification begins.

Figure 6.3 shows the solidification kinetics and evolution in time of the mean flux for different values of $\gamma$. Solid lines correspond to numerical simulations, whereas circles refer to the solutions of the reduced formulation. The results are shown for $\beta = 10$. Since the asymptotic analysis reveals that for $\gamma \ll \beta$ non-classical effects become negligible by

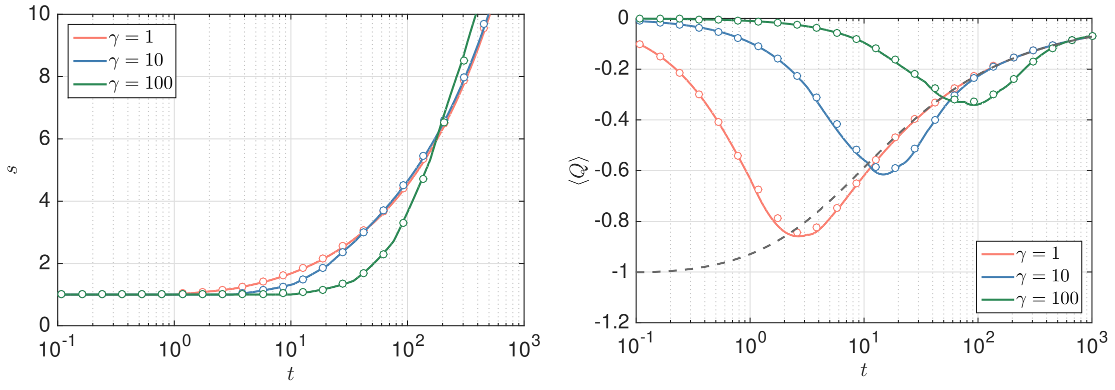

**(a)** **(b)**

**Figure 6.3:** Evolution of the solid-liquid interface and the mean flux according to the MCE for $\beta = 10$ and different values of the Cattaneo number $\gamma$. Solid lines refer to the numerical solutions of the MC-model, whereas circles represent the solutions to the quasi-steady formulation. The dashed line in panel (b) represents the mean flux according to Fourier's law.

the time the solid starts growing, the case $\gamma = 0$ is not shown in Fig. 6.3 (a), as it is indistinguishable from the case $\gamma = 1$. However, the mean flux for the $\gamma = 0$ case is shown in Fig. 6.3 (b), where it can be clearly observed how the limit $\gamma \to 0$, i.e. the Fourier case, represents a singular limit of the problem. In all cases, the agreement between the numerical simulations and the solutions of the reduced model is excellent. Simulations for larger values of $\beta$ (not shown here) also provide excellent agreement between both methods.

In Fig. 6.3 (a) we can see how the start of the solidification process is delayed as $\gamma$ increases. This is caused by the fact that, for large values of $\gamma$, heat propagates in the form of a thermal waves with finite speed $\gamma^{-1/2}$ for a longer period and solidification begins after the wave hits the right extreme of the seed crystal when $t = O(\gamma^{1/2})$. The asymptotic analysis reveals that solidification begins when $t = O(\gamma^{1/2}\beta^{1/2})$. Hence, for $\gamma = 10$ and $\gamma = 100$, solidification begins when $t \approx 10$ and $t \approx 32$ respectively, which is confirmed in Fig. 6.3 (a). The case $\gamma = 100$ shows an interesting evolution of the interface. On one hand, the start of the interface motion is delayed due to the slower speed of the thermal wave through the crystal. On the other hand, the long-term rate of solidification is higher than for smaller values of $\gamma$ due to the delayed increase of the flux, which reaches its largest value when $t = O(\gamma)$, where its value is larger than the flux corresponding to smaller relaxation times. In this sense, solidification begins later as we increase $\gamma$, but the long-term solidification rate is larger until the classical solidification kinetics, where $s \sim t^{1/2}$, are recovered.

In Fig. 6.3 (a) we observe that, as $\gamma$ decreases, the flux converges earlier to the profile described by the classical formulation. As $\gamma$ increases, the initial MC flux decreases, in accordance with the fact that $Q = O(\gamma)$ for early times. The decrease in the mean flux from its initial value of zero is due to the repeating sequence of constructive wave reflections that occurs at the boundaries of the solid. As $\gamma$ decreases and the thermal-wave speed increases, these reflections occur more frequently, thereby leading to a more rapid decrease in the mean flux. The Fourier case can therefore be interpreted as a limit whereby these reflections occur infinitely frequently, leading to an instantaneous jump in the mean flux from its initial value of zero. The asymptotic analysis also reveals an increase of the flux for $t \gg \gamma^{1/2}$, with the order of magnitude being proportional to $(\beta/\gamma)^{1/2}$. This can be observed in Fig. 6.3 (b) and agrees with the asymptotic analysis.

### 6.6.2 GK conduction with enhanced memory

We now assume that $\gamma, \beta \gg 1$ with $\eta = O(1)$. The asymptotic analysis reveals there are four time regimes. When $t \ll 1$, Fourier's law is recovered with a small effective thermal conductivity (ETC) defined by $\zeta = \eta^2/\gamma$. Changes in the temperature and flux from their initial values only occur in a thin layer near $x = 0$. When $t = O(1)$, heat propagates towards the liquid as a wave. The form of this wave is analogous to a viscoelastic pressure wave. Contrary to the MC case, here the wavefront (with position given by $x_f(t)$) is not sharp but diffuse with a (dimensionless) width that scales like $w = O(\zeta^{1/2}t^{1/2})$. When $t = O(\gamma^{1/2})$ we find that the thermal and flux waves undergo a sequence of reflections at the boundaries of the solid that is analogous to the MC case, where now the width of the diffuse wavefront continuously increases. The choice of the fourth time regime depends on the relative size of $\gamma$ to $\beta$. In all cases, non-local effects become negligible, solidification begins, and the dynamics become analogous to the third time regime of the MC case.

The evolution in time of the solid-liquid interface and the mean flux is shown in Fig. 6.4 for different values of $\gamma$. The mean flux corresponding to the Fourier model is also shown (dashed, gray line). The remaining dimensionless parameters have been set to $\eta = 1$ and $\beta = 10$. In addition, we have plotted the case $\gamma = 1$, which reproduces the classical

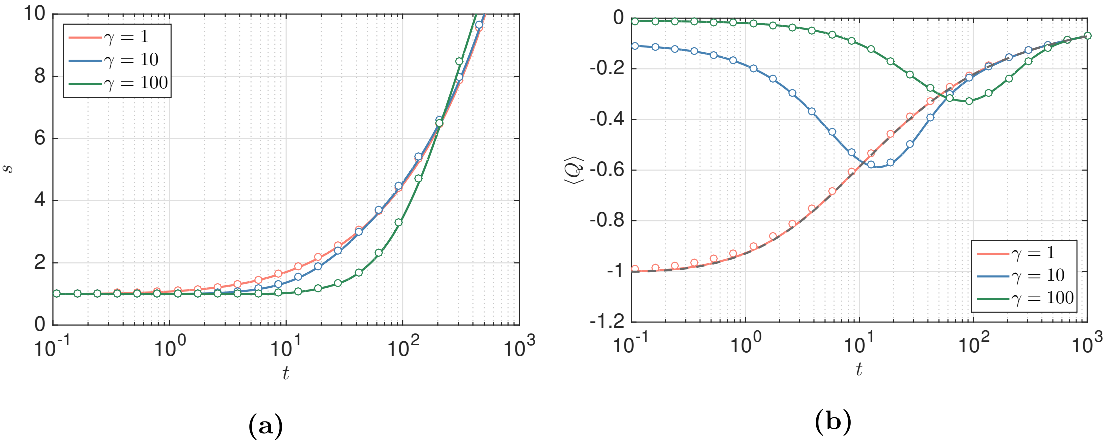

**(a)** **(b)**

**Figure 6.4:** Evolution of the solid-liquid interface and the mean flux according to the GKE in the limit of large memory effects. The remaining dimensionless parameters are $\eta = 1$ and $\beta = 10$. Solid lines refer to the numerical solutions of the GK-model, whereas circles represent the solutions to the quasi-steady formulation. The dashed line in panel (b) represents the mean flux according to the classical formulation.

solidification kinetics due to the Fourier resonance phenomenon, as shown by the perfect match of the corresponding fluxes in Fig. 6.4 (b). Similarly to the MC case, we note that the agreement between the numerical simulations and the solutions of the reduced model is remarkable.

By comparing Figs. 6.3 (a) and 6.4 (a), it can be observed that the solidification kinetics in the GK case are very similar to those in the MC case. This was already anticipated by the asymptotic analysis, which predicts that non-local effects become negligible by the time solidification begins. In fact, the key differences between the MC and GK formulations with large relaxation times do not appear in the solidification process, since it is essentially captured by the same equations (see third and fourth time regimes of Secs. 6.4.1 and 6.4.2 respectively), but in the initial conduction through the crystal, as can be observed by comparing Figs. 6.3 (b) and 6.4 (b). However, notice that these initial differences between the MC and GK formulations disappear for $t = O(\gamma^{1/2}\beta^{1/2})$ and hence both fluxes coincide by the time solidification begins. The different behaviour for smaller times is caused by the different underlying physics in each model. The MCE predicts a wave-like heat propagation through the crystal, whereas the GKE initially recovers Fourier's law with an effective thermal conductivity $\zeta$. In the case of Fourier resonance, the ETC becomes $\zeta = 1$ and it coincides with the bulk thermal conductivity.

As revealed by the asymptotic analysis, the flux in this specific limit of the GK model is very similar to the MC model and differences appear only for small times. The evolution of the flux profiles for the MC and GK cases is shown in Fig. 6.5. To clearly illustrate the wave-like propagation of heat in the MC and GK models, we increase $\gamma$ to 100 in both cases, using $\eta = 1$ for the GK case, and fix $\beta = 10$ as before. We can observe that differences in both formulations indeed appear only for small times and in the way the moving wave front $x_f(t)$ evolves in time. The right panels in Fig. 6.5 show the time regimes when heat propagates in the form of thermal waves. A sharp wavefront moving at a speed $\gamma^{1/2}$ can be clearly observed in the MC case, in contrast to the GK case, which has a diffuse interface.

### 6.6.3 GK conduction with enhanced non-local effects

In this case we assume $\eta, \beta \gg 1$ and $\gamma = O(1)$. From the asymptotic analysis we know that there are three time regimes to consider. In the first regime, $t = O(\eta^{-2})$, Fourier's law is recovered with a large value of the ETC, $\zeta \gg 1$, and no solidification occurs. Due to the high value of the ETC, this regime describes the propagation of a large heat flux into the seed crystal. The second time regime depends on the relative size of $\eta^2$ to $\beta$, but in any case the system enters a quasi-steady regime. In the distinguished limit $\beta/\eta^2 = O(1)$, the second time regime is given by $t = O(1)$, and the flux is driven by memory and non-local effects, i.e. the history and rate of change of the temperature gradient, rather than the temperature gradient itself. As time increases, the strength of these non-classical transport mechanisms diminishes and solidification decelerates, causing the position of the solid-liquid interface to reach a temporary steady state. However, as the third time regime, $t = O(\beta)$, is entered, the contributions to the flux from the temperature gradient become large enough to balance and then dominate the non-classical mechanisms, re-initiating the process of solidification. For large times, the classical solidification kinetics, $s \sim t^{1/2}$, are recovered. Similar time regimes were observed in Hennessy et al. [107], although in their case the magnitude of the flux for small times is not as large as here due to their use of a Newton condition at $x = 0$ rather than a fixed-temperature condition.

The evolution of the interface and the mean flux is shown in Fig. 6.6, where lines and circles again represent solutions computed numerically and via the reduced formulation.

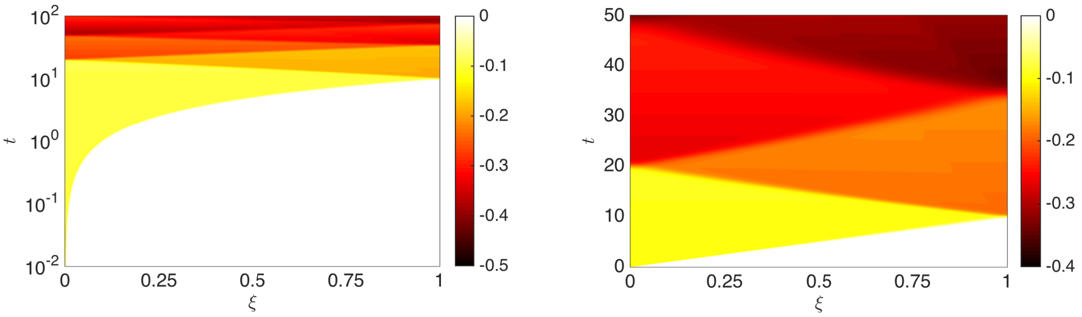

**(a)** Maxwell-Cattaneo conduction

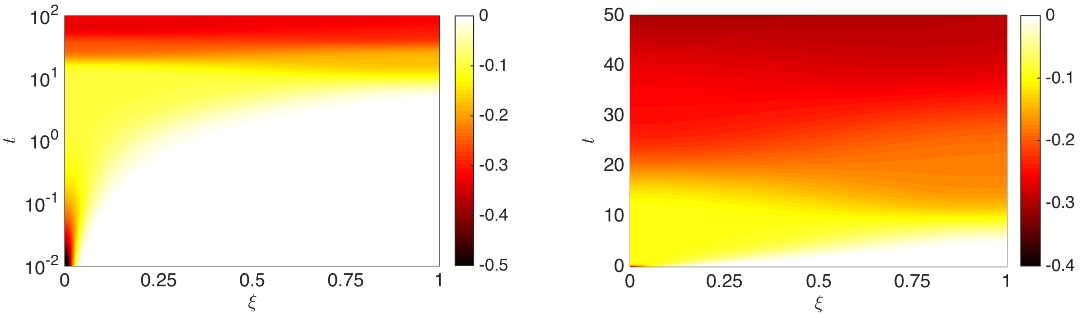

**(b)** Guyer-Krumhansl conduction

**Figure 6.5:** Heat maps showing the evolution in time of the spatial distribution of the flux in terms of the transformed variable $\xi = x/s$, according to the MCE and the GKE. For the latter we have set $\eta = 1$. In both cases $\beta = 10$ and $\gamma = 100$. The panels in the right column focus on the time regime that captures the wave-like propagation of heat.

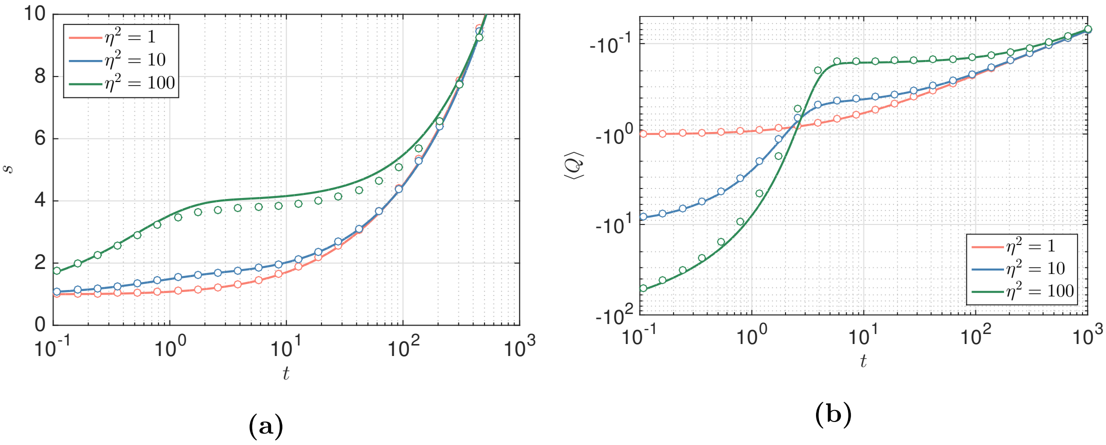

**(a)** **(b)**

**Figure 6.6:** Evolution of the solid-liquid interface and the mean flux according to the GKE in the limit of large non-local effects. The remaining dimensionless parameters are $\gamma = 1$ and $\beta = 10$. Lines refer to the numerical simulations, whereas circles represent the solutions to the quasi-steady formulation.

Due to the large variation of the magnitude of $\langle Q \rangle$, the results in Fig. 6.6 (b) are shown using logarithmic scales on both axes. As in the case of enhanced memory effects, we also show the results for $\eta = 1$, which reduces to the classical model due to the Fourier resonance phenomenon. In general, there is good agreement between the solution to the reduced formulation and numerical simulations, with some small discrepancies in Fig. 6.6 (a) that may be attributed to the terms being neglected in the asymptotic analysis. Larger discrepancies may be observed in Fig. 6.6 (a) for $t \ll 1$, where the reduced formulation predicts smaller values (in magnitude) of the heat flux than the numerical simulations. This error is due to the reduced model not capturing these small-time regimes.

As predicted by the asymptotic analysis, the initial solidification rate increases as the non-local parameter $\eta$ is increased. This is attributed to the increase in the ETC, which enhances the transport of thermal energy to the solidification front. The rapid initial growth of the solid is solely driven by non-Fourier conduction mechanisms; the contribution to the flux from the instantaneous temperature gradient is negligible for small times. As time increases and the solid grows in size, memory and non-local effects weaken and the solidification rate process undergoes a substantial decrease, as seen in Fig. 6.6 when $\eta^2 = 100$. The mean flux relaxes to roughly the Fourier contribution, $\langle Q \rangle \simeq -1/s$; however, due to the rapid initial growth of the solid ($s \gg 1$), this contribution is strongly diminished

**Table 6.1:** Values of the time and flux scales and the dimensionless parameters $\gamma$ and $\eta^2$ depending on the size of the seed crystal. The Stefan number has been fixed to 10.

| $s_c^*$ [nm] | $\tau_D^*$ [ps] | $Q_0^*$ [W/mm$^2$] | $\gamma$ | $\eta$ |
|---|---|---|---|---|
| 2 | 0.43 | 1.9 | 75 | 7.7 |
| 5 | 2.7 | 0.77 | 12 | 3.0 |
| 10 | 11 | 0.38 | 3.0 | 1.5 |

compared to the case of pure Fourier conduction. As a result, when solidification is re-initiated on $O(\beta)$ time scales, it proceeds at a greatly reduced rate.

In summary, the dynamics that occur in the case of GK conduction with strong non-local effects are the opposite of those that occur in the limit of strong memory effects or for MC conduction. In the former case $\eta \gg 1$ with $\gamma = O(1)$, the mean thermal flux is initially much greater and then much smaller in magnitude than the Fourier prediction, which leads to solidification kinetics that are much faster and then much slower than the Fourier case. However, if $\gamma \gg 1$ with $\eta = O(1)$ (or $\eta = 0$), then there is a prolonged period where the mean thermal flux is initially much smaller and then slightly larger in magnitude than the Fourier prediction, resulting in relatively slower and then faster solidification kinetics.

### 6.6.4 Application to the solidification of Si

Silicon is a material of high interest for nanoscale applications and an obvious choice for the validation of theoretical models. In Fig. 6.7 we plot the evolution of the solid-liquid interface and the mean flux according to the classical, MC and GK formulations for different sizes of the seed crystal. The corresponding non-classical parameters are given in Table 6.1. The results have been calculated numerically for $\beta = 10$, which corresponds to an initial temperature jump $\Delta T^* = 173.2$ K. The case $\beta = 100$ ($\Delta T^* = 17.3$ K) leads to all curves in panels (a), (c), (e) collapsing and thus no differences between classical and non-classical solidification kinetics can be observed. To give the results in dimensional form, we have written $\langle Q^* \rangle = Q_0^* \langle Q \rangle$ and $t^* = \tau_D^* t$, with $Q_0^*$ and $\tau_D^*$ given in Table 6.1 for each of the seed crystal sizes.

Panels (a), (c) and (e), where we plot the evolution of the solid-liquid interface, show that

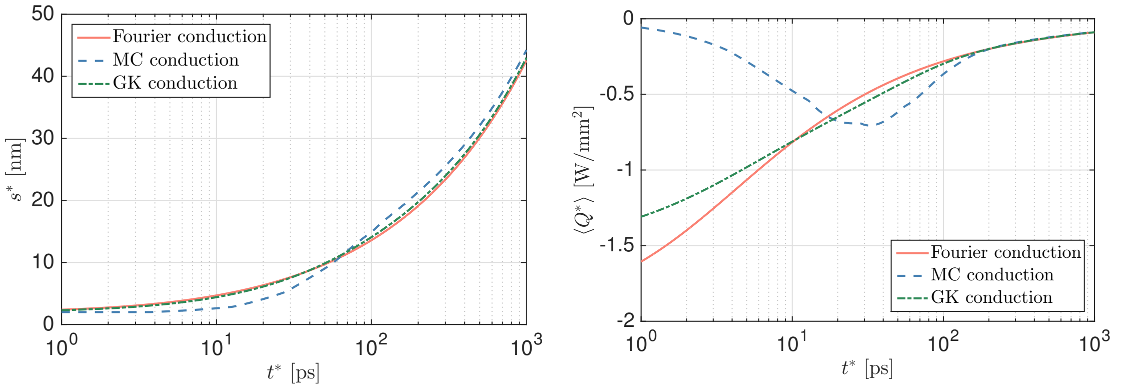

**(a)** $s_c^* = 2$ nm **(b)** $s_c^* = 2$ nm

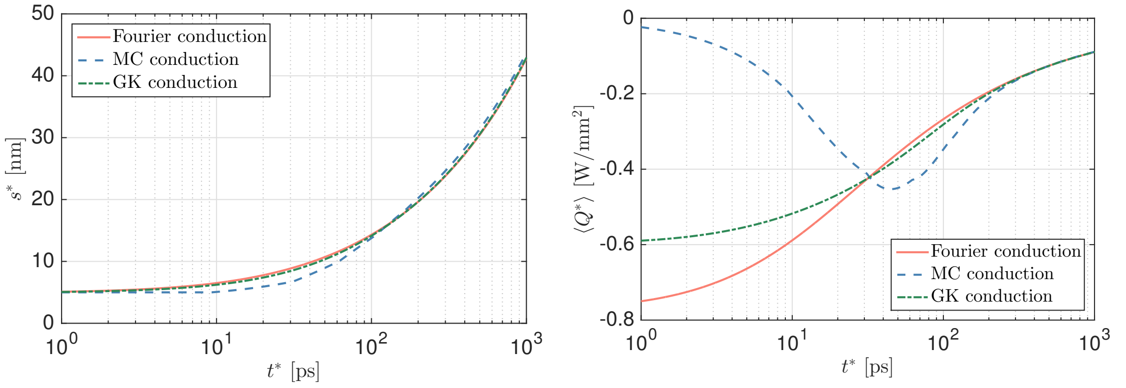

**(c)** $s_c^* = 5$ nm **(d)** $s_c^* = 5$ nm

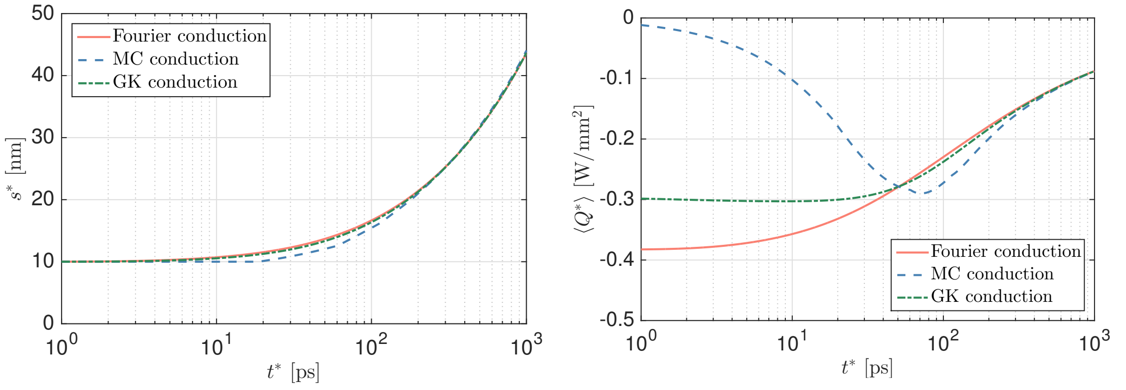

**(e)** $s_c^* = 10$ nm **(f)** $s_c^* = 10$ nm.

**Figure 6.7:** Evolution of the solid-liquid interface and the mean flux according to Fourier's law (red, solid lines), the MCE (blue, dashed lines) and the GKE (green, dashed-dotted lines) for $\beta = 10$ and different sizes of the seed crystal. The values of $\gamma$ and $\eta$ are given in Table 6.1.

the presence of non-classical effects does not cause any major differences in the solidification kinetics. In fact, the Fourier and GK models lead to virtually identical behaviours in the evolution of the solid-liquid interface for the three seed crystal sizes considered. In the case of the MC model, there is a delay in the start of the solidification, which from a physical point of view can be understood from the fact that heat is initially propagated in the form of thermal waves with finite speed, contrary to the Fourier and GK models. Furthermore, the asymptotic analysis of the MC model reveals that in the cases $s_c^* = 2$ nm and $s_c^* = 5$ nm, where $\gamma$ is relatively large, solidification starts for $t^* \approx 11.78$ ps and $t^* \approx 29.36$ ps respectively, which is in good agreement with Fig. 6.7 (a).

Although differences in the plots corresponding to $s^*$ are small, panels (b), (d) and (f), which show the evolution in time of the mean flux, suggest that the choice of the underlying model does have a crucial impact on how heat will propagate through the crystal for small times ($< 100$ ns). It can be observed how the qualitative behaviour of the Fourier and GK fluxes is similar whereas they have large differences with respect to the MC flux. These differences are a direct consequence of the different behaviours for small times, since in the latter heat is initially propagated in the form of heat waves whereas for the GK and classical models the initial heat propagation corresponds to a diffusive process. Therefore, the results shown in Fig. 6.7 suggest that non-classical mechanisms can be detected by measuring the total heat flux through the solid.

The similarities between the solidification kinetics of the Fourier and GK models could exist for two reasons. Firstly, the asymptotic analysis shows non-classical effects become less important for the solidification process as the Stefan number increases. Secondly, the ratio $\zeta = \eta^2/\gamma = 3\ell^{*2}/(\alpha^*\tau_R^*)$ does not depend on the initial size of the seed crystal. Using the values provided in Table B.1, for silicon we find $\zeta \approx 0.77$, which implies that the similarities may be caused by the system being close to the case of Fourier resonance ($\zeta = 1$).

In Fig. 6.8 (a) we show the solidification kinetics for three different seed crystal sizes and for a larger temperature jump of $\Delta T^* = 500$ K, which reduces the Stefan number to $\beta \approx 3.46$. The results show that the similarities between the Fourier and GK models persist, which indicates that the largeness of the Stefan number was not causing the similarities in the solidification kinetics observed in Fig. 6.7, panels (a), (c) and (e).

Thus, we now explore whether these similarities are caused by Fourier resonsance phenomenoma by varying the size of the ETC $\zeta$. In Fig. 6.8 (b) we show how the solidification kinetics vary when changing the order of magnitude of $\tau_R^*$ while keeping the value of $\ell^*$

fixed, which leads to variations in $\zeta$ across two orders of magnitude. In the cases where $\zeta \ll 1$ or $\zeta \gg 1$, the non-Fourier signatures predicted by the asymptotic analysis can be observed. This shows that the similarities between the solidification kinetics in the Fourier and GK models are indeed caused by the fact that $\zeta$ is close to unity. Hence, evidence of non-classical heat transport can be found in measurements of the solidification front only in the cases $\zeta \gg 1$ or $\zeta \ll 1$.

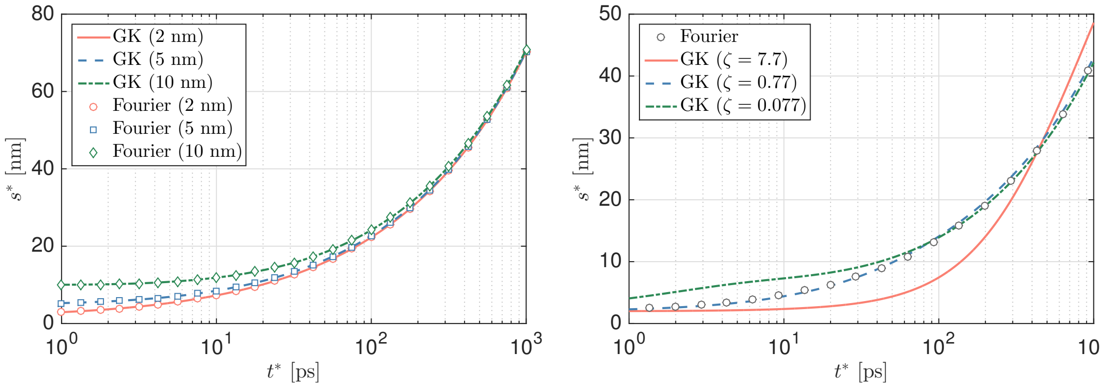

**(a)** **(b)**

**Figure 6.8:** (a) Evolution of the solid-liquid interface according to GK (lines) and Fourier (symbols) models for different initial seed crystal sizes and a temperature jump $\Delta T^* = 500$ K ($\beta \approx 3.46$). (b) Evolution of the solid-liquid interface according to the GK (lines) and Fourier (circles) models for an initial seed crystal of size $s_c^* = 2$ nm and a temperature jump $\Delta T^* = 173.16$ K ($\beta = 10$). The solutions plotted in solid (red), dashed (blue) and dashed-dotted (green) lines correspond to the GK model using $0.1 \cdot \tau_R^*$, $\tau_R^*$ and $10 \cdot \tau_R^*$, where $\tau_R^*$ is the extrapolated value given in Table B.1.

From the results of this study we can conclude that non-classical conduction mechanisms do not lead to significant changes in the solidification kinetics in situations near Fourier resonance, despite the fact that the dimensionless parameters characterising these effects are large. Hence, in this case non-classical heat transport mechanisms are unlikely to be detected from measurements of the solidification front. However, the analyses predict that large deviations can occur in the thermal flux, which is a better quantity to use in the detection of non-classical transport mechanisms and which can be measured both experimentally and in molecular dynamics simulations [82].

## 6.7 Conclusion

In this chapter we have studied non-classical heat transport in phase-change processes as described by the Maxwell-Cattaneo (MC) and Guyer-Krumhansl (GK) equations via the solidification kinetics of a one-dimensional liquid bath. Based on a detailed asymptotic analysis we proposed a simplified formulation which reduces the moving boundary problem to a set of two ordinary differential equations for the position of the interface and the mean flux through the solid. Comparisons of the results provided by this reduced formulation against numerical simulations have shown excellent agreement. When the non-classical terms become dominant, the study shows that we can observe large deviations from the classical solidification kinetics described by Fourier's law. However, in GK conduction near Fourier resonance, for example with silicon, the non-classical effects almost cancel each other out. This leads to similar evolution of the phase-change front between the GK and Fourier models. However, the propagation of heat through the solid is affected by the choice of the constitutive equation to a greater extent. We conclude that a possible strategy to determine the presence of non-classical effects is studying the heat conduction through the growing solid rather than the position of the interface, since the prior seems to give more information even in cases that are close to Fourier resonance. Moreover, due to the different small-time behaviours, measuring the flux could also indicate which of the considered models is more realistic, since the MC model does not have Fourier resonance. Although we focused on MC and GK conduction laws, the reduction framework developed here can be applied to alternative non-Fourier models based on continuum theory and used to study other modes of phase change such as melting as well.

# 7 | Conclusions

## 7.1 English version

The work presented in chapters 3 to 6 can be divided in two categories. In chapters 3 and 4 we have used the Guyer-Krumhansl formalism to derive predictive models for the effective thermal conductivity of nanowires that are in excellent agreement with the available experimental data. In chapters 5 and 6 we have explored different extensions of the classical Stefan problem to account for non-classical features such as memory and non-localities. The main conclusions are summarized below.

### 7.1.1 Heat transfer in nanostructures

In chapters 3 and 4 we used the Guyer-Krumhansl formalism to present a mathematical model able to capture the size-dependence of the thermal conductivity of nanowires, which is crucial for applications involving heat management in nanostructures [31]. We utilized the correspondence with the equations arising in fluid dynamics to propose a slip boundary condition which is meant to capture the different heat transfer regimes. This form of boundary condition has been used in previous studies [7, 73, 156, 264] and it is generally assumed that the slip length $\ell_s^*$ is proportional to the mean free path $\ell^*$, i.e. $\ell_s^* = C\ell^*$. Conversely to the previous studies, where the parameter $C$ is effectively used as a fitting parameter, we propose an exponential which does not only depend on the temperature, but also on the relative size of the nanowire to $\ell^*$.

In the case of circular nanowires, considered in chapter 3, the governing equations can be solved explicitly and an analytical expression for the effective thermal conductivity (ETC) can be found. Our choice of a slip length shows very good agreement with experimental data provided by Li et al. [145]. It is important to stress out that this excellent agreement has been achieved without the introduction of any additional fitting parameters. We also show that the steady state temperature profile is not linear anymore as with the classical formulation, but it satisfies a nonlinear ordinary differential equation which is analogous to the Reynolds equation for the pressure in fluid mechanics. The analogy with this framework allows us to understand the behaviour of the flux for large values of the Knudsen number Kn, where non-classical effects dominate heat transport. In this limiting situation, which can be compared to a fluid with large viscosity, we find that the magnitude of the flux is inversely proportional to Kn. The performance of our model has been compared against other models in the literature. Two models were based on the Guyer-Krumhansl formalism and differ only by the choice of the boundary condition at the surface of the nanowire. The results show that this formalism represents a powerful tool for deriving models to predict the thermal conductivity of nanowires when the correct boundary conditions are applied.

In chapter 4 we considered rectangular nanorods, of which thin films are a particular limit. The presence of corners in the rectangular cross-section suggests that the parameter $C$ might not be uniform along the surface of the nanorod, which implies that, in general, numerical methods must be employed to calculate the longitudinal component of the flux and consequently the ETC. However, it is possible to make analytical progress if some simplifying assumptions are made.

1. In the limit $L_1^* \gg L_2^*$, which corresponds to the thin film limit, we have shown that it is possible to reduce the governing equation to an ordinary differential equation which can be integrated to give an analytical solution of the flux and therefore an expression for the ETC for an arbitrary, non-uniform choice of $C$.

2. If we assume that $C$ is uniform along the cross-sectional boundary, the problem can be solved analytically in terms of an eigenfunction expansion. The terms of the double series decay as $(nm)^{-2}$, hence a small number of terms sufficient to obtain good accuracy with numerical simulations. For particular choices of non-uniform expressions of the slip parameter, we have shown that it is possible to find an equivalent uniform expression.

3. In the case $\mathrm{Kn} \ll 1$, the classical Fourier flux is recovered except near the nanorod's

surface, where we find boundary layers of width $O(\mathrm{Kn})$. Neglecting contributions of order $O(\mathrm{Kn}^2)$ near the corners we have derived an analytical expression for the ETC for arbitrary, non-uniform slip parameters.

4. In the limit of large Knudsen number it is possible to introduce a new scaling for the flux and integrate the governing equations to find an analytical expression of the ETC, valid for any choice of $C$, provided $C \gg \mathrm{Kn}^{-1}$.

When comparing the model aganist experimental data [121] between 1 K and 300 K, we found excellent agreement using an exponential expression for $C$ similar to the circular case. In this case we had to introduce one fitting parameter. The lack of experimental data hinders the exploration of dependencies on the Knudsen number, as done in the case of circular cross-sections, where experimental data for different nanowire radii had been available.

Finally, the analytical expressions for different geometries have been utilized to compare the thermal response of nanowires with circular and rectangular cross-sections and thin film as a limit of the latter. By expressing the different ETCs in terms of an effective Knudsen number $\mathcal{K} = \ell^*/\sqrt{A^*}$, where $A^*$ is the cross-sectional area, we have concluded that nanowires with square and circular cross-sections represent the geometries with best performance, with the latter showing slightly higher values of the ETC. This can be attributed to the presence of corners in the rectangular case, which causes a worse phonon transport due an increased scattering rate next to them. As we reduce the height/width ratio, approaching the thin film limit, the efficiency decreases due to heat transport being dominated by scattering at the upper and lower surfaces.

### 7.1.2 Non-Fourier phenomena in phase change processes

In chapters 5 and 6 we explored different non-classical formulations of the Stefan problem to account for non-Fourier effects appearing at small time- and length scales. In particular, we studied the effects of extensions to Fourier's law in a solidification process in one spatial dimension using numerical simulations and asymptotic methods.

In chapter 5 we consider an effective Fourier law with a thermal conductivity that depends on the size of the growing solid. This size-dependent conductivity was proposed by

Alvarez and Jou [5] to account for non-local effects occurring at length scales comparable to the phonon mean free path. Additionally, we utilized a Newton cooling condition at the boundary of the solid. In contrast to previous studies, which generally assume that heat conduction dominates over the heat exchange at the cooled boundary by taking the Biot number Bi to be order unity or larger, we study the more realistic limit $\mathrm{Bi} \ll 1$.

A small time analysis demonstrated that the initial (dimensionless) solidification rate $\lambda$ is finite, in contrast to the classical formulation with fixed temperature conditions and constant conductivity. In general, $\lambda$ satisfies a transcendental equation which has to be solved numerically. However, performing an asymptotic analysis of the equation based on $\mathrm{Bi} \ll 1$ and $\beta \gg 1$, we derived an expansion in terms of powers of $\mathrm{Bi}/\beta$.

As suggested by the dependence of the initial solidification rate on the Biot number, solidification decelerates as we decrease Bi. Interestingly, intuitively a slower solidification would imply a longer presence of non-classical effects, since the size of growing solid is comparable to the phonon mean free path for a longer period of time. This, for instance, can be observed when increasing $\beta$, also suggested by the fact that $\lambda \propto \mathrm{Bi}/\beta$. However, results showed that the non-classical effects introduced by the size-dependent thermal conductivity disappear as the Biot number decreases. The reason for these surprising results is the fact that a small Biot number is an indicator for poor heat conduction through the solid compared to the heat exchange with the environment and so the choice of the thermal conductivity does not significantly affect the heat conduction through the solid, whereas increasing the Stefan number can be interpreted as decreasing the temperature difference between the environment and the initial liquid bath, leading so to a deceleration of the solidification kinetics.

In chapter 6 we consider the Maxwell-Cattaneo and Guyer-Krumhansl equations. We considered an one-dimensional, liquid bath which solidifies from a small seed crystal. In this way, the process could be divided into two major time regimes, one describing the non-classical heat conduction through the crystal and the second one focusing on the phase change process. We have performed an asymptotic analysis and proposed a numerical scheme to determine the position of the solid-liquid interface and the mean heat flux through the growing solid. The asymptotic analysis has shown that, by the time solidification begins, the temperature profile is linear in space. Based on this we proposed a simplified formulation of the problem, where the governing equations are reduced to two ODEs, one determining the position of the interface and the second determining the mean heat flux through the solid. The agreement of the reduced model and the full numerical solution is remarkable for both Maxwell-Cattaneo and Guyer-Krumhansl models.

In the Maxwell-Cattaneo model, the start of the solidification process is delayed due to the finite speed of propagation of heat through the seed crystal. However, due to the increase in magnitude of the flux, the growth rate is larger than for the Fourier case after a certain period of time. Interestingly, in the case of silicon the solidification kinetics according to the Guyer-Krumhansl model reproduce the classical model. This has been attributed to the Fourier resonance phenomenon, where the non-classical effects cancel each other out. However, the behaviour of the flux through the solid is affected by the choice of the heat conduction model and non-Fourier heat transfer mechanisms can be observed even in situations near Fourier resonance, which indicates that measuring this quantity in experiments or molecular dynamics simulations could be a good strategy to determine the presence of non-Fourier effects in phase change processes.

### 7.1.3 Concluding remarks

In this work we have shown that the Guyer-Krumhansl formalism is a promising tool for understanding non-classical mechanisms and, in particular, for capturing the size-dependence of the effective thermal conductivity in nanostructures, which can be crucial for the development of novel technologies and for the improvement of existing ones. On the same note, we have provided new strategies to determine the existence of these non-classical mechanisms in liquid-solid phase transitions. In this way, the results of this work may be applied both in industry and experimental research areas.

Our main focus during this work has been the Guyer-Krumhansl equation, from which the Maxwell-Cattaneo equation is a special limit. Thus, besides the points described previously, a natural way to extend this study is the consideration of other models of heat conduction as those described in chapter 2, although this would require a deeper understanding of the physical parameters related to those models. In the case of the thermomass model, a non-linear term is introduced in the governing equations.

## 7.2 Versió catalana

El contingut dels capítols 3 al 6 es pot dividir en dues parts. D'una banda, els capítols 3 i 4 hem utilitzat l'equació de Guyer i Krumhansl per a descriure la conducció de calor en situacions estacionàries en nanoestructures, mentres que d'altra banda, en els capítols 5 i 6 ens hem centrat més en l'anàlisi matemàtic de nous models que descriuen un procés de solidificació.

En els capítols 3 i 4 hem proposat models matemàtics per a descriure la conductivitat tèrmica de nanoestructures en dependència de la seva mida característica, efecte que és causat per mecanismes de transport de calor que apareixen a nanoescala. El model proposat en aquests capítols estava basat en la equació de Guyer i Krumhansl i el model hidrodinàmic derivat d'aquesta. A més, les equacions han estat combinades amb condicions de contorn similars a les que apareixen a la dinàmica de fluids i que han resultat essencials per al nostre estudi. En el cas de nanofils de secció transversal circular (capítol 3), s'ha aconseguit replicar dades experimentals corresponents a diferentes mides sense utilitzar cap paràmetre d'ajust. De fet, el model només requereix unes magnituds que es poden calcular a partir de informació microscòpica intrínseca de cada material.

Al capítol 4 hem treballat amb nanofibres amb seccions transversals rectangulars, de les quals les nanocapes en són un cas límit. Degut a la presència de cantonades, on el comportament dels fonons és diferent respecte a com es comporten lluny d'elles, les condicions de vora ja no eren, a priori, uniformes al llarg de tota la superfície exterior del material com en el cas dels nanofils circulars. Degut a aquest canvi, les equacions només es podien resoldre numèricament, tot i que ha estat possible trobar solucions analítiques sota certes condicions. En el cas uniforme, hem pogut trobar una solució en forma d'expansió en una base ortonormal de funcions, mentres que en el cas límit d'una nanocapa hem trobat una expressió analítica. El model amb condicions uniformes s'ha ajustat molt bé a les dades experimentals disponibles, tot i que hem hagut d'incloure un paràmetre d'ajust.

Comparant els dos models per a diferentes geometries, hem pogut concloure que, per a un valor de l'àrea fixat, el nanofil circular és el millor conductor, mentres que el conductor menys efectiu és el cas límit de la nanocapa. Els resultats obtinguts en aquests capítols ja han estat publicats [40, 41].

En els capítols 5 i 6 hem utilitzat diverses extensions de la llei clàssical de Fourier per a descriure processos de canvi de fase, coneguts matemàticament com a problemes de Stefan. En concret, hem considerat el cas unidimensional semi-infinit que representa un líquid immers en un procés de solidificació. En el capítol 5 hem utilitzat un model en el que la conductivitat tèrmica clàssica és intercanviada per una funció de la mida del sòlid proposada per Alvarez i Jou. L'estudi es centrava en proposar mètodes de resolució basats en la discretització de l'espai i del temps i en l'anàlisi asimptòtic del problema, dividint el procés en diferents règims temporals on els mecanismes físics canvien. Per a aquest model hem utilitzat unes condicions de vora basades en la llei de refredament de Newton. Segons els resultats de l'estudi, aquesta reformulació del problema de Stefan només té efectes sobre el creixament del sòlid quan l'anomenat número de Biot és prou gran, cosa que no és d'esperar en situacions pràctiques.

Al capítol 6 hem formulat el problema de Stefan fent ús de l'equació de Guyer i Krumhansl, de la qual l'equació de Maxwell i Cattaneo n'és un cas particular. Per a simplificar l'anàlisi matemàtic, hem considerat que la temperatura a la superfície en contacte amb l'ambient fred és igual a la de l'ambient. Hem proposat una mètode de resolució basat en les diferències finites. A més hem fet un anàlisi asimptòtic complet del problema per al dos models considerats. A partir d'aquest anàlisi hem estat capaços de proposar unes equacions reduïdes amb les quals podem resoldre el problema solucionant només dues equacions diferencials amb gran precisió respecte a la solució numèrica del problema. En el cas del silici, hem vist que el procés de solidificació no és veia afectat en excés en el cas de l'equació de Guyer i Krumhansl, mentres que el model de Maxwell i Cattaneo provocava que el procés comenci amb retard degut a que físicament aquest model descriu la propagació de la calor en forma d'ones amb velocitat finita, al contrari que el model clàssic o el de Guyer i Krumhansl. En canvi, es podien observar diferències notables en quant al flux de calor dintre del sòlid. Això indicava que aquest observable pot ser important per a investigar la presència de nous mecanismes de transferència de calor en situacions de canvi de fase.

Els results obtinguts en aquests darrers capítols han estat recentment enviats a revistes científiques per a la seva revisió i posterior publicació [38, 39].

# A | Calculation of thermal properties using the kinetic collective model

The values of bulk thermal conductivity $k^*(T^*)$ and non-local length $\ell^*(T^*)$, shown in Fig. A.1, have been obtained in the framework of the KCM. In this model, the thermal conductivity is split in the well-known kinetic regime and a collective contribution emerged from momentum conserving (normal) phonon collisions [105, 234]. The total thermal conductivity can be expressed thus as an interpolation between the kinetic and collective contributions weighted by a switching factor $\Sigma(T^*)$, which accounts for the relative abundance of normal versus resistive (Umklapp and mass defect) scattering rates:

$$k^* = \Sigma \cdot k^*_{\text{col}} + (1 - \Sigma) \cdot k^*_{\text{kin}}. \tag{A.1}$$

In the same line, the non-local length $\ell$, related to the phonon mean free paths, can be expressed as an interpolation through $\Sigma$ between the collective limit derived by Guyer and Krumhansl [106] and the kinetic one derived recently at first order [231],

$$\ell^* = \Sigma \cdot \ell^*_{\text{col}} + (1 - \Sigma) \cdot \ell^*_{\text{kin}}. \tag{A.2}$$

These two magnitudes calculated from first principles are the only ones required to solve the hydrodynamic heat transport equation. For these calculations, an open-source code [232] has been used.

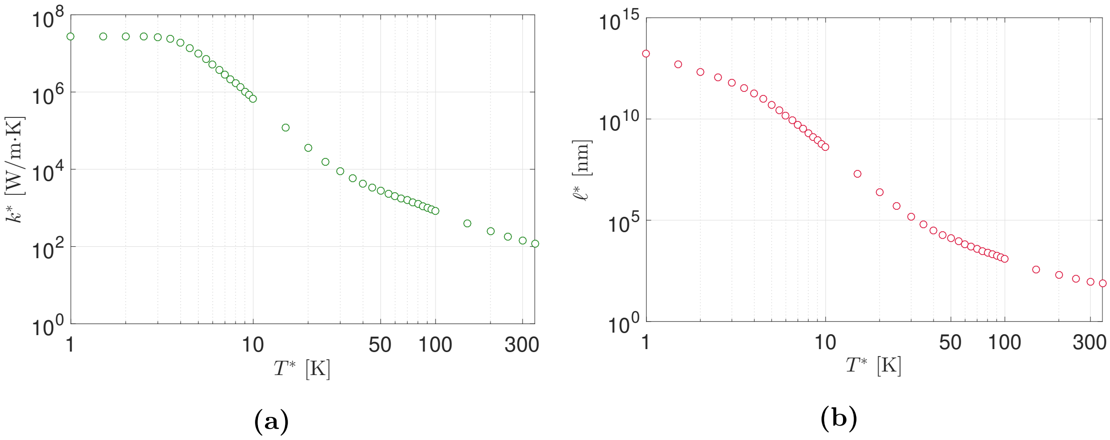

**(a)** **(b)**

**Figure A.1:** Bulk values of (a) the thermal conductivity $k^*$ and (b) the non-local length $\ell^*$, both in terms of the temperature $T^*$ obtained from the KCM framework.

# B | Thermal properties of silicon near phase change temperature

Silicon is a semiconductor of high interest for many nanoscale applications. Most of the studies found in the literature use data corresponding to room temperature. However, phase change occurs at temperatures which are much larger and therefore it is more sensible to use parameters corresponding to these higher temperatures.

For silicon, the phase change temperature and the latent heat are $T_\mathrm{f}^* = 1687$ K and $L_\mathrm{m}^* = 1787 \times 10^3$ J/kg [167]. Since the coefficient of thermal expansion is of the order of $10^{-6}$ K$^{-1}$ [188], we can assume a constant value for the density. Based on Mills and Courtney [167] we take $\rho^* = 2296$ kg/m$^3$. Near the phase change temperature, the thermal conductivity and specific heat capacity of silicon are $k^* \approx 22.1$ W/m·K and $c^* \approx 1032$ J/kg·K [76, 118]. The thermal diffusivity is therefore $\alpha^* \approx 9.33 \times 10^{-6}$ m$^2$/s.

Determining the relaxation time $\tau_R^*$ and the mean free path $\ell^*$ is a more difficult task. Using the kinetic collective model (KCM) [65], which has demonstrated to be a powerful tool for predicting the thermal properties of various materials [234, 235], we are able to estimate their values for up to 1000 K, as shown in Fig. B.1. To find an approximate value for these quantities near phase change temperature, we have fitted these values to an expression of the form $aT^{*-b}$, which is also shown in Fig. B.1. We find $a \approx 1.16 \times 10^{-7}$ and $b \approx 1.11$ for the relaxation time, whereas for the mean free path the best fit is obtained taking $a \approx 4.58 \times 10^{-5}$ and $b \approx 1.16$. From these expressions we find $\tau_R^* \approx 32.16$ ps and $\ell^* \approx 8.79$ nm at $T^* = 1600$ K.

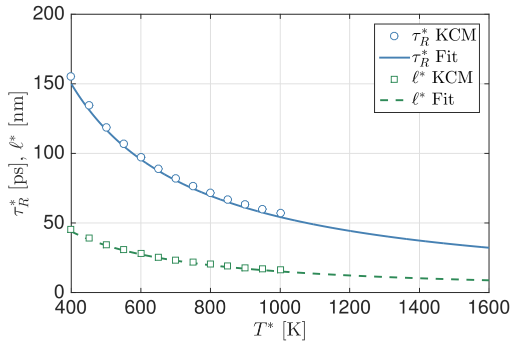

**Figure B.1:** Relaxation time and mean free path of phonons for silicon in the range 400 K$< T^* <$ 1600 K. Symbols refer to data provided by the KCM [234], whereas lines correspond fitting those values to an expression of the form $aT^{*-b}$.

**Table B.1:** Values of the thermophysical properties of Si at 1600 K [76, 118, 167, 234].

| Property | Symbol | Value | SI Units |
|---|---|---|---|
| Thermal conductivity | $k^*$ | 22.1 | W/m·K |
| Specific heat capacity | $c^*$ | 1032 | J/kg·K |
| Density | $\rho^*$ | 2296 | kg/m$^3$ |
| Thermal diffusivity | $\alpha^*$ | $9.33\times10^{-6}$ | m$^2$/s |
| Phase change temperature | $T_\mathrm{f}^*$ | 1687 | K |
| Latent heat | $L_\mathrm{m}^*$ | $1787\times10^3$ | J/kg |
| Relaxation time | $\tau_R^*$ | 32.16 | ps |
| Mean free path | $\ell^*$ | 8.79 | nm |

# Bibliography

[1] F. Ahmad, A. K. Pandey, A. B. Herzog, J. B. Rose, C. P. Gerba, and S. A. Hashsham. Environmental applications and potential health implications of quantum dots. *Journal of Nanoparticle Research*, 14(8):1038, 2012.

[2] H. Ahmadikia and A. Moradi. Non-Fourier phase change heat transfer in biological tissues during solidification. *Heat and Mass Transfer*, 48(9):1559–1568, 2012.

[3] P. M. Ajayan and O. Z. Zhou. Applications of carbon nanotubes. In *Carbon nanotubes*, pages 391–425. Springer, 2001.

[4] V. Alexiades and A. D. Solomon. *Mathematical Modeling Of Melting And Freezing Processes*. CRC Press, 1992.

[5] F. X. Alvarez and D. Jou. Memory and nonlocal effects in heat transport: From diffusive to ballistic regimes. *Applied Physics Letters*, 90(8):083109, 2007.

[6] F. X. Alvarez and D. Jou. Size and frequency dependence of effective thermal conductivity. *Journal of Applied Physics*, 103(9):094321, 2008.

[7] F. X. Alvarez, D. Jou, and A. Sellitto. Phonon hyrodynamics and phonon-boundary scattering in nanosystems. *Journal of Applied Physics*, 105(1):014317, 2009.

[8] I. S. Amiri, H. Mohammadi, and M. Hosseinghadiry. *Device Physics, Modeling, Technology, and Analysis for Silicon MESFET*, chapter Invention and Evaluation of Transistors and Integrated Circuits. Springer, Cham, 2019.

[9] M. Asheghi, Y. K. Leung, S. S. Wong, and K. E. Goodson. Phonon-boundary scattering in thin silicon layers. *Applied Physics Letters*, 71(13):1798–1800, 1997.

[10] M. Asheghi, M. N. Touzelbaev, K. E. Goodson, Y. K. Leung, and S. S. Wong. Temperature-dependent thermal conductivity of single-crystal silicon layers in SOI substrates. *Journal of Heat Transfer*, 120(1):30–36, 1998.

[11] M. Ashenghi, Y. K. Leung, S. S. Wong, and K. E. Goodson. Phonon-boundary scattering in thin silicon layers. *Applied Physics Letters*, 71(13):1798–1800, 1997.

[12] M. Asta, C. Beckermann, A. Karma, W. Kurz, R. Napolitano, M. Plapp, G. Purdy, M. Rappaz, and R. Trivedi. Solidification microstructures and solid-state parallels: Recent developments, future directions. *Acta Materialia*, 57(4):941–971, 2009.

[13] AZOM. Silicon, 2001.

[14] T. Bachels, H. J. Güntherodt, and R. Schäfer. Melting of isolated tin nanoparticles. *Physical Review Letters*, 85(6):1250, 2000.

[15] J. M. Back, S. W. McCue, M. H.-N. Hsieh, and T. J. Moroney. The effect of surface tension and kinetic undercooling on a radially-symmetric melting problem. *Applied Mathematics and Computation*, 229:41–52, 2014.

[16] M. Bamberger and B. Prinz. Determination of heat transfer coefficients during water cooling of metals. *Materials Science and Technology*, 2(4):410–415, 1986.

[17] P. R. Bandaru. Electrical properties and applications of carbon nanotube structures. *Journal of Nanoscience and Nanotechnology*, 7(4-5):1239–1267, 2007.

[18] A. Beardo, M. Calvo-Schwarzwälder, J. Camacho, T. G. Myers, P. Torres, L. Sendra, F. X. Alvarez, and J. Bafaluy. Hydrodynamic heat transport in compact and holey silicon thin films. *Physical Review Applied*, 11:034003, 2019.

[19] S. Berber, Y.-K. Kwon, and D. Tománek. Unusually high thermal conductivity of carbon nanotubes. *Physical Review Letters*, 84(20):4613, 2000.

[20] T. L. Bergman, F. P. Incropera, D. P. DeWitt, and A. S. Lavine. *Fundamentals of Heat and Mass Transfer*. John Wiley & Sons, 7th edition, 2011.

[21] R. Berman, E. L. Foster, and J. M. Ziman. Thermal conduction in artificial sapphire crystals at low temperatures I. Nearly perfect crystals. *Proceedings of the Royal Society of London. Series A. Mathematical and Physical Sciences*, 231(1184):130–144, 1955.

[22] R. Berman, F. E. Simon, and J. M. Ziman. The thermal conductivity of diamond at low temperatures. *Proceedings of the Royal Society of London. Series A. Mathematical and Physical Sciences*, 220(1141):171–183, 1953.

[23] J.-B. Biot. Memoire sur la propagation de la chaleur. *Bibliotheque Brittanique*, 27:310–329, 1804.

[24] L. Boltzmann. Weitere Studien über das Wärmegleichgewicht unter Gasmolekülen. *Sitzungsberichte der Akademie der Wissenschaften Wien*, 66(II):275–370, 1872.

[25] S. Both, B. Czél, T. Fülöp, G. Gróf, A. Gyenis, R. Kovács, P. Ván, and J. Verhás. Deviation from the Fourier law in room-temperature heat pulse experiments. *Journal of Non-Equilibrium Thermodynamics*, 41(1):41–48, 2016.

[26] D. A. Broido, M. Malorny, G. Birner, N. Mingo, and D. A. Stewart. Intrinsic lattice thermal conductivity of semiconductors from first principles. *Applied Physics Letters*, 91(23):231922, 2007.

[27] S. D. Brorson, J. G. Fujimoto, and E. P. Ippen. Femtosecond electronic heat-transport dynamics in thin gold films. *Physical Review Letters*, 59(17):1962, 1987.

[28] P. Buffat and J. P. Borel. Size effect on the melting temperature of gold particles. *Physical Review A*, 13(6):2287, 1976.

[29] G. Bulman, P. Barletta, J. Lewis, N. Baldasaro, M. Manno, A. Bar-Cohen, and B. Yang. Superlattice-based thin-film thermoelectric modules with high cooling fluxes. *Nature Communications*, 7:10302, 2016.

[30] G. Caginalp. Stefan and Hele-Shaw type models as asymptotic limits of the phase-field equations. *Physical Review A*, 39:5887–5896, 1989.

[31] D. G. Cahill, P. V. Braun, G. Chen, D. R. Clarke, S. Fan, K. E. Goodson, P. Keblinski, W. P. King, G. D. Mahan, A. Majumdar, H. J. Maris, S. R. Phillpot, E. Pop,

and L. Shi. Nanoscale thermal transport. II. 2003–2012. *Applied Physics Reviews*, 1(1):011305, 2014.

[32] D. G. Cahill, W. K. Ford, K. E. Goodson, G. D. Mahan, A. Majumdar, H. J. Maris, R. Merlin, and S. R. Phillpot. Nanoscale thermal transport. *Journal of Applied Physics*, 93(2):793–818, 2003.

[33] J. Caldwell and C.-C. Chan. Spherical solidification by the enthalpy method and the heat balance integral method. *Applied Mathematical Modelling*, 24(1):45–53, 2000.

[34] J. Caldwell and Y. Y. Kwan. Numerical methods for one-dimensional Stefan problems. *Communications in Numerical Methods in Engineering*, 20(7):535–545, 2004.

[35] J. Caldwell and Y. Y. Kwan. Starting solutions for the boundary immobilization method. *Communications in Numerical Methods in Engineering*, 21(6):289–295, 2005.

[36] J. Caldwell and S. Savovic. Numerical solution of Stefan problem by variable space grid method and boundary immobilisation method. *Journal of Mathematical Sciences*, 13(1):67–79, 2002.

[37] J. Callaway. Model for lattice thermal conductivity at low temperatures. *Physical Review*, 113(4):1046, 1959.

[38] M. Calvo-Schwarzwälder. Non-local effects and size-dependent properties in Stefan problems with Newton cooling. *arXiv preprint arXiv:1902.00401v2*, 2019.

[39] M. Calvo-Schwarzwälder, M. G. Hennessy, and T. G. Myers. The one-dimensional Stefan problem with non-Fourier heat conduction. *arXiv preprint arXiv: XXXX*, 2019.

[40] M. Calvo-Schwarzwälder, M. G. Hennessy, P. Torres, T. G. Myers, and F. X. Alvarez. Effective thermal conductivity of rectangular nanowires based on phonon hydrodynamics. *International Journal in Heat and Mass Transfer*, 126:1120–1128, 2018.

[41] M. Calvo-Schwarzwälder, M. G. Hennessy, P. Torres, T. G. Myers, and F. X. Alvarez. A slip-based model for the size-dependent effective thermal conductivity of nanowires. *International Communications in Heat and Mass Transfer*, 91:57–63, 2018.

[42] B.-Y. Cao and Z.-Y. Guo. Equation of motion of a phonon gas and non-Fourier heat conduction. *Journal of Applied Physics*, 102(5):053503, 2007.

[43] H. B. G. Casimir. Note on the conduction of heat in crystals. *Physica*, 5(6):495–500, 1938.

[44] C. Cattaneo. A form of heat conduction equation which eliminates the paradox of instantaneous propagation. *Compte Rendus*, 247(4):431–433, 1958.

[45] A. Cepellotti, G. Fugallo, L. Paulatto, M. Lazzeri, F. Mauri, and N. Marzari. Phonon hydrodynamics in two-dimensional materials. *Nature Communications*, 6:6400, 2015.

[46] A. N. Ceretani, N. N. Salva, and D. A. Tarzia. An exact solution to a Stefan problem with variable thermal conductivity and a Robin boundary condition. *Nonlinear Analysis: Real World Applications*, 40:243–259, 2018.

[47] C.-W. Chang, D. Okawa, H. Garcia, A. Majumdar, and A. Zettl. Breakdown of Fourier's law in nanotube thermal conductors. *Physical Review Letters*, 101(7):075903, 2008.

[48] A. Chavez-Valdez, M. S. P. Shaffer, and A. R. Boccaccini. Applications of graphene electrophoretic deposition. A review. *The Journal of Physical Chemistry B*, 117(6):1502–1515, 2013.

[49] G. Chen. Ballistic-diffusive heat-conduction equations. *Physical Review Letters*, 86(11):2297, 2001.

[50] G. Chen. Ballistic-diffusive equations for transient heat conduction from nano to macroscales. *Journal of Heat Transfer*, 124(2):320–328, 2002.

[51] G. Chen. Multiscale simulation of phonon and electron thermal transport. *Annual Review of Heat Transfer*, 17, 2014.

[52] G. Chen, D. Borca-Tasciuc, and R. G. Yang. Nanoscale heat transfer. *Encyclopedia of Nanoscience and Nanotechnology*, 17:429–459, 2004.

[53] S. Chen, B. Merriman, S. Osher, and P. Smereka. A simple level set method for solving Stefan problems. *Journal of Computational Physics*, 135(1):8–29, 1997.

[54] T.-G. Chen, P. Yu, R.-H. Chou, and C.-L. Pan. Phonon thermal conductivity suppression of bulk silicon nanowire composites for efficient thermoelectric conversion. *Optics Express*, 18(103):A467–A476, 2010.

[55] Y. Chen, D. Li, J. R. Lukes, and A. Majumdar. Monte carlo simulation of silicon nanowire thermal conductivity. *Journal of Heat Transfer*, 127(10):1129–1137, 2005.

[56] A. B. Chinen, C. M. Guan, J. R. Ferrer, S. N. Barnaby, T. J. Merkel, and C. A. Mirkin. Nanoparticle probes for the detection of cancer biomarkers, cells, and tissues by fluorescence. *Chemical Reviews*, 115(19):10530–10574, 2015.

[57] K. Cho, X. Wang, Z. G. Nie, S andd Chen, and D. M. Shin. Therapeutic nanoparticles for drug delivery in cancer. *Clinical Cancer Research*, 14(5):1310–1316, 2008.

[58] F.-C. Chou, J. Lukes, X.-G. Liang, K. Takahashi, and C.-L. Tien. Molecular dynamics in microscale thermophysical engineering. *Annual Review of Heat Transfer*, 10(10), 1999.

[59] S. Ciraci, A. Buldum, and I. P. Batra. Quantum effects in electrical and thermal transport through nanowires. *Journal of Physics: Condensed Matter*, 13(29):R537, 2001.

[60] J. Crank and P. Nicolson. A practical method for numerical evaluation of solutions of partial differential equations of the heat-conduction type. In *Mathematical Proceedings of the Cambridge Philosophical Society*, volume 43, pages 50–67, 1947.

[61] V. Cregan and T. G. Myers. Modelling the efficiency of a nanofluid direct absorption solar collector. *International Journal of Heat and Mass Transfer*, 90:505–514, 2015.

[62] J. Crepeau. Josef Stefan: His life and legacy in the thermal sciences. *Experimental Thermal and Fluid Science*, 31(7):795–803, 2007.

[63] H. Darcy. *Les fontaines publiques de la ville de Dijon.* Victor Dalmont, 1856.

[64] S. H. Davis. *Theory of Solidification.* Cambridge Monographs on Mechanics. Cambridge University Press, 2001.

[65] C. De Tomas, A. Cantarero, A. F. Lopeandia, and F. X. Alvarez. From kinetic to collective behavior in thermal transport on semiconductors and semiconductor nanostructures. *Journal of Applied Physics*, 115(16):164314, 2014.

[66] C. De Tomas, A. Cantarero, A. F. Lopeandia, and F. X. Alvarez. Thermal conductivity of group-IV semiconductors from a kinetic-collective model. *Proceedings of the Royal Society A: Mathematical, Physical and Engineering Sciences*, 470(2169):20140371, 2014.

[67] F. Delogu. Structural and energetic properties of unsupported Cu nanoparticles from room temperature to the melting point: molecular dynamics simulations. *Physical Review B*, 72(20):205418, 2005.

[68] Z.-S. Deng and J. Liu. Non-Fourier heat conduction effect on prediction of temperature transients and thermal stress in skin cryopreservation. *Journal of Thermal Stresses*, 26(8):779–798, 2003.

[69] Z. Ding, J. Zhou, B. Song, V. Chiloyan, M. Li, T.-H. Liu, and G. Chen. Phonon hydrodynamic heat conduction and Knudsen minimum in graphite. *Nano Letters*, 18(1):638–649, 2017.

[70] P. A. M. Dirac. *The Principles of Quantum Mechanics*. Oxford University Press, 1930.

[71] Y. Dong, B.-Y. Cao, and Z.-Y. Guo. Generalized heat conduction laws based on thermomass theory and phonon hydrodynamics. *Journal of Applied Physics*, 110(6):063504, 2011.

[72] Y. Dong, B.-Y. Cao, and Z.-Y. Guo. Temperature in nonequilibrium states and non-Fourier heat conduction. *Physical Review E*, 87(3):032150, 2013.

[73] Y. Dong, B.-Y. Cao, and Z.-Y. Guo. Size dependent thermal conductivity of si nanosystems based on phonon gas dynamics. *Physica E: Low-dimensional Systems and Nanostructures*, 56:256–262, 2014.

[74] G. Dresselhaus, M. D. Dresselhaus, and R. Saito. *Physical properties of carbon nanotubes*. World scientific, 1998.

[75] W. A. Ebert and E. M. Sparrow. Slip flow in rectangular and annular ducts. *Journal of Basic Engineering*, 87(4):1018–1024, 1965.

[76] Efunda. Thermal conductivity: Silicon. `http://www.efunda.com/materials/elements/TC_Table.cfm?Element_ID=Si`. Accessed: 20/03/2019.

[77] F. Ercolessi, W. Andreoni, and E. Tosatti. Melting of small gold particles: Mechanism and size effects. *Physical Review Letters*, 66(7):911, 1991.

[78] A. Esen and S. Kutluay. A numerical solution of the Stefan problem with a Neumann-type boundary condition by enthalpy method. *Applied Mathematics and Computation*, 148(2):321–329, 2004.

[79] J. D. Evans and J. R. King. Asymptotic results for the Stefan problem with kinetic undercooling. *The Quarterly Journal of Mechanics and Applied Mathematics*, 53(3):449–473, 2000.

[80] A. Fick. Ueber diffusion. *Annalen der Physik*, 170(1):59–86, 1855.

[81] B. J. Florio and T. G. Myers. The melting and solidification of nanowires. *Journal of Nanoparticle Research*, 18(6):1–12, 2016.

[82] F. Font. A one-phase Stefan problem with size-dependent thermal conductivity. *Applied Mathematical Modelling*, 63:172–178, 2018.

[83] F. Font and F. Bresme. Transient melting at the nanoscale: A continuum heat transfer and nonequilibrium molecular dynamics approach. *Journal of Physical Chemistry C*, 122(30):17481–17489, 2018.

[84] F. Font and T. G. Myers. Spherically symmetric nanoparticle melting with a variable phase change temperature. *Journal of Nanoparticle Research*, 15(12):2086, 2013.

[85] F. Font, T. G. Myers, and S. L. Mitchell. A mathematical model for nanoparticle melting with density change. *Microfluidics and Nanofluidics*, 18(2):233–243, 2015.

[86] J. Fourier. *Theorie analytique de la chaleur*. Chez Firmin Didot, père et fils, 1822.

[87] M. Fujii, X. Zhang, H. Xie, H. Ago, K. Takahashi, T. Ikuta, H. Abe, and T. Shimizu. Measuring the thermal conductivity of a single carbon nanotube. *Physical Review Letters*, 95(6):065502, 2005.

[88] E. C. Garnett, M. L. Brongersma, Y. Cui, and M. D. McGehee. Nanowire solar cells. *Annual Review of Materials Research*, 41:269–295, 2011.

[89] M. Ge, J. Rong, X. Fang, and C. Zhou. Porous doped silicon nanowires for lithium ion battery anode with long cycle life. *Nano letters*, 12(5):2318–2323, 2012.

[90] D. E. Glass, M. Necati Ozisik, S. S. McRae, and W. S. Kim. Formulation and solution of hyperbolic Stefan problem. *Journal of Applied Physics*, 70(3):1190–1197, 1991.

[91] M. E. Glicksman. *Principles of solidification.* Springer, 2011.

[92] W. A. Goddard, D. Brenner, S. E. Lyshevski, and G. J. Iafrate. *Handbook of Nanoscience, Engineering, and Technology.* Electrical Engineering Handbook. Taylor & Francis, 3rd edition, 2012.

[93] T. R. Goodman. The Heat-Balance Integral and its application to problems involving a change of phase. *Transactions of the ASME*, 80:335–342, 1958.

[94] K. E. Goodson and Y. S. Ju. Heat conduction in novel electronic films. *Annual Review of Materials Science*, 29(1):261–293, 1999.

[95] I. Grattan-Guinness. Joseph Fourier and the revolution in mathematical physics. *IMA Journal of Applied Mathematics*, 5(2):230–253, 1969.

[96] J. M. Greenberg. A hyperbolic heat transfer problem with phase changes. *IMA Journal of Applied Mathematics*, 38(1):1–21, 1987.

[97] D. J. Griffiths and D. F. Schroeter. *Introduction to Quantum Mechanics.* Cambridge University Press, 2018.

[98] G. Guisbiers and S. Pereira. Theoretical investigation of size and shape effects on the melting temperature of ZnO nanostructures. *Nanotechnology*, 18(43):435710, 2007.

[99] Y. Guo and M. Wang. Phonon hydrodynamics and its applications in nanoscale heat transport. *Physics Reports*, 595:1–44, 2015.

[100] Y. Guo and M. Wang. Phonon hydrodynamics for nanoscale heat transport at ordinary temperatures. *Physical Review B*, 97:035421, Jan 2018.

[101] Z.-Y. Guo and Q.-W. Hou. Thermal wave based on the thermomass model. *Journal of Heat Transfer*, 132(7):072403, 2010.

[102] Z.-Y. Guo and Y.-S. Xu. Non-Fourier heat conduction in IC chip. *Journal of Electronic Packaging*, 117(3):174–177, 1995.

[103] S. C. Gupta. *The Classical Stefan Problem: basic concepts, modelling and analysis*. Elsevier, 2003.

[104] R. A. Guyer and J. A. Krumhansl. Dispersion relation for second sound in solids. *Physical Review*, 133:A1411–A1417, 1964.

[105] R. A. Guyer and J. A. Krumhansl. Solution of the Linearized Phonon Boltzmann Equation. *Physical Review*, 148(2):766, 1966.

[106] R. A. Guyer and J. A. Krumhansl. Thermal Conductivity, Second Sound, and Phonon Hydrodynamic Phenomena in Nonmetallic Crystals. *Physical Review*, 148(2):778, 1966.

[107] Hennessy, M G and Calvo-Schwarzwälder, M and Myers, T G. Asymptotic analysis of the Guyer-Krumhansl-Stefan model for nanoscale solidification. *Applied Mathematical Modelling*, 61:1–17, 2018.

[108] Hennessy, M G and Calvo-Schwarzwälder, M and Myers, T G. Modelling ultra-fast nanoparticle melting with the Maxwell-Cattaneo equation. *Applied Mathematical Modelling*, 69:201–222, 2019.

[109] A. S. Henry and G. Chen. Spectral phonon transport properties of silicon based on molecular dynamics simulations and lattice dynamics. *Journal of Computational and Theoretical Nanoscience*, 5(2):141–152, 2008.

[110] M. Highland, B. C. Gundrum, Y. K. Koh, R. S. Averback, D. G. Cahill, V. C. Elarde, J. J. Coleman, D. A. Walko, and E. C. Landahl. Ballistic-phonon heat conduction at the nanoscale as revealed by time-resolved x-ray diffraction and time-domain thermoreflectance. *Physical Review B*, 76:075337, Aug 2007.

[111] J. M. Hill. *One-dimensional Stefan problems: an introduction.* Longman Scientific & Technical, 1987.

[112] M. G. Holland. Analysis of lattice thermal conductivity. *Physical Review*, 132(6):2461, 1963.

[113] K. M. Hoogeboom-Pot, J. N. Hernandez-Charpak, X. Gu, T. D. Frazer, E. H. Anderson, W. Chao, R. W. Falcone, R. Yang, M. M. Murnane, H. C. Kapteyn, and D. Nardi. A new regime of nanoscale thermal transport: Collective diffusion increases dissipation efficiency. *Proceedings of the National Academy of Sciences*, 112(16):4846–4851, 2015.

[114] J. Hu, X. Ruan, and Y. P. Chen. Thermal conductivity and thermal rectification in graphene nanoribbons: a molecular dynamics study. *Nano Letters*, 9(7):2730–2735, 2009.

[115] Y. Hu, L. Zeng, A. J. Minnich, M. S. Dresselhaus, and G. Chen. Spectral mapping of thermal conductivity through nanoscale ballistic transport. *Nature Technology*, 10:701–707, 2015.

[116] S. Huberman, R. A. Duncan, K. Chen, B. Song, V. Chiloyan, Z. Ding, A. A. Maznev, G. Chen, and K. A. Nelson. Observation of second sound in graphite at temperatures above 100 K. *arXiv preprint arXiv:1901.09160*, 2019.

[117] J. C. Hull. *Options, Futures, and Other Derivatives.* Pearson Education, 10th edition, 2017.

[118] R. Hull. *Properties of crystalline silicon.* IET, 1999.

[119] J. Hutton. *Dissertations on different subjects in natural philosophy.* A Strahan and T Cadell Edinburgh; London, 1792.

[120] P. Hyldgaard and G. D. Mahan. Phonon superlattice transport. *Physical Review B*, 56:10754–10757, Nov 1997.

[121] A. V. Inyushkin, A. N. Taldenkov, A. M. Gibin, A. V. Gusev, and H.-J. Pohl. On the isotope effect in thermal conductivity of silicon. *Physica Status Solidi (C)*, 1(11):2995–2998, 2004.

[122] E. Javierre, C. Vuik, F. J. Vermolen, and S. Van der Zwaag. A comparison of numerical models for one-dimensional Stefan problems. *Journal of Computational and Applied Mathematics*, 192(2):445–459, 2006.

[123] H. Jiang, K.-S. Moon, H. Dong, F. Hua, and C. P. Wong. Size-dependent melting properties of tin nanoparticles. *Chemical Physics Letters*, 429(4-6):492–496, 2006.

[124] P. Jiang, X. Qian, and R. Yang. Tutorial: Time-domain thermoreflectance (TDTR) for thermal property characterization of bulk and thin film materials. *Journal of Applied Physics*, 124(16):161103, 2018.

[125] J. A. Johnson, A. A. Maznev, J. Cuffe, J. K. Eliason, A. J. Minnich, T. Kehoe, C. M. Sotomayor Torres, G. Chen, and K. A. Nelson. Direct measurement of room-temperature nondiffusive thermal transport over micron distances in a silicon membrane. *Physical Review Letters*, 110(2):025901, 2013.

[126] D. D. Joseph and L. Preziosi. Heat waves. *Reviews of Modern Physics*, 61(1):41, 1989.

[127] D. Jou, J. Casas-Vazquez, and G. Lebon. *Extended Irreversible Thermodynamics*. Springer, 2nd edition, 1996.

[128] Y. S. Ju. Phonon heat transport in silicon nanostructures. *Applied Physics Letters*, 87(15):153106, 2005.

[129] Y. S. Ju and K. E. Goodson. Phonon scattering in silicon films with thickness of order 100 nm. *Applied Physics Letters*, 74(20):3005–3007, 1999.

[130] D. Juric and G. Tryggvason. A front-tracking method for dendritic solidification. *Journal of Computational Physics*, 123(1):127–148, 1996.

[131] P. L. Kapitza. Heat transfer and superfluidity of helium II. *Physical Review*, 60:354–355, 1941.

[132] P. L. Kapitza. The study of heat transfer in helium II. *Journal of Physics(Moscow)*, 4:181, 1941.

[133] C. Kittel. *Introduction to Solid State Physics.* Wiley, 8th edition, 2004.

[134] R. Kofman, P. Cheyssac, Y. Lereah, and A. Stella. Melting of clusters approaching 0D. *European Physical Journal*, 9:441–444, 1999.

[135] A. Kumar, S. Kumar, V. K. Katiyar, and S. Telles. Phase change heat transfer during cryosurgery of lung cancer using hyperbolic heat conduction model. *Computers in biology and medicine*, 84:20–29, 2017.

[136] S. Kutluay, A. R. Bahadir, and A. Özdeş. The numerical solution of one-phase classical Stefan problem. *Journal of Computational and Applied Mathematics*, 81(1):135–144, 1997.

[137] S. L. Lai, J. Y. Guo, V. Petrova, G. Ramanath, and L. H. Allen. Size-dependent melting properties of small tin particles: nanocalorimetric measurements. *Physical Review Letters*, 77(1):99, 1996.

[138] G. Lamé and B. Clapeyron. Mémoire sur l'équilibre intérieur des corps solides homogènes. *Journal für die reine und angewandte Mathematik*, 7:145–169, 1831.

[139] L. Landau. Theory of the superfluidity of helium II. *Physical Review*, 60:356–358, 1941.

[140] G. Lebon. Heat conduction at micro and nanoscales: a review through the prism of extended irreversible thermodynamics. *Journal of Non-Equilibrium Thermodynamics*, 39(1):35–59, 2014.

[141] E. Lee, C. Wang, J. Yurek, and R. Ma. A new frontier for quantum dots in displays. *Information Display*, 34(6):10–13, 2018.

[142] E. K. Lee, L. Yin, Y. Lee, J. W. Lee, S. J. Lee, J. Lee, S. N. Cha, D. Whang, G. S. Hwang, and K. Hippalgaonkar. Large thermoelectric figure-of-merits from SiGe

nanowires by simultaneously measuring electrical and thermal transport properties. *Nano letters*, 12(6):2918–2923, 2012.

[143] S. Lee, D. Broido, K. Esfarjani, and G. Chen. Hydrodynamic phonon transport in suspended graphene. *Nature Communications*, 6:6290, 2015.

[144] S. Lepri, R. Livi, and A. Politi. Thermal conduction in classical low-dimensional lattices. *Physics Reports*, 377(1):1–80, 2003.

[145] D. Li, Y. Wu, P. Kim, L. Shi, P. Yang, and A. Majumdar. Thermal conductivity of individual silicon nanowires. *Applied Physics Letters*, 83(14):2934–2936, 2003.

[146] H.-L. Li and B.-Y. Cao. Radial ballistic-diffusive heat conduction in nanoscale. *Nanoscale and Microscale Thermophysical Engineering*, pages 1–15, 2018.

[147] W. Li, N. Mingo, L. Lindsay, D. A. Broido, D. A. Stewart, and N. A. Katcho. Thermal conductivity of diamond nanowires from first principles. *Physical Review B*, 85(19):195436, 2012.

[148] H. S. Lim, C. K. Ong, and F. Ercolessi. Surface effects in vibrational and melting properties of Pb clusters. *Zeitschrift für Physik D Atoms, Molecules and Clusters*, 26(1):45–47, 1993.

[149] L. Lindsay, D. A. Broido, and T. L. Reinecke. Ab initio thermal transport in compound semiconductors. *Physical Review B*, 87(16):165201, 2013.

[150] F. Liu and D. L. S. McElwain. A computationally efficient solution technique for moving-boundary problems in finite media. *IMA Journal of Applied Mathematics*, 59(1):71–84, 1997.

[151] J. Liu and M. Xu. Some exact solutions to Stefan problems with fractional differential equations. *Journal of Mathematical Analysis and Applications*, 351(2):536–542, 2009.

[152] W. Liu and M. Asheghi. Phonon–boundary scattering in ultrathin single-crystal silicon layers. *Applied Physics Letters*, 84(19):3819–3821, 2004.

[153] W. Liu and M. Asheghi. Thermal conductivity measurements of ultra-thin single crystal silicon layers. *Journal of heat transfer*, 128(1):75–83, 2006.

[154] Z. Liu, J. Xu, D. Chen, and G. Shen. Flexible electronics based on inorganic nanowires. *Chemical Society Reviews*, 44(1):161–192, 2015.

[155] X. Lü, J. H. Chu, and W. Z. Shen. Modification of the lattice thermal conductivity in semiconductor rectangular nanowires. *Journal of applied physics*, 93(2):1219–1229, 2003.

[156] Y. Ma. Size-dependent thermal conductivity in nanosystems based on non-Fourier heat transfer. *Applied Physics Letters*, 101:211905, 2012.

[157] A. Majumdar. Effect of interfacial roughness on phonon radiative heat conduction. *Journal of Heat Transfer*, 113(4):797–805, 1991.

[158] A. Majumdar. Microscale heat conduction in dielectric films. *Journal of Heat Transfer*, 115(1):7–16, 1993.

[159] Y. D. Mao and M. T. Xu. Non-Fourier heat conduction in a thin gold film heated by an ultra-fast-laser. *Science China Technological Sciences*, 58:638–649, 2015.

[160] F. Márkus and K. Gambár. Heat propagation dynamics in thin silicon layers. *International Journal of Heat and Mass Transfer*, 56(1-2):495–500, 2013.

[161] G. Marshall. A front tracking method for one-dimensional moving boundary problems. *SIAM Journal on Scientific and Statistical Computing*, 7(1):252–263, 1986.

[162] S. Maruyama. A molecular dynamics simulation of heat conduction in finite length SWNTs. *Physica B: Condensed Matter*, 323(1-4):193–195, 2002.

[163] J. C. Maxwell. On the dynamical theory of gases. *Philosophical Transactions of the Royal Society of London*, 157:49–88, 1867.

[164] S. W. McCue, B. Wu, and J. M. Hill. Micro/nanoparticle melting with spherical symmetry and surface tension. *IMA Journal of Applied Mathematics*, 74(3):439–457, 2009.

[165] A. J. H. McGaughey and M. Kaviany. Phonon transport in molecular dynamics simulations: formulation and thermal conductivity prediction. *Advances in heat transfer*, 39:169–255, 2006.

[166] A. J. H. McGaughey, E. S. Landry, D. P. Sellan, and C. H. Amon. Size-dependent model for thin film and nanowire thermal conductivity. *Applied Physics Letters*, 99(13):083109, 2011.

[167] K. C. Mills and L. Courtney. Thermophysical properties of silicon. *ISIJ international*, 40(Suppl):S130–S138, 2000.

[168] A. A. Minakov and C. Schick. Heat conduction in ultrafast thin-film nanocalorimetry. *Thermochimica Acta*, 640:42–51, 2016.

[169] N. Mingo and D. A. Broido. Carbon nanotube ballistic thermal conductance and its limits. *Physical Review Letters*, 95:096105, 2005.

[170] N. Mingo and D. A. Broido. Length dependence of carbon nanotube thermal conductivity and the ?problem of long waves? *Nano Letters*, 5(7):1221–1225, 2005.

[171] N. Mingo, L. Yang, D. Li, and A. Majumdar. Predicting the thermal conductivity of Si and Ge nanowires. *Nanoletters*, 3(12):1713–1716, 2003.

[172] S. L. Mitchell and T. G. Myers. Improving the accuracy of heat balance integral methods applied to thermal problems with time dependent boundary conditions. *International Journal of Heat and Mass Transfer*, 53(17-18):3540–3551, 2010.

[173] S. L. Mitchell and M. Vynnycky. Finite-difference methods with increased accuracy and correct initialization for one-dimensional Stefan problems. *Applied Mathematics and Computation*, 215(4):1609–1621, 2009.

[174] G. E. Moore. Cramming more components onto integrated circuits. *Electronics*, 38(8):114, 1965.

[175] A. M. Mullis. Rapid solidification within the framework of a hyperbolic conduction model. *International Journal of Heat and Mass Transfer*, 40(17):4085–4094, 1997.

[176] K. A. Muttalib and S. Abhinav. Suppressing phonon transport in nanowires: A simple model for phonon-surface-roughness interaction. *Physical Review B*, 96:075403, Aug 2017.

[177] T. G. Myers. Optimizing the exponent in the heat balance and refined integral methods. *International Communications in Heat and Mass Transfer*, 36(2):143–147, 2009.

[178] T. G. Myers. Optimal exponent heat balance and refined integral methods applied to stefan problems. *International Journal of Heat and Mass Transfer*, 53(5-6):1119–1127, 2010.

[179] T. G. Myers. Mathematical modelling of phase change at the nanoscale. *International Communications in Heat and Mass Transfer*, 76:59–62, 2016.

[180] T. G. Myers and F. Font. On the one-phase reduction of the Stefan problem with a variable phase change temperature. *International Communications in Heat and Mass Transfer*, 61:37–41, 2015.

[181] T. G. Myers, M. M. MacDevette, F. Font, and V. Cregan. Continuum mathematics at the nanoscale. *Journal of Mathematics in Industry*, 4(11), 2014.

[182] T. G. Myers and S. L. Mitchell. Application of the combined integral method to stefan problems. *Applied Mathematical Modelling*, 35(9):4281–4294, 2011.

[183] T. G. Myers, S. L. Mitchell, and F. Font. Energy conservation in the one-phase supercooled Stefan problem. *International Communications in Heat and Mass Transfer*, 39(10):1522–1525, 2012.

[184] T. N. Narasimhan. Fourier's heat conduction equation: History, influence, and connections. *Reviews of Geophysics*, 37(1):151–172, 1999.

[185] A. Nie, J. Liu, C. Dong, and H. Wang. Electrical failure behaviors of semiconductor oxide nanowires. *Nanotechnology*, 22(40):405703, 2011.

[186] H. Ockendon and J. R. Ockendon. *Viscous flow.* Cambridge University Press, 1995.

[187] G. S. Ohm. *Die galvanische Kette, mathematisch bearbeitet.* TH Riemann, 1827.

[188] Y. Okada and Y. Tokumaru. Precise determination of lattice parameter and thermal expansion coefficient of silicon between 300 and 1500 K. *Journal of Applied Physics*, 56(2):314–320, 1984.

[189] L. Onsager. Reciprocal relations in irreversible processes. I. *Physical Review*, 37(4):405–426, 1931.

[190] P. K. Panigrahi. *Transport Phenomena in Microfluidic Systems.* John Wiley & Sons Singapore Pte. Ltd, 2016.

[191] R. E. Peierls. *Quantum Theory of Solids.* Oxford University Press, 1955.

[192] V. Peshkov. Determination of the velocity of propagation of the second sound in helium ii. *Journal of Physics USSR*, 10:389–398, 1946.

[193] I. Ponomareva, D. Srivastava, and M. Menon. Thermal conductivity in thin silicon nanowires: phonon confinement effect. *Nano Letters*, 7(5):1155–1159, 2007.

[194] H. W. C. Postma, T. Teepen, Z. Yao, M. Grifoni, and C. Dekker. Carbon nanotube single-electron transistors at room temperature. *Science*, 293(5527):76–79, 2001.

[195] E. W. Prohofsky and J. A. Krumhansl. Second-sound propagation in dielectric solids. *Physical Review*, 133:A1403–A1410, 1964.

[196] T. Q. Qiu and C. L. Tien. Heat transfer mechanisms during short-pulse laser heating of metals. *Journal of Heat Transfer*, 115(4):835–841, 1993.

[197] K. T. Regner, D. P. Sellan, Z. Su, C. H. Amon, A. J. H. McGaughey, and J. A. Malen. Broadband phonon mean free path contributions to thermal conductivity measured using frequency domain thermoreflectance. *Nature Communications*, 4:1640, 2013.

[198] M. Reibold, P. Paufler, A. A. Levin, W. Kochmann, N. Pätzke, and D. C. Meyer. Materials: Carbon nanotubes in an ancient Damascus sabre. *Nature*, 444(7117):286, 2006.

[199] H. Ribera and T. Myers. A mathematical model for nanoparticle melting with size-dependent latent heat and melt temperature. *Microfluidics and Nanofluidics*, 20(11):147, 2016.

[200] M. M. Rojo, B. Abad, C. V. Manzano, P. Torres, X. Cartoixà, F. X. Alvarez, and M. M. Gonzalez. Thermal conductivity of $Bi_2Te_3$ nanowires: How size affects phonon scattering. *Nanoscale*, 9(20):6741–6747, 2017.

[201] M. E. Rose. A method for calculating solutions of parabolic equations with a free boundary. *Mathematics of Computation*, pages 249–256, 1960.

[202] D. M. Rowe. *Thermoelectrics Handbook: Macro to Nano*. CRC Press, 2018.

[203] N. Sadoun, E.-K. Si-Ahmed, and P. Colinet. On the refined integral method for the one-phase stefan problem with time-dependent boundary conditions. *Applied Mathematical Modelling*, 30(6):531–544, 2006.

[204] M. Saiz-Bretín, A. V. Malyshev, F. Domínguez-Adame, D. Quigley, and R. A. Römer. Lattice thermal conductivity of graphene nanostructures. *Carbon*, 127:64–69, 2018.

[205] O. V. Salata. Applications of nanoparticles in biology and medicine. *Journal of Nanobiotechnology*, 2(1):3, 2004.

[206] S. Salsa. *Partial differential equations in action: from modelling to theory*, volume 99. Springer, 2016.

[207] N. N. Salva and D. A. Tarzia. Explicit solution for a Stefan problem with variable latent heat and constant heat flux boundary conditions. *Journal of Mathematical Analysis and Applications*, 379(1):240–244, 2011.

[208] A. P. S. Sawhney, B. Condon, K. V. Singh, S.-S. Pang, G. Li, and D. Hui. Modern applications of nanotechnology in textiles. *Textile Research Journal*, 78(8):731–739, 2008.

[209] J. Segura. Bounds for ratios of modified Bessel functions and associated Turán-type inequalities. *Journal of Mathematical Analysis and Applications*, 374(2):516–528, 2011.

[210] A. Sellitto, F. X. Alvarez, and D. Jou. Temperature dependence of boundary conditions in phonon hydrodynamics of smooth and rough nanowires. *Journal of Applied Physics*, 107(11):114312, 2010.

[211] A. Sellitto, F. X. Alvarez, and D. Jou. Geometrical dependence of thermal conductivity in elliptical and rectangular nanowires. *International Journal of Heat and Mass Transfer*, 55(11):3114–3120, 2012.

[212] A. Sellitto, I. Carlomagno, and D. Jou. Two-dimensional phonon hydrodynamics in narrow strips. *Proceedings of the Royal Society of London A: Mathematical, Physical and Engineering Sciences*, 471(2182), 2015.

[213] J.-H. Shim, B.-J. Lee, and Y. W. Cho. Thermal stability of unsupported gold nanoparticle: a molecular dynamics study. *Surface science*, 512(3):262–268, 2002.

[214] J.-H. Shin and M. R. Deinert. A model for the latent heat of melting in free standing metal nanoparticles. *Journal of Chemical Physics*, 140:164707, 2014.

[215] J. Shiomi and S. Maruyama. Non-Fourier heat conduction in a single-walled carbon nanotube: Classical molecular dynamics simulations. *Physical Review B*, 73(20):205420, 2006.

[216] M. E. Siemens, Q. Li, R. Yang, K. A. Nelson, E. H. Anderson, M. M. Murnane, and H. C. Kapteyn. Quasi-ballistic thermal transport from nanoscale interfaces observed using ultrafast coherent soft X-ray beams. *Nature Materials*, 9(1):26, 2010.

[217] G. D. Smith. *Numerical Solution of Partial Differential Equations: Finite Difference Methods*. Clarendon Press, 1985.

[218] S. L. Sobolev. Transport processes and traveling waves in systems with local nonequilibrium. *Soviet Physics Uspekhi*, 34(3):217, 1991.

[219] S. L. Sobolev. Two-temperature Stefan problem. *Physics Letters A*, 197(3):243–246, 1995.

[220] S. L. Sobolev. The local-nonequilibrium temperature field around the melting and crystallization front induced by picosecond pulsed laser irradiation. *International Journal of Thermophysics*, 17(5):1089–1097, 1996.

[221] S. L. Sobolev. Rapid phase transformation under local non-equilibrium diffusion conditions. *Materials Science and Technology*, 31(13):1607–1617, 2015.

[222] M. Soini, I. Zardo, E. Uccelli, S. Funk, G. Koblmüller, A. Fontcuberta i Morral, and G. Abstreiter. Thermal conductivity of GaAs nanowires studied by micro-Raman

spectroscopy combined with laser heating. *Applied Physics Letters*, 97(26):263107, 2010.

[223] A. D. Solomon, V. Alexiades, D. G. Wilson, and J. Drake. On the formulation of hyperbolic Stefan problems. *Quarterly of Applied Mathematics*, 43(3):295–304, 1985.

[224] J. Stefan. Über die Theorie der Eisbildung, insbesondere über die Eisbildung im Polarmeere. *Annalen der Physik*, 278(2):269–286, 1891.

[225] B. Stritzker, A. Pospieszczyk, and J. A. Tagle. Measurement of lattice temperature of silicon during pulsed laser annealing. *Physical Review Letters*, 47(5):356, 1981.

[226] J. Sun and S. L. Simon. The melting behavior of aluminum nanoparticles. *Thermochimica Acta*, 463(1):32–40, 2007.

[227] N. Taniguchi. On the basic concept of nanotechnology. *Proceedings of the International Conference on Production Engineering, Tokyo*, pages 18–23, 1974.

[228] L. Tisza. Transport phenomena in helium II. *Nature*, 141(3577):913, 1938.

[229] R. C. Tolman. The effect of droplet size on surface tension. *The Journal of Chemical Physics*, 17(3):333–337, 1949.

[230] S. Torii and W.-J. Yang. Heat transfer mechanisms in thin film with laser heat source. *International Journal of Heat and Mass Transfer*, 48(3):537–544, 2005.

[231] P. Torres. *Thermal transport in semiconductors: first principles and phonon hydrodynamics.* PhD thesis, Universitat Autònoma de Barcelona, 2017.

[232] P. Torres. *Kinetic Collective Model: BTE-based hydrodynamic model for thermal transport*, 2018 (accessed November 13, 2018).

[233] P. Torres, C. de Tomas, A. Lopeandia, X. Cartoixà, and F. X. Alvarez. Thermal conductivity of bulk and nanoscaled Si/Ge alloys from the kinetic collective model. *arXiv preprint arXiv:1506.01522*, 2015.

[234] P. Torres, A. Torelló, J. Bafaluy, J. Camacho, X. Cartoixà, and F. X. Alvarez. First principles Kinetic-Collective thermal conductivity of semiconductors. *Physical Review B*, 95(4):165407, 2017.

[235] P. Torres, A. Ziabari, A. Torelló, J. Bafaluy, J. Camacho, X. Cartoixà, A. Shakouri, and F. X. Alvarez. Emergence of hydrodynamic heat transport in semiconductors at the nanoscale. *Physical Review Materials*, 2(7):076001, 2018.

[236] T. Tsuzuki. Commercial scale production of inorganic nanoparticles. *International Journal of Nanotechnology*, 6(5-6):567–578, 2009.

[237] D. Y. Tzou. The generalized lagging response in small-scale and high-rate heating. *International Journal of Heat and Mass Transfer*, 38(17):3231–3240, 1995.

[238] D. Y. Tzou. Nonlocal behaviour in phonon transport. *International Journal of Heat and Mass Transfer*, 54(1):475–481, 2011.

[239] D. Y. Tzou. *Macro- to Microscale Heat Transfer: The Lagging Behavior*. Taylor & Francis, 2014.

[240] D. Y. Tzou and Z.-Y. Guo. Nonlocal behavior in thermal lagging. *International Journal of Thermal Sciences*, 49(7):1133–1137, 2010.

[241] P. Ván, A. Berezovski, T. Fülöp, G. Gróf, R. Kovács, Á. Lovas, and J. Verhás. Guyer-Krumhansl-type heat conduction at room temperature. *EPL (Europhysics Letters)*, 118(5):50005, 2017.

[242] R. Venkatasubramanian, E. Siivola, T. Colpitts, and B. O'Quinn. Thin-film thermoelectric devices with high room-temperature figures of merit. *Nature*, 413:597–602, 2001.

[243] B. Vermeersch, J. Carrete, N. Mingo, and A. Shakouri. Superdiffusive heat conduction in semiconductor alloys. I. Theoretical foundations. *Physical Review B*, 91:085202, 2015.

[244] B. Vermeersch, A. M. S. Mohammed, G. Pernot, Y. R. Koh, and A. Shakouri. Superdiffusive heat conduction in semiconductor alloys. II. Truncated Lévy formalism for experimental analysis. *Physical Review B*, 91:085203, 2015.

[245] P. Vernotte. Les paradoxes de la theorie continue de l'equation de la chaleur. *Comptes*

*Rendus Hebdomadaires Des Seances De L Academie Des Sciences*, 246(22):3154–3155, 1958.

[246] V. R. Voller. An exact solution of a limit case Stefan problem governed by a fractional diffusion equation. *International Journal of Heat and Mass Transfer*, 53(23-24):5622–5625, 2010.

[247] H.-D. Wang. *Theoretical and Experimental Studies on Non-Fourier Heat Conduction Based on Thermomass Theory.* Springer Theses. Springer, 2014.

[248] M. Wang, B.-Y. Cao, and Z.-Y. Guo. General heat conduction equations based on the thermomass theory. *Frontiers in Heat and Mass Transfer*, 1(1):1–8, 2010.

[249] M. Wang and Z.-Y. Guo. Understanding of temperature and size dependences of effective thermal conductivity of nanotubes. *Physics Letters A*, 374(42):4312–4315, 2010.

[250] M. Wang, N. Yang, and Z.-Y. Guo. Non-Fourier heat conductions in nanomaterials. *Journal of Applied Physics*, 110(6):064310, 2011.

[251] J. C. Ward and J. Wilks. Second sound and the thermo-mechanical effect at very low temperatures. *The London, Edinburgh, and Dublin Philosophical Magazine and Journal of Science*, 43(336):48–50, 1952.

[252] H. Weber. *Die Partiellen Differential-Gleichungen der Mathematischen Physik.* Vieweg und Sohn, Braunschweig, 1901.

[253] R. B. Wilson and D. G. Cahill. Anisotropic failure of Fourier theory in time-domain thermoreflectance experiments. *Nature Communications*, 5:5075, 2014.

[254] C. R. M. Wronski. The size dependence of the melting point of small particles of tin. *British Journal of Applied Physics*, 18(12):1731, 1967.

[255] B. Wu, S. W. McCue, P. Tillman, and J. M. Hill. Single phase limit for melting nanoparticles. *Applied Mathematical Modelling*, 33(5):2349–2367, 2009.

[256] S. Xiong, W. Qi, Y. Cheng, B. Huang, M. Wang, and Y. Li. Universal relation for size dependent thermodynamic properties of metallic nanoparticles. *Physical Chemistry Chemical Physics*, 13(22):10652–10660, 2011.

[257] M. Xu. Slip boundary condition of heat flux in knudsen layers. *Proceedings of the Royal Society of London A: Mathematical, Physical and Engineering Sciences*, 470(2161), 2014.

[258] M. Xu and X. Li. The modeling of nanoscale heat conduction by Boltzmann transport equation. *International Journal of Heat and Mass Transfer*, 55(7-8):1905–1910, 2012.

[259] Y.-S. Xu and Z.-Y. Guo. Heat wave phenomena in IC chips. *International Journal of Heat and Mass Transfer*, 38(15):2919–2922, 1995.

[260] N. Yang, G. Zhang, and B. Li. Violation of Fourier's law and anomalous heat diffusion in silicon nanowires. *Nano Today*, 5(2):85–90, 2010.

[261] Y. Yao, M. T. McDowell, I. Ryu, H. Wu, N. Liu, L. Hu, W. D. Nix, and Y. Cui. Interconnected silicon hollow nanospheres for lithium-ion battery anodes with long cycle life. *Nano letters*, 11(7):2949–2954, 2011.

[262] Z. M. Zhang. *Nano/Microscale Heat Transfer*. McGraw Hill Professional, 2007.

[263] Y. Zhou, Y.-J. Wang, and W.-K. Bu. Exact solution for a Stefan problem with latent heat a power function of position. *International Journal of Heat and Mass Transfer*, 69:451–454, 2014.

[264] C.-Y. Zhu, W. You, and Z.-Y. Li. Nonlocal effects and slip heat flow in nanolayers. *Scientific Reports*, 7:9568, 2017.

[265] A. Ziabari, P. Torres, B. Vermeersch, Y. Xuan, X. Cartoixà, A. Torelló, J.-H. Bahk, Y. R. Koh, M. Parsa, P. D. Ye, F. X. Alvarez, and A. Shakouri. Full-field thermal imaging of quasiballistic crosstalk reduction in nanoscale devices. *Nature Communications*, 9(1):255, 2018.

[266] J. M. Ziman. *Electrons and Phonons: The Theory of Transport Phenomena in Solids*. Oxford University Press, 2001.